Vertical profiling of aerosol optical properties with multiwavelength aerosol lidar during the Saharan Mineral Dust Experiments

Der Fakultät für Physik und Geowissenschaften

der Universität Leipzig

eingereichte

Dissertation

zur Erlangung des akademischen Grades

Doctor rerum naturalium

Dr. rer. nat.

vorgelegt

von Diplom–Meteorologe Matthias Tesche

geboren am 27. Januar 1981 in Leipzig

Gutachter: Prof. Dr. Manfred Wendisch

Prof. Dr. Lucas Alados–Arboledas

Tag der Verleihung: 18. Juli 2011

Bibliographische Beschreibung:

Tesche, Matthias
Vertical profiling of aerosol optical properties with multiwavelength aerosol lidar during the Saharan Mineral Dust Experiments
Universität Leipzig, Dissertation
163 S., 220 Lit., 43 Abb., 4 Tab.

Referat:

Die vorliegende Arbeit beschäftigt sich mit der Auswertung und den Ergebnissen von Mehrwellenlängen–Polarisations–Ramanlidarmessungen, die im Rahmen des Saharastaubschließungsexperiments Saharan Mineral Dust Experiment (SAMUM) durchgeführt wurden. Das SAMUM–Projekt erstreckte sich über zwei Intensivmesszeiträume im Mai und Juni 2006 in Marokko (SAMUM–1) und im Januar und Februar 2008 auf den Kapverdischen Inseln (SAMUM–2). Desweiteren werden zusätzliche Lidarmessungen besprochen, die im Mai und Juni 2008 auf den Kapverdischen Inseln durchgeführt wurden. Die geometrischen und optischen Eigenschaften der während dieser Experimente mit mehreren hochmodernen Lidargeräten beobachteten Mineralstaub- und Biomassenverbrennungsaerosolschichten werden anhand von Fallstudien und mehrwöchigen, höhenaufgelösten Mittelwerten beschrieben. Zudem werden Kalibrierungen und Korrekturen vorgestellt, die zur Qualitätssicherung der gewonnenen Messdaten durchgeführt wurden. Ein im Rahmen der Arbeit entwickeltes, auf quantitativen Messungen des linearen Partikeldepolarisationsverhältnisses basierendes Verfahren zur höhenaufgelösten Trennung der Anteile von Mineralstaub und Biomassenverbrennungsaerosol an den während SAMUM–2 gemessenen Rücktreu- und Extinktionsprofilen wird vorgestellt und angewandt.
Die Auswertung der Mehrwellenlängenlidarmessungen der SAMUM–Kampagnen ermöglichte eine spektral aufgelöste Charakterisierung der optischen Eigenschaften von Saharastaubpartikeln. Besondere Aufmerksamkeit wurde auf die Bestimmung der intensiven Parameter Extinktions–zu–Rückstreuverhältnis (Lidarverhältnis), lineares Partikeldepolarisationsverhältnis sowie Ångströmexponent der Rückstreu- und Extinktionskoeffizienten gelegt. Die im Rahmen von SAMUM bei den Wellenlängen 355, 532 und 1064 nm durchgeführten Lidarmessungen ergaben mittlere Lidarverhältnisse von 55±5 sr für reinen Saharastaub. Während SAMUM wurden außerdem erstmals quantitative Messergebnisse des linearen Partikeldepolarisationsverhältnisses von reinem Saharastaub bei mehreren Wellenlängen gewonnen. Die mittleren Werte dieser Größe lagen bei 0.26±0.06 (355 und 1064 nm), 0.31±0.03 (532 nm) und 0.37±0.07 (710 nm). Diese Erkenntnisse liefern wichtige Informationen für die Auswertung von Messungen mit weniger fortschrittlichen Lidargeräten. Die durch SAMUM gewonnenen Erkenntnisse der optischen Eigenschaften von Mineralstaub erlauben eine eindeutige Identifikation des Staubanteils in Aerosolschichten im Abluftbereich der Wüsten. Zudem wurden Richtgrößen ermittelt, die zur Validierung von Modellen zur Beschreibung von Lichtstreuung an großen, nicht–kugelförmigen Teilchen verwendet werden können. Derartige Streumodelle werden für die Auswertung von Messungen der optischen Eigenschaften von Mineralstaubpartikeln mit passiven Sensoren benötigt und befinden sich zur Zeit eher in einer frühen Entwicklungsphase.

Contents

1 Introduction

Together with sea salt, mineral dust is the most abundant natural aerosol in the atmosphere. When lifted over the Earth's deserts, mineral dust can form deep layers in which particles are transported over thousands of kilometers (Goudie and Middleton 2001). Thus despite having just few distinct sources, desert dust is distributed over the entire globe. The main transport regimes are from the Saharan desert to the Caribbean and southern America (Prospero and Carlson 1972, Kaufman et al. 2005, Liu et al. 2008a, b, Ben-Ami et al. 2009, Schepanski et al. 2009, Huang et al. 2010, Evan and Mukhopadhyay 2010) or over the Mediterranean to Europe and the Middle East (Balis et al. 2004, Mona et al. 2006, Pérez et al. 2006a, Papayannis et al. 2008, Müller et al. 2009), from the Arabic peninsula to the Indian ocean (Sokolik et al. 2001), and from the central Asian deserts Gobi and Taklimakan over Korea and Japan (Uematsu et al. 1983, Liu et al. 2003, Uno et al. 2008) to the west coast of northern America (Duce et al. 1980, Parrington et al. 1983, Husar et al. 2001, VanCuren and Cahill 2002). Dust deposits are found in coral reefs all over the world (Garrison et al. 2003). Dust is hypothesized to be the main source of nutrients in the Amazon rain forest. Saharan dust is also assumed to influence the formation of tropical cyclones in the mid–Atlantic (Evan et al. 2006, Wu 2007, Sun et al. 2008).

Mineral dust in the atmosphere absorbs and scatters sunlight and thus influences the Earth's radiation budget. The magnitude and sign of the dust radiative forcing strongly depends on the optical properties and the spatial and vertical distribution of dust in the atmosphere as well as the reflectance of the underlying surface (Myhre et al. 2003, Heinold et al. 2009). Furthermore, the size and strongly irregular shape of mineral dust particles poses large difficulties to radiative–transfer modeling, especially if it comes to reproducing the results of remote–sensing measurements that strongly depend on the shape of the scatterers (Müller et al. 2010b). Because classical Mie theory (which is valid for spheres, Mie 1908) cannot be applied for these calculations, elaborate light–scattering models have to be developed (Mishchenko et al. 1997, Nousiainen et al. 2003, Kalashnikova et al. 2005, Nousiainen 2009, Gasteiger et al. 2011).

To improve our knowledge of the complex interaction of mineral dust particles with the radiation field, Sokolik et al. (2001) recommended to arrange column closure experiments on mineral dust with focus on height–resolved investigations of the chemical, microphysical, optical, and radiative properties of dust particles. Even though ten years passed since this recommendation, still only few comprehensive, vertically resolved investigations of mineral dust exist. Several case studies of the duration, transport paths, and vertical extent of dust outbreaks towards Europe, America, Korea, and

Japan as observed with lidar[1], especially in the framework of the European Aerosol Research Lidar Network (EARLINET, Bösenberg et al. 2001) and the Asian Dust Network (AD–Net, Murayama et al. 2001), are reported. Such cases are presented, e.g., by Murayama et al. (2001), Mattis et al. (2002), Ansmann et al. (2003), Müller et al. (2003), Balis et al. (2004), Mona et al. (2006), Pérez et al. (2006a), Papayannis et al. (2008), and Müller et al. (2009). Furthermore, large experiments like the Puerto Rican Dust Experiment (PRIDE, Reid et al. 2003), the Saharan Dust Experiment (SHADE, Tanré et al. 2003), the Dust and Biomass–burning Experiment (DABEX, Haywood et al. 2008), and the United Arab Emirates Unified Aerosol Experiment (UAE^2, Reid et al. 2008) were conducted during the last decade. However, no significant progress in the quantification of the direct climate impact of mineral dust and in the parameterization of the radiative effects of this kind of aerosol in numerical models was achieved. This deficiency might be due to several reasons. First, the experiments and case studies only captured snapshots of the actual dust situation and cannot be used to generalize the effects associated with mineral dust. For instance, SHADE in the region of Cape Verde lasted only for ten days in September 2000. Second, the experiments were not designed to collect the data necessary to understand all the feedback mechanisms related to mineral dust. For example, PRIDE in the Caribbean in June and July of 2001 did not aim at a closure between *in situ* and remote–sensing measurements but rather focused on a general scale analysis. Third, the experiments simply were too far away from the source region (PRIDE in the Caribbean and SHADE at Cape Verde) and did not encounter pure dust conditions that are needed for a reliable aerosol characterization. And forth, the lack of adequate profiling of the dust extinction coefficient (e.g., during the UAE^2 experiment in August and September of 2004) prohibits a detailed view on the relationship between the optical, microphysical, and chemical properties of dust particles, their morphological characteristics, and their radiative impact.

Therefore, the first **SA**haran **M**ineral d**U**st experi**M**ent (SAMUM–1, Heintzenberg 2009) was conducted in southern Morocco in May and June of 2006. SAMUM–1 incorporated comprehensive lidar measurements of extensive and intensive aerosol parameters and vertically resolved, airborne *in situ* observations to study the microphysical, chemical, optical, and radiative properties of mineral dust. The lidar station was used as an anchor for airborne particle sampling and radiation measurements. Flight patterns were arranged to cover the atmospheric column in the vicinity of the laser beam. This approach facilitated closure studies of optical remote measurements and coinciding, co–located *in situ* measurements. These studies were performed near the source region of Saharan dust, at a minimum influence of maritime and anthropogenic particles. Thus SAMUM–1 constituted the first column closure experiment on pure mineral dust in the tradition of the North Atlantic Regional Aerosol Characterization Experiment 2 (ACE–2, Russell and Heintzenberg 2000) and the Lindenberg Aerosol Characterization Experiment 1998 (LACE 98, Ansmann et al. 2002a).

In the second step of the SAMUM project—and following the suggestions given by Sokolik et al. (2001)—measurements comparable to the ones during SAMUM–1 were performed in January and February of 2008 at Cape Verde (SAMUM–2a, Ansmann

[1]light detection and ranging; a technique of active remote sensing that uses a laser as light source

et al. 2011), thousands of kilometers west of the regions of dust emission and in the center of the regime of long–range transport of dust from Africa to the Americas. As during SAMUM–1, monitoring of the aerosol stratification with ground–based lidar enabled an optimized strategy for airborne measurements, i.e., the research aircraft could be piloted directly into the height regions of interest. Additional lidar measurements were conducted at Cape Verde in May and June of 2008 (SAMUM–2b) to characterize the geometrical and optical properties of the dust layer during summer transport conditions. Because this campaign is not a part of the original SAMUM–2 column closure experiment, no airborne *in situ* observations were performed during this period.

As yet, the lidar observations during SAMUM constitute the most comprehensive data set on mineral dust to be collected. State–of–the–art lidars (like the ones that participated in SAMUM) enable vertical profiling of the backscatter and extinction coefficients of the aerosol particles in the atmospheric column above the measurement site. Furthermore, intensive properties like the Ångström exponent or the lidar–specific parameters extinction–to–backscatter ratio (lidar ratio) and particle depolarization ratio can be measured. Intensive particle properties depend on the shape, size, and complex refractive index of the aerosol particles and can be used for aerosol characterization (Müller et al. 2007). Profiling of these parameters allows one to draw conclusions about the kind of the particles present over the lidar. Because lidar measurements of pure mineral dust plumes are scarce (mostly it cannot be clarified whether an observed dust plume was altered during transport to the lidar site or not), the observations of SAMUM provide first–hand insight into intensive parameters of pure Saharan dust. In addition, the extensive parameters (i.e., backscatter and extinction coefficients) can be used to characterize the progression and intensity of a dust event. Profiles of the extinction coefficient are an important input parameter for radiative–transfer modeling which is used to investigate the radiative (climate) effect of mineral dust in the atmosphere.

This dissertation presents the analysis of the measurements performed with the Backscatter Extinction lidar–Ratio Temperature Humidity Apparatus (BERTHA) lidar during SAMUM in Morocco and at Cape Verde in the context of the SAMUM column closure observations. The optical properties of Saharan dust are characterized by means of profiles of extensive and intensive parameters. Calibrations and corrections necessary for quality assurance of the collected data and a depolarization–based method for the height–resolved separation of the contributions of different aerosol types to the measured optical aerosol profiles are presented and discussed. The thesis starts with an overview of the SAMUM experiments and a review of the source regions of Saharan dust together with the seasonal variation of the aerosol conditions west of the African continent in Chapter 2. Chapter 3 gives the theoretical background of the processes studied in the framework of this work and summarizes the measurement techniques and data analysis methods which were applied for this purpose. An overview of the capabilities for aerosol characterization with lidar follows in Chapter 4, before the remote–sensing instruments that were employed during the SAMUM campaigns are introduced in Chapter 5. The data collected in Morocco and at Cape Verde are presented and discussed in Chapter 6. The summary in Chapter 7 illustrates the comprehensive results of the individual campaigns and concludes this thesis.

2 The SAMUM Campaigns

> *Samum* ["poison wind", English *simoom*, Arabic *samūm*, from *samma*, to poison, from Aramaic *sammā*, drug, poison]: a strong, dry, dust–laden local wind that occurs in the Sahara, Palestine, Israel, Jordan, Syria, and the deserts of the Arabian Peninsula. It rarely lasts for longer than 15–20 minutes and is characterized by a temperature of more than 50 °C and very low humidity—harsh conditions that may cause a heat stroke to an exposed creature.
>
> *Source:* wikipedia.org

The **SA**haran **M**ineral d**U**st experi**M**ent (SAMUM) focused on the characterization of the microphysical, chemical, optical, and radiative properties of mineral dust aerosol together with its temporal and spatial distribution near the Sahara—the Earth's largest source of this kind of particles—and in the regime of intercontinental transport over the Atlantic ocean. The SAMUM consortium is a research group (Forschergruppe) funded by the German Science Foundation (Deutsche Forschungsgemeinschaft) and is a cooperation of atmospheric scientists of the University of Bremen, the Technical University of Darmstadt, the Gutenberg University of Mainz, the Ludwig–Maximilians–University of Munich, the Leibniz Institute for Tropospheric Research (IfT), Leipzig, and the German Aerospace Center (DLR), Oberpfaffenhofen. The combined expertise of these institutes allowed for a detailed investigation of dust–related effects including airborne particle sampling and radiation measurements.

Section 2.1 gives an overview of the rationale of the SAMUM project and its two–step approach. Sections 2.2 and 2.3 describe the source regions of mineral dust in northern Africa, the seasonal patterns of aerosol transport, and the influence of biomass–burning aerosols to the aerosol layers over the tropical east Atlantic. An overview of the instrumentation at the field sites in Morocco and at Cape Verde is given in Section 2.4.

2.1 Concept and Design

After the First International Workshop on Mineral Dust which was held from 9–11 June 1999 in Boulder, USA, Sokolik et al. (2001) recommended "*urgent needs for future work*" regarding the characterization of mineral dust aerosol and its radiative properties. As mentioned in Chapter 1, several large field experiments (e.g., PRIDE, SHADE, DABEX, and UAE^2) were conducted since this dictum was spoken. However, until

SAMUM none followed the idea of a two–step column closure experiment for mineral dust: one near the source region and one in the regime of long–range transport.

Mineral dust particles show very different radiative behavior depending on their elevation, their state of mixing with other aerosol types, and the albedo of the underlying surface. Therefore, they have to be characterized as close to the source as possible, i.e., under pure dust conditions immediately after the emission. Only when this is done, conclusions can be drawn from observations that are performed far away from the source regions, e.g., to study in which way aging of dust particles affects the optical properties of mineral dust. Consequently, the SAMUM project was designed to consist of two column closure experiments with identical layout. The first experiment (SAMUM–1, Heintzenberg 2009) was conducted in Morocco close to major source regions of mineral dust in central Algeria and western Tunisia (Knippertz et al. 2009). Measurements of microphysical, optical, radiative, chemical, and morphological properties of mineral dust particles were performed during the one–month period. Dust transport and radiative effects were investigated by means of modeling studies. Eighteen months later, a second experiment (SAMUM–2, Ansmann et al. 2011) was performed on Santiago, the main island of the Republic of Cape Verde, which is located in the regime of intercontinental long–range transport of mineral dust and biomass–burning smoke from Africa towards the Americas.

Figure 2.1 gives an overview of the location of the measurement sites (stars) during SAMUM–1 (red) and SAMUM–2 (green). The red and green patterns around the measurement sites denote the area that was covered by aircraft measurements during the respective experiments. The boxes mark the approximate geographical area that influenced the observations during the respective experiment. Further features of Figure 2.1 are discussed in the next section.

2.2 Dust Sources in Northern Africa

The source regions of Saharan dust are identified by geographical considerations and satellite remote sensing (Goudie and Middleton 2001, Prospero et al. 2002, Schepanski et al. 2007). Other than one might initially guess, the major Saharan sand seas and dune fields are no dominant regions of dust mobilization. It is rather found that the source regions are located at topographical lows or in the vicinity of mountain ranges (Goudie and Middleton 2001, Prospero et al. 2002, Engelstaedter et al. 2006). The main source regions of Saharan dust are the Bodélé depression in Chad and a large area in the west Sahara that covers northern Mali, southern Algeria, and eastern Mauritania and extends to the Atlantic coast of Mauritania. A simplified overview of the main dust sources in North Africa is given in Figure 2.1. Gray shaded areas denote mountain ranges (i.e., Atlas Mountains, Adrar des Ifoghas, Ahaggar Mountains, Eneddi Plateau, Massif de l'Aïr, and Tibesti Massif). Dust source regions identified in the studies by Goudie and Middleton (2001), Prospero et al. (2002), Engelstaedter et al. (2006), Schepanski et al. (2007), and Knippertz et al. (2009) are illustrated as yellow areas. The

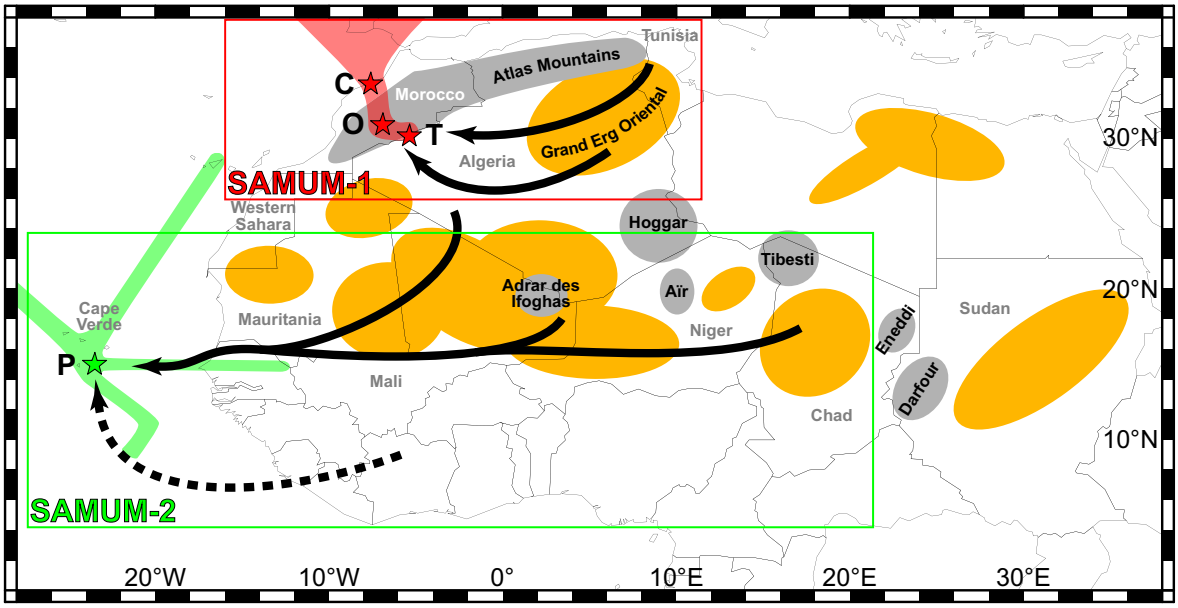

Figure 2.1: Location of the Moroccan measurement sites Casablanca (C), Ouarzazate (O), and Tinfou (T) during SAMUM–1 (red) and of Praia (P) during SAMUM–2 at Cape Verde (green) together with flight patterns (red and green shades around the measurement sites), source regions of mineral dust (yellow), mountain ranges (gray), and favorable transport paths (arrows). The boxes mark the regions that had an impact on the respective experiments.

arrows denote the transport paths of Saharan dust (solid) and biomass–burning smoke (dashed, see Section 2.3) to the measurement sites in Morocco (summer of 2006) and at Cape Verde (winter of 2008), as identified by Knippertz et al. (2009) and Knippertz et al. (2011), respectively.

Dust emission and dust source activation generally is associated with strong surface winds like the Harmattan, the dry northeasterly winds that dominate over most of the Sahara and Sahel during the northern hemispheric dry season (December to March). Engelstaedter and Washington (2007) note that the annual cycle of the activity of the dust sources in western Africa is controlled by dry convection which comes along with an increase in the occurrence of small–scale high–wind events. Furthermore, dust is often mobilized in the morning hours, when the nocturnal low–level jet breaks down with the beginning evolution of the planetary boundary layer and momentum is mixed to the surface (Knippertz 2008, Schepanski et al. 2009). Other likely meteorological effects that cause the strong winds necessary to trigger dust mobilization are squall lines and density currents which are associated with moist convection (Knippertz 2008, Knippertz et al. 2009, Schepanski et al. 2007, 2009).

The region of influence for the findings of SAMUM–1 is marked by a red box in Figure 2.1. From the synoptic analysis and together with the mineralogical properties of the collected particle samples (Kandler et al. 2009), Knippertz et al. (2009) conclude that the mineral dust observed at the SAMUM–1 measurement sites originated from a geographical area which stretches from western Tunisia to central Algeria (marked

as Grand Erg Oriental). The emission of mineral dust from these source regions was related to cold surges from the Mediterranean in association with eastward passing upper–level waves and lee cyclogeneses south of the Atlas Mountains. Furthermore, dust was emitted locally due to a cut–off low over northwestern Africa and gust fronts that were caused by dry thunderstorms (Knippertz et al. 2007). Dust was advected to the measurement sites directly from the source regions (black arrows in Algeria), which minimizes the impact of maritime, anthropogenic, or biogenic aerosols to the usually 4–5–km deep dust layers observed at Ouarzazate during SAMUM–1.

The region that needs to be considered as possible influence for the measurements of SAMUM–2a is indicated by a green box in Figure 2.1. Compared to SAMUM–1 in Morocco the advection of dust to the measurement site at Cape Verde during winter is more complex and occurs over a period of up to five days (Knippertz et al. 2011). During winter and spring, anticyclonic conditions over northern Africa and cold–air intrusions from mid–latitudes cause intense Saharan dust storms (Kalu 1979). These storms can be enhanced by evaporational cooling (Knippertz and Fink 2006, Knippertz 2008). The resulting intensification of the Harmattan causes localized emissions (Washington and Todd 2005) and in strong cases long, fast–moving dust fronts (Knippertz and Fink 2006, Slingo et al. 2006). The intensity of the subtropical anticyclone over the eastern Atlantic and northern Africa determines the emission and westward transport of mineral dust from northern Africa. This association is supported by modeling studies which find a positive correlation of dust transport and North Atlantic Oscillation (Mahowald et al. 2003, Ginoux et al. 2004, Chiapello et al. 2005). The dust transport path observed during SAMUM–2a (black arrow over Chad, Niger, Mali, and Mauritania in Figure 2.1, Knippertz et al. 2011) is in agreement with the observations of Chiapello et al. (1997) who found this so–called Sahelian transport pattern to be typical for December and January. Chiapello et al. (1997) also state that this transport pattern causes the most intense dust events and the highest surface dust concentrations at Cape Verde. During the other months, dust is mostly advected from the northern and western Sahara. The dashed arrow in Figure 2.1 indicates the route of transport of biomass–burning aerosol from southern West Africa to Cape Verde during winter. This topic is approached in the next section.

2.3 Aerosol in the Outflow Region of West Africa

The long–range transport of Saharan dust from Africa to the Americas shows a pronounced seasonal dependence which is strongly related to the movement of the inter–tropical convergence zone (ITCZ). During summer, dust is transported by the easterlies within a warm, dry, and well–separated Saharan air layer (SAL, Prospero and Carlson 1972, 1980). Up to 4–6 km deep aerosol layers are transported to the Caribbean Sea, the Gulf of Mexico, and the southern United States (Prospero and Carlson 1972, Karyampudi et al. 1999, Kaufman et al. 2005, Liu et al. 2008b, Ben-Ami et al. 2009, 2010, Schepanski et al. 2009, Huang et al. 2010, Evan and Mukhopadhyay 2010). During winter, when the ITCZ retreats south, dust layers are restricted to a height of 1–2 km

(Chiapello et al. 1995). Now, Saharan dust is transported to South America or deposited into the ocean (Kaufman et al. 2005, Liu et al. 2008b, Ansmann et al. 2009c, Ben-Ami et al. 2009, Schepanski et al. 2009). Furthermore, the dust layer is topped by biomass–burning aerosol from fires in southern West Africa (Prospero and Carlson 1972, Kalu 1979, Cooke et al. 1996, Barbosa et al. 1999, Ben-Ami et al. 2009, Schepanski et al. 2009). These lofted layers can also contain significant amounts of mineral dust (Johnson et al. 2008b, Tesche et al. 2009b).

Figure 2.2 illustrates the seasonal variation of the position of the ITCZ—over the equator in winter and in a band between 10° and 20° N in summer—and its influence on the transport of Saharan dust and biomass–burning smoke to Cape Verde in winter (left panel) and summer (right panel). The upper panels show Moderate Resolution Imaging Spectroradiometer (MODIS[1]) fire counts for a ten–day time period during SAMUM–2a (left) and SAMUM–2b (right), respectively[2]. The lower panels show the mean aerosol optical thickness (AOT, same color scale for both pictures) at 550 nm for the exact duration of the two SAMUM–2 campaigns (see Section 2.4) as measured with MODIS. The AOT maps were compiled using the GES–DISC (Goddard Earth Sciences Data and Information Services Center) Interactive Online Visualization ANd aNalysis Infrastructure (Giovanni[3]). The white area over northern Africa represents regions with high surface albedo for which AOT cannot be derived with MODIS. The pictures in the lower panels also include an example of representative 72–h backward trajectories compiled with the Hybrid Single–Particle Lagrangian Integrated Trajectory Model (HYSPLIT[4]) arriving over the SAMUM–2 measurement site of Praia at Cape Verde at heights of 500 m (dashed), 2500 m (solid), and 4500 m (dotted).

During winter, dust layers over the tropical North Atlantic are often topped by or mixed with biomass–burning aerosol that originates from a band of fires that stretches from the equator to about 15° N and is shown in red in Figure 2.2a. The heavy biomass–burning activity is caused by agricultural practice (Cooke et al. 1996, Barbosa et al. 1999). The resulting band of high aerosol load is represented by the red to green colors in the MODIS AOT plot in Figure 2.2c. The second area of high AOT centered at 20° N and west of the Mauritanian coast represents dust outbreaks from northern Africa which pass Cape Verde to the north or linger over the North Atlantic before eventually being transported to Central Europe. West African savanna fires were investigated during the African Monsoon Multidisciplinary Analysis (AMMA) campaign in January and February of 2006 (Haywood et al. 2008). It is suggested that dust is transported southwards with the Harmattan winds and mixes with the fire emissions over southern West Africa. The resulting dust/smoke mixture accumulates over the Gulf of Guinea and adjacent land (Pelon et al. 2008). Deep convection was found to play an important role for vertical mixing rather than the buoyancy effect of the fire plumes itself (Johnson et al. 2008b). At latitudes north of about 10° N, mid–tropospheric southerlies can advect biomass–burning aerosol northward where it slips over the relatively cooler and

[1] http://modis.gsfc.nasa.gov/
[2] MODIS fire maps are accessible at http://rapidfire.sci.gsfc.nasa.gov/firemaps/
[3] http://daac.gsfc.nasa.gov/giovanni/
[4] http://ready.arl.noaa.gov/HYSPLIT.php

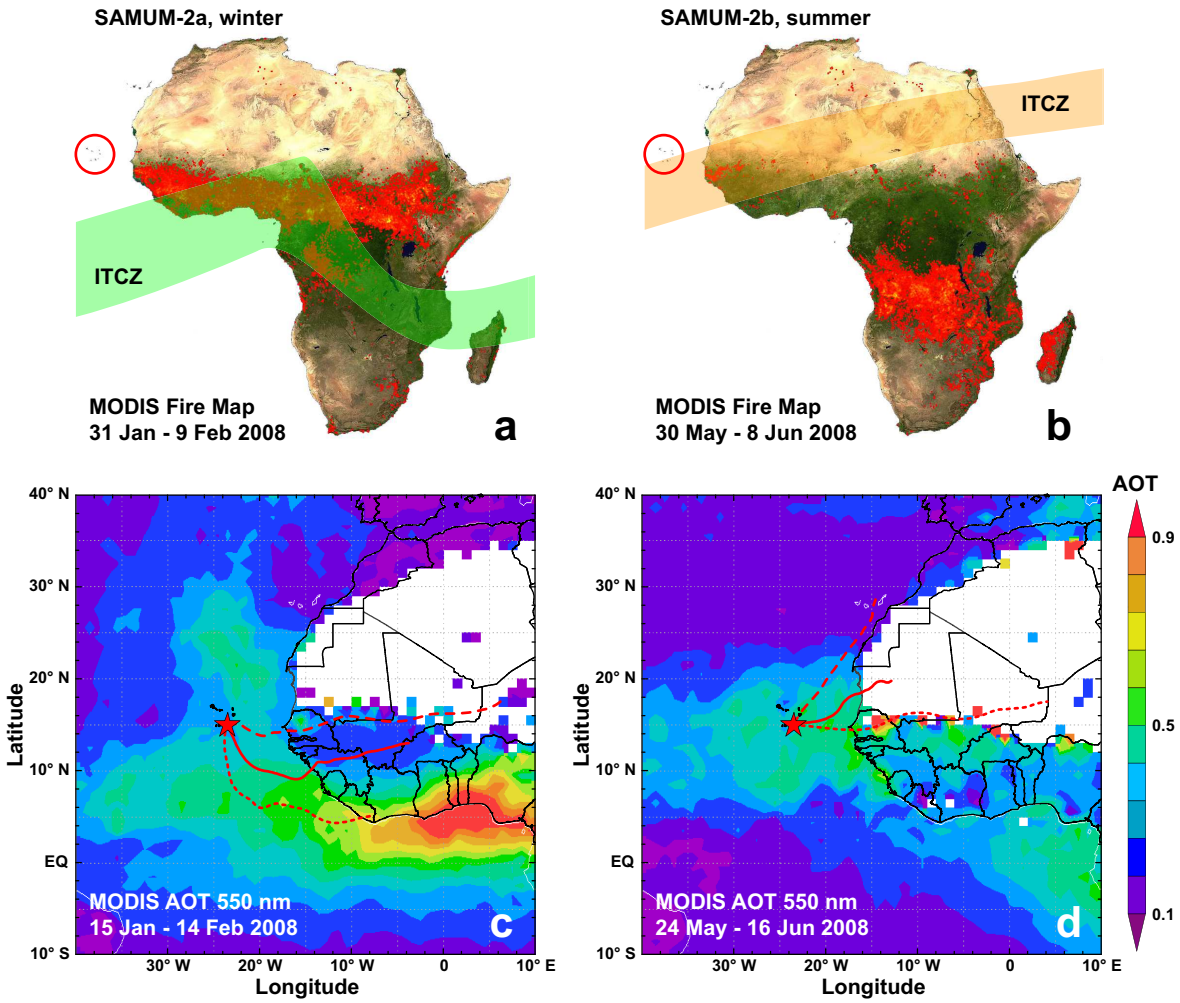

Figure 2.2: Position of the ITCZ during winter (a, green area) and summer (b, orange area) underlaid with MODIS maps of active fires in 10–day example periods during SAMUM–2a and SAMUM–2b, respectively. Red circles mark the location of Cape Verde west of the African continent. The lower panels show MODIS mean AOT at 550 nm for the duration of the SAMUM–2 measurements during winter (c) and summer (d) of 2008. The red lines show examples of 72–h backward trajectories that arrive within the observed aerosol layers at heights of 500 m (dashed), 2500 m (solid), and 4500 m (dotted).

drier desert air. The southerly position of the ITCZ (shown as green band) allows for a westerly transport of the dust/smoke mixture. The example backward trajectories in Figure 2.2c reveal that (dust) aerosol from North Africa is transported to the measurement site at lower heights while the trajectories at larger heights extend into the region that is dominated by biomass–burning smoke (see arrows in the green box in Figure 2.1).

Aerosol conditions west of the African continent are very different during summer (i.e., during SAMUM–2b). As illustrated by the orange area in Figure 2.2b the ITCZ is now shifted northward. The area of biomass–burning activity on the other hand occurs

in the region of Angola, Zambia, and the Democratic Republic of the Congo. Consequently, conditions similar to SAMUM–1 in Morocco (one deep plume of pure mineral dust from northern Africa, now above a maritime boundary layer) were expected to prevail during the summer measurements of SAMUM–2 (Karyampudi et al. 1999). The advection of mineral dust to the measurement site at Cape Verde during summer strongly depends on the occurrence of a local surface low over southern Mauritania which increases the pressure gradient between the African heat low and the Azores high. This frontier of different air masses stretches over the tropical North Atlantic. Its location varies with the position of the Azores high. Figure 2.2d also shows two distinct areas of increased optical depth. One is located at the equator west of the region of summertime biomass–burning activity. The other plume is located in a band between 5° and 25° N, southwest of the western Sahara. The example trajectories show that air that is advected to the measurement site within the boundary layer (500 m height, dashed line) usually originates over the Atlantic ocean while at larger heights (2500 m, solid, and 4500 m, dotted) the trajectories pass the desert areas of northern Africa. Ultimately, pure mineral dust is transported over the tropical North Atlantic and passes the Cape Verde islands on its way to the Caribbean.

Liu et al. (2008a) and Ben-Ami et al. (2009) present seasonally, spatially, and vertically resolved observations of Saharan dust over the North Atlantic based on a one–year data set of measurements with the Cloud–Aerosol Lidar and Infrared Pathfinder Satellite Observations satellite (CALIPSO[5], Winker et al. 2009). Both studies corroborate that dust is transported at lower latitudes and heights during winter, compared to summer conditions. This is in agreement with the concept of the seasonal dependence of dust transport over the Atlantic ocean. However, such detailed and height–resolved studies are only possible with active remote–sensing instruments like the CALIPSO lidar. Liu et al. (2008a) did not aim at resolving the contribution of biomass–burning smoke to the mixed plume while Ben-Ami et al. (2009) concluded that the bad signal–to–noise ratio of the CALIPSO signals impedes a detailed investigation of mixed dust/smoke layers like the ones observed during SAMUM–2a. Thus the separation of the contributions of mineral dust and biomass–burning smoke to the West African aerosol plume is not only one of the main topics of the analysis of the SAMUM–2a measurements (see Section 4.2 and Tesche et al. 2009b) but also a challenging task for future studies—especially for space–borne missions which offer the best foundation for the investigation of the large–scale phenomena of intercontinental dust transport (Kaufman et al. 2005, Ben-Ami et al. 2010).

2.4 Field Sites

SAMUM–1 was conducted from 15 May to 7 June 2006 in Morocco as a column closure experiment for pure and freshly emitted mineral dust. Two measurement sites were chosen for this campaign. Ground–based *in situ* (size distribution, morphology,

[5]http://www-calipso.larc.nasa.gov/

chemical composition, optical, and hygroscopic properties) and Sun photometer measurements were performed at Tinfou (30.14° N, 5.36° W, 684 m above sea level (asl), see Figure 2.1) as close as possible to the desert (Dinter et al. 2009, Heese et al. 2009, Kaaden et al. 2009, Kandler et al. 2009, Müller et al. 2009, Schladitz et al. 2009). A second site with a hangar for the small Partenavia aircraft which conducted regional flights (Bierwirth et al. 2009) and appropriate infrastructure for ground–based lidar measurements (Freudenthaler et al. 2009, Heese et al. 2009, Tesche et al. 2009a) was established at the airport of Ouarzazate (30.90° N, 6.90° W, 1133 m asl, see Figure 2.1). Ouarzazate is located in a flat basin encircled by two almost parallel steep mountain chains of the High Atlas (more than 4000 m high) and the Anti–Atlas/Jebel Saghro (up to 2700 m high). Three lidar systems and two Sun photometers of IfT and the Meteorological Institute of Munich University (MIM) were deployed at this site. Radiosondes were launched at least twice a day, around noon and after sunset, as well as during dedicated measurements. In addition to the instruments deployed at the two aforementioned sites, the Falcon research aircraft of DLR was stationed at Mohamed V. International Airport of Casablanca (33.59° N, 7.61° W, 15 m asl, see Figure 2.1) and conducted 17 flights between 18 May and 7 June 2006 (Esselborn et al. 2009, Petzold et al. 2009, Weinzierl et al. 2009) to perform *in situ* particle sampling and airborne high–spectral–resolution lidar (HSRL) measurements including overpasses of the ground stations. Huge efforts were taken to combine ground–based and airborne *in situ* sampling of particles, active and passive remote sensing from ground, aircraft, and satellites, and modeling of the radiative effects and the life cycle of mineral dust to gain new insight into the complex processes associated with mineral dust particles. The upper panels of Figure 2.3 shows the two research aircraft and the two field sites for the remote–sensing and *in situ* observations at Ouarzazate airport and Tinfou, respectively. Table 2.1 gives an overview of the properties that were measured during the SAMUM experiments in Morocco and at Cape Verde.

About 18 months after the first experiment, SAMUM–2 was conducted at the airport of Praia (15.00° N, 23.50° W, 75 m asl, see Figure 2.1), Cape Verde, to investigate the complex mixture of mineral dust from northern Africa and biomass–burning smoke from southern West Africa. The North African dust plume arrives at Cape Verde after 2–5 days of transport (Knippertz et al. 2011) and dust properties (e.g., particle size distribution, chemical composition, optical properties, or radiative effects) might be altered with respect to the pure dust layers observed during SAMUM–1. Furthermore, dust transport patterns undergo a seasonal change (see Section 2.3). The investigation of a possible change of dust properties during transport was an additional focus of the second experiment.

Most of the instruments that participated in SAMUM–1 were transported to the airport of Praia, the capital of Cape Verde. This time, remote–sensing and *in situ* instruments were operated at one single site (see Figure 2.1). Measurements comparable to the ones during the campaign in Morocco were performed from 15 January to 14 February 2008 (SAMUM–2a). Impressions of the SAMUM–2 measurement setup are given in the lower panels of Figure 2.3. The Falcon flights covered the entire area of transport from the African west coast to Cape Verde and beyond (see green area in Figure 2.1). Flights

Table 2.1: Measurement platforms applied and parameters observed during the SAMUM experiments. Details about the instruments can be found in the overview papers by Heintzenberg (2009) and Ansmann et al. (2011) and in the respective publications of the two SAMUM Special Issues in Tellus 61B and 63B.

	vertical profiles
ground, Raman lidar	backscatter and extinction coefficients, depolarization ratio
ground, radiosonde	temperature, dew point, relative humidity, wind speed and direction
Falcon, HSRL	backscatter and extinction coefficients, depolarization ratio
Falcon, *in situ*	particle number concentration, size distribution, complex refractive index, volatile particle fraction
Falcon, dropsonde	temperature, dew point, relative humidity
Doppler lidar[1]	horizontal and vertical wind speed, wind direction
	column–integrated optical properties
Sun photometer	spectral AOT, Ångström exponent, scattering phase function
	radiation measurements
Partenavia[2]	spectral surface albedo, radiative fluxes at visible and infrared (IR) wavelengths
Falcon[1]	spectral surface albedo, radiative fluxes at visible and IR wavelengths
ground	Radiative fluxes at visible and IR wavelengths
	airborne particle sampling
Partenavia[2]	size distribution, morphology, chemical composition, complex refractive index
Falcon	size distribution, morphology, chemical composition, complex refractive index
	ground–based *in situ* measurements
absorption photometer	complex refractive index
particle sampling	size distribution, morphology, chemical composition, complex refractive index
particle spectrometer	size distribution
humidified particle spectrometer	hygroscopic growth factor

[1]only during SAMUM–2, [2]only during SAMUM–1

crossing the aerosol plume as well as local column closure flights were performed. The smaller Partenavia aircraft that measured spectral radiance and surface albedo during the first campaign did not attend in SAMUM–2. The respective instruments were installed aboard the Falcon aircraft.

Additional lidar measurements of the summer dust plume over Cape Verde were performed from 24 May to 16 June 2008 (SAMUM–2b) with BERTHA of IfT (see Section 5.4) to study the seasonal change of the aerosol transport pattern in the outflow region of West Africa that is governed by the movement of the ITCZ (see Section 2.3). These lidar measurements were only supported by Sun photometer and radiosondes.

However, in addition to the winter measurements a unique data set of summer dust conditions in the regime of long–range transport was collected.

Results of the lidar measurements with BERTHA that are conducted, analyzed, and discussed in the framework of this thesis are published in Ansmann et al. (2008, 2009a, b, c, 2011), Freudenthaler et al. (2009), Gasteiger et al. (2011), Groß et al. (2011a, b), Heinold et al. (2009, 2011a, b), Knippertz et al. (2009, 2011), Mattis et al. (2009), Müller et al. (2007, 2009, 2010a, b), Otto et al. (2009), Tesche et al. (2009a, b, 2011a, b), and Wandinger et al. (2010).

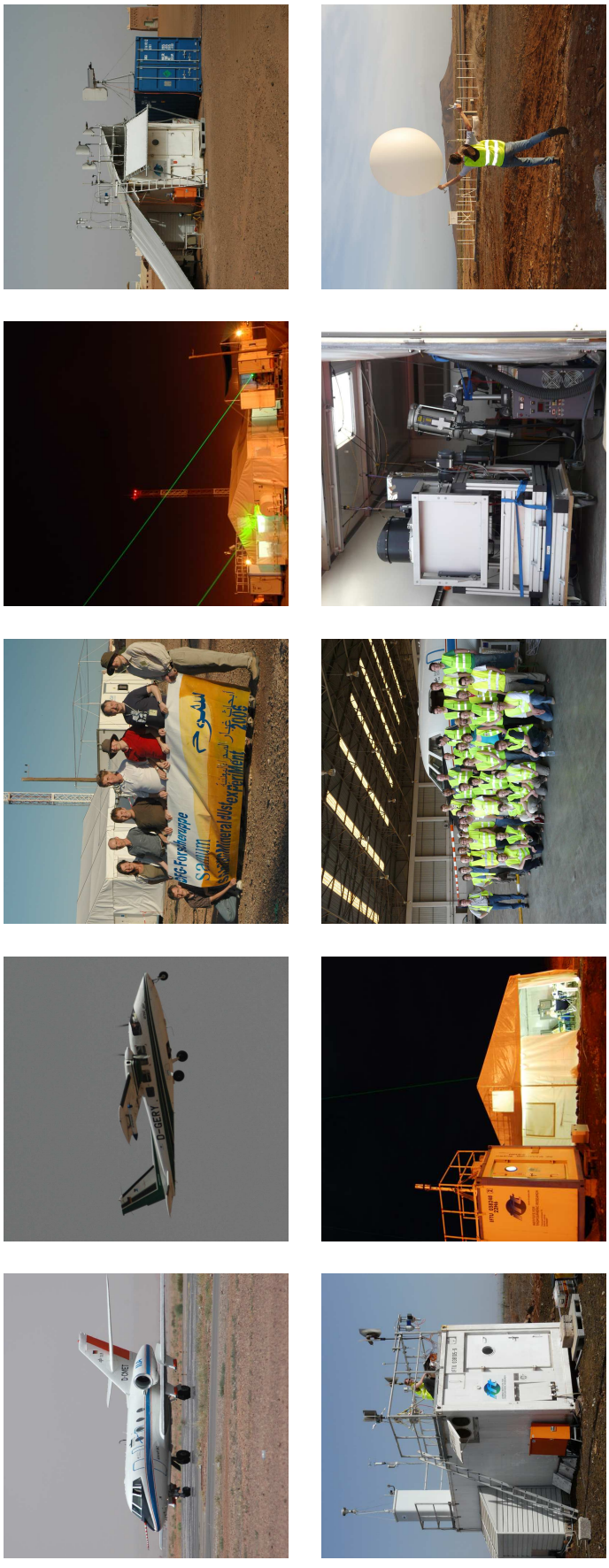

Figure 2.3: Impressions of the measurement setup during SAMUM–1 (upper panels) and SAMUM–2 (lower panels).

3 Theory

This chapter provides the theoretical background of active optical remote sensing. Properties of light and light scattering are summarized. The basic lidar techniques applied within this work are presented. Special emphasis is drawn on the theory of Raman and polarization lidar. Details on the application of these lidar techniques for aerosol characterization and aerosol–type separation are presented later in Chapter 4. The properties of the lidar systems that were employed during the SAMUM campaigns and the corrections and calibrations, which were performed to assure data quality, will be presented in Chapter 5.

3.1 Light Scattering in the Atmosphere

The term visible light describes that part of the electromagnetic spectrum in the wavelength range from approximately 400 nm to 700 nm that is sensed by the human eye. The wider definition of light also includes ultraviolet (UV) radiation with wavelengths below 400 nm and infrared (IR) radiation with wavelengths longer than 700 nm. Measurements presented within this work cover the spectral range from the UV to the near IR.

Light in the atmosphere becomes visible for the human eye after the interaction with scatterers. These scatterers can be molecules, cloud droplets, aerosol particles, as well as rain or snow. When interfering with scatterers light might also be absorbed. The sum of scattering and absorption within a certain volume is called extinction. Light extinction depends on the wavelength λ of incident light. Its measure is the volume extinction coefficient α_λ that describes the attenuation of light traveling through a medium. In the atmosphere, strong light extinction causes a decrease in visibility which can easily be observed during, e.g., haze or fog.

The intensity of scattered light of a certain wavelength varies with the size, the shape, and the complex refractive index of a scatterer. It furthermore strongly depends on the direction of scattering which is defined by the zenith angle Θ and the azimuth angle Φ in spherical coordinates. The intensity of light that is scattered in the direction (Θ, Φ) is described by the scattering phase function $p_\lambda(\Theta, \Phi)$ (van de Hulst 1957, Bohren and Huffman 1983). It is a dimensionless function whose integral over all directions is generally normalized to unity. The scattering phase function displays distinctive features for different scatterers, especially in sidewards and backward direction.

The integral of the scattering phase function of an ensemble of scatterers is propor-

tional to the volume extinction coefficient (which also incorporates the effect of light absorption). The extinction coefficient can be directly measured with Raman lidar (see Section 3.3.2). Scattering in the direction of propagation of the incident beam of light ($\Theta = 0°$) is referred to as forward scattering while scattering in the direction of the primary source ($\Theta = 180°$) is referred to as backward scattering or backscattering. The intensity of the backscattered light is described by the volume backscatter coefficient. The backscatter coefficient strongly depends on the effective size and the mean refractive index of an ensemble of scatterers. The latter quantity is a refractive index that describes the overall effect of the particle ensemble and might vary strongly from values for individual particles in the scattering volume. The imaginary part of the refractive index controls the absorptive properties of a particle. The field of view of a lidar receiver telescope (also called receiver field of view, RFOV) is usually chosen in a way that only light scattered at angles close to $\Theta = 180°$ is detected. In this work, the light that is collected by the receiver telescope of a lidar system is referred to as backscattered light. The backscatter coefficient is one of the basic deliverables of a lidar measurement (see Section 3.3.1). It is proportional to the scattering phase function at 180°. Information about $p_\lambda(180°)$ is hard to obtain otherwise and can be valuable if the performance of radiative–transfer models needs to be evaluated (Müller et al. 2010a, b).

In physical terms, light is an electromagnetic wave with an electric field vector $\boldsymbol{E}$ that is periodically oscillating perpendicular to the direction of propagation (z–direction). It is called linearly polarized, if the oscillation is restricted to a single plane. The x and y components of the wave are in phase and the field vector draws a line in the x–y–plane. The electric field vector rotates with time, if a 90° phase shift occurs between its x and y components. It now draws a circle in the x–y–plane and is called circularly polarized. If the phase shift differs from 90°, light is called elliptically polarized. The latter also is the general case of polarization (van de Hulst 1957, Bohren and Huffman 1983). Natural sunlight is unpolarized because it consists of a multitude of waves that are polarized in an infinite variety of ways. A polarization lidar (see Section 3.3.4) on the other hand uses a laser as an artificial light source which usually emits linearly polarized light .

The intensity and the state of polarization of a light beam are fully described by its Stokes vector $\boldsymbol{S} = (I, Q, U, V)$. The four elements of this vector are called Stokes parameters and characterize the total intensity I, the intensity along the x and y axes Q, the intensity along the $+45°$ and $-45°$ axes U, and the intensity that is right–hand circular and left–hand circular V. The latter parameter describes the rotation of the electric field vector in case of elliptically polarized light. The Stokes vector is often normalized to its first element, i.e., I equals unity. For example, the Stokes vector of unpolarized light is $\boldsymbol{S} = (1, 0, 0, 0)$, while it is $\boldsymbol{S} = (1, 1, 0, 0)$ for linearly (along the x axis) and $\boldsymbol{S} = (1, 0, 0, 1)$ for (left–handed) circularly polarized light.

Figure 3.1a illustrates the angles and directions involved when a beam of light is scattered by a single particle. $\boldsymbol{S}_0$ and $\boldsymbol{S}$ denote the Stokes vector of the incident and scattered beam, respectively. The scattering process can alter the direction and the

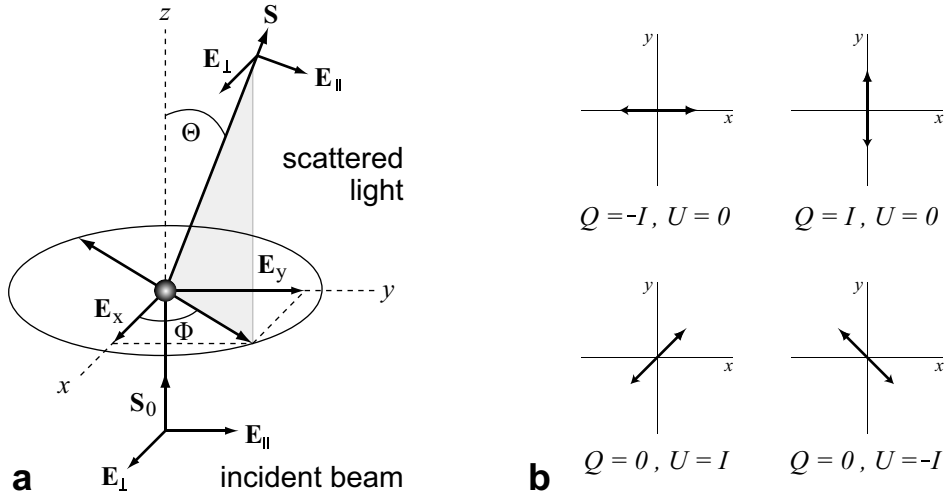

Figure 3.1: Transformation of an electromagnetic wave after being scattered by a single particle (a) and planes of polarization of linearly polarized light for different Stokes parameters Q and U (b).

state of polarization of a light beam. The diagrams in Figure 3.1b show the image of the electric field vector in the x–y–plane for some cases of linear polarization. Circles and ellipses would occur in case of circularly and elliptically polarized light, respectively.

The relation between the intensity and state of polarization of scattered light $\boldsymbol{S}$ and the intensity and state of polarization of incident light $\boldsymbol{S}_0$ is fully described as

$$\boldsymbol{S} = \mathbf{F}(\Theta, \Phi)\boldsymbol{S}_0 \,.$$

The normalized 4×4 transformation matrix $\mathbf{F}$ is dimensionless and is referred to as scattering matrix. It consists of 16 elements $F_{ij}(\Theta, \Phi)$ that depend on the scattering angles Θ and Φ (van de Hulst 1957, Bohren and Huffman 1983). In case of first–order scattering by randomly oriented non–spherical particles having a plane of symmetry, e.g., spheroids, the matrix simplifies to

$$\mathbf{F}(\Theta) = \begin{bmatrix} F_{11} & F_{12} & 0 & 0 \\ F_{12} & F_{22} & 0 & 0 \\ 0 & 0 & F_{33} & -F_{43} \\ 0 & 0 & F_{43} & F_{44} \end{bmatrix} \tag{3.1}$$

and becomes diagonal for exact backscattering when $F_{12}(180°) = F_{43}(180°) = 0$,

$$\mathbf{F}(180°) = \begin{bmatrix} F_{11} & 0 & 0 & 0 \\ 0 & F_{22} & 0 & 0 \\ 0 & 0 & F_{33} & 0 \\ 0 & 0 & 0 & F_{44} \end{bmatrix} = \begin{bmatrix} a_1 & 0 & 0 & 0 \\ 0 & a_2 & 0 & 0 \\ 0 & 0 & -a_2 & 0 \\ 0 & 0 & 0 & a_1 - 2a_2 \end{bmatrix}, \tag{3.2}$$

with only two independent parameters a_1 and a_2.

Then the first element $F_{11}(\Theta) = a_1(\Theta)$ is identical to the phase function $p(\Theta)$. Usually, all elements of the transformation matrix are normalized to the first element $F_{11} = a_1$.

In case of backscattering by spherical particles the normalized scattering matrix simplifies to

$$\mathbf{F}(180^\circ) = \begin{bmatrix} 1 & 0 & 0 & 0 \\ 0 & 1 & 0 & 0 \\ 0 & 0 & -1 & 0 \\ 0 & 0 & 0 & -1 \end{bmatrix}. \tag{3.3}$$

Transforming an incident beam of linearly polarized light with this matrix preserves the state of polarization as it is observed for backscattering by spherical cloud droplets.

A polarization lidar applies laser light of a well–defined state of polarization and detects alterations of the Stokes parameters Q and/or U (if linearly polarized light is emitted) or V (if circularly polarized light is emitted) which are caused by backscattering particles or hydrometeors. Such measurements not only provide information on the scattering phase function but also on other elements of the scattering matrix (3.2). The polarization lidar technique and the lidar–specific parameter depolarization ratio are discussed in Section 3.3.4.

Depending on the wavelength λ of the incident light and the size (radius r) of the scatterers, different kinds of scattering are discerned. Rain drops and ice crystals are very large compared to the wavelength of incident light ($r \gg \lambda$). While these scatterers show no wavelength dependence of the intensity of scattered light, refraction of light at their surfaces can cause optical phenomena like rainbows or halos. If the size of the scatterers decreases to the dimension of the wavelength of incident light ($r \approx \lambda$), the intensity of scattering is approximately proportional to the inverse of the wavelength but can also vary strongly depending on the kind of scatterers. This case is often called Mie scattering, despite the fact that this term originally refers to scattering of electromagnetic waves by spherical objects of various size (Mie 1908). The size of atmospheric aerosol particles ranges from a few nanometers to several micrometers. Thus, these particles are very effective scatterers of electromagnetic waves with wavelengths from the UV to the IR (van de Hulst 1957, Bohren and Huffman 1983).

The interaction of light with air molecules that are much smaller than the wavelength of light ($r \ll \lambda$) is called Rayleigh scattering. This process is strongly wavelength–dependent (proportional to λ^{-4}). The blue sky is caused by Rayleigh scattering because the blue part of the visible spectrum is scattered much stronger than light of larger wavelength.

For most scattering processes the energy and wavelength of the scattered photon are equal to those of the incident photon. This is called elastic scattering. For a very small fraction of scattered light a wavelength shift between incident and scattered photon can be observed. This inelastic Raman scattering is caused by an excitation or disexcitation of the scattering molecule by incident photons changing its vibrational, rotational, or vibrational–rotational level of energy.

A Raman scattering molecule absorbs energy by being excited to a higher energy level while the frequency of the scattered photon is decreased. The wavelength of the scat-

tered photon is shifted towards the red and the process is called Stokes Raman scattering with

$$\tilde{\nu}_{\text{out}} = \tilde{\nu}_{\text{in}} - |\Delta\tilde{\nu}| \ .$$

The frequency of scattered light, $\tilde{\nu}_{\text{out}}$, compared to the frequency of incident light, $\tilde{\nu}_{\text{in}}$, is shifted by $|\Delta\tilde{\nu}|$. The scattering molecule might also loose energy to the scattered photon and decrease its energy level. The frequency of the scattered photon is now increased and the wavelength is shifted towards the blue. This case is called anti–Stokes Raman scattering with

$$\tilde{\nu}_{\text{out}} = \tilde{\nu}_{\text{in}} + |\Delta\tilde{\nu}| \ .$$

A molecule is always in a certain state of vibrational–rotational energy. The frequency shift $|\Delta\tilde{\nu}|$ is caused by a change of the vibrational, rotational, or vibrational–rotational energy level of the scattering molecule. It is characteristic for the scattering molecule and can be calculated as

$$\Delta\tilde{\nu} = \tilde{\nu}_{\text{in}} - \tilde{\nu}_{\text{out}} = \frac{\Delta E}{hc_0} \, . \tag{3.4}$$

$\tilde{\nu} = 1/\lambda = \nu/c_0$ in cm^{-1} is the wavenumber (usually used in spectroscopy) of the scattered photon, ΔE is the difference between the rotational–vibrational energy levels of the scattering molecule before and after scattering, h is the Planck constant and c_0 the speed of light in vacuum. The frequency (wavelength) shift for changes of the vibrational energy level of the molecule is much larger compared to the one for changes of the rotational energy level. Thus light originating from vibrational–Raman scattering can easier be separated from elastically scattered light. This effect is used in the receiver of a regular Raman lidar. The intensity of Raman scattered light on the other hand is much lower than the intensity of Rayleigh scattering. Thus, the detection of Raman signals is usually restricted to the night when background noise is minimized. Nowadays, narrow–bandwidth filters and interferometers can be used to detect pure rotational–Raman scattering as well. Such rotational–Raman lidars apply frequency–stabilized (seeded) lasers and are able to detect elastic–backscatter signals at the exact laser wavelength and rotational–Raman signals at selected wavelengths of the rotational–Raman spectrum. Because it is less sensitive to background light, this technique enables the measurement of backscatter and extinction profiles even during daytime.

3.2 Lidar Principle and Lidar Equation

Lidar (Light Detection and Ranging, Hinkley 1976, Measures 1984, Weitkamp 2005) is an instrument of active remote sensing that benefits from light scattering. Compared to the well–known radar technique (Radio Detection and Ranging) very short wavelengths from the UV to the near IR which allow for the detection of much smaller scatterers are used. While atmospheric radars can be applied to studies of clouds and precipitation, lidar in atmospheric research is used for the investigation of aerosols, trace gases, or winds (by using aerosols as tracers). Nowadays, lidar is also an established technique for temperature and humidity profiling.

A lidar uses a pulsed laser as light source which allows for a range–resolved measurement of the parameters of interest with high temporal resolution. Compared to passive sounders which make use of natural sources of radiation (e.g., sunlight or terrestrial radiation), lidar instruments usually demand high financial and professional efforts because they include their own light source. The Sun photometer (SPM) is a passive sounder which is commonly used for remote–sensing of the atmosphere. It uses the sun as light source and thus can only operate during daytime and under mostly cloudless conditions. Furthermore, it only provides integrated properties of the entire investigated atmospheric column.

A lidar basically consists of a transmitter that emits short laser pulses and a receiver whose telescope collects backscattered light and directs it to a receiver (Wandinger 2005a). In the receiver, the backscattered photons are separated according to their wavelength and acquired with very high temporal resolution. In the special case of atmospheric aerosol lidar that is discussed in this thesis and will be referred to from here, the emitted laser light is usually linearly polarized. Commonly, commercially available Nd:YAG lasers are used as light source. These lasers emit light at the fundamental wavelength of 1064 nm. The emitted light can be frequency–doubled (to 532 nm) or frequency–tripled (to 355 nm). Most aerosol lidars measure the backscattered light by means of photomultiplier tubes (PMTs). The latter can be set to detect individual pulses of single photons (photon counting detection mode, pc) or a voltage (analog detection mode, a). The intensity of the backscattered light (which varies depending on the aerosol concentration in the atmosphere) is adjusted by means of neutral–density filters within the light's path to avoid saturation of the PMTs.

In the atmosphere the emitted laser light is scattered by molecules and other obstacles (e.g., aerosols, clouds, or precipitation) in its way. Because the speed of light c is known, the distance R between the lidar and the location of scattering can be calculated as

$$R = \frac{ct}{2}\,. \tag{3.5}$$

Note that detected light traveled from the lidar to the air volume of backscattering and then returned back to the receiver telescope. Because the distance is covered twice, the factor 2 is introduced in Equation (3.5).

The vertical resolution of a lidar system is determined by the temporal resolution of the data acquisition. Usual acquisition times of 50–400 ns result in a range resolution of 7.5–60.0 m. Most lidar systems point upward with zenith angles of $\Theta_\mathrm{Z} = 0° - 5°$. In that case, range R equals height $z = R\cos\Theta_\mathrm{Z}$.

The detected signal is described by the lidar equation:

$$P_{\lambda_0}(R) = \frac{P_{0,\lambda_0}\tau_\mathrm{p} c A_\mathrm{T}}{2}\frac{\eta_{\lambda_0} O_{\lambda_0}(R)}{R^2}\beta_{\lambda_0}(R)\exp\left[-2\int_0^R \alpha_{\lambda_0}(\xi)\mathrm{d}\xi\right]. \tag{3.6}$$

The range–resolved received power $P_{\lambda_0}(R)$ depends on the emitted power P_{0,λ_0} of a laser pulse at an emitted wavelength λ_0, the laser pulse length τ_p, the speed of light c, the area of the receiver telescope A_T, the wavelength–dependent transmission η_{λ_0} of the receiver

optics, the geometric form factor $O_{\lambda_0}(R)$, the inverse square distance, the wavelength–dependent volume backscatter coefficient $\beta_{\lambda_0}(R)$ at the place of backscattering, and a transmission term that is expressed by an exponential function. The latter describes the attenuation of light on the way to the place of scattering and back. The function $O_{\lambda_0}(R)$ characterizes the geometric overlap between the laser beam and the RFOV. $O_{\lambda_0}(R)$ varies between zero near the lidar and unity at a height of complete overlap beyond which its effect does no longer need to be accounted for. The overlap function can be determined according to the method described in Section 5.4.3.1.

The parts of Equation (3.6) that show no range dependence can be summarized in a constant system term

$$E_{\lambda_0} = \frac{1}{2} P_{0,\lambda_0} \tau_{\mathrm{p}} c A_{\mathrm{T}} \tag{3.7}$$

that is characteristic for every lidar. It depends on the setup of the transmitter and receiver of a system. The area of the telescope A_{T} dictates the solid angle A_{T}/R^2 of the cone of volume of signal detection.

The strong range dependence of the detected signal causes a dynamic range of several orders of magnitude which needs to be handled by the data acquisition system. To keep the amount of collected data manageable, several laser pulses are averaged before data storage. The measurements with the IfT lidar system BERTHA (see Section 5.4) that will be discussed in this thesis were performed with a spatial and temporal resolution of 60 m and 10–30 s, respectively.

On the way from the emitting laser to the location of scattering and back to the lidar receiver, photons can be absorbed or scattered. The sum of absorption and scattering describes the attenuation of light traveling through a medium and is called extinction. In the atmosphere emitted laser light can interact with molecules and particles. Thus, the volume backscatter coefficient β (in $\mathrm{m^{-1}sr^{-1}}$) and the volume extinction coefficient α (in $\mathrm{m^{-1}}$) need to be split into contributions of particles (superscript p) and molecules (superscript m) as

$$\beta_\lambda(R) = \beta_\lambda^{\mathrm{p}}(R) + \beta_\lambda^{\mathrm{m}}(R) = \int n^{\mathrm{p}}(R,r) \frac{\mathrm{d}\sigma_{\mathrm{sca}}^{\mathrm{p}}(r,\pi)}{\mathrm{d}\Omega} \mathrm{d}r + n^{\mathrm{m}}(R) \frac{\mathrm{d}\sigma_{\mathrm{sca}}^{\mathrm{m}}(\pi)}{\mathrm{d}\Omega} \tag{3.8}$$

and

$$\alpha_\lambda(R) = \alpha_\lambda^{\mathrm{p}}(R) + \alpha_\lambda^{\mathrm{m}}(R) = \int n^{\mathrm{p}}(R,r) \sigma_{\mathrm{ext}}^{\mathrm{p}}(r) \mathrm{d}r + n^{\mathrm{m}}(R) \sigma_{\mathrm{ext}}^{\mathrm{m}} \,. \tag{3.9}$$

$n^{\mathrm{p}}(r)$ (in $\mathrm{m^{-3}m^{-1}}$) denotes the number concentration of aerosol particles of a certain size while n^{m} (in $\mathrm{m^{-3}}$) refers to the number concentration of air molecules. $\mathrm{d}\sigma_{\mathrm{sca}}^{\mathrm{p,m}}(\pi)/\mathrm{d}\Omega$ represents the differential scattering cross section (in $\mathrm{m^2sr^{-1}}$) of particles and molecules for the backward direction ($\Theta = \pi$). The extinction cross section (in $\mathrm{m^2}$) of particles and molecules is characterized as $\sigma_{\mathrm{ext}}^{\mathrm{p,m}}$. The differential scattering cross section is known for different molecules. Profiles of the molecular number concentration $n^{\mathrm{m}}(R)$ of air molecules can be derived from profiles of temperature and pressure originating from radiosonde ascents or standard atmospheric models (Bucholtz 1995).

3.3 Basic Lidar Techniques

During the last decades lidar has been used for various kinds of measurements from simple range finding over the detection of trace gases and the profiling of meteorological parameters to aerosol and cloud measurements. This thesis is focused on lidar measurements of tropospheric aerosols. Thus, common lidar techniques for the detection and characterization of atmospheric particles used in SAMUM are introduced in the next subsections.

3.3.1 Elastic–backscatter Lidar

Elastic backscatter lidar (Hinkley 1976, Measures 1984, Kovalev 2004, Ansmann and Müller 2005) is the basic version of a lidar system. Light is detected at the wavelength λ_0 of the emitted laser light. Thus, the dependence on wavelength is dropped in the equations of this section. During the day, when the strong background of sunlight complicates the detection of Raman–scattered light, Klett's method (Klett 1981, 1985, Fernald 1984) is applied to analyze the SAMUM lidar measurements at the laser wavelengths of 355, 532, and 1064 nm. For quality assurance daytime lidar measurements are usually compared to coincident SPM observations.

When dealing with elastic backscatter data a problem emerges: two unknown quantities, $\beta(R)$ and $\alpha(R)$, appear in Equation (3.6) while only one signal is detected. According to Equations (3.8) and (3.9), the backscatter coefficient and the extinction coefficient comprise contributions of particles and molecules. Because $\beta(R)$ and $\alpha(R)$ cannot be retrieved independent of each other, extinction–to–backscatter ratios (or lidar ratios)

$$S^{\mathrm{p}}(R) = \frac{\alpha^{\mathrm{p}}(R)}{\beta^{\mathrm{p}}(R)} \tag{3.10}$$

and

$$S^{\mathrm{m}} = \frac{\alpha^{\mathrm{m}}(R)}{\beta^{\mathrm{m}}(R)} \approx \frac{8\pi}{3}\,\mathrm{sr} \tag{3.11}$$

for particles and molecules, respectively, are introduced to substitute one of the two unknowns. The molecular lidar ratio S^{m} is constant with height. The particulate lidar ratio $S^{\mathrm{p}}(R)$ on the other hand depends on the size, shape, and refractive index of the scattering particles. Therefore, it can be used for aerosol characterization (see Section 3.3.2). For the analysis of signals of an elastic backscatter lidar a reasonable value of $S^{\mathrm{p}}(R)$ needs to be assumed. In cases of complex aerosol stratification with layers of different origin, the particle lidar ratio can show strong vertical variations. In that case, height dependencies can introduce large errors to the retrieval of β and α (Sasano et al. 1985). The SAMUM–2a measurements which will be discussed in Section 6.2 give a good impression of how the particle lidar ratio might vary throughout the atmospheric column under complex aerosol conditions.

According to Klett's method (Klett 1981, 1985, Fernald 1984, Sasano et al. 1985) the backscatter coefficient can be calculated by assuming a value of the particle lidar ratio

as

$$\beta^{\mathrm{p}}(R) = -\beta^{\mathrm{m}}(R) + \frac{U(R, R_0)}{V(R_0) - 2\int_{R_0}^{R} S^{\mathrm{p}}(\xi) U(\xi, R_0) \mathrm{d}\xi}\,, \tag{3.12}$$

with

$$U(R, R_0) = P(R) R^2 \exp\left[-2\int_{R_0}^{R} \left[S^{\mathrm{p}}(\xi) - S^{\mathrm{m}}\right] \beta^{\mathrm{m}}(\xi) \mathrm{d}\xi\right] \tag{3.13}$$

and

$$V(R_0) = \frac{P(R_0) R_0^2}{\beta^{\mathrm{p}}(R_0) + \beta^{\mathrm{m}}(R_0)}\,. \tag{3.14}$$

To obtain a profile of the particle backscatter coefficient a reference value $\beta^{\mathrm{p}}(R_0)$ at a reference height R_0 has to be chosen. Naturally, the reference height is chosen to be in an aerosol–free layer where particle backscatter is negligible. These conditions are usually met in the free troposphere. If the reference height is set below the height of the aerosol layer of interest ($R_0 < R$) one speaks of forward integration or the Klett forward algorithm. Due to the possibility of a discontinuity in the denominator, the solutions of this algorithm can become unstable, if the lidar ratio is chosen inappropriately. Trustworthy results are obtained, if the boundaries of the integrals in Equations (3.12) and (3.13) are switched and backward integration is performed by setting $R_0 > R$. This method is referred to as Klett backward algorithm and always results in stable solutions.

The particle extinction coefficient can be obtained by multiplying the particle backscatter coefficient retrieved by one of Klett's methods with the particle lidar ratio. However, a reasonable estimate of $S^{\mathrm{p}}(R)$ is needed to obtain reliable solutions. The assumption of a particle lidar ratio can easily introduce large errors, especially if it is set constant with height (Sasano et al. 1985).

3.3.2 Raman Lidar

In contrast to an elastic–backscatter lidar a Raman lidar (Ansmann et al. 1992, Ansmann and Müller 2005, Wandinger 2005b) is equipped with channels for the detection of light that is inelastically backscattered by air molecules. For aerosol measurements, usually Raman scattering from nitrogen as a reference gas with known concentration is applied. The additional information allows for an independent calculation of particle backscatter and extinction coefficients and thus a direct measurement of particle lidar ratios. Most of today's Raman lidar systems detect vibrational–Raman scattering since it features a significant wavelength shift between incident and Raman scattered light and the two signals can be separated easily by means of beam splitters and interference filters. Pure rotational–Raman lidars use frequency–stabilized (seeded) lasers and narrow–bandwidth interference filters or spectrometers, sometimes in combination with interferometers, to detect rotational–Raman signals of oxygen and nitrogen for aerosol and temperature profiling even during daytime (Arshinov et al. 2005, Behrendt 2005).

BERTHA emits laser light at the tree Nd:YAG wavelengths 355, 532, and 1064 nm (see Section 5.4). The receiver of BERTHA is equipped with channels for the detection of vibrational–rotational–Raman scattering from nitrogen at 387 and 607 nm (emitted wavelength $\lambda_0 = 355$ and 532 nm, respectively), and of rotational–Raman scattering from nitrogen and oxygen at 532 nm ($\lambda_0 = 532$ nm).

Light is emitted at the laser wavelength λ_0 and detected at the Raman–shifted wavelength λ_R after being inelastically scattered. Thus, a second lidar equation that accounts for the wavelength shift needs to be introduced:

$$P_{\lambda_\mathrm{R}}(R) = \frac{E_{\lambda_\mathrm{R}}\eta_{\lambda_\mathrm{R}}O(R)}{R^2}\beta_{\lambda_\mathrm{R}}(R)\exp\left[-\int_0^R\left[\alpha_{\lambda_0}(\xi)+\alpha_{\lambda_\mathrm{R}}(\xi)\right]\mathrm{d}\xi\right]. \tag{3.15}$$

The transmission term is changed compared to Equation (3.6) because light is now attenuated at the wavelength λ_0 on its way to the scatterer and at the wavelength λ_R on the way back to the lidar receiver. Raman backscattering is purely molecular and can be calculated for the inelastically scattering molecules of concentration $n_\mathrm{R}(R)$ as done in Equation (3.8) with the respective terms adopted to the wavelength λ_R.

As described in Ansmann and Müller (2005) the detection of Raman scattered light enables a direct calculation of the particle extinction coefficient from the detected Raman signal as

$$\alpha^\mathrm{p}_{\lambda_0}(R) = \frac{\frac{\mathrm{d}}{\mathrm{d}R}\ln\left[\frac{n_\mathrm{R}}{P_{\lambda_\mathrm{R}}(R)R^2}\right] - \alpha^\mathrm{m}_{\lambda_0}(R) - \alpha^\mathrm{m}_{\lambda_\mathrm{R}}(R) + \frac{\mathrm{d}}{\mathrm{d}R}\ln O_{\lambda_\mathrm{R}}(R)}{1+\left(\frac{\lambda_0}{\lambda_\mathrm{R}}\right)^{\mathring{a}(R)}}. \tag{3.16}$$

The terms $n_\mathrm{R}(R)$, $\alpha^\mathrm{m}_{\lambda_0}(R)$, and $\alpha^\mathrm{m}_{\lambda_\mathrm{R}}(R)$ only depend on the state of the atmosphere and can be calculated for given profiles of pressure and temperature. Their uncertainties can be minimized by using profiles of nearby soundings. In case of full overlap between laser beam and RFOV the term $\frac{\mathrm{d}}{\mathrm{d}R}\ln O_{\lambda_\mathrm{R}}(R)$ vanishes from Equation (3.16). The Ångström exponent $\mathring{a}$ (Ångström 1964) which will be discussed in detail in Section 4.1 is expected to be independent of height in this retrieval. The uncertainty resulting from a wrong assumption of $\mathring{a}$ is of the order of about 3% (Ansmann et al. 1992). A value of $\mathring{a} \approx 1$ has been proven to be a reliable value. In case of rotational–Raman scattered light, incident and scattered wavelengths are nearly the same. The factor $\lambda_0/\lambda_\mathrm{R}$ becomes unity resulting in a 2 in the denominator in Equation (3.16).

The combination of signals from elastic–backscatter and Raman channels provides two independent signals to derive the two unknowns in Equation (3.6). The particle backscatter coefficient can be calculated from the system of Equations (3.6, 3.15) without the assumption of a particle lidar ratio as

$$\begin{aligned}\beta^\mathrm{p}_{\lambda_0}(R) &= -\beta^\mathrm{m}_{\lambda_0}(R) + \left[\beta^\mathrm{p}_{\lambda_0}(R_0)+\beta^\mathrm{m}_{\lambda_0}(R_0)\right] \\ &\quad\times\frac{P_{\lambda_\mathrm{R}}(R_0)P_{\lambda_0}(R)}{P_{\lambda_0}(R_0)P_{\lambda_\mathrm{R}}(R)}\frac{n_\mathrm{R}(R)}{n_\mathrm{R}(R_0)} \\ &\quad\times\frac{\exp\left[-\int_{R_0}^R\left[\alpha^\mathrm{p}_{\lambda_\mathrm{R}}(\xi)+\alpha^\mathrm{m}_{\lambda_\mathrm{R}}(\xi)\right]\mathrm{d}\xi\right]}{\exp\left[-\int_{R_0}^R\left[\alpha^\mathrm{p}_{\lambda_0}(\xi)+\alpha^\mathrm{m}_{\lambda_0}(\xi)\right]\mathrm{d}\xi\right]}.\end{aligned} \tag{3.17}$$

As in Klett's method, values of particle backscatter coefficient $\beta^{\mathrm{p}}_{\lambda_0}(R_0)$ at the emitted wavelength λ_0 need to be estimated at a certain reference height R_0. The presence of aerosol–free layers simplifies the choice of appropriate reference values. The profile of the molecular backscatter coefficient $\beta^{\mathrm{m}}_{\lambda_0}(R)$ is calculated from the profiles of pressure and temperature (Bucholtz 1995).

The error in the calculation of the particle extinction coefficient is mostly due to signal noise. The statistical error can be reduced by increasing the averaging time and by choosing appropriate vertical smoothing lengths. The influence of trace–gas absorption is negligible since wavelengths outside of any absorption bands are chosen for Raman lidar measurements. During measurements in the framework of SAMUM, radiosondes were launched for the determination of vertical profiles of temperature and pressure. Inversions in the applied temperature profile influence the profiles of density and thus of nitrogen concentration n_{R} in Equations (3.16) and (3.17). Errors in the density profile may cause significant errors of the particle extinction coefficient in height regions with temperature inversions (Ansmann et al. 1992).

Temporal and spatial smoothing intervals have to be chosen in a way that fast variations of atmospheric conditions (e.g., clouds in the lidar signal) do not introduce significant errors to the retrieved profiles of optical parameters. Thus, before the analysis of a measurement the range–corrected signal was screened for temporal inhomogeneities which are most likely caused by clouds. A detailed discussion of the errors of backscatter and extinction coefficients can be found in the Appendix.

Because vibrational–Raman signals are about three orders of magnitude smaller than typical Rayleigh signals and up to five orders of magnitude smaller than signals of the aerosol–laden planetary boundary layer, they are detected best during nighttime in the absence of strong background noise. Narrow–bandwidth interference filters and interferometers for the detection of pure rotational–Raman signals can improve the daytime capability of a Raman lidar system as described by Arshinov et al. (2005) and Behrendt (2005). When no Raman signals can be detected, backscatter coefficients can be calculated from the signals of the elastic channels according to Klett's method as described in Section 3.3.1.

3.3.3 High Spectral Resolution Lidar

An alternative to Raman lidar is provided by the high–spectral–resolution–lidar (HSRL) technique (Shimizu et al. 1983, Shipley et al. 1983, Alvarez et al. 1990, Piironen and Eloranta 1994, Liu et al. 1999, Hair et al. 2001, Eloranta 2005, Esselborn et al. 2008) which is briefly introduced in this section because measurements with an airborne HSRL aboard the Falcon are discussed in this work.

As in case of Raman lidar HSRL allows for an independent detection of particle backscatter and extinction coefficients. Furthermore, it provides full daytime capability. However, the optical setup is less robust than that of a Raman lidar and a well–calibrated HSRL demands significant efforts and extensive operative care. Instead

of using inelastic backscatter by air molecules, HSRL makes use of the movement of molecules and aerosol particles. Atmospheric particles move slowly while air molecules are subject to Brownian diffusion which causes a Doppler broadening of the Cabannes line. However, spectral broadening of the aerosol backscatter is negligible. In the HSRL channel the aerosol signal is suppressed with an appropriate narrow–bandwidth filter so that a pure molecular signal can be measured. In addition, a total channel detects a signal of backscatter by both molecules and aerosols. As in the case of Raman lidar, a set of equations can be utilized to calculate aerosol backscatter and extinction coefficients from the two measured signals without assuming a particle lidar ratio.

The suppression of the aerosol signal in the molecular channel can be achieved by the use of narrow–bandwidth interferometers or atomic or molecular vapor filters. For several operating systems, an iodine absorption cell shaped up as most convenient and reliable solution (Shimizu et al. 1983, Piironen and Eloranta 1994, Liu et al. 1999, Hair et al. 2001, Esselborn et al. 2008). The laser wavelength is tuned to an absorption line of the substance in the absorption cell while the laser needs to be frequency–stabilized. The transmission of the absorption cell at the laser wavelength needs to be controlled to know the suppression of the aerosol signal and to obtain reliable results. A detailed review of the HSRL technique can be found in Eloranta (2005).

3.3.4 Polarization Lidar

Chapter 5 shows that all SAMUM lidars were equipped with channels for the detection of light that is polarized parallel and perpendicular to the plane of polarization of the emitted laser light. Highly reliable measurements of the linear particle depolarization ratio at several wavelengths are one of the main accomplishments of the SAMUM lidar measurements. Thus, and because plenty of effort was put into an accurate characterization of the polarization properties of the BERTHA receiver (see Section 5.4), this section about polarization lidar will be more elaborate than the previous ones.

The polarization lidar technique (Schotland et al. 1971, Sassen 1974, 1991, Cairo et al. 1999, Sassen 2005) makes use of the fact that laser light emitted by a lidar can have a certain state of polarization which might be altered through scattering (see Section 3.1). Polarization lidars apply lasers which emit light that is linearly polarized to a degree of more than 99%. Some lidar systems transform the linearly polarized light to circularly polarized light by means of optical retarders before sending it into the atmosphere (Eloranta 2005, Flynn et al. 2007). However, all lidar systems mentioned in this thesis apply linearly polarized light. Thus, if not stated differently, linearly polarized light and quantities refering to linear depolarization are discussed.

Usually, the receiver of a polarization lidar detects backscattered light in two separated detection channels representing two planes of polarization, parallel ($\parallel$) and perpendicular ($\perp$) with respect to the plane of polarization of the emitted laser light. Thus, the lidar equation (3.6) has to be rewritten to account for the states of polarization of the

backscattered light as

$$^{\parallel}P_{\lambda}(R) = \frac{E_{\lambda}\,{}^{\parallel}\eta_{\lambda}\,{}^{\parallel}O_{\lambda}(R)}{R^2}\,{}^{\parallel}\beta_{\lambda}(R)\exp\left[-2\int_0^R {}^{\parallel}\alpha_{\lambda}(\xi)\mathrm{d}\xi\right] \tag{3.18}$$

for light that has the same state of polarization as the emitted laser light (co–polarized) and

$$^{\perp}P_{\lambda}(R) = \frac{E_{\lambda}\,{}^{\perp}\eta_{\lambda}\,{}^{\perp}O_{\lambda}(R)}{R^2}\,{}^{\perp}\beta_{\lambda}(R)\exp\left[-\int_0^R \left({}^{\parallel}\alpha_{\lambda}(\xi) + {}^{\perp}\alpha_{\lambda}(\xi)\right)\mathrm{d}\xi\right] \tag{3.19}$$

for light whose state of polarization is perpendicular to the one of the emitted laser light (cross–polarized). The term in the exponential function in Equations (3.18) and (3.19) characterizes the atmospheric transmission ${}^{\parallel}\tau$ and ${}^{\perp}\tau$ of co– and cross–polarized light, respectively.

In the area of active remote sensing all parameters are understood to be measured as a function of height and wavelength. Thus, for simplicity of the equations presented in this section an explicit illustration of the dependence on range and wavelength of the appearing parameters is not accounted for.

In lidar research, the general term depolarization ratio (Schotland et al. 1971) usually refers to the ratio of the signals measured in the perpendicular (cross–polarized) and parallel (co–polarized) channel as

$$\delta = \frac{{}^{\perp}P}{{}^{\parallel}P} = \frac{{}^{\perp}\beta}{{}^{\parallel}\beta}\exp\left[{}^{\parallel}\tau - {}^{\perp}\tau\right]. \tag{3.20}$$

Equation (3.20) is obtained from the ratio of Equations (3.18, 3.19) by assuming equal system characteristics and overlap functions for the channels that detect backscattered light which is co– and cross–polarized with respect to the plane of polarization of the emitted laser light. Atmospheric transmission usually does not depend on the state of polarization. Thus the exponential term in Equation (3.20) vanishes. Therefore, the linear volume depolarization ratio δ^{v}, which comprises the contributions of molecules and aerosol particles, is defined as

$$\delta^{\mathrm{v}} = \frac{{}^{\perp}\beta}{{}^{\parallel}\beta} = \frac{{}^{\perp}\beta^{\mathrm{p}} + {}^{\perp}\beta^{\mathrm{m}}}{{}^{\parallel}\beta^{\mathrm{p}} + {}^{\parallel}\beta^{\mathrm{m}}}. \tag{3.21}$$

If one considers molecules and particles independently, the linear molecular (Rayleigh) depolarization ratio

$$\delta^{\mathrm{m}} = \frac{{}^{\perp}\beta^{\mathrm{m}}}{{}^{\parallel}\beta^{\mathrm{m}}} \tag{3.22}$$

and the linear particle depolarization ratio

$$\delta^{\mathrm{p}} = \frac{{}^{\perp}\beta^{\mathrm{p}}}{{}^{\parallel}\beta^{\mathrm{p}}} \tag{3.23}$$

can be introduced. The latter is an intensive quantity of the ensemble of scattering particles and can be used for aerosol characterization (see Section 4.1).

To obtain a formula for the retrieval of δ^{p}, Equations (3.22) and (3.23) are rearranged to ${}^{\perp}\beta^{\mathrm{p,m}}$ and ${}^{\parallel}\beta^{\mathrm{p,m}}$. The resulting terms are used together with the relations

$$\beta = {}^{\perp}\beta + {}^{\parallel}\beta$$

and

$$\beta^{\mathrm{p,m}} = {}^{\perp}\beta^{\mathrm{p,m}} + {}^{\parallel}\beta^{\mathrm{p,m}}$$

to replace ${}^{\perp,\parallel}\beta^{\mathrm{p,m}}$ in Equation (3.21). Transformation leads to the equation for the calculation of the linear particle depolarization ratio from the measured lidar profiles of particle backscatter coefficient and linear volume depolarization as

$$\delta^{\mathrm{p}} = \frac{\beta^{\mathrm{m}}(\delta^{\mathrm{v}} - \delta^{\mathrm{m}}) + \beta^{\mathrm{p}}\delta^{\mathrm{v}}(1 + \delta^{\mathrm{m}})}{\beta^{\mathrm{m}}\left(\delta^{\mathrm{m}} - \delta^{\mathrm{v}}\right) + \beta^{\mathrm{p}}\left(1 + \delta^{\mathrm{m}}\right)}\,. \tag{3.24}$$

Reliable information about the kind of observed particles can only be extracted from the particle depolarization ratio. For its calculation, i.e., the extraction of the contribution of molecules to the measurements of the volume depolarization ratio, measurements of the particle backscatter coefficient are required. As mentioned earlier the molecular backscatter can be calculated from soundings or extracted from atmospheric models. The molecular depolarization ratio is a constant factor which depends on the bandwidth of the interference filters in the lidar receiver.

Note on the Physical Relevance of the Particle Depolarization Ratio

In a recent paper Gimmestad (2008) criticized the general treatment of polarized light in the field of lidar research, i.e., the use of the unphysical volume depolarization ratio δ^{v} which is described to be a legacy of the early days (Schotland et al. 1971) of lidar applications. Indeed, the arbitrary definition of δ^{v} in Equation (3.21) is owing to the measurement principle of the polarization lidar technique and suggests that light is backscattered to the receiver at only two distinct and orthogonal states of polarization. Actually, the backscattered light consists of a polarized component (P_{pol}, same state of polarization as the emitted laser beam) and an unpolarized component (P_{unpol}):

$$P = P_{\mathrm{pol}} + P_{\mathrm{unpol}}\,. \tag{3.25}$$

While the polarized light is detected in the parallel channel ($P_{\mathrm{pol}} = {}^{\parallel}P_{\mathrm{pol}}$), the unpolarized light contributes to the measurements of both the parallel and perpendicular channel ($P_{\mathrm{unpol}} = {}^{\parallel}P_{\mathrm{unpol}} + {}^{\perp}P_{\mathrm{unpol}}$, with ${}^{\parallel}P_{\mathrm{unpol}} = {}^{\perp}P_{\mathrm{unpol}}$). As a consequence of its arbitrary definition as the ratio of the perpendicular to the parallel signal, the linear depolarization ratio cannot be directly used in radiative transfer or scattering theory. Therefore, Gimmestad (2008) suggests the use of a physically meaningful depolarization factor d (Flynn et al. 2007). It covers a range from zero to unity and describes the propensity of the scattering medium to depolarize the incident polarization.

Using the depolarization parameter d and the relations of the previous paragraph, Equation (3.25) is rewritten as

$$P = (1 - d)P + dP\,. \tag{3.26}$$

Following the definition of Equation (3.20), the depolarization ratio is expressed as

$$\delta = \frac{{}^{\perp}P_{\text{unpol}}}{{}^{\parallel}P_{\text{unpol}} + {}^{\parallel}P_{\text{pol}}} = \frac{\frac{1}{2}dP}{(1-d)P + \frac{1}{2}dP} = \frac{d}{2-d}\,. \tag{3.27}$$

By introducing d, Equation (3.2) simplifies to

$$\mathbf{F}(180^\circ) = \begin{bmatrix} 1 & 0 & 0 & 0 \\ 0 & 1-d & 0 & 0 \\ 0 & 0 & d-1 & 0 \\ 0 & 0 & 0 & 2d-1 \end{bmatrix}. \tag{3.28}$$

A non–depolarizing medium is described by $d = 0$. In that case, Matrix (3.28) equals Matrix (3.3). The formalism allows for the retrieval of the complete transformation matrix for backscattering by randomly oriented particles with rotational symmetry because it depends on just one parameter d that can be retrieved from measurements of the linear volume depolarization ratio (i.e., for the entire scattering volume) as

$$d^{\text{v}} = \frac{2\delta^{\text{v}}}{1+\delta^{\text{v}}} \tag{3.29}$$

and for the contribution of aerosol particles as

$$d^{\text{p}} = \frac{2\delta^{\text{p}}}{1+\delta^{\text{p}}}\,. \tag{3.30}$$

Furthermore, a direct relation between the depolarization ratio (as a lidar parameter) and the transformation matrix (from scattering theory/radiative–transfer theory) is established.

For the sake of completeness, the depolarization parameter d also needs to be introduced to Equations (3.18) and (3.19). Thus, the co– and cross–polarized backscatter coefficients ${}^{\parallel}\beta = (1-d/2)\beta$ and ${}^{\perp}\beta = (d/2)\beta$, respectively, are replaced by expressions that refer to the total backscatter coefficient. In the framework of this thesis, however, the "traditional" linear depolarization ratio is applied for the investigation of atmospheric aerosol particles, because it can be directly compared with results from the other SAMUM lidars and literature values. A transformation from the "*legacy parameter*" (Gimmestad 2008) to the depolarization parameter can easily be achieved by using Equation (3.30).

4 Aerosol Characterization with Lidar

After the introduction of the basic lidar techniques in Section 3.3 this chapter focuses on the possibilities that emerge when these techniques are combined in state–of–the–art multiwavelength polarization Raman lidars like the ones applied during the SAMUM campaigns. Section 4.1 shows that the parameters measured with such systems can be used for aerosol characterization. If properly calibrated, their data products furthermore allow for a height–resolved separation of the contributions of individual aerosol types to a mixed aerosol plume after a method which was developed within the work of this thesis and is described in Section 4.2. Finally, Section 4.3 briefly introduces how microphysical properties of spherical aerosol particles can be retrieved from lidar data at multiple wavelengths.

For the measurements of SAMUM–2a, the aerosol–type separation method (see Section 4.2) is used to obtain individual data sets of backscatter and extinction coefficients for mineral dust and biomass–burning smoke. This separation is necessary, because the inversion algorithm described in Section 4.3 was not designed to be applied to optical data of large non–spherical particles like mineral dust. It can only be used to retrieve microphysical properties from the data set of pure biomass–burning smoke. This aerosol type consists of rather small particles for which shape effects play a minor role.

4.1 Aerosol Typing

Modern multiwavelength polarization Raman lidars use high–power Nd:YAG lasers to emit light at two or three of the wavelengths of 355, 532, and 1064 nm. The measured profiles of backscatter coefficients at 355, 532, and 1064 nm, of extinction coefficients at 355 and 532 nm, and of the volume depolarization ratio at one or more of the emitted wavelengths can be used to calculate optical aerosol parameters that are sensitive to size, shape, and refractive index of atmospheric particles. These parameters can be used for aerosol characterization (Ansmann and Müller 2005, Müller et al. 2007, Freudenthaler et al. 2009).

The particle lidar ratio and the particle depolarization ratio were already introduced in Equations (3.10) and (3.23), respectively. The Ångström exponent $\mathring{a}$ (Ångström 1964) contains information about the spectral slope of a quantity. For the backscatter coefficient β, the extinction coefficient α, and the lidar ratio S measured at the two wavelengths λ_1 and λ_2 the respective Ångström exponents are calculated as (Ansmann

et al. 2002b):

$$\mathring{a}^{\beta}_{\lambda_1/\lambda_2} = \frac{\ln\left(\beta_{\lambda_1}/\beta_{\lambda_2}\right)}{\ln\left(\lambda_2/\lambda_1\right)}\,, \tag{4.1}$$

$$\mathring{a}^{\alpha}_{\lambda_1/\lambda_2} = \frac{\ln\left(\alpha_{\lambda_1}/\alpha_{\lambda_2}\right)}{\ln\left(\lambda_2/\lambda_1\right)} = \frac{\ln\left(\left[\beta_{\lambda_1} S_{\lambda_1}\right] / \left[\beta_{\lambda_2} S_{\lambda_2}\right]\right)}{\ln\left(\lambda_2/\lambda_1\right)} = \mathring{a}^{\beta}_{\lambda_1/\lambda_2} + \mathring{a}^{S}_{\lambda_1/\lambda_2}\,, \tag{4.2}$$

and

$$\mathring{a}^{S}_{\lambda_1/\lambda_2} = \frac{\ln\left(S_{\lambda_1}/S_{\lambda_2}\right)}{\ln\left(\lambda_2/\lambda_1\right)}\,. \tag{4.3}$$

Ångström exponents of zero denote wavelength independence of the investigated quantity which is due to scattering by large particles (see Section 3.1). Scattering by small particles on the other hand shows a strong wavelength dependence and causes values of $\mathring{a}$ that are larger than unity (Eck et al. 1999).

Profiles of the lidar ratio give information about the size, shape, and the absorption properties (i.e., the imaginary part of the refractive index) of aerosol particles. The lidar ratio decreases with particle size and increases with particle absorption efficiency. Typically, non–spherical particles have higher lidar ratios than spherical particles of the same size. The different effects might compensate each other which leads to similar lidar ratios for totally different particle types. For instance, lidar ratios of urban haze (small and highly absorbing) and mineral dust (large, non–spherical, and less absorptive) are similar with values of 50–55 sr (Ackermann 1998, Müller et al. 2007, Tesche et al. 2009b).

In such an ambiguous case the shape–dependent particle depolarization ratio provides further insight. As explained in Sections 3.1 and 3.3.4, scattering by spheres does not alter the state of polarization of light, i.e., light is not depolarized. Thus $\delta^{\mathrm{p}}_{\lambda} \approx 0$ for spherical particles. It increases with particle non–sphericity and in case of a mixture of spherical and non–spherical particles (see Section 4.2). However, quantitative (highly accurate) measurements of the particle depolarization ratio are scarce and the parameter (or the easier to obtain volume depolarization ratio) is in most cases only used qualitatively to distinguish non–spherical (mainly ice crystals or mineral dust) from spherical particles (Schotland et al. 1971, Sassen 1991, 2005).

The optical properties of the aerosol types observed during SAMUM (i.e., mineral dust, maritime aerosol, biomass–burning smoke, and a mixture of dust and smoke) are reported by Freudenthaler et al. (2009), Groß et al. (2011a, b) and Tesche et al. (2009a, 2011a, b) and will be discussed in detail in later sections of this thesis.

4.2 Aerosol–type Separation

Section 2.3 described that during winter the aerosol plume over the eastern tropical Atlantic consists of a mixture of mineral dust from northern Africa and biomass–burning aerosol from southern West Africa. Most lidar measurements during SAMUM–2a at Cape Verde showed particle depolarization ratios which were too high to represent

pure smoke and too low to imply pure mineral dust. Hence, layers of a mixture of the two aerosol types were present during these observation. In case of such aerosol mixtures, knowledge of the vertical distribution of the individual aerosol types is crucial for an understanding of their radiative effects (Myhre et al. 2008).

Several methods to separate profiles of particle backscatter and extinction related to fine–mode (biomass–burning smoke, urban haze) and coarse–mode aerosol (sea salt, desert dust) are presented in the literature (Kaufman et al. 2003, Léon et al. 2003, Sugimoto et al. 2003, Shimizu et al. 2004, Sugimoto and Lee 2006, Nishizawa et al. 2007, Huneeus and Boucher 2007). Most of these algorithms use a predetermined log–normal aerosol model which consists of a fine mode and a coarse mode with fixed size distributions and refractive–index characteristics. For the retrieval of fine–mode– and coarse–mode–related backscatter and extinction profiles radiative–transfer calculations are performed with varying particle concentration in the fine and coarse mode of the aerosol model. The final solution is the one that minimizes the difference between the model calculations and the initial observations with a lidar (e.g., CALIPSO) and/or a radiometer (e.g., MODIS). Sugimoto et al. (2003) and Shimizu et al. (2004) apply lidar measurements of the 532–nm particle depolarization ratio in their retrieval. By assuming an Asian dust depolarization ratio of 0.35 and a value of 0.02–0.05 for polluted eastern Asian air (during periods free of desert dust) the contribution of the dust backscattering to the volume backscatter coefficient of particles as a function of height is obtained.

The method developed in the framework of this thesis (Tesche et al. 2009b) is based on precise measurements of the particle depolarization ratio and assumes typical depolarization ratios for the individual aerosol types of a two–component aerosol mixture. It does not require further assumptions or model calculations to obtain the contribution of different aerosol types to the measured optical properties. The method is similar to the ones introduced by Sugimoto et al. (2003) and Shimizu et al. (2004). However, previous approaches always applied data obtained with elastic–backscatter lidar which only allows for the determination of backscatter coefficients (see Section 3.3.1). The method presented in this section, for the first time uses multiwavelength Raman lidar measurements of the particle backscatter coefficient at 355, 532, and 1064 nm and the particle extinction coefficient at 355 and 532 nm.

The technique is similar to the one used for separating the contributions of molecules and particles to the volume depolarization ratio to obtain Equation (3.24). It benefits from the characterization of dust optical properties that was obtained from the measurements of SAMUM–1. The particle depolarization ratio is assumed to contain contributions of mineral dust (superscript d) and less depolarizing aerosols (superscript nd for non–dust). Similarly to Equation (3.21), $\delta_\lambda^{\mathrm{p}}$ can be rewritten as

$$\delta_\lambda^{\mathrm{p}} = \frac{{}^{\perp}\beta_\lambda^{\mathrm{d}} + {}^{\perp}\beta_\lambda^{\mathrm{nd}}}{{}^{\parallel}\beta_\lambda^{\mathrm{d}} + {}^{\parallel}\beta_\lambda^{\mathrm{nd}}} \,. \tag{4.4}$$

The relationships

$$\beta_\lambda^{\mathrm{x}} = {}^{\perp}\beta_\lambda^{\mathrm{x}} + {}^{\parallel}\beta_\lambda^{\mathrm{x}} \,,$$

$$
\begin{aligned}
{}^{\parallel}\beta_{\lambda}^{\mathrm{x}} &= \frac{\beta_{\lambda}^{\mathrm{x}}}{1+\delta_{\lambda}^{\mathrm{x}}}\,, \\
{}^{\perp}\beta_{\lambda}^{\mathrm{x}} &= \frac{\beta_{\lambda}^{\mathrm{x}}\delta_{\lambda}^{\mathrm{x}}}{1+\delta_{\lambda}^{\mathrm{x}}}
\end{aligned}
$$

with x = d or nd are used to replace ${}^{\perp}\beta_{\lambda}^{\mathrm{d}}$, ${}^{\parallel}\beta_{\lambda}^{\mathrm{d}}$, ${}^{\perp}\beta_{\lambda}^{\mathrm{nd}}$, and ${}^{\parallel}\beta_{\lambda}^{\mathrm{nd}}$ in Equation (4.4). This results in

$$
\delta_{\lambda}^{\mathrm{p}} = \frac{\frac{\beta_{\lambda}^{\mathrm{d}}\delta_{\lambda}^{\mathrm{d}}}{1+\delta_{\lambda}^{\mathrm{d}}} + \frac{\beta_{\lambda}^{\mathrm{nd}}\delta_{\lambda}^{\mathrm{nd}}}{1+\delta_{\lambda}^{\mathrm{nd}}}}{\frac{\beta_{\lambda}^{\mathrm{d}}}{1+\delta_{\lambda}^{\mathrm{d}}} + \frac{\beta_{\lambda}^{\mathrm{nd}}}{1+\delta_{\lambda}^{\mathrm{nd}}}}\,. \tag{4.5}
$$

Simple conversion leads to

$$
\delta_{\lambda}^{\mathrm{p}} = \frac{\beta_{\lambda}^{\mathrm{d}}\delta_{\lambda}^{\mathrm{d}}(1+\delta_{\lambda}^{\mathrm{nd}}) + \beta_{\lambda}^{\mathrm{nd}}\delta_{\lambda}^{\mathrm{nd}}(1+\delta_{\lambda}^{\mathrm{d}})}{\beta_{\lambda}^{\mathrm{d}}(1+\delta_{\lambda}^{\mathrm{nd}}) + \beta_{\lambda}^{\mathrm{nd}}(1+\delta_{\lambda}^{\mathrm{d}})}\,. \tag{4.6}
$$

After substituting $\beta_{\lambda}^{\mathrm{nd}}$ by $\beta_{\lambda}^{\mathrm{p}} - \beta_{\lambda}^{\mathrm{d}}$, a solution is obtained for (Tesche et al. 2009b)

$$
\beta_{\lambda}^{\mathrm{d}} = \beta_{\lambda}^{\mathrm{p}} \frac{\left(\delta_{\lambda}^{\mathrm{p}} - \delta_{\lambda}^{\mathrm{nd}}\right)\left(1+\delta_{\lambda}^{\mathrm{d}}\right)}{\left(\delta_{\lambda}^{\mathrm{d}} - \delta_{\lambda}^{\mathrm{nd}}\right)\left(1+\delta_{\lambda}^{\mathrm{p}}\right)}\,. \tag{4.7}
$$

The dust backscatter coefficient can be derived, if $\beta_{\lambda}^{\mathrm{p}}$ and $\delta_{\lambda}^{\mathrm{p}}$ of a certain wavelength are measured and $\delta_{\lambda}^{\mathrm{d}}$ and $\delta_{\lambda}^{\mathrm{nd}}$ are known.

Figure 4.1 is a visualization of Equation (4.7) for the measurement of two–component mixtures of maritime aerosol + biomass–burning smoke (green), maritime aerosol + mineral dust (blue), and biomass–burning smoke + mineral dust (red) at 532 nm. The third mixture represents the conditions observed in the elevated layers over Cape Verde during winter (Tesche et al. 2009b, 2011a, b). An investigation of the second aerosol mixture is presented by Groß et al. (2011b). In Figure 4.1, the particle depolarization ratios for maritime aerosol, biomass–burning smoke, and mineral dust are assumed to be $\delta^{\mathrm{o}} = 0.03$, $\delta^{\mathrm{s}} = 0.05$, and $\delta^{\mathrm{d}} = 0.31$, respectively. In the framework of this thesis, the separation was performed at $\lambda = 532\,\mathrm{nm}$. Detailed measurements of $\delta_{532}^{\mathrm{d}} = 0.31 \pm 0.03$ were conducted during SAMUM–1 (see Section 6.1.4). The 532–nm smoke depolarization ratio is assumed to be 0.05±0.02. As discussed in Tesche et al. (2009b) most values published in the literature (Murayama et al. 1999, Fiebig et al. 2002, Sugimoto et al. 2003, Murayama et al. 2004, Müller et al. 2005, Sugimoto and Lee 2006, Chen et al. 2007a, Heese and Wiegner 2008) accumulate around this number. The particle depolarization ratio of maritime aerosol of 0.03 was measured during SAMUM–2 (Groß et al. 2011a, b). It can be seen from the red line in Figure 4.1, that for 532–nm particle depolarization ratios of 0.14–0.18 that were usually observed in the elevated, mixed dust/smoke layers over Cape Verde during winter (see Section 6.2.3 and Groß et al. 2011a), the contribution of dust varies between 40%–60%. The aerosol–type separation is complicated, if the contrast between the particle depolarization ratios of the individual aerosol types decreases (see green line in Figure 4.1).

Once $\beta_{\lambda}^{\mathrm{d}}$ is known from Equation (4.7) the contribution of the non–dust component can be derived as

$$
\beta_{\lambda}^{\mathrm{nd}} = \beta_{\lambda}^{\mathrm{p}} - \beta_{\lambda}^{\mathrm{d}}\,. \tag{4.8}
$$

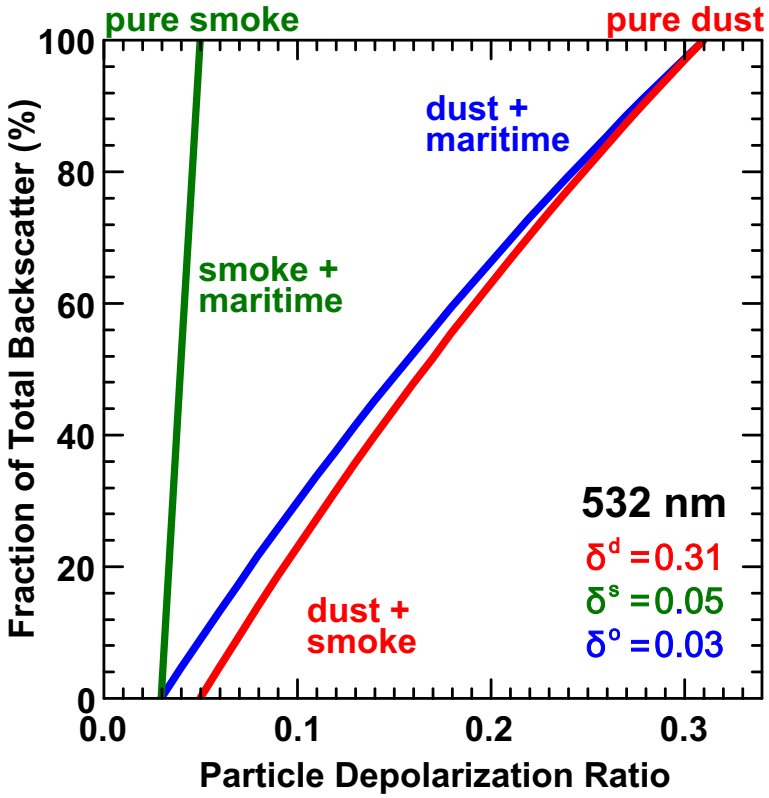

Figure 4.1: Visualization of Equation (4.7) for two–component mixtures of mineral dust, biomass–burning smoke, and maritime aerosol at 532 nm. δ^{d}, δ^{s}, and δ^{o} are the particle depolarization ratios assumed for the respective aerosol types.

To fully exploit the potential of this new approach, the separation also has to be performed for the 532–nm extinction coefficient and for the measurements at the other laser wavelengths of 355 and 1064 nm. Ultimately, this approach results in data sets of three backscatter (355, 532, and 1064 nm) and two extinction coefficients (355 and 532 nm) for the dust and non–dust components. This configuration is often referred to as a 3+2 data set. It constitutes the minimum set of input parameters needed for the retrieval of microphysical particle properties by means of an inversion algorithm that will be described in Section 4.3. Scattering by large non–spherical mineral dust particles cannot be properly described with Mie theory. Because of that, the aforementioned inversion algorithm cannot be applied to lidar data which incorporate contributions of mineral dust. If the aerosol–type separation is used to subtract the contribution of dust to the measured optical parameters, the resulting data set for pure biomass–burning smoke (small particles with insignificant shape effects) can be used to retrieve informations about the effective radius and the single–scattering albedo (SSA) of these particles.

To obtain a 3+2 data set of the non–dust component, one has to proceed as follows. The dust backscatter coefficient β^{d}_{532} is multiplied by the dust lidar ratio S^{d}_{532} to obtain the dust extinction coefficient $\alpha^{\mathrm{d}}_{532}$. Subtraction of $\alpha^{\mathrm{d}}_{532}$ from the total particle extinction coefficient results in the extinction coefficient of the non–dust particles. Extensive

measurements of the dust lidar ratios at 355 nm and 532 nm, and of dust Ångström exponents of backscatter and extinction are discussed in Section 6.1 and published in Tesche et al. (2009a).

By using the backscatter–related Ångström exponent $\mathring{a}^{\beta,\mathrm{d}}_{\lambda_1,\lambda_2}$ and the extinction–related Ångström exponent $\mathring{a}^{\alpha,\mathrm{d}}_{\lambda_1,\lambda_2}$ measured for pure dust during SAMUM–1 (Tesche et al. 2009a) one obtains

$$\beta^{\mathrm{d}}_{\lambda} = \beta^{\mathrm{d}}_{532} \left(\frac{532}{\lambda} \right)^{\mathring{a}^{\beta,\mathrm{d}}_{\lambda,532}} , \tag{4.9}$$

with λ being 355 or 1064 nm, and

$$\alpha^{\mathrm{d}}_{355} = \alpha^{\mathrm{d}}_{532} \left(\frac{532}{355} \right)^{\mathring{a}^{\alpha,\mathrm{d}}_{355,532}} . \tag{4.10}$$

Finally, the non–dust backscatter and extinction coefficients

$$\beta^{\mathrm{nd}}_{\lambda} = \beta^{\mathrm{p}}_{\lambda} - \beta^{\mathrm{d}}_{\lambda} \tag{4.11}$$

and

$$\alpha^{\mathrm{nd}}_{\lambda} = \alpha^{\mathrm{p}}_{\lambda} - \alpha^{\mathrm{d}}_{\lambda} \tag{4.12}$$

are obtained together with estimates of the non–dust lidar ratio $S^{\mathrm{nd}}_{\lambda}$=$\alpha^{\mathrm{nd}}_{\lambda}/\beta^{\mathrm{nd}}_{\lambda}$ and the non–dust Ångström exponents $\mathring{a}^{\beta,\mathrm{nd}}_{355,532}$, $\mathring{a}^{\beta,\mathrm{nd}}_{532,1064}$, and $\mathring{a}^{\alpha,\mathrm{nd}}_{355,532}$.

In case of state–of–the–art multiwavelength polarization Raman lidar, one single instrument is sufficient to determine all the required input parameters. The method can be applied to observations of next–generation space lidars such as high–spectral–resolution lidars measuring particle extinction at 355 and 532 nm, particle backscatter at 355, 532, and 1064 nm and the depolarization ratio. The prospects of such lidars are currently assessed by space agencies. Furthermore, approaches that simply cut an assumed aerosol size distribution into a fine and a coarse mode (e.g., *in situ* measurements or the AERONET retrieval, Eck et al. 2010) ignore the effects of small mineral dust particles in the fine mode or large smoke particles in the coarse mode. The lidar–based method presented here separates aerosol types rather than fine–mode and coarse–mode fractions.

4.3 Inversion with Regularization

The method of inversion with regularization is the standard application for the retrieval of microphysical particle properties from multiwavelength aerosol lidar measurements (Müller et al. 1999b, a, 2000, Veselovskii et al. 2002, Ansmann and Müller 2005, Kolgotin and Müller 2008). The method turned out to be reliable for application to the findings of various field experiments that allowed for comparisons to *in situ* particle sampling (Ansmann et al. 2002b, Wandinger et al. 2002, Müller et al. 2003, 2005, Tesche et al. 2008).

The relationship between optical and microphysical properties of a population of scattering particles can be expressed as a set of Fredholm equations of the first kind

$$g_p = \int_{r_{\min}}^{r_{\max}} K_p(r,m)n(r)\mathrm{d}r + \epsilon_p^{\exp}\,, \tag{4.13}$$

which cannot be solved analytically. The optical input data $g_p = \beta_\lambda, \alpha_\lambda$ are affected by a measurement error $\epsilon_p^{\exp}$. The entire inversion procedure is targeted at finding the actual number size distribution $n(r)$ of the atmospheric aerosol particles that produced the measured optical data. Previous studies have shown that a set of three backscatter and two extinction coefficients (i.e., a 3+2 data set) represents the minimum number of input parameters needed for particle characterization (Müller et al. 2001, Veselovskii et al. 2002). Thus modern Raman lidars with a Nd:YAG laser as the light source are designed to measure three backscatter coefficients at 355, 532, and 1064 nm and two extinction coefficients at 355 and 532 nm. Such systems are also referred to as 3+2 (Raman) lidar.

The geometric cross section πr^2 of a particle in combination with the respective dimensionless backscatter or extinction efficiency $Q_p(r,m)$ forms the kernel function

$$K_p(r,m) = \pi r^2 Q_p(r,m)\,. \tag{4.14}$$

Scattering efficiencies depend on the particle radius r, the complex refractive index m, and the wavelength λ of the scattered light. They can be calculated using Mie theory (Mie 1908, van de Hulst 1957, Bohren and Huffman 1983), if scatterers are of spherical shape or can be approximated by spheres.

Equation (4.13) represents an ill–posed, non–linear problem that needs to be solved numerically. The solutions of the problem are not accurately defined and are very sensitive to changes in the input data. In other words: mathematically correct solutions are not necessarily physically trustworthy. The instability of the solutions can only be controlled by introducing meaningful boundary conditions. To minimize the number of *a priori* assumptions in the retrieval, $n(r)$ is described as a combination of triangular base functions $B_j(r)$ and weight factors w_j as

$$n(r) = \sum_{j=1}^{N} w_j B_j(r) + \epsilon_p^{\mathrm{math}}(r)\,. \tag{4.15}$$

The deviation between the real and the constructed particle number size distribution is described by the mathematical residual error $\epsilon_p^{\mathrm{math}}(r)$. The index j denotes the number of the applied base functions which is typically set to 8.

The problem of the inversion procedure is to obtain the weight factors in Equation (4.15). Equation (4.15) is used to rewrite Equation (4.13) as

$$g_p = \sum_j A_{pj}(m)w_j + \epsilon_p\,. \tag{4.16}$$

The kernel matrix $A_{pj}(m)$ represents the product of the individual kernel functions $K_p(r,m)$ and their base functions $B_j(r)$:

$$A_{pj}(m) = \int_{r_{\min}}^{r_{\max}} K_p(r,m) B_j(r) \mathrm{d}r \,. \tag{4.17}$$

The sum of experimental and mathematical errors is combined to $\epsilon_p = \epsilon_p^{\exp} + \epsilon_p^{\mathrm{math}}$. It describes the deviation of the measured backscatter and extinction coefficients from the respective values used in the inversion. Conversion leads to the vectors of optical input data $\mathbf{g} = [g_p]$, weight factors $\mathbf{w} = [w_j]$, and errors $\boldsymbol{\epsilon} = [\epsilon_p]$ in a vector matrix equation

$$\mathbf{g} = \mathbf{A}\mathbf{w} + \boldsymbol{\epsilon} \,. \tag{4.18}$$

The weight matrix $\mathbf{A} = [A_{pj}]$ contains the elements derived from Equation (4.17). After rearrangement the weight factors are obtained as

$$\mathbf{w} = \mathbf{A}^{-1}\mathbf{g} + \boldsymbol{\epsilon}' \quad \text{with} \quad \boldsymbol{\epsilon}' = \mathbf{A}^{-1}\boldsymbol{\epsilon} \,. \tag{4.19}$$

The resulting solution space enables a reproduction of the input data within their error bars $\boldsymbol{\epsilon}$. Because these solutions might still be unstable or physically meaningless, regularization (e.g., the demand for smooth solutions of $n(r)$) is used to reduce the number of solutions by restricting the highest acceptable difference between the vectors $\mathbf{A}\mathbf{w}$ and $\mathbf{g}$ to

$$e^2 \geq \|\boldsymbol{\epsilon}\|^2 = \|\mathbf{A}\mathbf{w} - \mathbf{g}\|^2 + \gamma\Gamma(n) \,. \tag{4.20}$$

Only solutions that minimize $\boldsymbol{\epsilon}$ are accepted. The penalty term $\Gamma(n)$ is controlled by the Lagrange multiplier γ and suppresses oscillations in the resulting particle size distribution. It is defined as

$$\Gamma(n) = \mathbf{w}^{\mathrm{T}}\mathbf{H}\mathbf{w}. \tag{4.21}$$

$\mathbf{w}^{\mathrm{T}}$ is the transposed vector $\mathbf{w}$. The matrix $\mathbf{H}$ contains the demand for smoothness which stretches over three base functions. Finally, the weight factor is retrieved as

$$\mathbf{w} = (\mathbf{A}^{\mathrm{T}}\mathbf{A} + \gamma\mathbf{H})^{-1}\mathbf{A}^{\mathrm{T}}\mathbf{g} \,. \tag{4.22}$$

For one input data set only a fraction of the solutions of the inversion algorithm represents trustworthy results. This necessitates a careful analysis of the inversion output. In the end, several hundred trustworthy solutions out of hundreds of thousand of mathematical inversion results are averaged. A mean particle number concentration and a mean complex refractive index are obtained. The surface–weighted (effective) mean radius is calculated as the ratio of surface–area and volume concentrations as

$$r_{\mathrm{eff}} = \frac{\int n(r) r^3 \mathrm{d}r}{\int n(r) r^2 \mathrm{d}r} \tag{4.23}$$

and used as a measure of mean particle size. Finally, the single–scattering albedo is calculated from the retrieved parameters by means of Mie calculations.

In this thesis, final inversion results for the microphysical properties of biomass–burning aerosol are obtained as an average of the findings of six individual inversions. The

first run is performed with the original 3+2 data set which was retrieved through aerosol–type separation (see Section 4.2). In the additional five inversion runs, up to 20% of random noise are added to the input data (see also Tesche et al. 2008). This procedure provides insight into the possible spread of inversion results for slight variations in the input parameters (i.e., errors) and furthermore gives an indication of the general reliability of the input data set. A meaningless combination of input parameters is unlikely to reproduce physically meaningful solutions (even though it might be mathematically possible) which pass the analysis of the inversion calculations.

5 Instrumentation

An assembly of three ground–based polarization Raman lidars and an airborne HRSL was applied during SAMUM–1 and SAMUM–2a. This combination of instruments was necessary to cover the temporal and vertical distribution of aerosol particles in the entire atmospheric column as well as to obtain quality–assured results in terms of backscatter, extinction, and depolarization–ratio profiles. Each system was dedicated to a certain objective. A combination of all lidar measurements results in profiles from a few hundred meters up to several kilometers at various wavelengths. The next sections introduce the lidar systems whose measurements contributed to this thesis. At first, the MUltiwavelength LIdar System (MULIS) and the POrtable LIdar System (POLIS) of the Meteorological Institute of the University of Munich (MIM) and the airborne HSRL of DLR are described in Sections 5.1, 5.2, and 5.3, respectively. Thereafter, special emphasis is drawn to the description of the IfT lidar BERTHA, whose measurements are presented in this thesis. Calibration measurements which emerged to be necessary to obtain quality–assured profiles of the 532–nm backscatter coefficient and the 710–nm particle depolarization ratio with this instrument are discussed in detail in Sections 5.4.2 and 5.4.3, respectively. Section 5.5 is focused on the Sun photometers that participated in the SAMUM experiments. The sounding strategy of SAMUM is described in Section 5.6. At last, the trajectory models that were used to determine the origin of the observed aerosol layers are briefly introduced in Section 5.7.

5.1 MULIS

The main task of MULIS (Wiegner et al. 1995, Freudenthaler et al. 2009, Groß et al. 2011b) of MIM during SAMUM was the measurement of the linear particle depolarization ratio at 532 nm. The instrument was designed for high–quality measurements of the linear volume depolarization ratio with careful considerations of instrumental effects and calibration errors (Freudenthaler et al. 2009). The system emits pulses of linearly polarized light at 355, 532, and 1064 nm and is capable of scanning. Apart from the elastic–backscatter signals at the laser wavelengths, Raman signals are measured at 387 and 607 nm. During SAMUM–1 Raman signals were measured at 387 nm only. The comparably low height of laser–beam RFOV overlap allows for the determination of extinction coefficients down to a range of about 300 m from the instrument.

At 532 nm backscattered light is separated to contributions of co– and cross–polarized light for the measurement of the depolarization ratio. A rotating half–wave plate

(HWP[1]) is used for regular calibration measurements to determine profiles of the linear volume depolarization ratio. A detailed description of the instrument and the method for measurements of the linear volume depolarization ratio can be found in Freudenthaler et al. (2009).

Profiles of the linear volume depolarization ratio derived with MULIS were used for the correction of polarization–dependent receiver transmission of the BERTHA 532–nm elastic–backscatter channel (see Section 5.4.3.2) and the extrapolation of measurements of the linear volume depolarization ratio from 710 nm to 532 nm (see Section 5.4.3.3).

5.2 POLIS

POLIS (Heese et al. 2002, Freudenthaler et al. 2009) is the second lidar of MIM which participated in SAMUM (Heese et al. 2009, Groß et al. 2011b). Its contribution is complementary to the measurements of the larger systems since POLIS shows with 150 m the lowest height of full overlap of all systems (Groß et al. 2011b). Therefore, POLIS is able to obtain reliable results in the lowermost parts of the atmosphere that cannot be seen by BERTHA and only in part by MULIS. POLIS is a light–weight system for mobile operation from a car or an airplane. It emits pulses of linearly polarized light at 355 nm. Backscattered light is collected by a 20–cm telescope. POLIS features two measurement channels and can be operated either as a Raman lidar or as a polarization lidar. In Raman mode elastic–backscatter signals at 355 nm and Raman signals at 387 nm are detected. The Raman mode is usually applied during nighttime. In the depolarization mode elastically backscattered light at 355 nm is discerned with respect to its plane of polarization parallel and perpendicular to the plane of polarization of the emitted laser light. During daytime, measurements of the linear volume depolarization ratio were performed and the particle backscatter coefficient was determined using Klett's method with lidar ratios retrieved from earlier or later nighttime measurements (see Section 3.3.1).

5.3 HSRL

The airborne lidar that was operated during SAMUM–1 and SAMUM–2a was an HSRL aboard the Falcon 20 research aircraft of DLR (Esselborn et al. 2008). This system was used to provide information about the vertical structure of the aerosol layers over wide spatial distances for subsequent *in situ* measurements (Weinzierl et al. 2009) and for lidar case studies (Esselborn et al. 2009). The airborne measurements complement the statistical investigations of the ground–based lidar systems whose observations are restricted to one spot.

[1] A half–wave plate rotates the plane of polarization of incident light by twice the value of its rotation angle.

The HSRL emits laser pulses at 532 and 1064 nm with a frequency of 100 Hz which facilitates a high spatial resolution of the measurement. Apart from the elastic–backscatter signals at the laser wavelengths, pure molecular signals are detected at 532 nm. This enables the direct calculation of the backscatter and extinction coefficients even during daytime (see Section 3.3.3). In the depolarization channel at 532 nm, the co– and cross–polarized components of the backscattered light are measured separately. A calibration method similar to that of Freudenthaler et al. (2009) is applied to assure reliable results of the linear volume depolarization ratio. Depolarization ratio measurements of reduced data quality were also performed at 1064 nm.

5.4 BERTHA

The Backscatter Extinction lidar–Ratio Temperature Humidity profiling Apparatus (BERTHA) of IfT Leipzig was the most powerful lidar applied during the SAMUM campaigns. A detailed description of the system is given by Althausen et al. (2000) and Tesche et al. (2009b). The detection of signals at various wavelengths (including Raman signals) and at different states of polarization allows for an extensive characterization of aerosol particles according to the properties introduced in Section 4.1. After an introduction to the system, corrections that needed to be applied for quality assurance of the data collected during SAMUM are explained. In the framework of the thesis, a calibration of the transmission properties of the receiver optics together with an implementation of an HWP for regular calibration measurements according to the method of Freudenthaler et al. (2009) led to a tremendous improvement in the detection of the linear volume depolarization ratio during SAMUM–2 compared to SAMUM–1.

5.4.1 System Properties and Data Analysis

BERTHA (Althausen et al. 2000) is a transportable lidar system that is housed in a 20–ft sea container and was exclusively designed for field experiments. It is equipped with a scanning unit that allows for measurements at zenith angles from $\Theta_Z = -90°$ to 90° within one azimuthal plane. During transport and off–time the scanning unit is housed in the lidar container. BERTHA uses two powerful Nd:YAG lasers as light sources. One emits light pulses at 355, 532, and 1064 nm with a repetition rate of 30 Hz. The second one is used to pump two Ti:Sa lasers that emit light pulses at 710 nm and at 400 and 800 nm, respectively, also with a frequency of 30 Hz. The six laser beams are aligned to one optical axis and guided through a tenfold beam expander telescope to reduce the beam divergence to less than 0.1 mrad (by expanding the beam to a diameter of 100 mm and 25 mm for the Nd:YAG and Ti:Sa wavelengths, respectively) before they are directed into the atmosphere. Backscattered light is collected with a 53–cm Cassegrain telescope and guided through a pinhole (that determines the telescope's field of view of 0.8 mrad for most of the channels) into the receiver unit where it is separated according to its wavelength and state of polarization.

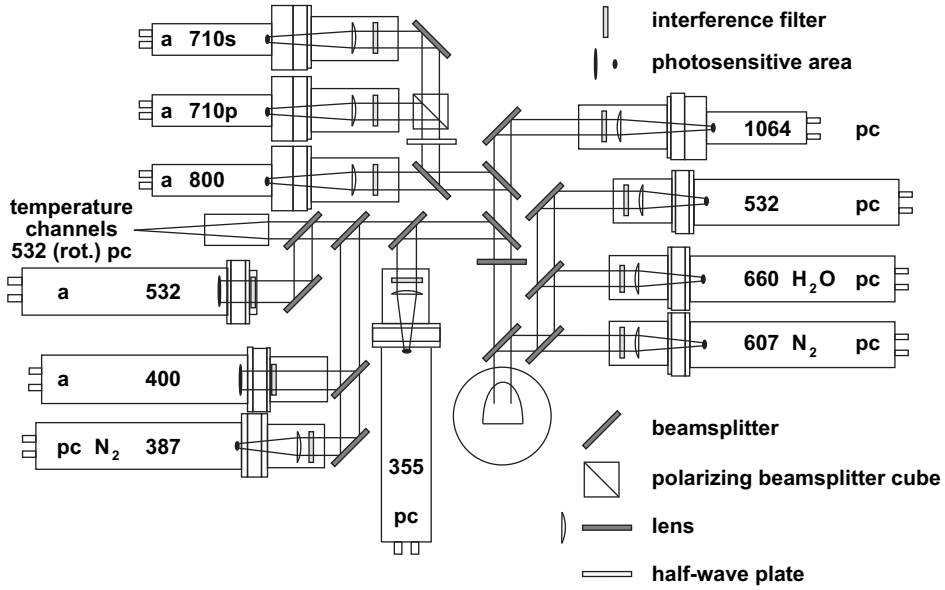

Figure 5.1: Sketch of the BERTHA receiver. Light is separated by dichroic beamsplitters according to its wavelength before it is detected with PMTs. Detection can be in photon counting (pc) or analog (a) mode. A PBS is used to separate parallel and perpendicular polarized light for measurements of the linear volume depolarization ratio at 710 nm. The HWP in front of the PBS is used for calibration measurements. The numbers in the PMTs denote the respective measurement wavelength.

Figure 5.1 shows the measurement channels of the receiver unit. Elastically backscattered light is measured at the six laser wavelengths. Furthermore, vibrational–rotational–Raman signals from nitrogen at 387 and 607 nm and from water vapor at 660 nm as well as pure rotational–Raman signals (Stokes and anti–Stokes lines) from oxygen and nitrogen at around 532 nm are detected. The different signals are separated by means of dichroic beamsplitters and narrow–band interference filters. The use of a double–grating monochromator (Arshinov et al. 2005) allows for the detection of pure rotational–Raman signals and an additional elastic–backscatter signal at 532 nm during daytime. The rotational–Raman signals enable an independent determination of backscatter and extinction coefficients during day and night while vibrational–Raman signals can only be detected in the absence of sunlight. Because of their small field of view (0.10–0.15 mrad) the overlap of the rotational–Raman channels is only complete at a distance of 4–5 km from the lidar. Thus by using pure rotational–Raman signals, aerosol profiles can be determined only in case of several kilometer deep aerosol layers.

In the 710–nm depolarization channels, the cross– and parallel–polarized components of the backscattered light are measured separately. This separation is achieved by using a polarizing beamsplitter cube (PBS). During SAMUM–1 test measurements were performed with a sheet polarizer placed in front of the PBS to allow for calibration measurements to obtain the linear volume depolarization ratio without assuming a reference value at a certain height according to the method described in Freudenthaler et al. (2009). However, these measurements did not result in the desired quality of 710–nm volume depolarization–ratio profiles. Therefore, the sheet polarizer was replaced by

a HWP when BERTHA was back in Leipzig after the measurements in Morocco. With this setup, high–quality volume depolarization ratio profiling at 710 nm was possible during SAMUM–2. The absolute calibration and the method used for profiling of the volume depolarization ratio are described in Section 5.4.2.

Photomultiplier tubes (PMTs) are used as detectors. For the elastic–backscatter signals at 400, 532, 710, and 800 nm the analog PMT output is preamplified and digitized (12 bit, 10 MHz). The 355–nm and 1064–nm elastic–backscatter signals, the Raman signals and a part of the backscattered 532–nm photons are detected by photon–counting PMTs and acquired with a 300–MHz counting system. The raw signals are stored with spatial and temporal resolutions of 7.5–60.0 m and 10–30 s, respectively. All raw signal profiles are corrected for dead–time effects and sky background noise before being further processed.

During nighttime, when vibrational–Raman signals can be detected, aerosol backscatter and extinction profiles were calculated with the Raman method described in Section 3.3.2. During the day the noise of background light allows for the detection of elastic–backscatter signals only (except for the rotational–Raman channels). Thus Klett's method (Section 3.3.1) was used for the calculation of aerosol backscatter coefficients assuming reasonable values of the aerosol lidar ratio. For all analyzed measurements the corrections described in Sections 5.4.3.1 and 5.4.3.2 were applied.

For the analysis of BERTHA measurements 30–170 minutes of cloud–screened signals from a continuous measurement were averaged, depending on the temporal homogeneity of the aerosol layers and the measurement conditions. Vertical smoothing window lengths were varied from 300 m at lower heights to 1260 m in the upper part of optically dense aerosol layers. In this way, the statistical errors of the extinction coefficients were reduced to values of 5%–25%. Systematic uncertainties caused by the removal of Rayleigh–scattering and air–density effects from the backscatter signals are on the order of 5%–10%. The relative statistical error of the backscatter coefficients obtained with the Raman method is of the order of 5%–10%. The extinction coefficients estimated from the daytime backscatter coefficients can suffer from a wrong assumption of the aerosol lidar ratio and thus show large errors. However, during SAMUM–1 they are also obtained with comparably high accuracy of 10%–20% because the dust lidar ratio is well known from the nighttime Raman observations and the HSRL measurements. The time series of the dust lidar ratio showed a small standard deviation of about 10%. Thus it can be assumed that it does not introduce large uncertainties to the calculation of daytime backscatter and extinction coefficients in the homogeneous environment in Morocco. In polluted continental areas where the relative contributions of maritime particles, fresh or aged urban haze, and combustion smoke to the observed aerosol are unknown and may vary strongly with time and height, the uncertainty in the assumed lidar–ratio profile (and in the extinction estimation from backscatter profiles) is usually very high. A detailed discussion of the errors of all quantities derived from BERTHA measurements can be found in the Appendix.

5.4.2 Measurement of the Linear Volume Depolarization Ratio

For several decades, the polarization lidar technique has almost exclusively been used to define whether the scatterers in an investigated atmospheric volume are of spherical (e.g., urban aerosol or water droplets) or non–spherical shape (e.g., mineral dust or ice crystals, Schotland et al. 1971, Sassen 2005). Polarization lidars (for the measurement of the linear depolarization ratio) are equipped with depolarization channels for the detection of light that is co– and cross–polarized to the state of polarization of the emitted laser light (see Section 3.3.4). To obtain a profile of the linear volume depolarization ratio, the ratio of the signals measured in the perpendicular channel to the one measured in the parallel channel is formed. Then, a height range (calibration height) which is expected to be free of clouds and aerosol particles is selected. In that height range the signal–ratio profile is scaled to the molecular (Rayleigh) depolarization ratio which deviates from zero, because of the anisotropy of the air molecules. Literature values of this parameter (Bucholtz 1995) are in the range of 0.00395 (355 nm, Cabannes line only) to 0.01554 (355 nm, Cabannes line and rotational–Raman lines). The relative calibration is imprecise, if depolarizing aerosol particles are present in the calibration height range or if the bandwidth of the interference filters of the receiver are not accounted for properly. Pure Rayleigh scattering (i.e., the Cabannes line) is only measured in case of narrow–bandwidth filters. If the range of transmission of the interference filters is chosen larger, pure rotational–Raman scattering is detected as well. This effect increases the value of the molecular depolarization ratio which would be measured with the applied lidar system.

Because nowadays the particle depolarization ratio (see Equation (3.24)) is used for the characterization and investigation of aerosol particles (see Section 4), highly accurate measurements of the volume depolarization ratio need to be performed. To improve the accuracy of the depolarization–ratio profiling, absolute calibration techniques, which do not rely on a reference value in the atmosphere, have been developed (Reichardt et al. 2003, Alvarez et al. 2006, Freudenthaler et al. 2009). The methods described by Alvarez et al. (2006) and Freudenthaler et al. (2009) introduce calibration measurements with a rotatable HWP which is inserted into the optical path of the receiver (i.e., in front of the PBS) of a polarization lidar. The calibration measurements introduce a controlled amount of cross–talk to the signals measured in the depolarization channels. The additional measurements (with the HWP rotated to distinct angles) have to be performed before or after a regular lidar measurement to obtain the calibration factors which are needed for the retrieval of the volume depolarization ratio.

During the measurements of SAMUM–1, a sheet polarizer was placed in front of the PBS of the BERTHA receiver to enable calibration measurements according to the method of Freudenthaler et al. (2009) which is described in detail below. However, only few calibration measurements were performed to test the applicability of the method. After SAMUM–1, the sheet polarizer was replaced by a HWP (see Figure 5.1). The use of a HWP simplifies the calibration procedure, because this optical element does not alter the state of polarization of incident light, if it is set to its zero position. The sheet polarizer used for the calibration measurements during SAMUM–1 on the other hand

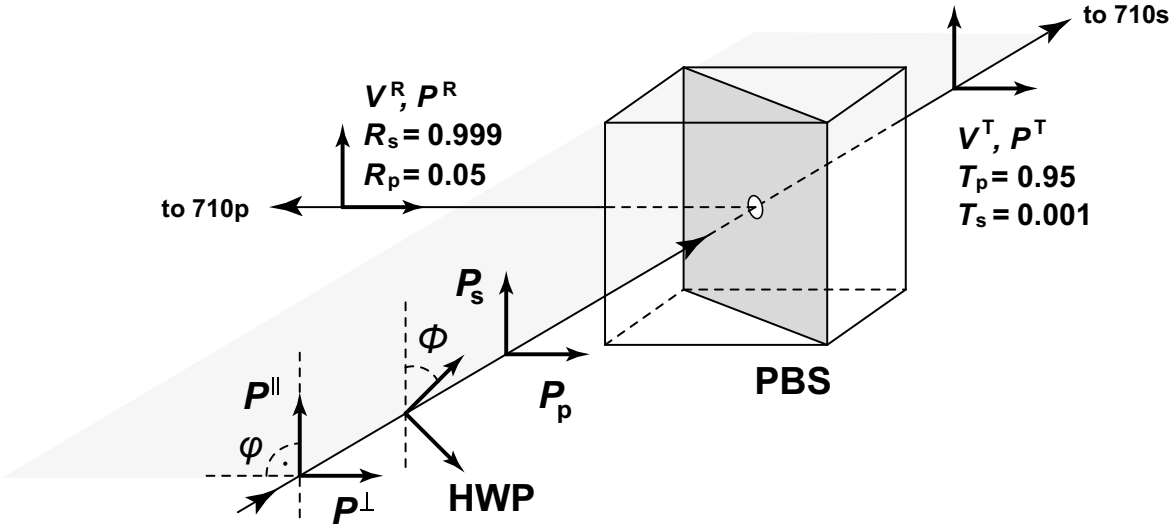

Figure 5.2: Separation of light of different states of polarization by passing a HWP and a PBS before being detected by the depolarization channels of BERTHA. $\perp$, $\parallel$ and s, p refer to the orientation with respect to the plane of polarization of the emitted laser light and to the incident plane of the PBS (light–gray area), respectively. Perpendicularly polarized light is transmitted while parallel polarized light is reflected. The respective properties of the PBS in the BERTHA receiver are stated in the figure.

always had to be removed from the receiver optics to allow for regular atmospheric measurements.

For depolarization–ratio profiling, co– (${}^{\parallel}P$) and cross–polarized (${}^{\perp}P$) light returning from the atmosphere needs to be detected. The separation of the two components of the backscattered light is done by means of a PBS with reflectance R_p and R_s and transmittance T_p and T_s for linearly polarized light parallel (p) and perpendicular (s) to the incident plane of the PBS, respectively. The setup of the PBS in the BERTHA receiver is shown in Figure 5.2. The light–gray shaded area denotes the incident plane of the PBS. P^R and P^T are the measured quantities in the reflected and transmitted path, respectively. The corresponding factors V^R and V^T describe the amplification of the optical elements in front of the PBS. The rotation of the plane of polarization of incoming light (with respect to the orientation of the emitted laser light) against the incident plane of the PBS is described by the angle φ which is 90° in case of BERTHA. This setup refers to an actual PBS which is designed for highest reflectivity (R_s) of light whose state of polarization is perpendicular to the incident plane of the PBS. This setup minimizes the cross–talk of parallel polarized light into the perpendicular channel, i.e., T_s is minimized. The values for the transmittance and reflectance of a PBS can be found in the manufacturer's fact sheet. For the PBS used in BERTHA the values $R_\mathrm{s} = 0.999$, $R_\mathrm{p} = 0.05$, $T_\mathrm{s} = 0.001$, and $T_\mathrm{p} = 0.95$ are used (see Figure 5.2). The rotating angle of the HWP is ϕ. For atmospheric measurements the HWP is set to its zero position $\phi = 0°$ with $\varphi = 90°$. This corresponds to the setup without the HWP because the plane of polarization of transmitted light is not rotated. For measurements with $\phi = 0°$, the linear volume depolarization ratio can be obtained

according to the relative calibration described in the beginning of this section (i.e., by choosing a reference value at a reference height). Because of the retarding effect of the HWP, a rotation of ϕ leads to a rotation of the plane of polarization (of the signals ${}^{\perp}P$ and ${}^{\parallel}P$) of $\varphi = 2\phi$. Freudenthaler et al. (2009) describe a calibration during which a HWP is successively rotated to angles of $\phi = +22.5°$ and $\phi = -22.5°$. In that case, the plane of polarization of light coming from the atmosphere is rotated by $\varphi = +45°$ and $\varphi = -45°$, respectively.

With BERTHA the linear depolarization ratio is measured at a wavelength of $\lambda = 710\,\mathrm{nm}$. As before, the dependence on wavelength and range is not explicitly marked in the subsequent equations that follow the general description of Freudenthaler et al. (2009). For an ideal instrument, the signals perpendicular and parallel to the incident plane of the PBS are described as

$$\begin{aligned} P_\mathrm{s}(\varphi) &= {}^{\parallel}P \sin^2\varphi + {}^{\perp}P \cos^2\varphi\,, \\ P_\mathrm{p}(\varphi) &= {}^{\parallel}P \cos^2\varphi + {}^{\perp}P \sin^2\varphi\,. \end{aligned} \tag{5.1}$$

In case of a lidar for the measurement of linear depolarization, parallel polarized light is emitted. Even in case of an abundance of depolarizing particles in the atmosphere, ${}^{\perp}P$ is much smaller than ${}^{\parallel}P$. Therefore, large systematic errors are introduced, if the perpendicular channel is contaminated with even a small amount of parallel polarized light. Further purity of the perpendicular signal is achieved by placing a sheet polarizer in front of the 710s–detector. For an actual PBS the different transmittance and reflectance of light of different states of polarization (i.e., T_p, T_s, R_p, and R_s) and the effect of the optical elements in the light's path before passing the PBS (i.e., V^R and V^T) need to be accounted for. The signals behind the PBS (i.e., the ones recorded with the data acquisition) can be described as

$$\begin{aligned} P^\mathrm{R}(\varphi) &= \left(P_\mathrm{p}(\varphi)R_\mathrm{p} + P_\mathrm{s}(\varphi)R_\mathrm{s}\right) V^\mathrm{R} \\ P^\mathrm{T}(\varphi) &= \left(P_\mathrm{p}(\varphi)T_\mathrm{p} + P_\mathrm{s}(\varphi)T_\mathrm{s}\right) V^\mathrm{T}\,. \end{aligned} \tag{5.2}$$

The relative amplification factor

$$V^* = \frac{V^\mathrm{R}}{V^\mathrm{T}}\,, \tag{5.3}$$

the signal ratio

$$\delta^*(\varphi) = \frac{P^\mathrm{R}(\varphi)}{P^\mathrm{T}(\varphi)}\,, \tag{5.4}$$

and the linear volume depolarization ratio after Equation (3.20) under the assumption of equal transmission of co– and cross–polarized light in the atmosphere, i.e.,

$$\delta = \frac{{}^{\perp}\beta}{{}^{\parallel}\beta} = \frac{{}^{\perp}P}{{}^{\parallel}P}\,, \tag{5.5}$$

are used together with Equation (5.2) to obtain Equation (9) of Freudenthaler et al. (2009):

$$\delta^*(\varphi) = V^* \frac{(1+\delta^\mathrm{v}\tan^2\varphi)R_\mathrm{p} + (\tan^2\varphi + \delta^\mathrm{v})R_\mathrm{s}}{(1+\delta^\mathrm{v}\tan^2\varphi)T_\mathrm{p} + (\tan^2\varphi + \delta^\mathrm{v})T_\mathrm{s}}\,. \tag{5.6}$$

Rearrangement of Equation (5.6) leads to Equation (10) of Freudenthaler et al. (2009):

$$V^* = \frac{(1+\delta^{\mathrm{v}}\tan^2\varphi)T_{\mathrm{p}} + (\tan^2\varphi+\delta^{\mathrm{v}})T_{\mathrm{s}}}{(1+\delta^{\mathrm{v}}\tan^2\varphi)R_{\mathrm{p}} + (\tan^2\varphi+\delta^{\mathrm{v}})R_{\mathrm{s}}}\delta^*(\varphi)\,. \tag{5.7}$$

To obtain reliable results of the linear volume depolarization ratio from the measured signals $P^{\mathrm{T}}(\varphi)$ and $P^{\mathrm{R}}(\varphi)$ the relative amplification ratio V^* needs to be obtained by means of calibration measurements. These calibration measurements need to be performed together with (i.e., before or after) the regular ($\phi = 0°$) atmospheric measurement.

$\phi = 22.5°$–calibration

A first calibration measurement is performed with the HWP rotated to either $\phi = +22.5°$ or $\phi = -22.5°$. This setting rotates the plane of polarization of incident light by $\varphi = +45°$ or $\varphi = -45°$, respectively. For an idealized setup, the rotation of the plane of polarization by 45° results in equal signal intensities in both depolarization channels. Deviations are caused by different amplification factors of the measurement channels. With $\tan^2(\pm 45°) = 1$, Equation (5.7) simplifies to

$$V^*_{22.5°} = \frac{T_{\mathrm{p}}+T_{\mathrm{s}}}{R_{\mathrm{p}}+R_{\mathrm{s}}}\frac{P^{\mathrm{R}}_{22.5°}}{P^{\mathrm{T}}_{22.5°}} = \frac{T_{\mathrm{p}}+T_{\mathrm{s}}}{R_{\mathrm{p}}+R_{\mathrm{s}}}\delta^*(\pm 22.5°) \tag{5.8}$$

and an amplification ratio which is independent of the volume depolarization ratio is obtained.

$\phi = \pm 22.5°$–calibration

If two calibration measurements are performed at the angles $\phi_1 = +22.5°$ and $\phi_2 = -22.5°$, the error in the determination of the amplification ratio is minimized. The error now mainly depends on the angle $\Delta\phi$ between ϕ_1 and ϕ_2 and increases with increasing difference of $\Delta\phi$ ($\Delta\varphi$) from 45° (90°). If two calibration measurements at $\phi = \pm 22.5°$ are performed, V^* is calculated as

$$V^*_{\pm 22.5°} = \frac{T_{\mathrm{p}}+T_{\mathrm{s}}}{R_{\mathrm{p}}+R_{\mathrm{s}}}\sqrt{\frac{P^{\mathrm{R}}_{+22.5°}}{P^{\mathrm{T}}_{+22.5°}}\frac{P^{\mathrm{R}}_{-22.5°}}{P^{\mathrm{T}}_{-22.5°}}} = \frac{T_{\mathrm{p}}+T_{\mathrm{s}}}{R_{\mathrm{p}}+R_{\mathrm{s}}}\sqrt{\delta^*(+22.5°)\delta^*(-22.5°)}\,. \tag{5.9}$$

Calculation of the linear volume depolarization ratio

For atmospheric measurements the HWP is set to its zero position ($\phi = 0°$). In case of the BERTHA receiver the angle between the state of polarization of the emitted laser light and the incident plane of the PBS is now $\varphi = 90°$. Co–polarized light is measured in the reflected branch of the PBS (as signal $P_{710\mathrm{p}}$ in channel 710p) while cross–polarized light is measured in the transmitted branch (as signal $P_{710\mathrm{s}}$ in channel 710s). Note that $R_{\mathrm{p}} = 0.999$ minimizes the contribution of parallel polarized light to the perpendicular channel. For $\varphi = 90°$, Equation (5.6) simplifies and can be rearranged to obtain

$$\delta^{\mathrm{v}} = \frac{{}^{\perp}P}{{}^{\parallel}P} = \frac{P^{\mathrm{T}}(90°)}{P^{\mathrm{R}}(90°)} = \frac{\frac{\delta^*}{V^*}T_{\mathrm{s}} - R_{\mathrm{s}}}{R_{\mathrm{p}} - \frac{\delta^*}{V^*}T_{\mathrm{p}}}\,. \tag{5.10}$$

For actual atmospheric measurements, the gain ratio $G \approx 0.726$ of the depolarization channels 710p and 710s (see Section 5.4.3.2 for the determination of G) needs to be accounted for and Equation (5.4) becomes

$$\delta^*(90°) = \frac{P^{\mathrm{R}}(90°)}{P^{\mathrm{T}}(90°)} = \frac{P_{710\mathrm{p}}}{G\,P_{710\mathrm{s}}}\,. \tag{5.11}$$

Thus the final equation for the calculation of the linear volume depolarization ratio with BERTHA by incorporating calibration measurements according to Freudenthaler et al. (2009) is

$$\delta^{\mathrm{v}} = \frac{\frac{P_{710\mathrm{p}}}{G\,P_{710\mathrm{s}}V^*}T_{\mathrm{s}} - R_{\mathrm{s}}}{R_{\mathrm{p}} - \frac{P_{710\mathrm{p}}}{G\,P_{710\mathrm{s}}V^*}T_{\mathrm{p}}}\,. \tag{5.12}$$

The linear particle depolarization ratio $\delta_\lambda^{\mathrm{p}}$ can be calculated according to Equation (3.23) from the profiles of $\delta_\lambda^{\mathrm{v}}$, $\beta_\lambda^{\mathrm{p}}$, $\delta_\lambda^{\mathrm{m}}$, and $\beta_\lambda^{\mathrm{m}}$ that are measured by lidar and calculated from the temperature and pressure profiles of a nearby sounding or a model atmosphere.

5.4.3 Corrections

When the lidar equation was introduced in Section 3.2 it was stated that the setup of the lidar receiver could introduce several errors that can be corrected for, if they are well known. This section discusses the correction of effects of the geometric overlap of laser beam and RFOV and the correction of polarization–dependent receiver transmission which needs to be accounted for when strongly depolarizing scatterers are present in the atmosphere. The latter effect demanded a detailed calibration of the polarization properties of the receiver optics of BERTHA. The calibration measurements and their results are described in detail below.

5.4.3.1 Overlap Correction

The lidar equation (3.6) accounts for the effects of an incomplete overlap of the emitted laser beam with the RFOV by means of a geometric form factor $O(R)$. If the overlap function is known, backscatter and extinction coefficients can be retrieved in a certain range below the height of complete overlap $O(R) = 1$. The overlap effect widely cancels out, if signal ratios are used as in case of the Raman method that retrieves accurate backscatter coefficients for heights very close to the surface. For a ground–based lidar with a large receiver telescope (such as BERTHA), the range of incomplete overlap covers the lowermost region of the atmosphere including the planetary boundary layer and the range of transition of a dominance of local sources to mesoscale aerosol transport. Smaller systems like MULIS and POLIS can have a range of complete overlap of only a few hundred meters (see Sections 5.1 and 5.2).

The overlap function of a lidar is determined by the divergence of the laser beam, the field of view of the receiver telescope, the imaging properties of the receiver system, and the distance between the laser beam and the telescope axis (in case of a bi–static

system). BERTHA is a monostatic lidar system with coinciding laser beam and telescope axis. The overlap function can vary from measurement channel to measurement channel. It is characteristic for every lidar and strongly depends on the field of application of an individual system, e.g., in stratospheric or mesospheric lidar measurements a large overlap height is used to suppress the strong signal of the lower atmosphere.

The overlap function can be obtained through simulations with a ray–tracing program, if the properties of the elements in the optical path are well known. It can also be retrieved experimentally by horizontal measurements within a well–mixed homogeneous aerosol layer or by following a method suggested by Wandinger and Ansmann (2002). The latter method can only be applied when measurements of a molecular signal are available as in the case of HSRL and Raman lidar. Recently, Su et al. (2010) investigated the potential of simultaneous (in space and time) measurements of ground–based and airborne/space–borne lidar measurements for the retrieval of the overlap function, if no Raman signals are detected.

To obtain the overlap function according to the method of Wandinger and Ansmann (2002) Equation (3.15) is rearranged to

$$O(R) = \frac{P_{\lambda_\mathrm{R}}(R)R^2}{C_0\beta_{\lambda_\mathrm{R}}(R)\exp\left[-\int_0^R \alpha_{\lambda_0}(\xi)+\alpha_{\lambda_\mathrm{R}}(\xi)\,\mathrm{d}\xi\right]}\,. \tag{5.13}$$

$C_0 = \eta_{\lambda_\mathrm{R}} E_{\lambda_\mathrm{R}}$ is a normalization factor that includes all constant system parameters. The backscatter profile is calculated according to the Raman method and is not affected by the overlap effect. A constant lidar ratio is assumed for the calculation of the extinction coefficient. The error in assuming a constant lidar ratio is minimized in case of a high transmission of the atmosphere, i.e., one has to choose a measurement under clean conditions with low AOT and without elevated aerosol layers. The AOT (also referred to as τ_λ) is defined as the height integral of the extinction coefficient

$$\tau_\lambda = \int_0^\infty \alpha_\lambda(\xi)\,\mathrm{d}\xi\,. \tag{5.14}$$

The transmission term in Equation (5.13) can be estimated from the extinction profile. In the retrieval C_0 is adjusted in a way that $O(R) = 1$ in the range of complete overlap. If $O(R)$ becomes unity, the factor can be neglected in the lidar equation (3.6).

During the two SAMUM campaigns the nighttime measurements on 11 May 2006 and on 9 February 2008 provided the best conditions for an experimental retrieval of the overlap function. From these two cases the overlap function obtained from the measurement on 11 May 2006 was found to be most reliable for the calculation of backscatter and extinction profiles and thus was applied in the analysis of all SAMUM measurements. The overlap function and its effect on the calculation of the extinction coefficient is shown in Figure 5.3. At 355 and 532 nm, complete overlap is reached at distances of 2000 m from the lidar system. In the extinction profiles, the overlap effect is also visible above the height of complete overlap. This is because the profiles were smoothed with a vertical window of 660 m to reduce signal noise. In the analysis

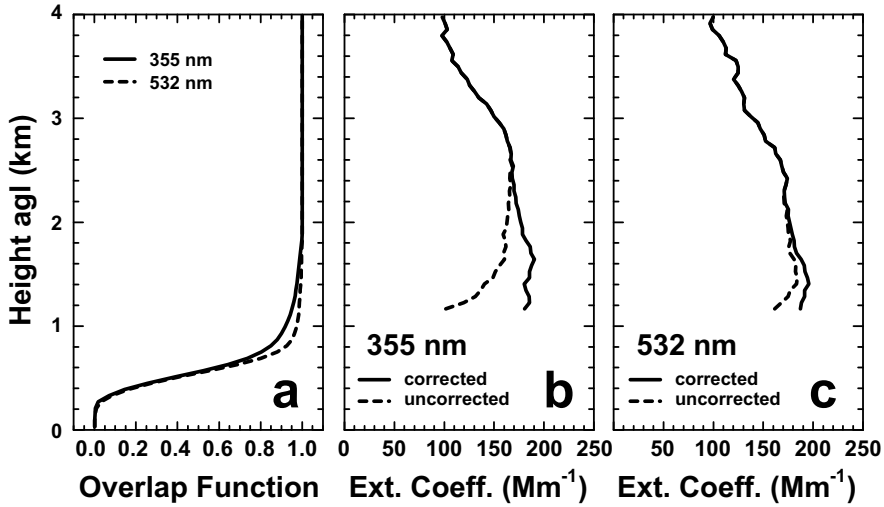

Figure 5.3: (a) Overlap functions at 355 nm (solid line) and 532 nm (dashed line) obtained from the nighttime measurement during clean conditions on 11 May 2006. Full overlap is reached in a distance of 2 km from the lidar at both wavelengths. The right graphs show the application of the respective overlap functions to the calculation of aerosol extinction coefficients at (b) 355 nm and (c) 532 nm for a SAMUM–1 nighttime measurement on 15 May 2006. Because of the applied signal smoothing length of 660 m, a difference between the corrected and uncorrected profiles can be seen above the height of complete overlap.

of the SAMUM measurements, the overlap correction usually allowed for a retrieval of extinction coefficients down to 1.2–1.6 km height above BERTHA (see Figure 5.3). However, one has to keep in mind that, due to the hot conditions at the measurement stations in Morocco and Cape Verde and the huge amount of heat that is produced by the four lasers in the container, air–conditioning problems might have led to changes in the actual overlap of BERTHA. In some cases, extinction profiles from BERTHA measurements were not reliable below 2000 m height. During SAMUM, this height range was covered by the smaller lidar systems POLIS and MULIS (see Sections 5.1 and 5.2) which show a complete overlap at distances from the lidar of 100 m to a few hundred meters, respectively.

5.4.3.2 Polarization–dependent Receiver Transmission

The optical elements of a lidar receiver can feature a dependence of their transmission on the state of polarization of incident light (Mattis et al. 2002, Grein 2006, Mattis et al. 2009, Tesche et al. 2009b). This possible source of systematic errors needs to be considered when building a lidar receiver. However, due to degradation or changes of the optical setup of the receiver, its polarization–dependent transmission properties might become unknown. In that case the transmission of the different measurement channels can be determined by means of calibration measurements (Grein 2006). These measurements and a method to correct for polarization–dependent receiver transmission are explained in this section.

Principle

The first SAMUM–1 measurements of highly depolarizing, non–spherical mineral dust particles revealed that BERTHA's 532–nm elastic–backscatter channel was strongly affected by polarization–dependent receiver transmission. Backscatter coefficients calculated from the signals of this channel and the respective 607–nm Raman channel were about twice as large as the ones obtained with MULIS. The effect was negligible (or rather masked) in earlier measurements performed with BERTHA during LACE 98 (Ansmann et al. 2002a) and the Indian Ocean Experiment (INDOEX, Franke et al. 2001) because large, non–spherical particles were not present during these experiments. Small particles cause no or only weak depolarization of the emitted laser light and the total signal $P(R) = {}^{\parallel}P(R)$ only consists of contributions of light that is polarized parallel to the emitted laser light.

As soon as large, non–spherical scatterers like mineral dust, volcanic ash, or ice crystals are present in the atmosphere, backscattered light becomes depolarized (see Sections 3.1 and 3.3.4) and a volume depolarization ratio larger than zero is detected. The depolarized component of the backscattered light can produce large measurement errors, if different states of polarization are transmitted with different efficiency through the optical elements of a lidar receiver. If not corrected for, this effect can introduce considerable errors to the retrieval of the backscatter coefficient. Furthermore, the depolarization ratio cannot be retrieved accurately, even if the co– and cross–polarized components of the backscattered light are measured separately.

Figure 5.4 illustrates the effect of polarization–dependent receiver transmission depending on the state of polarization of the emitted laser light. The two columns denote the effect of the orientation the the emitted parallel polarized laser light with respect to the incident plane of the optical elements in the lidar receiver. In the left column, light that is polarized parallel to the emitted laser light is oriented parallel to the incident plane of the optical elements (i.e., perpendicular to the plane of the paper). In the right column, the plane of polarization of parallel light is oriented perpendicularly to the incident plane of the optical elements (i.e., coincides with the plane of the paper). The upper line refers to signal returns by non–depolarizing particles ($\delta = 0$) while the lower line represents the conditions for depolarizing particles ($\delta = 0.2$). ${}^{\perp}\eta$ and ${}^{\parallel}\eta$ describe the transmission of cross– and co–polarized light, respectively. D_η is the ratio of the two transmissions. ${}^{\mathrm{p}}\eta$ and ${}^{\mathrm{s}}\eta$ describe the transmission with respect to the incident plane of the optical elements. The lidar receiver described in Figure 5.4 features the optical properties given in the header. These properties remain unaltered but cause different effects depending on the orientation of the emitted laser light and the depolarizing effect of the aerosol particles. If backscattered light is depolarized (lower line in Figure 5.4), the parallel and perpendicular polarized components of the detected light need to be treated according to the respective transmission of the receiver optics. Depending on the orientation of the plane of polarization of the emitted laser light, the different transmissions can cause weaker (left column, 11 instead of 12 photons, underestimation by 8%) or stronger (right column, 7 instead of 6 photons, overestimation by 17%) signals than would be observed in the absence of depolarizing scatterers (upper line).

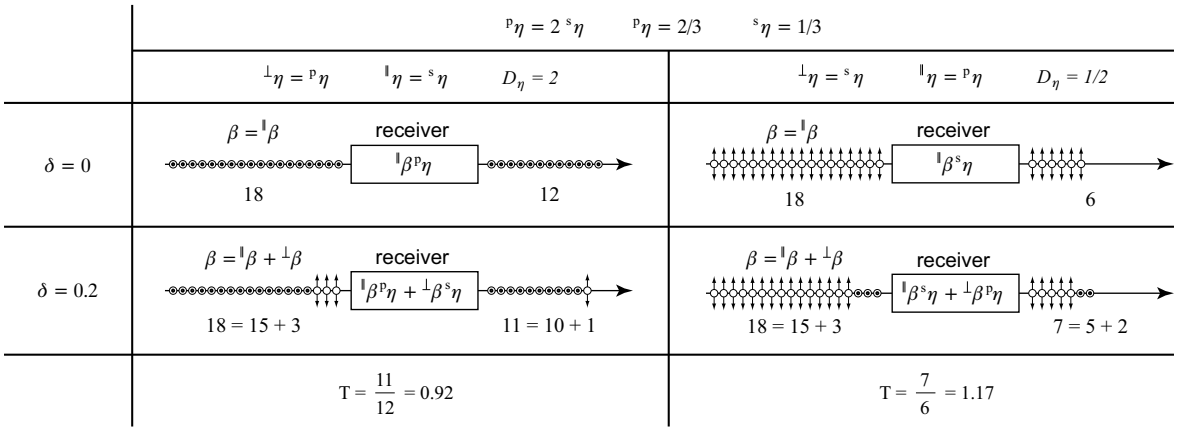

Figure 5.4: Visualization of the effect of polarization–dependent receiver transmission on the total signal of an affected measurement channel. The columns denote the configuration of the receiver. Co– and cross–polarized light is transmitted differently depending on the orientation with respect to the incident plane of the optical measurements. The lines describe the effect of different aerosols (non–depolarizing and depolarizing) on the detected signal. The actual amount of photons backscattered from the atmosphere with their respective state of polarization is drawn left of the receiver box while the detected photons are shown to the right. The figure is adopted from Mattis et al. (2009).

Correction

The effect of a polarization–dependent receiver transmission can be corrected for, if the transmission ratio of the affected channels and the volume depolarization ratio (as a measure of the non–sphericity of the particles and molecules within the scattering volume) at the respective wavelengths are known (Mattis et al. 2009, Tesche et al. 2009b). As before, the dependence on height and wavelength is dropped in the following equations to improve readability.

If a total signal is measured with different transmissions of light of different states of polarization, the individual transmissions for parallel and perpendicular polarized light must be included in the lidar equation (3.6). Also the transmission factor η for the total backscatter coefficient β has to be rewritten as

$$\eta\beta = {}^{\parallel}\eta^{\parallel}\beta + {}^{\perp}\eta^{\perp}\beta \tag{5.15}$$

to account for different states of polarization. The individual transmissions for co– and cross–polarized light are assumed to be independent of height. Because these factors cannot be derived easily, the transmission ratio

$$D = \frac{{}^{\perp}\eta}{{}^{\parallel}\eta} \tag{5.16}$$

is introduced. It can be determined experimentally through calibration measurements as described later in this section. Using Equations (5.15), (5.16), and (3.21), Equation (5.15) is rewritten as

$$\eta = {}^{\parallel}\eta\frac{D\delta^{v} + 1}{\delta^{v} + 1} = {}^{\parallel}\eta K\,. \tag{5.17}$$

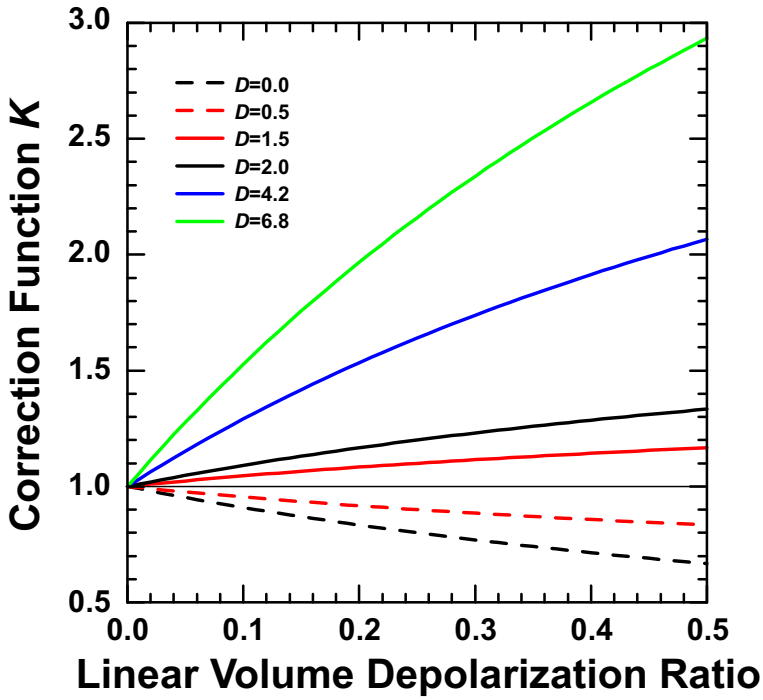

Figure 5.5: Behavior of the correction function K with respect to the linear volume depolarization ratio δ^{v} for different values of the transmission ratio D. Values of $D < 1$ generally cause less severe errors because the respective values of K are always larger than zero. The picture is similar to Figure 2 in Mattis et al. (2009).

K is a correction term that accounts for the influence of the transmission ratio of the lidar receiver and the volume depolarization ratio of the scattering particles on measurements of atmospheric parameters. Erroneous signals can be corrected by introducing K into the lidar equation (3.6).

As shown in Figure 5.5 the effect of polarization–dependent receiver transmission is smaller for $D < 1$ than for $D > 1$. This effect is related to the asymptotic behavior of K for $D \to 0$. The effect also depends on the plane of polarization of the emitted laser light. As will be described later, D is much larger than unity in case of the BERTHA 532–nm elastic–backscatter channel.

Figure 5.6 describes the application of the correction of a signal affected by polarization–dependent receiver transmission to 1–h mean values of a nighttime measurement on 4 June 2006 during SAMUM–1. The red line in Figure 5.6a is the backscatter coefficient calculated from the erroneous 532–nm elastic–backscatter signal. These values are about twice as high as the ones measured simultaneously with MULIS (black line). The MULIS volume depolarization ratio shown in Figure 5.6b was used to calculate the correction function needed for the revision of these inaccurate signals. Figure 5.6c shows the correction functions obtained for transmission ratios of $D = 4.76$ (light green) and $D = 6.76$ (dark green) according to the findings of the characterization measurements of the BERTHA receiver described below. These were used to calculate corrected 532–nm particle backscatter coefficients (light green and dark green in Fig-

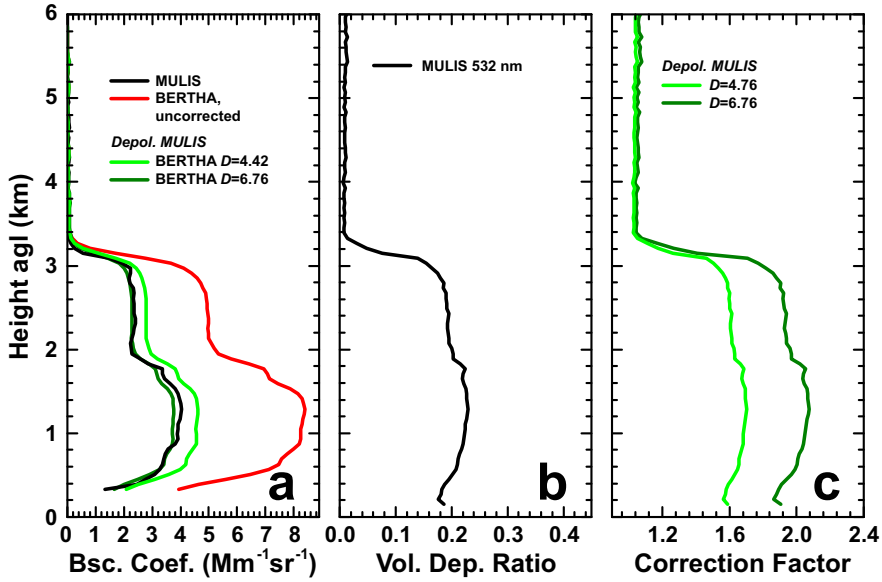

Figure 5.6: Correction of erroneous signals in the 532–nm elastic–backscatter channel (a) of a one–hour (0300–0400 UTC) nighttime measurement (5° zenith angle) on 4 June 2006 during SAMUM–1. The volume depolarization ratio (b) simultaneously measured with MULIS was used for the calculation of the correction function (c) that is needed for the revision of signals affected by depolarization–dependent receiver transmission. All profiles are smoothed with a window length of 180 m.

ure 5.6a) that are much smaller than the uncorrected ones and, in case of $D = 6.76$, are in good agreement with the results of MULIS measurements.

As is obvious from Equation (5.17), the correction function K for an affected measurement channel can only be determined, if the linear volume depolarization ratio and the transmission ratio at the respective wavelength are known. The latter can differ for different measurement channels but can be measured with a single calibration measurement. The crucial part of the correction is the knowledge of the volume depolarization ratio profile for individual measurements and wavelengths. During SAMUM–1 and SAMUM–2a, δ^{v} profiles at 532 nm were provided by MULIS measurements. During SAMUM–2b they were approximated using the method of depolarization extrapolation that is described in Section 5.4.3.3. In the following, a method for the experimental determination of the transmission ratio is presented.

Calibration of the BERTHA Receiver Optics

The transmission ratio can be obtained experimentally by illuminating the lidar receiver with light of defined states of polarization (Grein 2006, Mattis et al. 2009). Unpolarized light of a white–light lamp is led through a fiber that is coupled to an optical bench. The optical bench also holds a lens to collimate the light before its state of polarization is defined by means of a linear sheet polarizer. Linear polarized light is led through the lidar receiver and is detected by the individual measurement channels.

Calibration measurements to characterize the transmission properties of the BERTHA

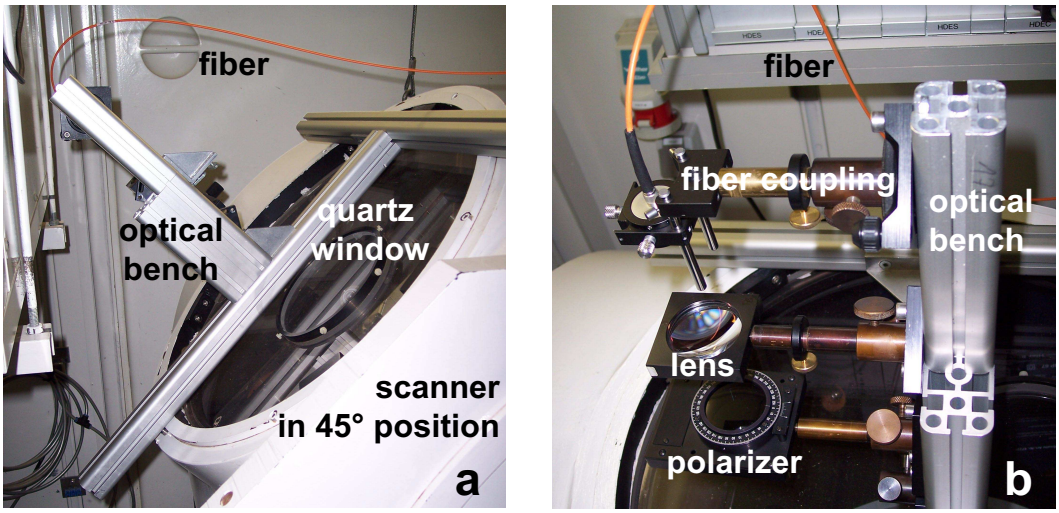

Figure 5.7: Setup for the investigation of the transmission ratios of the BERTHA receiver. (a) The optical bench holding the calibration setup is placed on the scanner and (b) the setup of fiber coupling, collimating lens, and sheet polarizer to illuminate the receiver telescope with light of a defined state of polarization.

receiver were performed in the framework of this thesis. After BERTHA was transported back to Leipzig from Morocco, the calibration setup was placed on the scanner as shown in Figure 5.7. Measurements were performed with the scanner set to zenith angles of 0°, 5°, 30°, and 45° which represent the modulation used during SAMUM: morning and noon measurements were performed at 45° zenith angle to avoid the sun from shining into the receiver telescope while evening and nighttime measurements were performed at zenith angles of 5° to avoid strong return signals from horizontally aligned ice crystals (Platt 1978, Platt et al. 1978, Westbrook et al. 2010). Zenith angles of 0° and 30° were rarely used during SAMUM–1 and not at all during SAMUM–2.

When the scanner was set to a certain zenith angle, a measurement series with the sheet polarizer set to 0°, 45°, and 90° was performed. This modulation was used to derive the offset angle ψ between the zero position of the polarizer and the true zero position which represents parallel polarized light (see below).

If co– and cross–polarized light is detected in separate measurement channels, the total signal is represented by the sum of the two channels as

$$P = P_{\max}\left({}^{\parallel}\eta\cos^2(\zeta+\psi) + {}^{\perp}\eta\sin^2(\zeta+\psi)\right), \tag{5.18}$$

with the angle ζ representing the position of the polarizer and the offset ψ between zero position of the polarizer and the true zero position of the lidar receiver. ${}^{\parallel}\eta$ and ${}^{\perp}\eta$ describe the transmissions of parallel and perpendicular polarized light, respectively. $P_{\max}$ denotes the maximum signal that is measured, if only parallel polarized light is detected, i.e., if the HWP is turned to a position that blocks cross–polarized light. The use of the transmission ratio leads to:

$$P = {}^{\parallel}\eta P_{\max}\left(\cos^2(\zeta+\psi) + D\sin^2(\zeta+\psi)\right).$$

If the ratio of measurements at different positions ζ_1 and ζ_2 of the polarizer is used,

$$\frac{P_2}{P_1} = \frac{\cos^2(\zeta_2+\psi) + D\sin^2(\zeta_2+\psi)}{\cos^2(\zeta_1+\psi) + D\sin^2(\zeta_1+\psi)},$$

and transformed accordingly, the transmission ratio D can be derived as

$$D_{21} = \frac{\cos^2(\zeta_2+\psi) - \frac{P_2}{P_1}\cos^2(\zeta_1+\psi)}{\frac{P_2}{P_1}\sin^2(\zeta_1+\psi) - \sin^2(\zeta_2+\psi)}. \tag{5.19}$$

Determination of the Offset Angle ψ
A series of measurements with three different polarizer positions ζ_1, ζ_2, and ζ_3 with a difference of 45° between each measurement is performed. The transmission ratios D_{21}, D_{31}, and D_{32} for the parallel and perpendicular channel, respectively, can be determined using the respective signal ratios P_2/P_1, P_3/P_1, and P_3/P_2 according to Equation (5.19). The offset angle is determined by minimizing the difference between the transmission ratios $D_{21}^{\perp/\parallel}$ and $D_{31}^{\perp/\parallel}$ when varying ψ.

Determination of the Gain Ratio G for Depolarization Measurements
For the calculation of the linear volume depolarization ratio according to the method of Freudenthaler et al. (2009) (see Section 5.4.2), the gain ratio $G = {}^{\perp}\eta_\mathrm{s}/{}^{\parallel}\eta_\mathrm{p}$ needs to be known. It describes the ratio of the amount of cross–polarized light (with respect to the state of polarization of the emitted laser light) measured in the perpendicular channel (with respect to the incident plane of the PBS) to the amount of co–polarized light measured in the parallel channel, i.e., G is a system constant that describes the intensity ratio of light of different states of polarization after it has passed all optical elements of the lidar receiver and is detected.

To obtain pure co– and cross–polarized signals ($P_\mathrm{p} = {}^{\parallel}\eta_\mathrm{p}\,{}^{\parallel}P$ and $P_\mathrm{s} = {}^{\perp}\eta_\mathrm{s}\,{}^{\perp}P$) measurements with negligible contributions of the unwanted inverse state of polarization are needed. In the case of the BERTHA receiver this is given for angles of the polarizer of $\zeta_1 + \psi \cong 90°$ (mainly cross–polarized light) and $\zeta_3 + \psi \cong 0°$ (mainly parallel polarized light). Light that passes the receiver telescope can be separated according to its state of polarization as

$$\begin{aligned} {}^{\parallel}P &= P_\mathrm{max}\cos^2(\zeta_3+\psi), \\ {}^{\perp}P &= P_\mathrm{max}\sin^2(\zeta_1+\psi). \end{aligned}$$

For the positions $\zeta_1 = 0°$ and $\zeta_3 = 90°$ the signals $P^1_\mathrm{p/s}$ oder $P^3_\mathrm{p/s}$ are measured in the parallel and perpendicular channel, respectively. From these signals the gain factor G for the depolarization channels can be calculated as

$$G = \frac{{}^{\perp}\eta_\mathrm{s}}{{}^{\parallel}\eta_\mathrm{p}} = \frac{P^1_\mathrm{s}\,{}^{\parallel}P}{P^3_\mathrm{p}\,{}^{\perp}P} = \frac{P^1_\mathrm{s}}{P^3_\mathrm{p}}\frac{\cos^2(\zeta_3+\psi)}{\sin^2(\zeta_1+\psi)}. \tag{5.20}$$

Table 5.1: Gain ratio G of the 710–nm depolarization channels and transmission ratios D of the total channels within the wavelength range of application of the linear sheet polarizer with respect to the zenith angle Θ_Z of the scanner unit. N denotes the number of calibration measurements.

Θ_Z	D_{400}	D_{532}	D_{607}	D_{660}	G_{710}	D_{800}	N
$-5°$	0.87 ± 0.07	4.18 ± 0.11	0.99 ± 0.02	1.10 ± 0.01	0.73 ± 0.01	1.93 ± 0.04	10
$0°$	0.87 ± 0.09	4.76 ± 0.08	0.97 ± 0.02	1.07 ± 0.01	0.74 ± 0.01	1.92 ± 0.04	5
$5°$	0.85 ± 0.00	4.42 ± 0.51	0.96 ± 0.00	1.04 ± 0.00	0.73 ± 0.00	2.00 ± 0.01	2
$30°$	0.88 ± 0.01	6.37 ± 0.14	0.95 ± 0.02	1.04 ± 0.02	0.70 ± 0.01	1.89 ± 0.05	2
$45°$	0.90 ± 0.01	6.76 ± 0.03	0.96 ± 0.00	1.03 ± 0.01	0.75 ± 0.01	1.69 ± 0.01	2

Calibration Results

The transmission ratio of the total channels (e.g., elastic–backscatter channels which detect both co– and cross–polarized light) can be calculated from the calibration measurements according to Equation (5.19), while Equation (5.20) needs to be applied when cross– and co–polarized light is measured in separate channels. The investigation of the BERTHA receiver with different zenith angles Θ_Z of the scanner results in transmission ratios around unity for the 400–nm, 607–nm, and 660–nm channels. At 532 nm values of $D(\Theta_Z = 5°) = 4.18$ and $D(\Theta_Z = 45°) = 6.76$ were derived. No information could be obtained for wavelengths of 355, 387, and 1064 nm because the spectral range of application of the sheet polarizer used for the calibration measurements did not cover the UV and IR. However, the comparison with other lidar systems does not indicate that these channels are affected by polarization–dependent receiver transmission. At 710 nm and 800 nm values of $G = 0.74$ and $D = 1.94$ were derived, respectively, independent of the zenith angle of the scanner. The calibration results for all wavelengths and zenith angles can be found in Table 5.1 and in Mattis et al. (2009).

The calibration measurements revealed that especially the 532–nm and 800–nm elastic–backscatter channels must be corrected for polarization–dependent receiver transmission. Table 5.1 shows that for the correction of the 532–nm elastic–backscatter channel it is necessary to consider the zenith angle of the scanner. The comparison of the corrected 532–nm backscatter profiles with the results of the unaffected rotational–Raman channels and with measurements of other lidar systems that participated in the SAMUM campaigns revealed that proper correction is obtained, if the transmission ratios $D(5°)$ and $D(45°)$ are used for zenith angles of 45° and 0°, respectively. This is most likely caused by a rotation of the plane of polarization of the emitted laser light after it is reflected by several aluminum mirrors of BERTHA's sending unit. Such a rotation can transform the linearly polarized laser light to elliptically polarized light.

5.4.3.3 Depolarization Extrapolation

Profiles of the linear volume depolarization ratio are crucial for the determination of reliable profiles of the backscatter coefficient (and consequently the lidar ratio) at wavelengths that are affected by polarization–dependent receiver transmission (see Sec-

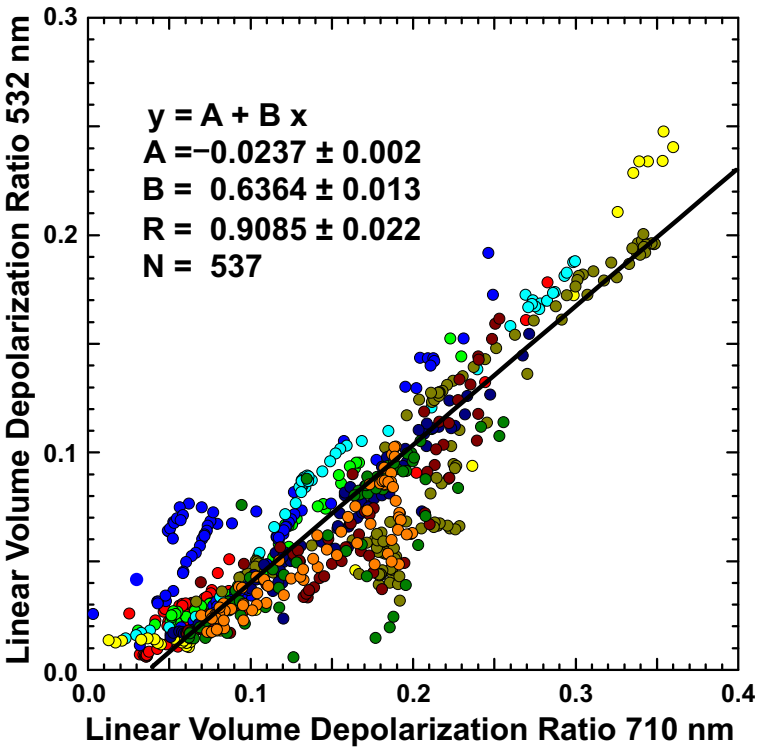

Figure 5.8: Correlation of linear volume depolarization ratios as measured with BERTHA at 710 nm and with MULIS at 532 nm. Different colors denote correlative measurements during 12 days of SAMUM–2a. The black line shows the linear relation used to transform BERTHA volume depolarization ratios measured at 710 nm to the respective ones at 532 nm.

tion 5.4.3.2). Profiles of $\delta^{\mathrm{v}}_{532}$ were needed to correct measurements of the 532–nm elastic–backscatter channel of BERTHA which is affected by the non–sphericity of the mineral dust particles measured during SAMUM. These profiles were provided with high quality from MULIS measurements. However, measurements with MULIS and BERTHA were not always performed simultaneously. Furthermore, MULIS was not available during SAMUM–2b. Therefore, a method to estimate profiles of $\delta^{\mathrm{v}}_{532}$ based on BERTHA measurements of the volume depolarization ratio at 710 nm was developed in the framework of this thesis.

Profiles of the volume depolarization ratio for all available simultaneous measurements of BERTHA and MULIS were transformed to an equal height resolution and investigated for correlation. Figure 5.8 shows twelve measurements with a total number of 537 data points that could be analyzed to obtain the linear relation

$$\delta^{\mathrm{v}}_{532} = -0.0237 + 0.6364\,\delta^{\mathrm{v}}_{710}\,. \tag{5.21}$$

For analysis of the SAMUM measurements, $\delta^{\mathrm{v}}_{532}$ was preferably taken from MULIS measurements. If no simultaneous MULIS measurements were performed or profiles of the 532–nm volume depolarization ratio were not available, erroneous signals of the 532–nm elastic–backscatter channel were corrected by using the 532–nm linear volume depolarization ratio derived from Equation (5.21).

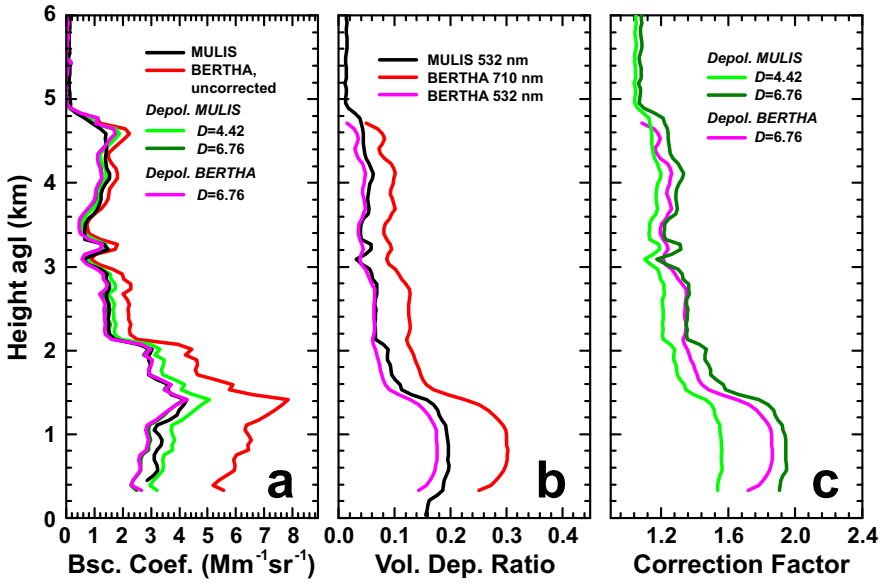

Figure 5.9: Correction of corrupt signals of the 532–nm elastic–backscatter channel (a) for unsmoothed one–hour (2132–2232 UTC) mean profiles of an evening measurement (5° zenith angle) on 31 January 2008 during SAMUM–2a. The 532–nm volume depolarization ratio (b) simultaneously measured with MULIS (black) and extrapolated (magenta line) from the 710–nm BERTHA measurement (red) was used for the calculation of the correction function (c). The correction with the extrapolated 532–nm volume depolarization ratio profile and a transmission ratio of $D = 6.76$ (magenta) leads to results comparable to the ones achieved with volume depolarization ratio profiles from MULIS (dark green).

Figure 5.9 shows an example of the application of the extrapolation method together with the correction of polarization–dependent receiver transmission during SAMUM–2a (analog to Figure 5.6). The magenta line in Figure 5.9c describes the 532–nm volume depolarization ratio extrapolated from BERTHA measurements at 710 nm. It is in reasonable agreement with the MULIS measurement at 532 nm. As in Figure 5.6, a good agreement between the corrected profiles (with $D = 6.76$), now using volume depolarization ratios from MULIS (dark green) and extrapolated from BERTHA (magenta), and the unaffected results from MULIS (black) is obtained.

The transformation of BERTHA volume depolarization ratio measurements from 710 nm to 532 nm was crucial for the analysis of SAMUM–2b measurements because as during SAMUM–1 signals of the 532–nm BERTHA elastic–backscatter channel were expected to be highly affected by polarization–dependent receiver transmission. Similar conditions as in Morocco with several kilometer deep dust layers were expected to prevail during SAMUM–2b since summer is the season of dust transport from Africa to the Americas (see Section 2.3). Measurements were performed only with BERTHA during this campaign. Figure 5.10 shows the results of the correction of depolarization–dependent receiver transmission for a measurement of SAMUM–2b. In contrast to Figures 5.6 and 5.9 only profiles obtained from BERTHA measurements are shown.

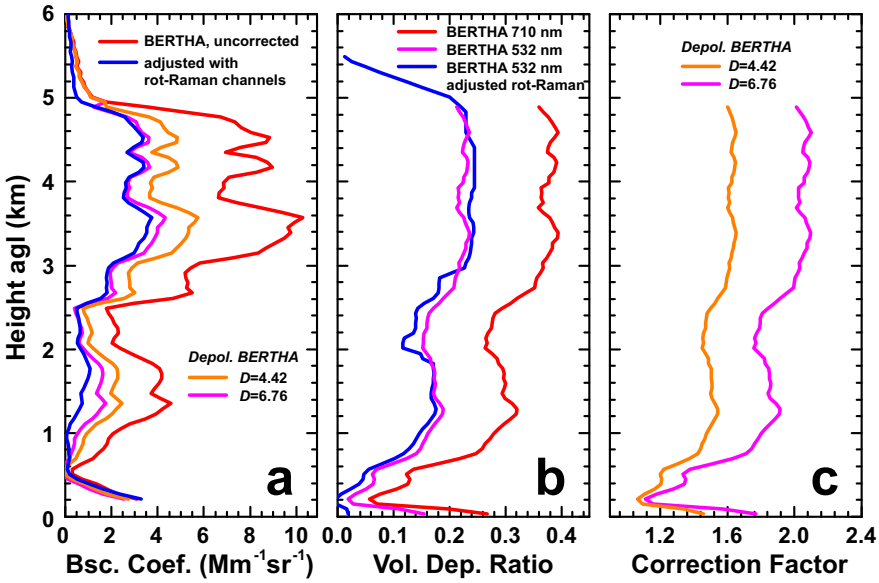

Figure 5.10: Correction of erroneous signals in the 532–nm elastic–backscatter channel (a) for unsmoothed three–hour (2330–0220 UTC) mean profiles of a nighttime measurement (5° zenith angle) on 3 June 2008 during SAMUM–2b. The 532–nm volume depolarization ratio (b) used to calculate the correction functions shown in (c) is extrapolated (magenta line) from the 710–nm BERTHA measurement (red line) while the blue line shows the volume depolarization ratio profile that was obtained by adjusting erroneous backscatter coefficients to unaffected ones measured with the rotational–Raman channels. The correction using the extrapolated 532–nm volume depolarization ratio profile and a transmission ratio of $D = 6.76$ leads to results that are in agreement with backscatter profiles from the rotational–Raman channels.

BERTHA's 532–nm rotational–Raman channels were operable during SAMUM–2b. The rotational–Raman channels consist of three individual channels which provide signals of Mie scattering and pure rotational–Raman scattering. This information can be used to derive backscatter and extinction profiles according to the Raman method, as is done for the combination of elastic (532 nm) and vibrational–Raman (607 nm) backscattering (see Section 3.3.2). The rotational–Raman channels are not affected by polarization–dependent receiver transmission and thus provide the possibility to validate the correction of the 532–nm elastic–backscatter signal that is done with a correction function based on the extrapolated 532–nm volume depolarization ratio profile. Furthermore, the comparison of affected (from 532–nm elastic–backscatter and 607 vibrational–Raman channel, red in Figure 5.10a) and unaffected (from the 532–nm rotational–Raman channels, blue in Figure 5.10a) 532–nm backscatter profiles can be used to derive an artificial 532–nm volume depolarization ratio profile (blue in Figure 5.10b), i.e., one that leads to good agreement between the unaffected and the corrected backscatter coefficients when used in Equation (5.17).

5.5 Sun Photometers

An important topic of the SAMUM campaigns is the improvement of the retrieval of aerosol properties from passive remote–sensing instruments in the presence of non–spherical particles. Thus several Sun photometers were deployed at the SAMUM ground stations to perform spectrally resolved measurements of the aerosol optical depth and the scattering phase function of the aerosol particles (Toledano et al. 2009, 2011). Additionally, these instruments provide valuable information for the analysis of elastic–backscatter signals using Klett's method and to extend lidar profiles down to the surface. They also were used as ground truth for satellite measurements during SAMUM–1 (Dinter et al. 2009, Kahn et al. 2009). Measurements of the optical depth at several wavelengths are used for the calculation of the the Ångström exponent according to Equation (4.2). However, these instruments only provide column–integrated results.

AERONET–Cimel

During SAMUM–1 and SAMUM–2a Cimel Sun photometers of the AErosol RObotic NETwork (AERONET, Holben et al. 1998) were placed at the lidar ground stations. During SAMUM–1 the instrument that usually measures from the rooftop of IfT in Leipzig was brought to Morocco to perform measurements from 11 May to 10 June 2006. The Sun photometer measured optical depth at 340, 380, 440, 500, 675, 870, 1020, and 1640 nm and sky radiances at different almucantar angles at 440, 675, 870, and 1020 nm. AERONET's Cimel Sun photometers are calibrated on a routine basis for quality assurance. The instrument used during SAMUM–1 was calibrated at Goddard Space Flight Center (AERONET Headquarter), Greenbelt, MD, before (winter of 2005) and after the SAMUM–1 campaign (autumn of 2006).

During SAMUM–2a a travel version (#90) of the Cimel Sun photometer was kindly provided by the AERONET staff. This instrument measured optical depth as well as sky radiances at 440, 675, 870, and 1020 nm only.

SSARA

The Sun–Sky Automatic Radiometer (SSARA) of the MIM performed almost continuous measurements during SAMUM–1 and SAMUM–2a (Toledano et al. 2009, 2011). SSARA measures optical depth in the range of 340–1550 nm and sky radiance at 439, 781, and 1030 nm. The comparisons of the AERONET Cimel instrument with SSARA show that the uncertainty in the optical depth is less than 0.01–0.02 at wavelengths $<$500 nm and $<$0.01 for the larger wavelengths (Toledano et al. 2009, 2011).

Dr Schulz & Partner SP1A

During the reduced setup of SAMUM–2b only one Sun photometer was present at Praia airport. IfT's exemplar of the SP1A of Dr Schulz & Partner GmbH[2], Buckow,

[2] www.drschulz.com

Germany, measures optical depth at 354, 370, 381, 402, 412, 441, 502, 533, 614, 675, 779, 856, 913, 947, 961, 1026, 1044, and 1069 nm. The instrument is equipped with filters for measurements of optical depth very close to the Nd:YAG laser wavelengths used for measurements with BERTHA. Direct sun measurements for the retrieval of aerosol optical depths were performed during both SAMUM–2 campaigns.

5.6 Radiosonde

During field campaigns with BERTHA a Vaisala sounding station is always incorporated in the measurement setup. Radiosonde ascents were performed accompanying every lidar measurement to obtain profiles of pressure, temperature, and humidity up to heights of 20–25 km. The information of pressure and temperature is used for the calculation of the molecular information needed for the retrieval of aerosol profiles. In the time before noon, between 1000 to 1200 local time (LT), usually a RS–92 windsonde (also measuring wind speed and direction) was launched while an older RS–80 was launched in the evening hours. During dedicated days radiosondes were launched during afternoon or late night as well.

5.7 Backward Trajectories

Backward trajectories used for air–mass analysis during the SAMUM campaigns were computed with the three–dimensional LAGRangian ANalysis TOol (LAGRANTO, Wernli and Davies 1997, Knippertz et al. 2009, 2011). LAGRANTO runs with operational analysis data on model levels provided by the European Centre for Medium–Range Weather Forecasts. The backward trajectories are calculated from 3–D wind fields for all grid points within the 3–D box from 30.0–31.0° N to 6.5–7.5° W for Ouarzazate, Morocco, during SAMUM–1 and from 14.5–15.5° N to 23.0–24.0° W for Praia, Cape Verde, during SAMUM–2 and from the ground to 400 hPa. From the computed 270 trajectories ensemble mean backward trajectories for the dust layer (from surface to dust layer top) and for the lower free troposphere (from dust layer top to the 400 hPa level, about 7.5 km height above sea level, asl) are determined. The ensemble means represent the main air flow in the two different layers. For some SAMUM–2 measurements backward trajectories were also calculated with the Hybrid Single–Particle Lagrangian Integrated Trajectory model (HYSPLIT, Draxler and Rolph 2003).

6 Results

This chapter presents the findings of the observations of the SAMUM campaigns in Morocco and at Cape Verde. For each of the three campaigns a general overview of the measurements and the prevailing meteorological situation is provided. Then, the respective aerosol conditions are described for representative case studies on the basis of measurements with Sun photometer, radiosonde, and lidar. For SAMUM–2a, a case of vertically resolved aerosol–type separation with subsequent inversion of the derived optical data set for pure biomass–burning smoke is discussed. Finally, the overall findings of the individual SAMUM campaigns are presented including mean profiles and histograms of the observed parameters. For SAMUM–2a this also includes a discussion of the general results of the aerosol–type separation for the observed dust/smoke mixture. The results presented in this chapter are (in part) published in Tesche et al. (2009a, b, 2011a, b).

6.1 SAMUM–1

SAMUM–1 lasted from 11 May to 10 June 2006. Lidar measurements at Ouarzazate were usually performed in the morning hours, after sunset, and during Falcon overpasses. Each lidar observation was accompanied by the launch of a radiosonde. A total of 50 radiosondes—Vaisala RS92 (pressure, temperature, humidity, wind speed, and wind direction) in the morning and Vaisala RS80 (pressure, temperature, and humidity) in the evening—was launched during SAMUM–1. Nighttime measurements of Raman scattering from nitrogen molecules were used to independently calculate profiles of backscatter and extinction and thus of the lidar ratio (see Section 3.3.2). Lidar ratios obtained from nighttime measurements were applied for the analysis of daytime measurements according to Klett's method (see Section 3.3.1). Sun photometer measurements of AOT at the respective wavelengths were used to validate the quality of the daytime lidar profiles.

6.1.1 Overview

Figure 6.1 gives an overview of the aerosol conditions during SAMUM–1. Sun photometer observations (upper panel) of the AOT at 500 nm (red dots) and the 440/870–nm Ångström exponent (white dots) show the temporal development of the column dust load over Ouarzazate. The vertical extent of the dust layer is shown in the lower panel.

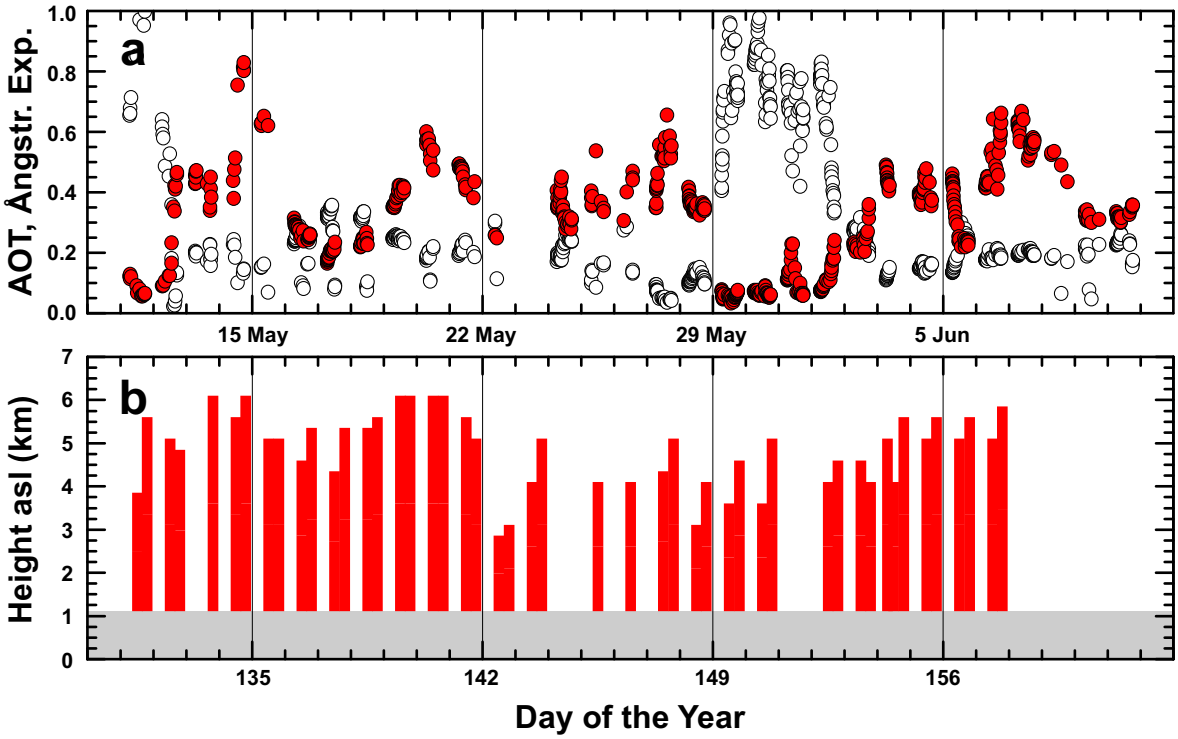

Figure 6.1: (a) One–month AERONET Sun photometer observations (11 May–10 June 2006) of 500–nm AOT (red dots) and 440/870–nm Ångström exponents (white dots). (b) Vertical extent of the dust layers as observed with lidar. The gray bar denotes the altitude of the measurement station of 1133 m asl.

The dust layer height was derived from the time–height displays of the range–corrected lidar signal and the volume depolarization ratio. Figure 6.1a shows two major dust periods with AOT above 0.2 and Ångström exponents below 0.4: from 12–29 May 2006 and after 2 June 2006 until the end of the campaign. Optimum conditions for the observations of pure mineral dust were given during these periods. Low AOTs and relatively high Ångström exponents were only observed on 11 May 2006 and between 29 May and 2 June 2006 when clean air was advected to the measurement site within a northwesterly flow from the Atlantic ocean. The measurements during the rather clean conditions in the evening of 11 May 2006 were used to derive the overlap function of BERTHA (see Section 5.4.3.1).

A detailed discussion of the meteorological conditions during SAMUM–1 as well as of the associated emission of mineral dust and its successive transport to the SAMUM–1 measurement sites can be found in Knippertz et al. (2009). The emission and transport of dust to southern Morocco during SAMUM–1 was found to be strongly related to cold surges from the Mediterranean which are associated with eastward passing upper–level waves and lee cyclones south of the Atlas mountains. Furthermore, dustiness during SAMUM–1 was caused by locally generated dry–convective plumes (Ansmann et al. 2009a) and by gust fronts associated with dry thunderstorms over desert areas in Mali and Algeria (Knippertz et al. 2007).

On 11–14 May 2006, an upper–level short–wave trough moved across northwestern Africa and triggered the formation of a low–level cyclone east of the Atlas mountains. Dusty air from eastern and central Algeria was advected to southern Morocco, along the northern flank of the low–level cyclone. Between 16 and 21 May 2006, northwestern Africa was dominated by an upper–level ridge and calm, sunny weather. The persistent surface high with the core over the eastern Atlas steered air from eastern and central Algeria towards Morocco. In the beginning of June, an upper–level ridge strengthened and surface pressure rose quickly after a period with changing weather conditions and thunderstorm activity. Although southern Morocco was influenced by air masses from the north and west in the beginning of this period, the strengthening of the low–level anticyclone led to advection of dustier air masses from the east. After 4 June 2006, the development of deep convection over the Atlas caused less defined advection conditions as was the case during the first dust period. Mixing of Saharan air with maritime and anthropogenically polluted air from northerly and westerly directions (and from the surroundings) cannot be excluded and may have influenced the observations to some extent. Generally, the synoptic analysis for the time range of SAMUM–1 points to source regions in the area of western Tunisia to central Algeria (see Figure 2.1 and Knippertz et al. 2009). This is consistent with the findings of the analysis of optical and mineralogical properties of *in situ* dust samples (Kandler et al. 2009). The periods of low dust concentration (see Figure 6.1) were associated with the presence of weak upper–level ridges and surface highs over the eastern Atlas. The corresponding slow winds caused advection of less dusty air from central and eastern Algeria.

The following sections discuss measurements with lidar, Sun photometer, and radiosonde on 15 May 2006 and 3 June 2006. These observations were performed during the first and second dust period, respectively. The two case studies were chosen because they represent typical conditions during the SAMUM–1 measurements with high AOTs and low Ångström exponents (15 May 2006) and provide an opportunity to compare the ground–based lidar observations with each other (15 May 2006) and with airborne measurements of the HSRL aboard the Falcon aircraft (3 June 2006). Some figures and parts of the text are taken from Tesche et al. (2009a), who present two additional case studies of 19 May 2006 and 4 June 2006. Results of measurements with BERTHA during SAMUM–1 can be found in Ansmann et al. (2008, 2009a, b), Esselborn et al. (2008, 2009), Freudenthaler et al. (2009), Haustein et al. (2009), Heinold et al. (2009), Knippertz et al. (2009), Mattis et al. (2009), Müller et al. (2007, 2009, 2010a, b), and Otto et al. (2009). For the measurements at Ouarzazate UTC corresponds to local time.

6.1.2 Measurement Case: 15 May 2006

Figure 6.2 shows 72–hour LAGRANTO backward trajectories arriving over Ouarzazate at 2100 UTC on 15 May 2006 (see Section 5.7). Dust was directly advected to the measurement site from central Algeria. Trajectories in the dust layer were over desert areas during the last three days before the arrival at Ouarzazate. The heavy dust load is also indicated by high particle optical depths of 0.5–0.8 at 500 nm on 14–15 May 2006

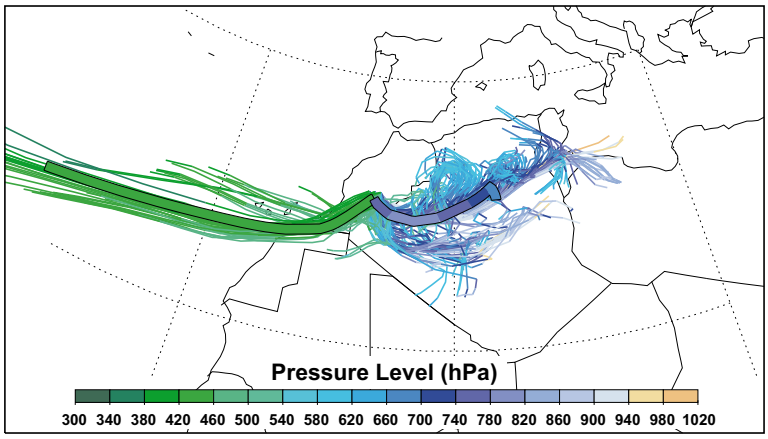

Figure 6.2: 72–h backward trajectories arriving over Ouarzazate at 2100 UTC on 15 May 2006. The ensemble mean trajectories for the dust layer (transport mainly from easterly directions) and for the free troposphere (transport mainly from westerly directions) are marked by thick lines. Trajectory colors indicates the pressure level of the air parcel during its travel along the trajectory.

in Figure 6.1. On 15 May 2006, the observations of all three ground–based Raman lidars were compared during a heavy dust period.

Lidar measurements during the morning (1021–1156 UTC) and evening (1927–2207 UTC) of 15 May 2006 are shown in Figure 6.3 in terms of time–height displays of the range–corrected signal and the volume depolarization ratio at 710 nm. Both are given with a temporal and spatial resolution of 10 s and 15 m, respectively. A thick and very homogeneous dust layer up to a height of 4.5 and 5.0 km agl is present during the morning and the evening, respectively. Well–mixed conditions were observed with lidar, i.e., high values of the depolarization ratio were found throughout the dust layer. No signals are shown below 1 km height agl due to the incomplete overlap of the laser beam and the RFOV (see Section 5.4.3.1). Meteorological profiles of the morning sonde (launched at 1039 UTC, dotted line in c and e) are shown in Figure 6.3b and d. They confirm the lidar–derived impression of a well–mixed dust layer. The top of the dust layer is marked by a temperature inversion, a strong decrease in relative humidity, and a change in wind direction. The virtual potential temperature Θ_v is calculated from the profiles of temperature and humidity. An almost height–independent Θ_v up to 4.5 km height agl indicates a well–mixed dust layer. The 1–h mean value of the daytime Sun photometer measurement (Figure 6.3a) reveals a low Ångström exponent (white dot) which represents a dominance of large particles, i.e., pure dust conditions. The AOT of 0.62 at 500 nm (green dot) is in good agreement with the lidar observations of 0.58 and 0.71 at 532 nm during noon and after sunset, respectively, which are displayed as bold green lines. To calculate the AOT from the lidar profiles the lowermost trustworthy value of the extinction coefficient was assumed to also represent the conditions in the overlap region. This is justified because constant extinction is also observed above the height of full overlap and because of the well–mixed state of the dust layer. The thin green lines mark an estimated error in lidar–derived AOT of 15%. The comparison of AOT from Sun photometer and lidar also gives a good impression

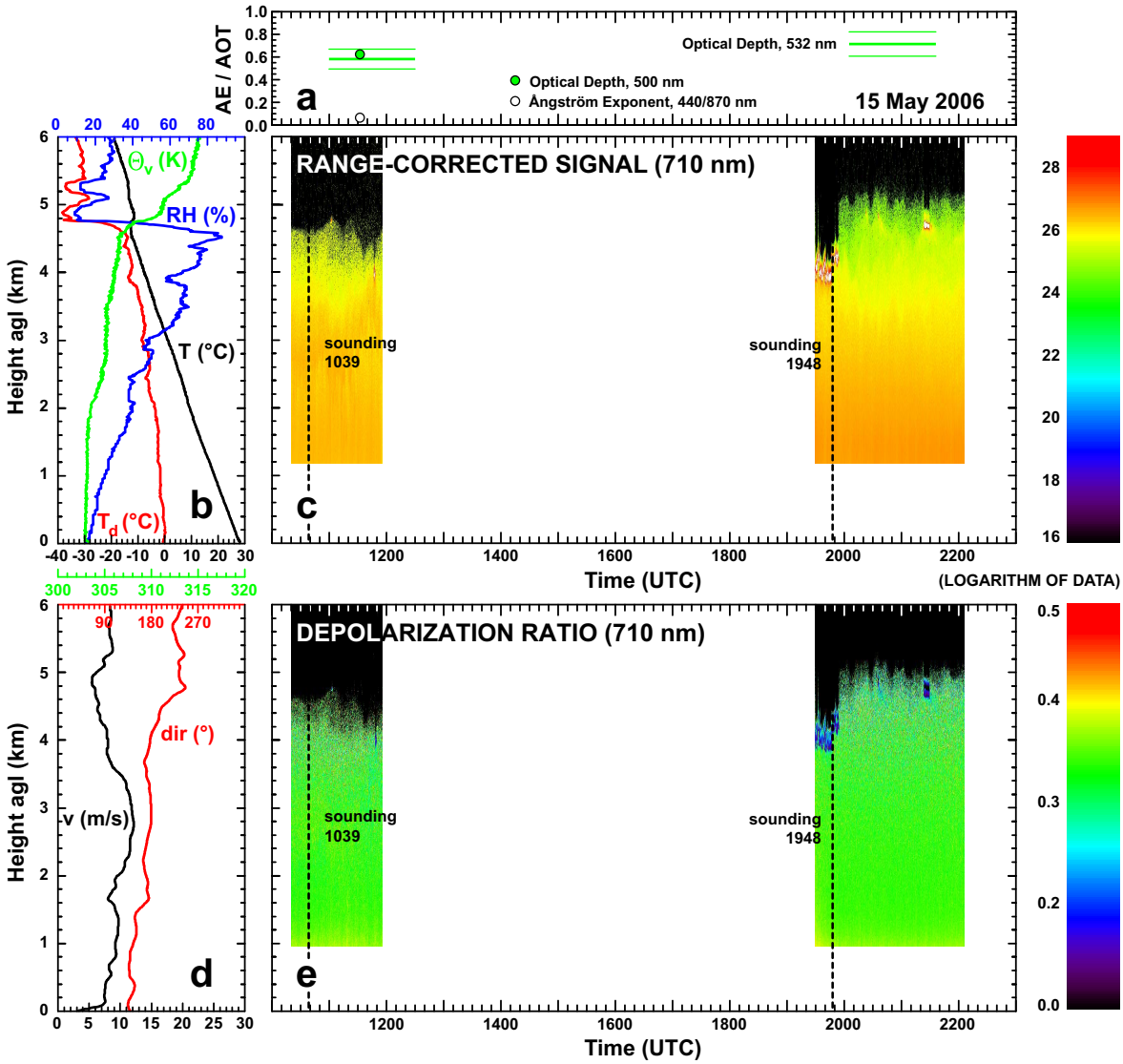

Figure 6.3: Sun photometer (a) and lidar observations (c and e) performed on 15 May 2006 together with the meteorological profiles (b and d) of the morning sonde launched at 1039 UTC (left dotted line in c and e). The different colors of the profiles, scales, and numbers in the sounding plots refer to temperature T (black in b), dew–point temperature T_d (red in b), relative humidity RH (blue in b), virtual potential temperature Θ_v (green in b), wind speed v (black in d) and wind direction dir (red in d). Dots in (a) denote the results of Sun photometer observations while lidar results are shown as bold (mean value) and thin (uncertainty range) horizontal green lines.

of the temporal homogeneity (stability) of the prevailing dust conditions. Water clouds (strong backscatter signal, low depolarization ratio) were observed in the beginning of the evening measurement and around 2130 UTC.

The profiles of the analysis of one hour (2015–2125 UTC) of the evening observations on 15 May 2006 when BERTHA, POLIS, and MULIS measured simultaneously are shown in Figure 6.4. All signals are vertically smoothed with window lengths of 300–660 m

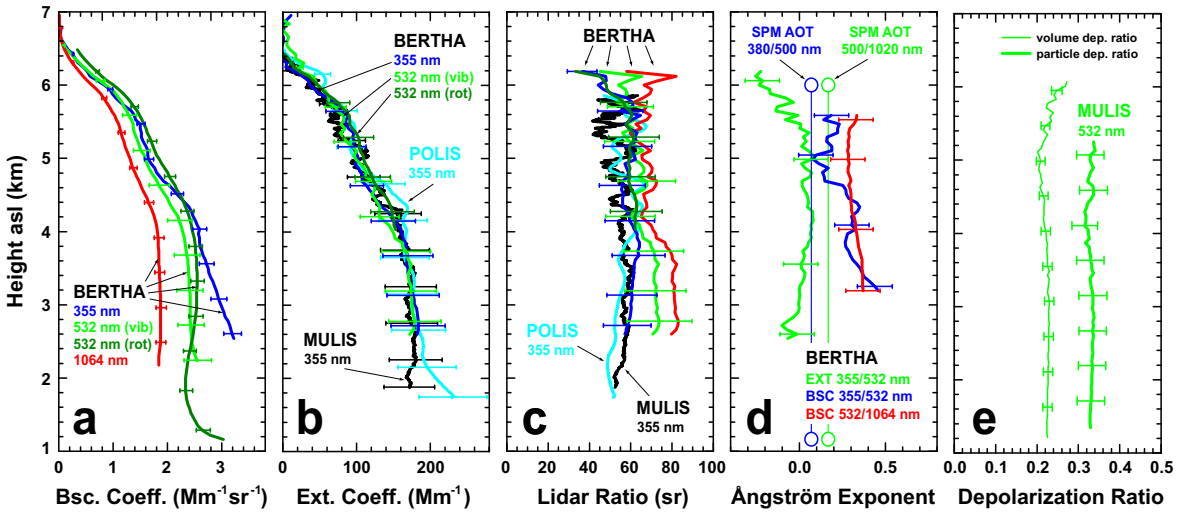

Figure 6.4: Cloud–screened 1–h (2025–2125 UTC) mean profiles measured with BERTHA, MULIS, and POLIS and derived from Sun photometer observations. Shown are (a) backscatter coefficients measured with BERTHA at 355 (dark blue), 532 (light and dark green), and 1064 nm (red); (b) extinction coefficients at 355 nm measured with BERTHA (dark blue), MULIS (black), POLIS (light blue) and at 532 nm measured with BERTHA only (light and dark green); (c) lidar ratios at 355 nm measured with BERTHA (dark blue), MULIS (black), and POLIS (light blue), at 532 nm measured with BERTHA (light and dark green), and at 1064 nm measured with BERTHA (red); (d) Ångström exponents measured with BERTHA (backscatter–related in dark blue and red and extinction–related in dark green) and derived from Sun photometer measurements (blue and green circles and thin lines); and (e) linear volume (thin) and particle (bold) depolarization ratios measured with MULIS at 532 nm.

(lower heights) and 300–2400 m (upper part of the dust layer). The backscatter coefficients at 355, 532, and 1064 nm shown in Figure 6.4a were measured with BERTHA. The two green lines (vib and rot) denote the results of the vibrational (532/607 nm, corrected for depolarization–dependent receiver transmission, see Section 5.4.3.2) and of the rotational–Raman channels, respectively. The backscatter coefficients show a weak wavelength dependence with backscatter–related Ångström exponents of 0.2–0.4 (blue and red line in d). Extinction coefficients measured with the three ground–based lidars are compared in Figure 6.4b. A very good agreement was found between the results of the different systems. Extinction coefficients were as high as 200 Mm^{-1} at 355 and 532 nm and were nearly equal for all systems. Error bars (one standard deviation) include signal noise and several signal corrections. A detailed discussion of the error calculation is given in the Appendix.

Figure 6.4c shows measurements of the dust lidar ratio at 355 and 532 nm. The profile at 1064 nm was retrieved by applying the 500/1020 nm extinction Ångström exponent from the Sun photometer measurements (column value, green circles in Figure 6.4d) to the 532–nm extinction coefficient and subsequent division with the 1064–nm backscatter coefficient. The homogeneous dust conditions suggest that the difference between column–integrated (Sun photometer) and height–resolved (lidar) inten-

sive particle properties (e.g., lidar ratio and Ångström exponent, see Section 4.1) are negligible. The profiles of the lidar ratio also indicate a well–mixed Saharan dust layer. Lidar ratios were around 55 sr at 355 nm during this heavy dust outbreak. The lidar ratio at 532 nm seems to be higher than the one at 355 nm. However, the error bar is rather large because of the uncertainty in all the corrections applied (see Section 5.4.3 and the Appendix). Thus the difference should be handled with care. Lidar ratios at 355 and 532 nm varied between 55 and 60 sr above 4 km height asl. As expressed in Equation (4.2), the (500/1020–nm) extinction–related Ångström exponent is smaller than the (532/1064–nm) backscatter–related Ångström exponent. Therefore, the lidar ratios at 1064 nm are slightly higher than the ones at 355 and 532 nm.

The Ångström exponents (for extinction EXT and backscatter BSC) from BERTHA observations are displayed in Figure 6.4d. In addition, values are calculated from the Sun photometer observation of AOT at 380, 500, and 1020 nm (circles connected by vertical lines). The Ångström exponents varied around 0–0.5 (backscatter, blue and red) and zero (extinction, green). The extinction–related Ångström exponents agree well with the ones derived from the Sun photometer observations taken before sunset.

Finally, Figure 6.4e shows the MULIS measurement of the linear volume and particle depolarization ratio at 532 nm. During SAMUM–1 only MULIS was able to measure the particle depolarization ratio with the desired high accuracy, i.e., with an error in the range of 10% (see Section 5.1). The observed particle depolarization ratio of 0.33 denotes dominance of highly non–spherical particles. The time series of the SAMUM–1 particle depolarization ratio measurements by Freudenthaler et al. (2009) reveals that the value which is characteristic for pure Saharan dust is 0.31±0.03. This finding—together with the observations of the dust lidar ratio—is one of the outstanding findings of the SAMUM–1 lidar observations (see Section 7). Numerical particle models which are designed to account for the radiative properties of non–spherical particles (e.g., Mishchenko et al. 1997, Dubovik et al. 2006) will have to reproduce the findings of SAMUM–1 to proof their reliability. As will be discussed later in this thesis, the non–spherical particle model developed in the framework of SAMUM–1 (Wiegner et al. 2009) and improved by Gasteiger et al. (2011) is able to retrieve dust lidar ratios and depolarization ratios which are in the range of the SAMUM observations.

Figure 6.4 shows how well the observations of the different lidar systems fit with each other. The homogeneous conditions met on 15 May 2006 allowed for a comparison of the column–integrated observations of the Sun photometer with the lidar measurements. The 5–km deep pure dust layer was very homogeneous and well–mixed throughout the entire day. Convective plumes that started to develop around noon contributed to the vertical mixing (Ansmann et al. 2009a).

6.1.3 Measurement Case: 3 June 2006

The measurements of the HSRL aboard the Falcon research aircraft were used for the validation of the dust data retrieval of the Multi–angle Imaging SpectroRadiometer

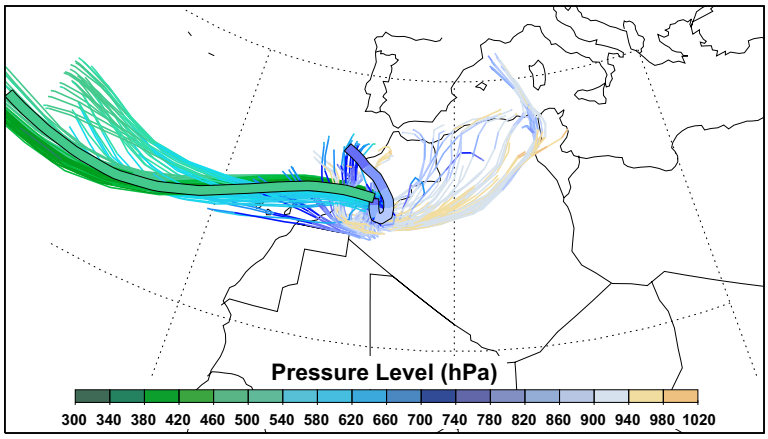

Figure 6.5: Same as Figure 6.2 but for backward trajectories arriving at 0500 UTC on 3 June 2006.

(MISR) aboard the Terra satellite (Kahn et al. 2009) as well as for the validation of radiative–transfer and dust–transport modeling (Bierwirth et al. 2009, Heinold et al. 2009, Otto et al. 2009). As mentioned in Section 3.3.3, HSRL instruments require careful supervision to obtain reliable results—especially if operated airborne. To validate the general performance of the new instrument and as a measure of data quality assurance, comparisons to measurements with BERTHA were performed for the overflights of the Ouarzazate lidar station (Esselborn et al. 2008). However, the well–established and robust Raman technique can only be applied during nighttime, in the absence of the background noise of sunlight (see Section 3.3.2). The only nighttime Falcon flight during SAMUM–1 was performed in the early morning of 3 June 2006. The research aircraft passed the airport station twice, at 0315 and at 0414 UTC. These overflights provided the best conditions to compare the observations of the airborne HSRL with that of the ground–based systems.

Figure 6.5 shows 72–h backward trajectories arriving over Ouarzazate at 0500 UTC on 3 June 2006. In the morning hours the second dust period described by Knippertz et al. (2009) was in its build–up phase. Only the lowermost trajectories show air coming from central Algeria. Above 2 km height agl air was transported to the measurement site from northerly and westerly directions. On 4 June 2006 (not shown) the trajectories arriving over Ouarzazate within the dust layer unambiguously point to source regions in central Algeria while the air masses which arrived above the dust layer usually were advected from the North Atlantic.

An overview of the measurements on 3 June 2006 is given in Figure 6.6. The observations of the Sun photometer (a), the meteorological profiles of the sonde launched at 0505 UTC (b and d), and the lidar measurements (c and e) from 0100 to 1320 UTC on 3 June 2006 are shown. In addition, the times of the Falcon overflights at 0315 and 0414 UTC are marked as white lines in the lidar plots. Times of soundings are marked by dashed black lines. The meteorological profiles and the lidar observations show that the dust layer extended to 3 km height agl. In the plot of the range–corrected signal and in the profile of the virtual potential temperature, a step is visible at 1.6–1.8 km

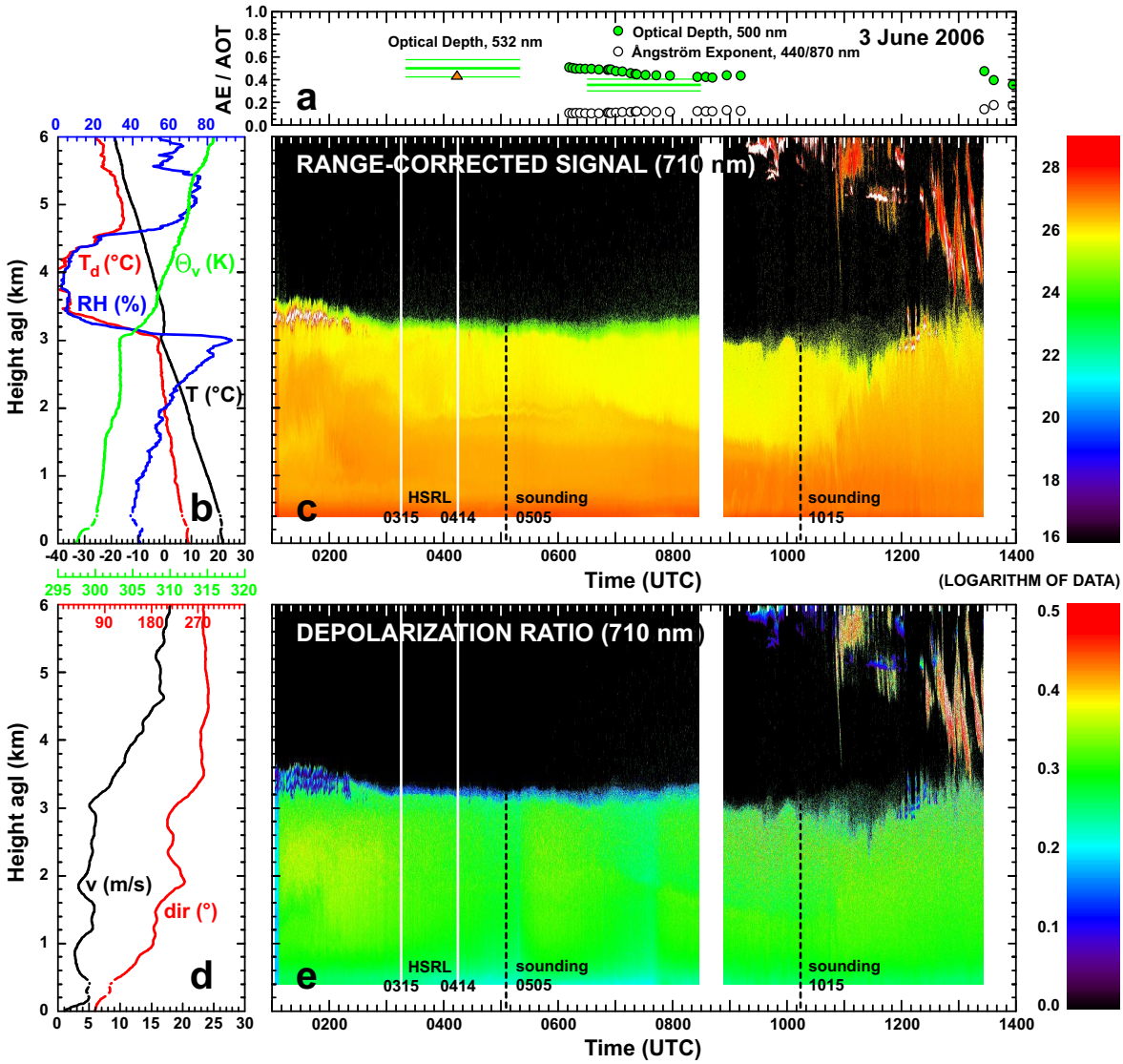

Figure 6.6: Same as Figure 6.3 but for the measurements on 3 June 2006. The meteorological profiles (b and d) originate from the sonde launched at 0505 UTC (left dotted line in c and e). The white lines in (c) and (e) mark the overflights of the DLR Falcon research aircraft. The orange triangle in (a) refers to the AOT measured with HSRL at 532 nm during the Falcon overflight at 0414 UTC.

height agl. The two–layer structure might be due to the ambiguous transport pattern which is visible in the backward trajectories shown in Figure 6.5. The sounding shows that the air was advected from desert areas in the lower layer and from westerly directions in the upper layer (Esselborn et al. 2009, Knippertz et al. 2009). However, the different layers are almost not visible in the plot of the depolarization ratio. The two–layered structure vanished after 1000 UTC when the updrafts of the evolving daytime boundary layer caused a mixing of the different layers and created one homogeneously mixed dust layer. At this time of the day, different dust advection patterns are no longer visible as stratified aerosol layers.

In the beginning of the measurements (0105–0230 UTC) thin altocumulus formed at the top of the dust layer where the relative humidity was close to 100%. These and the other liquid water clouds which occured later in the measurement at heights between 5 and 6 km agl can be identified by the low values (blue color) in the plot of the depolarization ratio. The blurry turquoise band at 3.2 km height agl (between 0215 and 0830 UTC) shows the decrease of the volume depolarization ratio at the dust layer top. Note that this quantity (in contrast to the particle depolarization ratio) is not intensive and depends on the concentration of the scattering particles (see Section 5.4.2). The molecular contribution at 710 nm is low which causes a small difference between volume and particle depolarization ratio profiles at this wavelength. The strong backscatter and depolarization signals above 3 km height agl after 1000 UTC were caused by ice virgae which precipitated from the water clouds. An investigation of the formation of ice–containing clouds within the dusty environment of SAMUM–1 can be found in Ansmann et al. (2008).

An average of 5.2 s of HSRL measurements at 0414 UTC resulted in an AOT of 0.42 at 532 nm (orange triangle in Figure 6.6a). The value of the BERTHA nighttime measurement (0320–0520 UTC, vertical green line in Figure 6.6a) of 0.5 is slightly larger than the Falcon snapshot. After sunrise the Sun photometer showed 500–nm AOTs in the range of the nighttime lidar observations. Until 1000 UTC the AOT dropped to 0.4 while the 440/870–nm Ångström exponents remained at values below 0.2. The lidar–derived AOT after sunrise (0630–0830 UTC) is much lower than the values measured with SPM. Because daytime lidar data analysis needs to consider the overlap effect of laser beam and RFOV (see Section 5.4.3.1) this underestimation can occur when large amounts of dust are present in the lowermost kilometer of the atmospheric column (as is suggested by the profiles shown in Figure 6.7).

Figure 6.7 shows aerosol profiles as measured with BERTHA (0400–0500 UTC), HSRL (at 0414 UTC), MULIS (0400–0500 UTC), and POLIS (0400–0500 UTC) on 3 June 2006. Except for the profiles of the particle depolarization ratio that will be discussed in detail below, error bars are not included to make the figure more straightforward. The two–layer structure in Figure 6.6c is also resolved by the backscatter and extinction coefficients. Maximum values at 532 nm were 2 $Mm^{-1}sr^{-1}$ and 4 $Mm^{-1}sr^{-1}$ (100 Mm^{-1} and 200 Mm^{-1}) in the upper and lower layer, respectively. No 355–nm profiles of BERTHA are shown due to bad data quality of the measurements at 355 nm and the noisy signal at 387 nm. The agreement between the backscatter and extinction coefficients and the lidar ratio derived from ground–based and airborne lidar measurements at 532 nm is very good. The lidar ratio was 40–50 sr in the upper layer and increased slightly in the desert dust layer below. Esselborn et al. (2009) and Weinzierl et al. (2009) discuss that the dust in the two layers can be traced back to different source regions in central and western Algeria.

On 3 June 2006 linear particle depolarization ratios (Figure 6.7e) could be measured at four wavelengths (Freudenthaler et al. 2009): 355 nm (POLIS, blue), 532 nm (HSRL, orange and MULIS, green), 710 nm (BERTHA, magenta), and 1064 nm (HSRL, red). The profiles are almost constant with height. The bold and thin dotted lines mark the

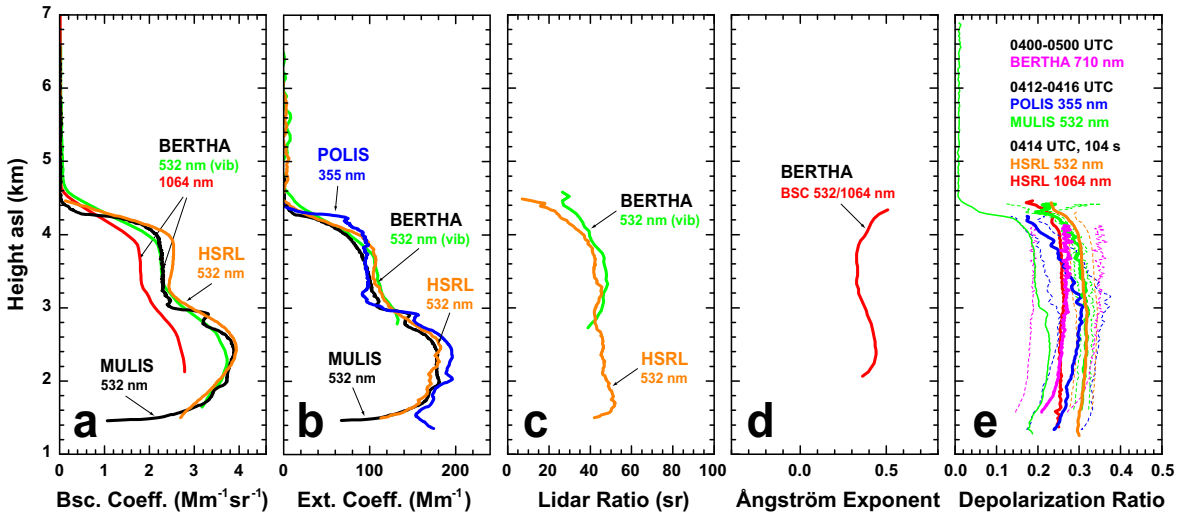

Figure 6.7: Same as Figure 6.4 but for the time range 0400–0500 UTC of the nighttime measurement on 3 June 2006 (a–d). HSRL profiles (orange lines) show 13–s averages at 0414 UTC when the Falcon passed the ground site. The plot of the linear depolarization ratio (e) shows results of measurements with BERTHA (710 nm, magenta, 0400–0500 UTC), HSRL (532 nm, orange and 1064 nm, red, 104–s mean around 0414 UTC), MULIS (532 nm, green, 0412–0416 UTC), and POLIS (355 nm, blue, 0412–0416 UTC). Solid bold lines refer to the mean particle depolarization ratio in the indicated time intervals while the respective error ranges are represented by thin dotted lines. The solid thin green line shows the 532–nm volume depolarization ratio as measured with MULIS. Error bars are not included in (a–d) for the sake of legibility.

measurement and the statistical errors, respectively. The calibration that is applied to the depolarization measurements with MULIS keeps the error of the 532–nm particle depolarization ratio below 10% (Freudenthaler et al. 2009). The other systems show considerably larger errors which are mostly caused by calibration uncertainties. The particle depolarization ratios measured with MULIS and HSRL at 532 nm are almost identical and show values of 0.31. A mean dust depolarization ratio of 0.31±0.03 was obtained from all the MULIS measurements during SAMUM–1 (Freudenthaler et al. 2009). The results at 710 and 1064 nm are lower than at 532 nm and show a mean value of 0.26. The POLIS measurement at 355 nm is located between the long–wavelength and the 532–nm profiles. As discussed in Section 5.4.2 the depolarization measurement with BERTHA was improved considerably after SAMUM–1. Thus the degree of confidence in the profile shown in Figure 6.7e is rather low. Instead, the results of the summer measurements at Cape Verde suggest that the dust depolarization ratio at 710 nm is in the range of 0.37±0.07 (see the detailed discussion in Section 6.3).

The reproduction of the spectrally resolved measurements of the dust depolarization ratio and of the dust lidar ratio will be the benchmark test for numerical models which try to handle light scattering by non–spherical particles (Müller et al. 2010a, b, Gasteiger et al. 2011). Because the lidar ratio incorporates the amount of scattering at 180° it is very sensitive to the shape of the scattering particles. Extinction coefficients on the

other hand can be reproduced quite well by now (Müller et al. 2010a, Heinold et al. 2009). The most difficult task will be to reproduce the large dust depolarization ratios. Promising approaches are to introduce scatterers with a rough surface or with more realistic shapes (e.g., highly irregular particles or particle agglomerates) comparable to the ones observed during SAMUM (Kandler et al. 2009, 2011, Gasteiger et al. 2011).

6.1.4 General Findings and Discussion

Saharan dust was present over Ouarzazate on more than 20 days during the four–week campaign. 53 morning and evening lidar measurements which lasted from 30 min to several hours were performed. In total, 135 h of lidar data were collected. 20% of this data set could not be analyzed due to the presence of clouds or problems with the lidar. A statistical overview of the 69 h of analyzed measurements with BERTHA is presented in terms of average profiles (four–week means, 660 m smoothing length) in Figure 6.8. Bold lines denote the obtained mean value. The corresponding standard deviations and extreme values for each height bin are shown as gray area and thin lines, respectively. The number N of individual profiles which could be considered for averaging varies for the different parameters due to several reasons. Daytime and nighttime profiles of backscatter coefficients were available (Figures 6.8a–c), but only nighttime profiles of the extinction coefficient were included in Figures 6.8d and e. To better compare 355–nm and 532–nm extinction values, rotational–Raman lidar measurements were excluded here. A few of the determined backscatter and extinction profiles showed a strong impact of the remaining laser–beam RFOV overlap effect (after correction, see Section 5.4.2), so that only the uppermost part of the height profile within the dust layer was considered as useful for comparison with the observations of the other ground–based lidars. These inappropriate profiles were removed from the data set.

Comparably constant extinction and backscatter properties were found in the lowermost 3 km of the atmosphere. The comparably smooth decrease of the backscatter and extinction values between 4–7 km height asl is attributed to the varying dust layer depth. Extinction coefficients were on average 100±50 Mm^{-1} at 355 and 532 nm in the lowest 3 km above ground and ranged from 30 Mm^{-1} on clear days to almost 250 Mm^{-1} during days with high dust burden (e.g., on 14 May 2006). Somewhat lower values were obtained at 1064 nm. In contrast to the extensive quantities, the intensive quantities (lidar ratio, Ångström exponent) varied only weakly with height. This corroborates that the dust plumes (observed in the early evening) were well–mixed. A wavelength dependence of the lidar ratio was not found. The dust lidar ratios were, on average, 53–55 sr at all three laser wavelengths. The standard deviation is small with values around 7 sr (355 and 532 nm). The profile of maximum 1064–nm lidar ratios shows values up to 80–100 sr and the corresponding standard deviation of 13 sr is comparably large. These high values may indicate that the assumption of constant dust properties from the late afternoon to the early evening was not always valid. If only the observations taken during the first well–defined dust period from 13 to 22 May 2006 are considered, the mean lidar ratios are 55±5 sr (355 nm), 56±5 sr (532 nm), and 59±7 sr (1064 nm). The same values were found by the other ground–based lidar (Freuden-

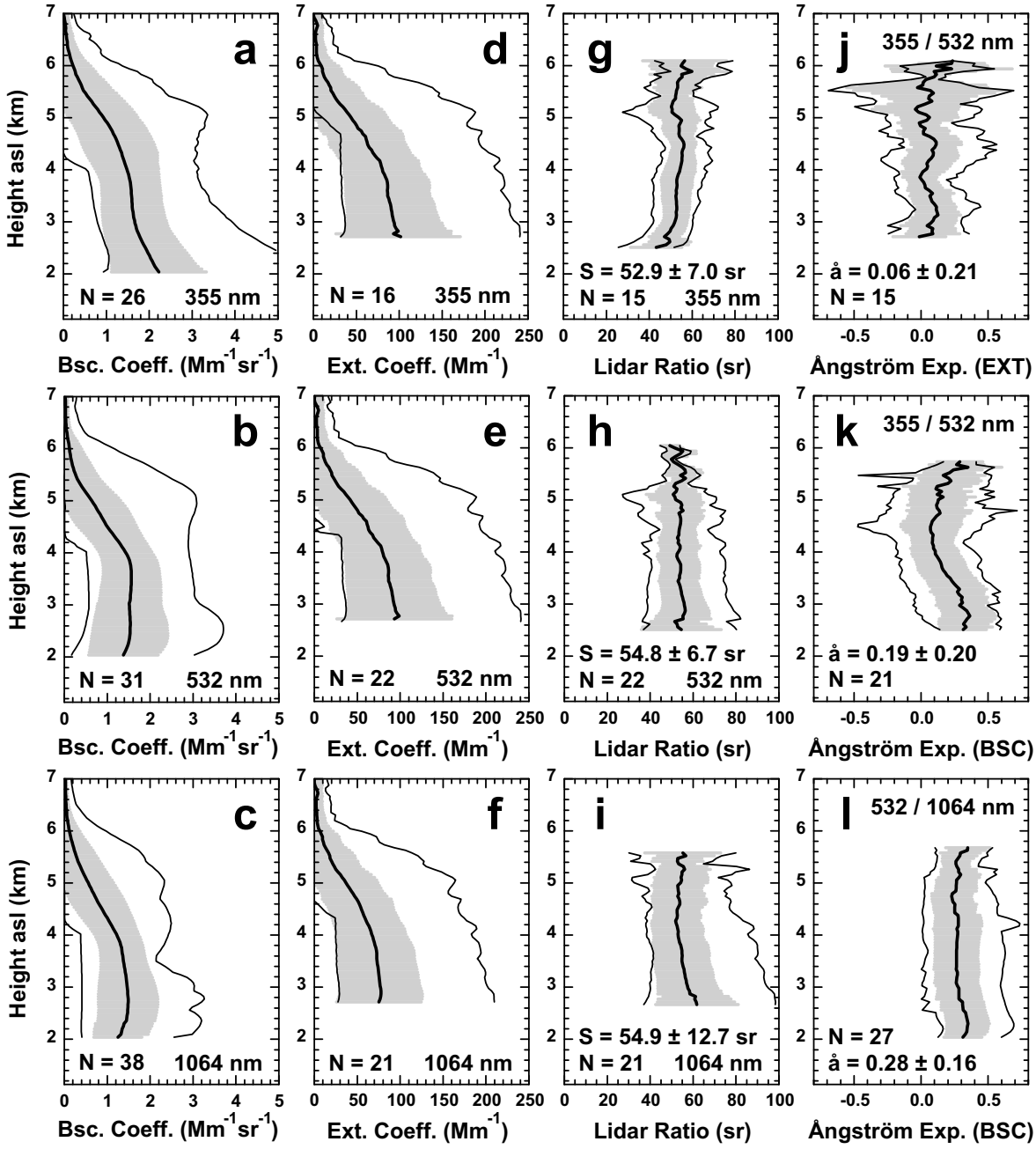

Figure 6.8: Mean profiles (thick black lines, 660 m smoothing length) and standard deviations (gray areas) of the backscatter coefficient (a–c), the extinction coefficient (d–f), and the lidar ratio (g–i) at 355, 532, and 1064 nm, and of extinction–related (j) and backscatter–related Ångström exponents (k and l) as measured with BERTHA during SAMUM–1. The thin lines show the range of observed values (minimum and maximum value) for each height bin. N denotes the number of averaged profiles. The mean values of the mean profiles (thick lines) are given as numbers for the lidar ratio S and the Ångström exponent $å$. The given values of mean standard deviation were calculated from the gray areas, i.e., they are the mean values of the standard–deviation height profiles.

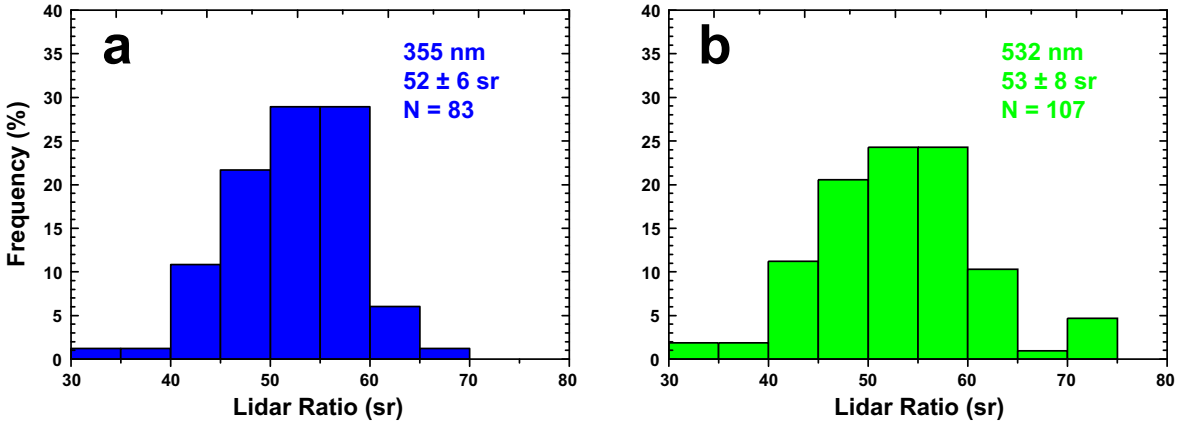

Figure 6.9: Frequency distributions of the dust lidar ratios at (a) 355 and (b) 532 nm derived from N vertical 500–m mean values of the measurements with the vibrational (355 and 532 nm) and rotational–Raman channels (532 nm).

thaler et al. 2009). The HSRL aboard the Falcon aircraft measured lidar ratios from 38–55 sr. By considering only cases for which the backward trajectories indicate the advection from desert regions, the lidar ratio is 50±4 sr (Esselborn et al. 2009). The Falcon flights were performed in the final phase of the first dust period on 19 and 20 May, on 28 May and during the second dust period on 3 and 4 June 2006 (Petzold et al. 2009, Weinzierl et al. 2009).

As briefly described in Section 6.1.2 the lidar ratio at 1064 nm was obtained as follows. In the first step, the particle backscatter coefficient profile at 1064 nm was computed from the elastic signal at 1064 nm and the Raman signal at 607 nm. In the second step, the profile of the 1064–nm extinction coefficient was estimated from the respective profile of the 532–nm extinction coefficient by assuming a height–independent 532/1064 nm Ångström exponent. This Ångström exponent was assumed to be equal to the 500/1020–nm Ångström exponent which was measured shortly before sunset by the Sun photometer. The individual profile of the 1064–nm lidar ratio was then obtained from the 1064–nm backscatter and extinction coefficients in the third and final step. In Figures 6.8f and i, only observations are included for which dust conditions were homogeneous during the late afternoon and early evening. This procedure is assumed to provide trustworthy profiles of the 1064–nm lidar ratio as long as the 532/1064–nm Ångström exponent can be considered to be independent of height.

The lidar–derived 355/532–nm extinction–related Ångström exponent always showed an almost height–independent behavior in the dust plumes. Therefore, a similar behavior can be expected for the 532/1064–nm extinction–related Ångström exponent. The individual profiles of the three different Ångström exponents were directly calculated from the respective lidar profiles of the extinction (355, 532 nm) and backscatter coefficients (355, 532, and 1064 nm). Only simultaneous observations were considered (Figures 6.8j–l). The mean extinction–related Ångström exponent in Figures 6.8j is almost zero, whereas the backscatter–related Ångström exponents show, on average, positive values around 0.2–0.3. The scatter in the data (see minimum–maximum range)

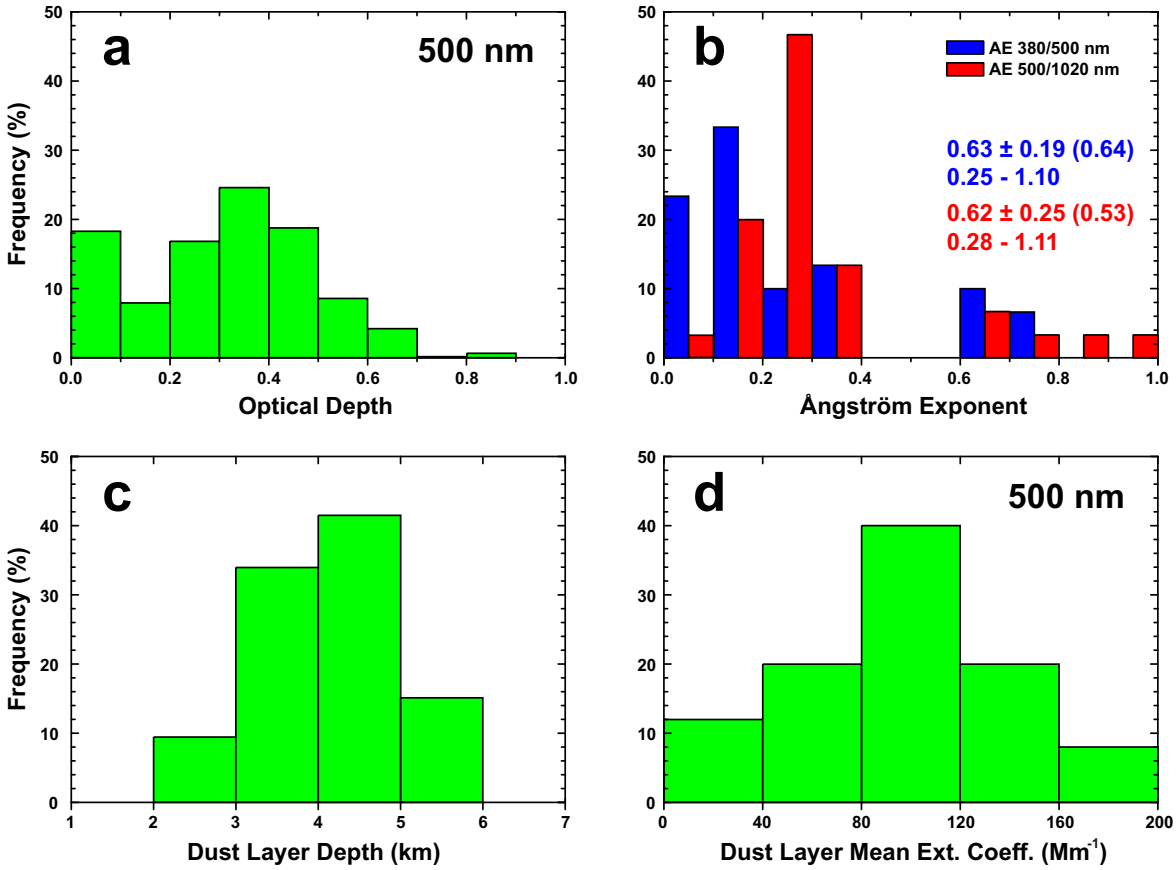

Figure 6.10: Frequency distributions of (a) 500–nm AOT and (b) Ångström exponents measured with Sun photometer as well as (c) the dust layer depth derived from lidar observations and (d) 500–nm dust layer mean extinction coefficient obtained by dividing the optical depth by the depth of the dust layer. Numbers in (b) indicate mean with standard deviation, median, and total range of the respective distributions.

is caused by atmospheric variability and uncertainties in the data analysis.

To compile the histograms shown in Figure 6.9 lidar–ratio profiles measured with BERTHA during 20 days of SAMUM–1 were cut into height intervals of 500 m. Thus the figure considers the majority of the determined values, even if only small height sections (<1000 m) could be analyzed. In contrast, Figure 6.8 contains the information of the full profiles. In the case of the 532–nm lidar ratio, vibrational–Raman signals (81 nighttime values) as well as rotational–Raman signals (additional 26 daytime observations) were analyzed. Again, the dust lidar ratio was found to be independent of wavelength. More than 80% of the 355–nm lidar ratios and about 70% of the 532–nm lidar ratios were in the range from 45–60 sr.

Histograms of the optical depth at 500 nm and the Ångström exponents for the wavelength pairs 380/500 nm and 500/1020 nm derived from the Sun photometer observations are shown in Figure 6.10a and b, respectively. As can also be seen in Figure 6.1, the optical depth at 500 nm was mostly between 0.2 and 0.6. Lower values were observed during 27 and 30 May 2009 when westerly winds brought clean air to

Ouarzazate (Knippertz et al. 2009). These also were the only days when Ångström exponents exceeded values of 0.6. Thus most of the time pure dust conditions with little maritime or urban influence prevailed. The photometer–derived Ångström exponents were at all positive. The mean values were 0.28±0.29 (380/500 nm) and 0.36±0.26 (500/1020 nm). The difference between the mean 380/500–nm Ångström exponent and the lidar–derived value (extinction–related value is about zero for the 355/532–nm spectral range, see Figures 6.8j) may be caused by the fact that the photometer provides column–integrated values which are influenced by aerosols close to the surface, whereas the values which are derived from the lidar measurements describe the aerosol properties above 3 km height asl only. A minor effect of anthropogenic pollution could be responsible for the higher Ångström exponents derived from the photometer observations. In the spectral range >500 nm the influence of sub–micron urban particles is much lower so that the agreement between photometer– and lidar–derived Ångström exponents is better.

The statistics of the dust layer top height are presented in Figure 6.10c. In addition, the dust layer mean extinction coefficient at 500 nm is shown in Figure 6.10d. The latter quantity is the ratio of the optical depth measured with Sun photometer to the dust layer height, simultaneously measured with BERTHA. Twenty five cases were analyzed. On average, the dust layer depth was 3.8±0.8 km. Most of the dust–layer mean extinction coefficients (75% out of all cases) ranged from 80 to 120 Mm^{-1} with a mean value of 95±40 Mm^{-1}. This finding is in good agreement with the lidar–derived mean extinction profiles in Figures 6.8d and e.

Plenty of measurements of Saharan (Mattis et al. 2002, Müller et al. 2003, Ansmann et al. 2003, DeTomasi et al. 2003, Balis et al. 2004, Amiridis et al. 2005, Mona et al. 2006, Müller et al. 2007, Papayannis et al. 2008) and Asian dust (Liu et al. 2002, Sakai et al. 2002, Murayama et al. 2003, 2004, Noh et al. 2007, Tesche et al. 2007, Chen et al. 2007b) with HSR and Raman lidars were published over the last 10 years. However, never before have such instruments been as close to a source region of mineral dust as during SAMUM–1. The lidar observations presented in the literature were usually performed at well–established sites which are located downstream of the dust sources (e.g., Korea, Japan, the Caribbean) or thousands of kilometers away and not even on the usual transport path (e.g., central Europe). The measurements performed at these stations strongly depend on synoptic–scale meteorological conditions and cannot be applied to derive a statistically significant data set for the characterization of the optical properties of pure mineral dust. Furthermore, most of the published studies only discuss the lidar ratio and do not present observations of the particle depolarization ratio and the Ångström exponent which are equally important for aerosol characterization and are needed for an unambiguous identification of the observed dust layers (see Section 4.1).

Measurements of EARLINET stations in the Mediterranean (Italy, Greece) often show values of the dust lidar ratio of around 40 sr at 351–355 nm (Balis et al. 2004, Mona et al. 2006). Mixing with maritime particles (with a lidar ratio of around 20–25 sr, Ansmann et al. 2002b, Franke et al. 2003) is assumed to be responsible for this effect

(Papayannis et al. 2008). The Ångström exponents, derived from the 355–nm and 532–nm backscatter coefficients, mostly range from 0.5–1.0 and therefore suggest a mixture of dust and non–dust particles (maritime and urban aerosols). Amiridis et al. (2005) analyzed four years of lidar observations at Thessaloniki, Greece, and found on average 355–nm lidar ratios of 57±29 sr for the Saharan–dust backward trajectory cluster. The large standard deviation mainly expresses the atmospheric variability caused by mixing of dust with maritime and anthropogenic particles during long–range transport. Mattis et al. (2002) were the first who presented observations of the wavelength dependence of the dust lidar ratio at 355 and 532 nm. These observations were taken in lofted and isolated plumes of two major Saharan dust outbreaks which reached northern Europe. The 355/532–nm extinction–related Ångström exponents were zero and the lidar ratios were around 75 sr at both wavelengths in the main dust layer. During another outbreak in August 2001, lidar ratios were slightly lower with values around 70 sr at 355 nm and 50–70 sr at 532 nm in layers between 3 and 8 km height.

A similar behavior of the lidar ratio in aged dust layers is also found in eastern Asia. Because of mixing with pollution (mainly causing lidar ratios <45 sr, Tesche et al. 2007) and maritime particles, lidar ratios are typically <50 sr in dust layers which are identified by backward trajectories (Sakai et al. 2002, Murayama et al. 2003, Chen et al. 2007b, Noh et al. 2007). Sakai et al. (2002) present a case measured over Japan with an increasing Ångström exponent (from 0 to 1) and relative humidity (from 20% to 60%) within a lofted layer assigned as dust layer according to backward trajectories. The authors hypothesize that such cases indicate a mixture of dust with sulfate particles. Murayama et al. (2003) observed another interesting case over Japan with complex layering and mixing. The measured Ångström exponent decreased from 1.5–2.0 below 2 km height to 0.3–1.0 at 3.0–3.5 km height. Only the uppermost layer above 3.5 km showed a clear dust signature with Ångström exponents of 0–0.5, particle depolarization ratios of 0.30–0.35, and lidar ratios from 45–60 sr at 532 nm. Murayama et al. (2004) performed the first simultaneous lidar observations of Asian dust over Japan at 355 and 532 nm. Similar lidar ratios of around 50 sr were found at both wavelengths in a lofted and isolated dust layer. Noh et al. (2007) present another lidar–ratio study in South Korea with values simultaneously measured at 355 and 532 nm and found lidar ratios between 50 and 60 sr at both wavelengths in a layer with an enhanced 532–nm volume depolarization ratio (close to 0.25). If the elevated layers which were investigated during these studies are assumed to consist of pure Asian dust (the high values of the particle depolarization ratio are taken as a measure of dust purity), the inferred optical properties are nearly identical to the ones found for Saharan dust during SAMUM–1. This is an important finding because even though the optical properties of mineral dust were studied intensively during SAMUM–1, it is not yet clear whether the findings for Saharan dust are also representative for Asian dust. Varying mineralogical properties (i.e., mainly the refractive index) of the different dust types might cause different optical properties. Especially the lidar ratio is very sensitive to variations of the complex refractive index (Gasteiger et al. 2011).

Previous field experiments which aimed at an improvement of the general understanding of the radiative effects of mineral dust particles did not incorporate such

advanced lidars for vertical profiling of dust optical properties as the ones applied during SAMUM—if height–resolved measurements were considered at all. Berthier et al. (2006) combined profiles of the particle backscatter coefficients derived from space–borne Lidar–in–space Technology Experiment (LITE, September 1994) observations with optical depths derived from METEOSAT–5 observations of dust outbreaks over the tropical North Atlantic west of Africa. They retrieved layer–integrated (column) dust lidar ratios of 57±27 sr at 532 nm. Here, the standard deviation may express to a large part the uncertainty in the retrieval. Léon et al. (2003) and Kaufman et al. (2003) combined aircraft lidar observations of particle backscatter–coefficient profiles and particle optical depths derived from MODIS data. These observations were done a few hundreds of kilometers west of Africa over the Atlantic during SHADE. Kaufman et al. (2003) derived a column lidar ratio of 63 sr at 530 and 1060 nm during a heavy dust outbreak with an optical depth of 0.9. From the results presented by Léon et al. (2003), it can be concluded that the column lidar ratio was close to 56 sr during a case with a dust optical depth of 0.8. To retrieve intensive particle properties for the measurements performed in the framework of DABEX (Haywood et al. 2008) additional model calculations had to be performed to obtain results from elastic–backscatter lidar measurements (Pelon et al. 2008). The only Raman lidar observations during DABEX were performed with POLIS which also participated in SAMUM (Heese and Wiegner 2008, Heese et al. 2009). As in Morocco, 355–nm lidar ratios around 55 sr were found for the dust layers over western Niger.

The reliable and well–accepted Raman lidar technique applied during SAMUM allows for a straightforward data retrieval without any assumptions or additional model calculations which introduce further uncertainties. The observations close to the Saharan source regions reveal wavelength–independent dust lidar ratios around 55 sr at 355, 532, and 1064 nm and Ångström exponents of backscatter and extinction that vary between 0 and 0.4 (see Figure 6.8).

Another important point of the SAMUM–1 lidar observations are the findings concerning the dust depolarization ratio and its wavelength dependence. These observations are presented by Freudenthaler et al. (2009) and Esselborn et al. (2009). The mean particle depolarization ratio for Saharan dust was found to be 0.31±0.03 and 0.27±0.04 at 532 and 1064 nm, respectively. Measurements at 355 nm (Freudenthaler et al. 2009, Heese et al. 2009) suggest a slightly lower value for the UV wavelength compared with the values at 532 nm. From the measurements during SAMUM–1 the same seems to be the case for 710 nm. However, the optical elements for calibration measurements according to the method of Freudenthaler et al. (2009) were added to the receiver only after BERTHA was back in Leipzig (see Section 5.4.2). Because the depolarization ratio measurements were performed with a provisional setup, the confidence in the findings of the 710–nm depolarization ratio during SAMUM–1 is rather low. Measurements for pure dust during SAMUM–2b at Cape Verde revealed that the dust depolarization ratio of 0.37±0.07 at 710 nm is slightly larger than at 532 nm (see Section 6.3.3).

In a recent paper, Sakai et al. (2010) discuss laboratory measurements of the particle depolarization ratio of Saharan and Asian dust at 532 nm. Such validation measure-

ments under controlled laboratory conditions are scarce. The authors find values of 0.39±0.05 at 532 nm for samples of Saharan and Asian dust. These values are slightly larger than the ones found during SAMUM–1. Sakai et al. (2010) claim that this is probably because of an underestimation of sub–micrometer particles that are inherently present in the atmosphere (and could not be reproduced from the dust sample). Convective plumes observed during SAMUM–1 showed increased depolarization ratios compared to the background of the well–mixed dust layer (Ansmann et al. 2009a). Such dust devils facilitate the mobilization and transport of giant particles with diameters larger than 60 μm.

The discussion of the dust lidar ratio and depolarization ratio will be continued in Section 6.3.3 and Chapter 7. These sections also discuss the high level of consistency of the results of the different SAMUM campaigns. From this it can be assumed that the optical properties inferred from the measurements in Morocco are trustworthy to properly represent the behavior of mineral (Saharan) dust.

What are the future implications of the findings of SAMUM–1? First of all, a guideline is given for the analysis of lidar measurements of mineral dust according to Klett's method (see Section 3.3.1). The dust lidar ratio of 55 sr at 355 and 532 nm should be used, if elevated layers can be unambiguously identified as pure dust layers. Second and more important (because it also is of interest for scientists outside of the lidar community) is the fact that with the lidar–relevant intensive dust parameters measured during SAMUM–1 thorough evaluations of dust models become possible. Such models are used to compute dust optical properties as a function of size distribution, particle morphology, and chemical composition (index of refraction). In the past, discrepancies between observations and model results were usually related to the possible influence of long–range transport and aging effects, i.e., of mixing, transformation, and/or removal processes, which can be used to legitimate a variety of solutions. Because the observations of SAMUM–1 were performed under pure dust conditions, differences between the observation and the model result can be assumed to originate from an inappropriate description of light scattering by the respective dust model.

Compared with an older study of the optical properties of Saharan dust (Müller et al. 2003), the non–spherical AERONET model presented in Dubovik et al. (2006) allows for a much better estimation of the dust lidar ratio. For several AERONET observations between 0630–0830 UTC on 19 May 2006, the calculations result in lidar ratios of 70–80 (440 nm), 70–75 (500 nm) and 55–70 sr (670, 870, and 1020 nm). Results of AERONET observations during SAMUM–1 and comparisons to coincident *in situ* and remote–sensing measurements are given by Müller et al. (2010a, b).

In the study of Wiegner et al. (2009), the non–spherical particle model developed in the framework of SAMUM produces a pronounced decrease of the lidar ratio with wavelength. Lidar ratios at 355 nm are almost twice as large as at 532 nm. At 1064 nm they are lower by a factor of about 1.5 compared to the value at 532 nm. Gasteiger et al. (2011) continued this work by introducing strongly irregularly shaped particles and agglomerates with a size parameter $x = 2\pi r/\lambda$ of up to 20.8 to the model. From intensive simulation studies, Gasteiger et al. (2011) draw several conclusions. First, a

mixture of absorbing and non–absorbing particles is necessary to reproduce a realistic wavelength dependence of the dust lidar ratio. Second, the influence of large particles dominates the dust depolarization ratio and values of this parameter are generally larger for irregularly shaped particles compared to spheroids. Third, the number of particles with small aspect ratios should be small to reproduce values in the range of the lidar measurements. And fourth, the variation of the complex refractive index shows the strongest effect on the calculated parameters. The last point clarifies that mineralogical inhomogeneities are hard to capture by a dust model. By comparing the results of simulations with different particle mixtures to the observations of SAMUM–1 and SAMUM–2a, Gasteiger et al. (2011) show that particle mixtures which reproduce the lidar measurements of one case usually fail for the next measurement case. Thus even though impressive progress was made with the help of the SAMUM–1 observations, the most challenging task for the future might be to find one or a few generalized particle mixtures which are able to reproduce actual measurements. Such dust models then need to be implemented in algorithms for the retrieval of aerosol optical properties from satellite measurements (e.g., MODIS, MISR, or CALIPSO) which also have to account for particle non–sphericity when dealing with mineral dust.

6.2 SAMUM–2a

The winter campaign of SAMUM–2, which (in this work) is referred to as SAMUM–2a, was performed from 15 January to 14 February 2008 at the airport of Praia, Cape Verde (see Section 2.4). Nearly the same instrumental setup as during SAMUM–1 was used for these investigations. As during SAMUM–1 in Morocco, lidar measurements were performed around noon and after sunset and accompanied by radiosonde ascends. Additional measurements were conducted when the CALIPSO satellite passed the ground site at a distance of less than 500 km. These measurements allow for a validation of the data products of the CALIPSO lidar with that of ground–based instruments.

This section presents an extensive case study of 31 January 2008 that includes the aerosol–type separation of Section 4.2 and successive inversion of the retrieved optical data sets to derive microphysical particle properties of biomass–burning smoke over Cape Verde. As before, the statistical results and general findings of the lidar observations are discussed at the end of this section. In addition, an overview of the results of the aerosol–type separation and the optical and microphysical properties of biomass–burning smoke over Cape Verde is given. Further SAMUM–2 case studies with BERTHA are discussed in Tesche et al. (2009a, 2011a, b). Results of measurements with BERTHA during SAMUM–2a can also be found in Ansmann et al. (2009b, c, 2011), Groß et al. (2011a, b), and Heinold et al. (2011a).

6.2.1 Overview

At Cape Verde, winter dust conditions are closely related to the movement and intensity of mid–latitude high–pressure systems and the associated strong pressure gradients at their southern flanks. This configuration causes dust emissions over Mauritania, Mali, and Niger followed by westward transport to Cape Verde within 1–5 days. In the meteorological overview of SAMUM–2a, Knippertz et al. (2011) identified three distinct dust periods and a phase in the end of the campaign during which pure dust layers were absent. During the first days of SAMUM–2a dust was emitted in Mauritania and neighboring countries and advected to Cape Verde within 1–3 days. Later in the campaign, more intense high–pressure systems over northern Algeria and France caused widespread dust emissions from multiple sources in Mali, Mauritania, Niger, and from the Bodélé Depression in Chad (see Figure 2.1). Transport of dust from these remote sources to Cape Verde typically takes 3–5 days. Around 3 February 2008 the subtropical high over northern Africa diminished and stayed fairly weak until the end of the campaign. This was the period when no more layers of pure dust were observed. On 9 February 2008 a cyclonic disturbance spread to the subtropical eastern Atlantic from mid–latitudes and caused westerly to northwesterly flow throughout the entire atmospheric column. During this day, clean maritime conditions with a purely maritime boundary layer prevailed at the measurement site (Groß et al. 2011a).

Figure 6.11 gives an overview of the AOT at 500 nm (red dots) and Ångström exponents for the wavelength pair 440/870 nm (white dots) measured with SSARA and

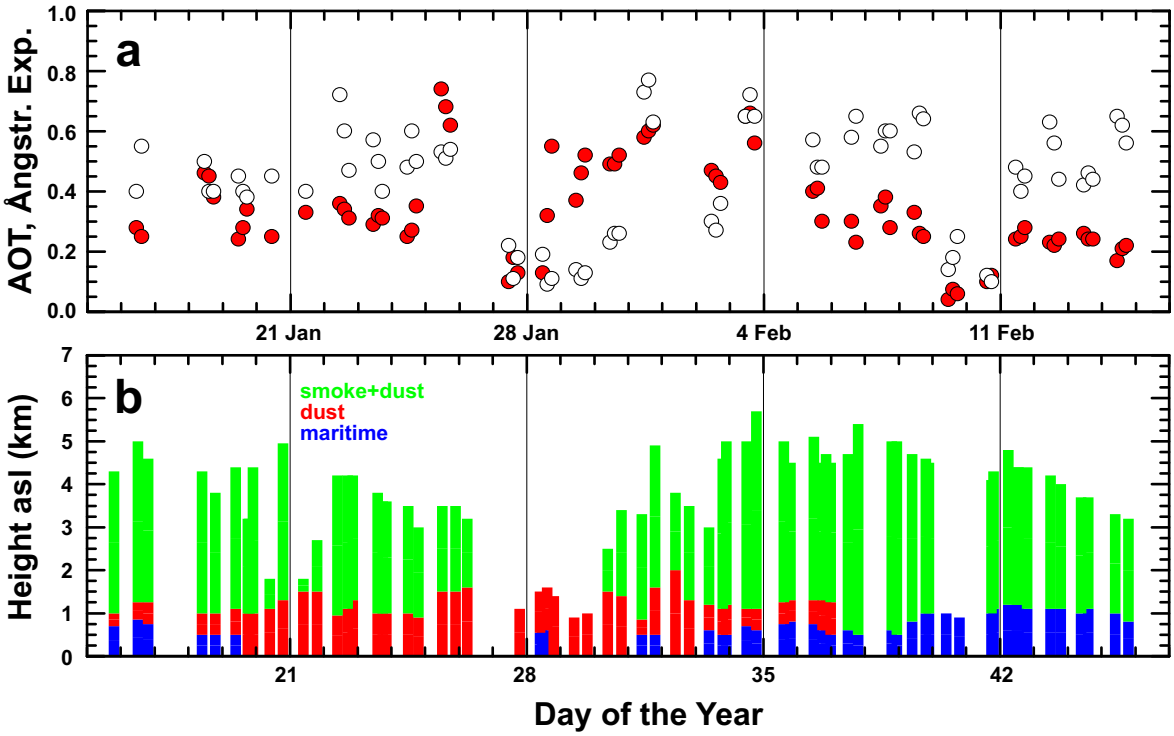

Figure 6.11: (a) One–month AERONET/SSARA Sun photometer observations (15 January–14 February 2008) of 500–nm AOT (red dots) and 440/870–nm Ångström exponents (white dots). (b) Vertical extent of the aerosol layers as observed with lidar. Different aerosol types are inferred from BERTHA measurements of the linear volume depolarization ratio at 710 nm: maritime (blue, $\delta^{v} \approx 0$), mineral dust (red, $\delta^{v} > 0.25$), and a mixture of mineral dust and biomass–burning smoke (green, $\delta^{v} \approx 0.1$–0.2).

the AERONET instrument (Toledano et al. 2011) as well as of the vertical extent of the observed aerosol layers as inferred from BERTHA measurements. Compared to the homogeneous, pure dust layers observed during SAMUM–1 in Morocco where the top of the dust layer could be retrieved from the display of the range–corrected signal (see Figures 6.3 and 6.6), complex aerosol stratification was observed during SAMUM–2a. The time–height displays of the linear volume depolarization ratio at 710 nm were used to identify layers of maritime aerosol ($\delta^{v} \approx 0$), mineral dust ($\delta^{v} > 0.25$), and a dust/smoke mixture ($\delta^{v} \approx 0.1$–0.2). Usually a maritime boundary layer was observed in the lowermost 0.4–1.0 km of the atmospheric column. During most days of SAMUM–2a, a mineral dust layer was present above the maritime boundary layer (or from the surface, if no maritime layer was present) to a height of 1.5 km asl. As shown for the SAMUM–1 measurements in Section 6.1, mineral dust layers can easily be distinguished in the lidar measurements by high values of the linear particle depolarization ratio. During most of the time a mixed layer of mineral dust from northern Africa and biomass–burning smoke from southern West Africa was observed above the mineral dust layer (see Section 2.3 and Tesche et al. 2009a, 2011a). From Figure 6.11 five different combinations of aerosol stratification can be distinguished for the time period of SAMUM–2a: (1) maritime+dust+smoke/dust on 10 days, (2) dust+smoke/dust on

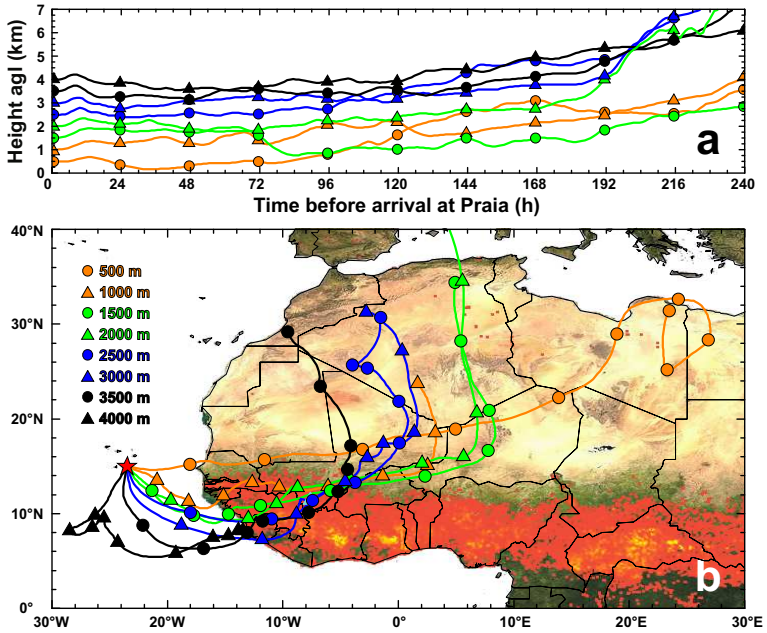

Figure 6.12: Ten–day HYSPLIT backward trajectories ending over Praia at 2200 UTC on 31 January 2008. The underlying MODIS fire map shows all locations of fires (red area) detected within the 10–day period from 21 to 30 January 2008.

10 days, (3) pure dust on 27–29 January 2008, (4) maritime+smoke/dust on 8 days, and (5) purely maritime on 9 February 2008.

6.2.2 Measurement Case: 31 January 2008

This section presents the results of the measurements that were performed on 31 January 2008. The chosen day is representative for the aerosol conditions encountered during SAMUM–2a and is used to give an overview of the observations performed at Praia airport. Furthermore, the high AOT of 0.6 at 532 nm and the high depth of the aerosol layer of 5 km during the evening measurement provide favorable conditions for an application of the aerosol–type separation which was presented in Section 4.2.

The 10–day HYSPLIT backward trajectories in Figure 6.12 provide information about the possible origin and sources of the African plume that was observed over Praia in the evening of 31 January 2008. As reviewed in Section 2.3, fire sources in southern West Africa are located in a latitudinal band stretching from about 3° N to 13° N during the dry season in northern hemispheric winter (Cooke et al. 1996, Barbosa et al. 1999). As in Figure 2.2, MODIS observations of active fires during the last ten days before 31 January 2008 are indicated as red area in the underlying map of western Africa in Figure 6.12. Backward trajectories at 0.5 and 1.0 km height (orange) indicate transport of pure dust from desert areas north of the belt of strong fire activity to Cape Verde. The backward trajectories that arrive at heights from 1.5–4.0 km (green, blue, and black) crossed areas of intense biomass–burning activity and desert regions about 3–6

days and 6–10 days prior to the arrival at the measurement site, respectively. As a result, the aerosol layer above 1.5 km height asl is expected to consist of a mixture of mineral dust and biomass–burning smoke.

As for the SAMUM–1 case studies, an overview of the measurements on 31 January 2008 is provided before these will be discussed in detail. The Sun photometer, lidar, and radiosonde observations presented in Figure 6.13 show a complex stratification of dust and smoke over Cape Verde. These conditions are representative of most observations during SAMUM–2a (see Section 6.2.1). Ångström exponents between 0.6 and 0.8 represent neither pure dust conditions (see Section 6.1) nor a dominance of small smoke aerosol particles. The latter would result in Ångström exponents above unity (see Section 4.1 and Eck et al. 1999). The 500–nm optical depth was 0.6 and stayed constant throughout the entire day as is indicated by similar values obtained from the lidar observations after sunset. This is somewhat surprising because the lidar observations during noon and in the evening look rather different. The depth of the total aerosol layer increased from 3 km to almost 5 km. The plot of the depolarization ratio (Figure 6.13e) also reveals that the dust layer was much deeper (1.5 km) in the evening compared to the daytime observation (0.8 km). However, the general structure of the aerosol layer remains unchanged in the time–height display of the 710–nm volume depolarization ratio: a two–layer system which is made up of a pure dust layer (green) close to the surface and a lofted mixed dust/smoke layer (blue). Note that the appropriate height of the boundary between the two layers cannot be extracted from the plot of the range–corrected signal (Figure 6.13c). In there, the transition from red to green suggests that the layer boundary is located at about 2 km height.

The profiles of humidity and temperature of the evening radiosonde launched at 2123 UTC (Figure 6.13b) indicate a shallow maritime boundary layer up to 350 m, a dry, almost well–mixed Saharan dust layer between 0.4 and 1.4 km, and a lofted aerosol layer with enhanced and varying relative humidity above 1.5 km height. According to the profiles of relative humidity and virtual potential temperature the lofted layer can be separated into two layers (1.5–3.4 and 3.4–5.0 km height). Thin cumulus clouds developed above 4.6 km after 2230 UTC. Thus swollen aerosol particles are expected to be present at the top of the moist aerosol layer above 3.8 km height. The RS80 radiosonde launched during the evening measurement is not capable of wind measurements. The wind profiles shown in Figure 6.13d were taken from the morning sonde launched at 1110 UTC. Northeasterly, southerly, and southwesterly winds prevailed in the dust layer and in the lower and upper parts of the lofted aerosol layer, respectively, on 31 January 2008. This observation is in agreement with the backward trajectories shown in Figure 6.12. Wind speed was 5–10 m/s and 5–15 m/s below and above 1.5 km height, respectively.

To extract all the information collected with the three ground–based lidar systems and to get profiles as close to the surface as possible, measurements of BERTHA, MULIS, and POLIS were combined in the way shown for 31 January 2008 in Figure 6.14. MULIS and POLIS cover the overlap range of BERTHA. Together, the three instruments measured the linear particle depolarization ratio at three different wavelengths.

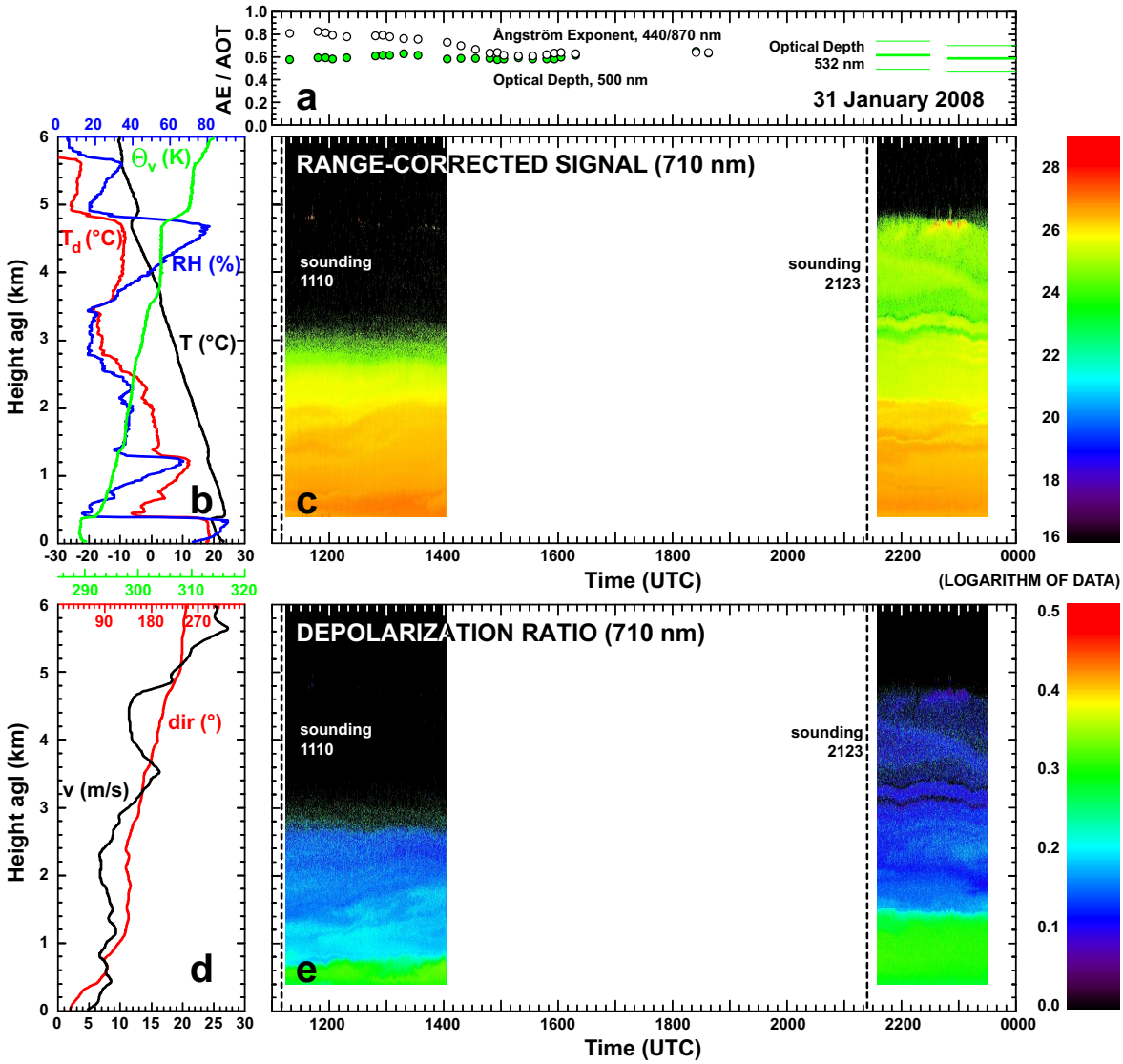

Figure 6.13: Same as Figure 6.3 but for the measurements on 31 January 2008 at Cape Verde. The meteorological profiles in (b) show the measurements of the evening sonde launched at 2123 UTC. Because this RS80 sonde is not capable of wind measurements, the profiles in (d) are taken from the morning sonde launched at 1110 UTC.

Furthermore, the quality of the results of the lidar systems was assured by repeated comparisons. The error bars of the measurements with BERTHA are discussed in the Appendix. The ones shown for the measurements with MULIS and POLIS are discussed in Freudenthaler et al. (2009) and Groß et al. (2011a). They were provided by the colleagues from Munich.

BERTHA backscatter coefficients (unsmoothed below 2.4 km height, 300 m smoothing length above) at 355 nm (dark blue), 532 nm (dark green), and 1064 nm (red) were combined with MULIS 532–nm profiles (light green, 82.5 m smoothing length, until 2 km height) and POLIS 355–nm profiles (light blue, 82.5 m smoothing length, until 2 km height). The combination was performed in a height range (1.4–2.0 km asl) of

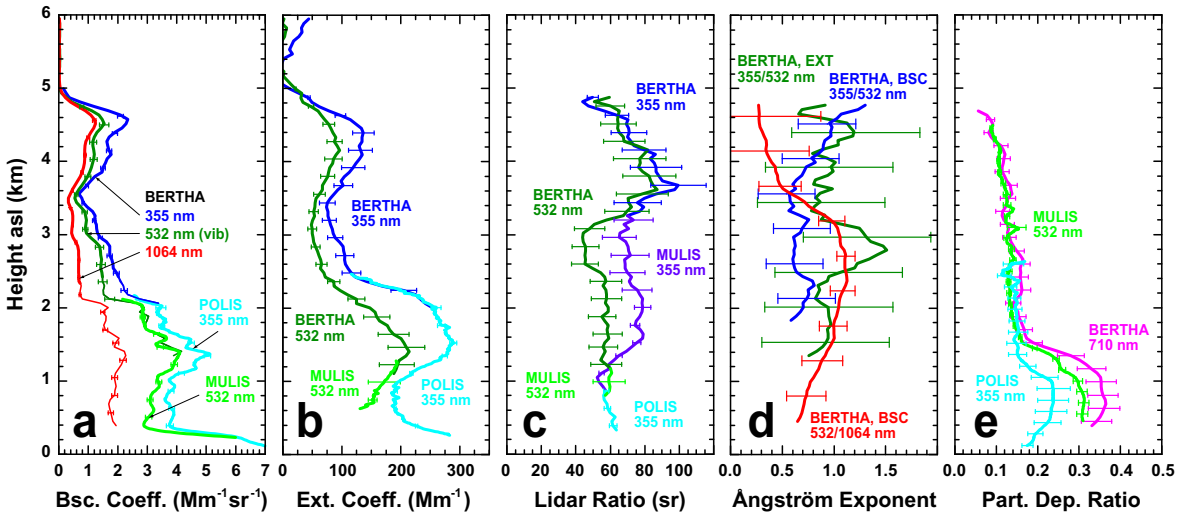

Figure 6.14: Evening measurement of 31 January 2008. Profiles of backscatter coefficients (a), extinction coefficients (b), lidar ratios (c), Ångström exponents (d), and linear depolarization ratios (e) are combined from measurements with BERTHA (2132–2232 UTC), MULIS (2015–2215 UTC), and POLIS (2015–2215 UTC). Colors indicate measurements of the different instruments at different wavelengths. Light blue: POLIS measurements of β, α, S, and δ^{p} at 355 nm. Dark blue: BERTHA measurements of β, α, and S at 355 nm as well as of $\mathring{a}^{\beta}_{355/532}$. Violet: MULIS measurements of S at 355 nm. Light green: MULIS measurements of β, α, S, and δ^{p} at 532 nm. Dark green: BERTHA measurements of β, α, and S at 532 nm as well as of $\mathring{a}^{\alpha}_{355/532}$. Magenta: BERTHA measurements of δ^{p} at 710 nm. Red: BERTHA measurements of β at 1064 nm and of $\mathring{a}^{\beta}_{532/1064}$.

trustworthy results of all lidar systems. The combined extinction profiles were derived in the same manner. BERTHA profiles at 355 nm (dark blue, 2.0–6.0 km height) and 532 nm (dark green, 1.2–6.0 km height) were smoothed with a window length of 300 m. Measurements with POLIS (355 nm, light blue, 0.2–2.4 km height) and MULIS (532 nm, light green, 0.6–1.2 km height) were smoothed with a window length of 82.5 m. The combined profiles of the lidar ratio were also obtained by using the results of the measurements of the individual systems. Ångström exponents calculated from the combined profiles in Figure 6.14a and b are found to be very noisy. Therefore, Figure 6.14d shows profiles derived from backscatter and extinction measurements with BERTHA that are smoothed with a window length of 660 m. The linear particle depolarization ratio profiles were obtained with POLIS (355 nm, light blue), MULIS (532 nm, light green), and BERTHA (710 nm, magenta). They are only slightly smoothed with vertical windows of 82.5 m (MULIS and POLIS) and 150 m (BERTHA). The profile of the particle depolarization ratio clearly separates the dust layer below 1.5 km from the mixed dust/smoke layer between 1.5 and 4.5 km height asl. In the dust layer values of 0.24, 0.30, and 0.35 were observed at 355, 532, and 710 nm, respectively. The values of 0.3 at 532 nm are in good agreement with the dust depolarization ratio of 0.31±0.03 observed during SAMUM–1 (Freudenthaler et al. 2009). As for SAMUM–1, an increase of the particle depolarization ratio with wavelength was found in the dust layer.

This effect can be reproduced in the modeling study by Gasteiger et al. (2011). A discussion of the results presented in this study is given in Section 6.1.4 and Chapter 7. Similarly high dust depolarization ratios (also with a wavelength dependence) were observed during SAMUM–2b (see Section 6.3). In the mixed dust/smoke layer, the particle depolarization ratio dropped to values of 0.12–0.16 for all three wavelengths. This wavelength independence in the mixed dust/smoke layer was found for most of the SAMUM–2a observations at 355, 532, and 710 nm (Groß et al. 2011a).

Figure 6.14 shows the highest backscatter ($5\,Mm^{-1}sr^{-1}$ at 355 nm and $4\,Mm^{-1}sr^{-1}$ at 532 nm) and extinction coefficients ($300\,Mm^{-1}$ at 355 nm and $200\,Mm^{-1}$ at 532 nm) at 1.0–2.0 km height, right were the transition between the pure dust layer and the mixed dust/smoke layer occurs. A second peak with half the value of the first one is visible at 4.5 km height. In the dust layer lidar ratios of 50–60 sr at 355 and 532 nm were similar to the observations of SAMUM–1 (see Section 6.1.4). With height, the lidar ratios increased and reached values of up to 80–100 sr within the mixed dust/smoke layer. The Ångström exponents mostly varied around unity. These findings correspond to a considerable contribution of small and absorbing smoke particles to the elevated layer.

To complete this case study, the application of the aerosol–type separation for multiwavelength lidar and high–quality particle depolarization ratio measurements (see Section 4.2) to the final analysis of the evening observations of 31 January 2008 is presented in Figure 6.15. The results obtained from a first analysis of the measurements in the evening of 31 January 2008 can be found in Tesche et al. (2009b). The method to separate the contributions of dust and smoke to the optical properties of the mixed dust/smoke plume could also be applied to six other days of SAMUM–2 (Tesche et al. 2011b). A discussion of the general findings is given in Section 6.2.3.

In contrast to the combined profiles presented in Figure 6.14, only BERTHA profiles (660–m smoothing length) measured between 2133 and 2232 UTC are shown in Figure 6.15a–d. They were used together with MULIS 532–nm depolarization ratio measurements (Figure 6.15e) to retrieve the contribution of dust and smoke to the 532–nm backscatter and extinction coefficients (see Section 4.2). These contributions are shown as solid and dashed lines, respectively, for dust (red) and smoke (green) in Figure 6.15f. Below 1.4 km height dust contributed 70%–100% to the measured total backscatter coefficient. This result agrees with the previous finding that an almost pure and well–mixed Saharan dust layer is present in the lowermost 1.5 km of the atmospheric column. The laser–beam RFOV overlap effect (see Section 5.4.3.1) prohibited a trustworthy retrieval of backscatter coefficients below a height of about 0.5 km on that day. Above 1.5 km height the contribution of dust to the optical properties decreased steadily. In the main part of the aerosol plume, dust contributed about 30%–40% to the measured backscatter and extinction coefficients. At the top of the aerosol layer, this value dropped to 10%. In addition to the lidar measurements, a profile of dust mass concentration as predicted with the Dust REgional Atmospheric Model (DREAM, Nickovic et al. 2001, Pérez et al. 2006a, b, Haustein et al. 2009) for 0000 UTC on 1 February 2008 is shown as blue line in Figure 6.15e. Dust mass concentration was highest within the lowermost kilometer with peak values of $100\,\mu g/m^3$. In the mixed

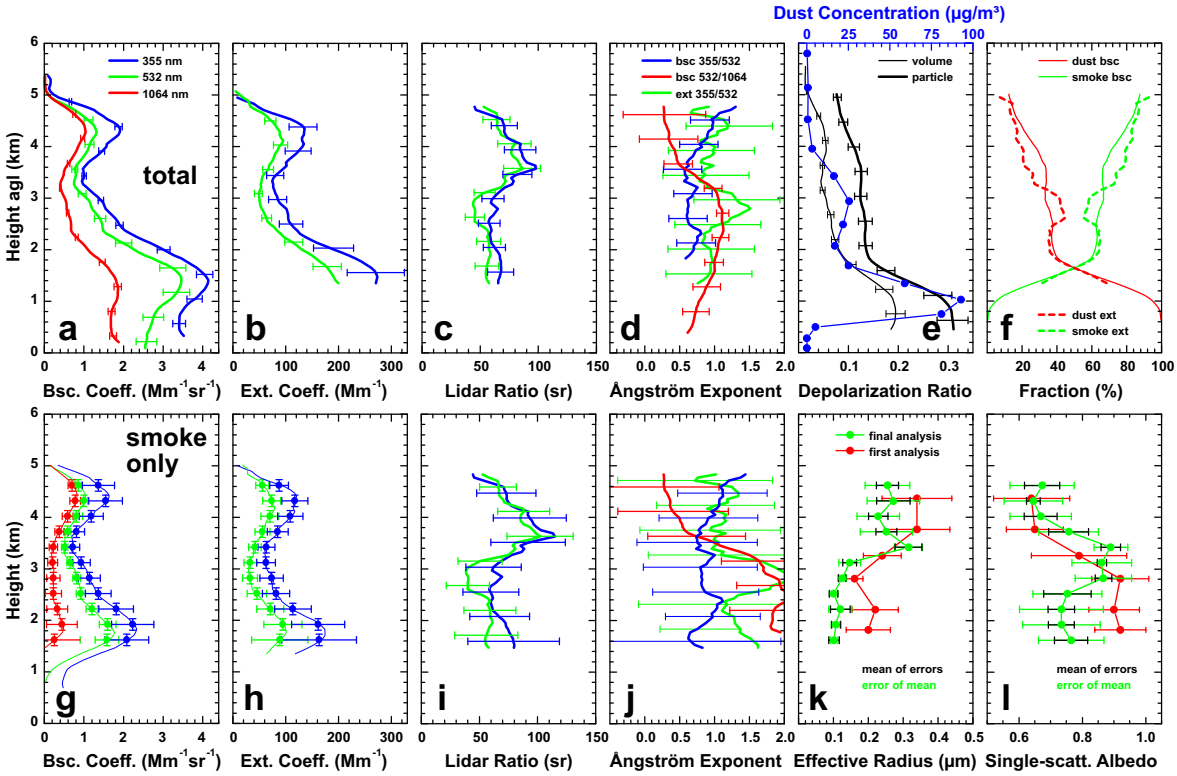

Figure 6.15: Aerosol–type separation applied to the combined measurements of BERTHA (β^{p}, α^{p}, S^{p}, and $\mathring{a}^{\mathrm{p}}$) and MULIS ($\delta^{\mathrm{v}}_{532}$ and $\delta^{\mathrm{p}}_{532}$) at 2133–2232 UTC on 31 January 2008. All profiles are smoothed with a window length of 660 m. The upper panel shows the total (dust+smoke) profiles (a–e), the dust concentration profile as obtained from the DREAM model (blue line in e), and the contributions of dust (red) and smoke (green) to the total backscatter (solid) and extinction (dotted) coefficients (f). The lower panel shows the findings of the separation in terms of profiles of optical properties (g–j), of the effective particle radius (k), and of the 532–nm SSA (l). Red profiles in (k) and (l) refer to the first analysis presented in Tesche et al. (2009a). The green profiles in these plots show the findings of the final analysis with quality–assured input profiles and higher vertical resolution presented in this thesis.

dust/smoke layer, the dust mass concentration was not larger than 25 μg/m^3. It decreased to zero as the contribution of dust to the measured optical properties decreased. Due to the low dust mass concentrations in the lowermost 0.5 km it seems likely that the dust model is able to resolve the maritime boundary layer.

The lower panel of Figure 6.15 shows the optical and microphysical properties retrieved for pure smoke aerosol after aerosol–type separation and subsequent inversion of the obtained optical data set. The smoke backscatter and extinction coefficients were retrieved as described in Section 4.2. Uncertainties in the retrieved backscatter profiles were computed by applying the law of Gaussian error propagation to the retrieval equations. The accuracy in the calculation was checked by means of a sensitivity study in which each of the individual input parameters was varied within the indicated range of values while the other input parameters were set to the climatological mean value.

The error curves in Figure 6.15g include the statistical uncertainty (signal noise) and signal calibration uncertainties in the retrieval of the particle backscatter coefficient of 5%–10%. The relative errors of the dust and smoke backscatter coefficients are about 10%–15% and 20%, respectively. Due to the overlap effect trustworthy particle extinction coefficients could only be determined above 1.5 km height agl. The dust extinction coefficient was determined from the dust backscatter coefficient (multiplied by the dust lidar ratio of 55 sr). Therefore, it is reliable down to heights of about 0.5 km. The backscatter coefficient was calculated from the ratio of the 532–nm signal to the 607–nm Raman signal. In the case of signal ratios the overlap effect widely cancels out (see Section 5.4.3.1). The uncertainty in the calculation of the total and smoke particle extinction coefficient is mainly a function of signal noise (statistical error). The uncertainty in the estimated dust extinction coefficient is about 25% taking the uncertainties in the computation of the dust backscatter coefficient and in the dust lidar ratio (13% uncertainty) into account. Because dust extinction values are on the order of 20±10 Mm^{-1} in the dust/smoke layer above 1.5 km, the influence of uncertainties in the dust extinction estimates of about 5 Mm^{-1} are of minor importance in the estimation of the smoke extinction profile. The relative error of the smoke extinction coefficient ranges from 20% to 40% within the lofted layer. A detailed description of the individual errors and error sources can be found in the Appendix.

Smoke extinction values around 80 Mm^{-1} (green profile in Figure 6.15h) indicate strong pollution. Heese and Wiegner (2008) measured total particle extinction coefficients of 100–200 Mm^{-1} in western Africa's Sahel region just south of the Saharan desert on 30 January 2006 during the AMMA campaign, when a thick lofted plume (2–5 km height) was advected from areas with strong fire activity in central Africa. During DABEX values of up to 800 Mm^{-1} were measured in aerosol plumes located over fire areas (Johnson et al. 2008b). The lidar ratios and Ångström exponents presented in Figure 6.15i and j, respectively, were derived from the backscatter and extinction coefficients of pure smoke (Figure 6.15g and h). The profiles of the lidar ratios and Ångström exponents also indicate the two–layer structure of the lofted aerosol plume as suggested by the radiosonde profiles of virtual potential temperature and relative humidity in Figure 6.13b. Smoke lidar ratios ranged from 40 to 80 sr in the lower part and from 80 to 100 sr in the upper part of the lofted aerosol layer at both 355 and 532 nm. Ångström exponents computed from the 355–nm and 532–nm backscatter and extinction coefficients were roughly 1.0–2.0 in the lower part and 1.0–1.5 in the upper part of the pollution plume. The backscatter–related Ångström exponents calculated from the 532–nm and 1064–nm backscatter coefficients dropped to low values in the upper layer. This observation indicates the presence of a bimodal aerosol distribution with a significant coarse–mode fraction consisting of swollen aerosol particles or the presence of a few drizzle droplets. Ansmann et al. (2002a) showed that the extinction–related Ångström exponent is equal to the sum of the backscatter–related Ångström exponent and the lidar–ratio–related Ångström exponent (not shown). Thus almost equal backscatter– and extinction–related 355/532–nm Ångström exponents in the upper part of the lofted layer indicate that the wavelength–dependence of the lidar ratio must have been small as it is the case in Figure 6.15i. The only exception is visible in the lowest part of the lofted layer below 3.0 km height.

In the final step of the separation procedure the 3+2 data sets (points in Figure 6.15g and h) for pure biomass–burning smoke were used as input for an inversion algorithm (see Section 4.3). The retrieved profiles of the effective radius and the single–scattering albedo of the smoke particles are shown in Figure 6.15k and l, respectively. The red profiles denote the findings presented in Tesche et al. (2009a). For this first analysis, backscatter and extinction profiles measured with BERTHA were combined with a preliminary 532–nm particle depolarization ratio profile measured with MULIS. A vertical average of 500 m was used to obtain the input data set for the inversion calculations. The green profiles represent the findings of the detailed analysis performed in the framework of this thesis. This final analysis was done with quality–assured MULIS 532–nm particle depolarization ratio profiles and combined profiles of the backscatter and extinction coefficients (see Section 6.2.2). Because the combined profiles of the observations of BERTHA and MULIS/POLIS provide an improved coverage of the lower 2–3 km of the atmospheric column, the biggest differences between the two data sets was found in this height range. The difference at larger heights is covered by the error bars of the retrieval results. Because the second method applies quality–assured input parameters for the aerosol–type separation, it is assumed to result in more reliable profiles of the microphysical particle properties. Furthermore, the input data set for the inversion calculations was obtained for vertical 250–m intervals which provides a better height resolution than the first analysis. The uncertainty of the inversion products considers errors introduced by the inversion procedure itself and up to 20% uncertainty in each of the five optical input parameters (see Section 4.3 for a description of the applied methodology). The results presented in this thesis were obtained from the final analysis. Thus only the respective profiles will be discussed. The effective radius showed a steady increase from 0.1 μm (dry aerosol particles) to 0.25 μm (swollen aerosol particles) with height. The single–scattering albedo was 0.75 in the lower part of the plume, increased to 0.85 (less absorbing particles) right in the center of the plume where the increase in the effective radius was observed, and decreased to values of 0.65 (highly absorbing particles) in the uppermost part of the lofted plume. The latter finding is in agreement with the rather high lidar ratios of 80–100 sr which indicate highly light–absorbing particles. The two layers that are visible in the profiles of backscatter and extinction are also obvious in the profiles of the inversion results.

6.2.3 General Findings and Discussion

As for the SAMUM–1 observations in Morocco (Figure 6.8) mean profiles of the SAMUM–2a measurements with BERTHA were calculated. Figure 6.16 shows backscatter coefficients at 355 nm (a), 532 nm (b), and 1064 nm (c), extinction coefficients at 355 nm (d) and 532 nm (e) as well as the respective lidar ratios (g and h) and backscatter– and extinction–related Ångström exponents (j, k, and l) for the number of measurements given in the figure. Particle depolarization ratios at 532 nm (f) were extrapolated from the measurements performed at 710 nm (i, see Section 5.4.3.3). As in Figure 6.8, the bold and thin black lines denote the mean profile and minimum and maximum values observed during N individual measurements. The gray–shaded

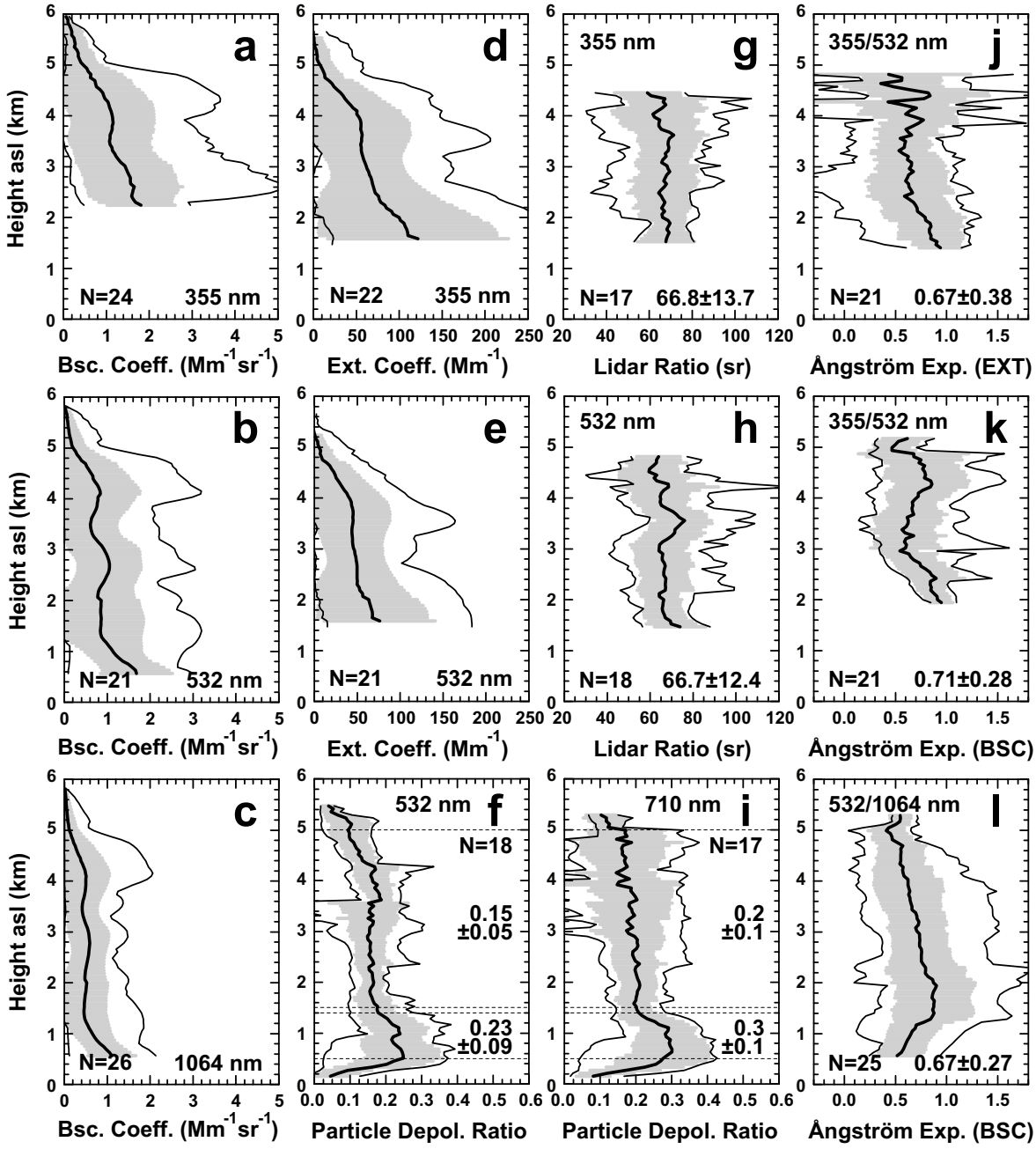

Figure 6.16: Same as Figure 6.8 but for the observations of SAMUM–2a. Mean profiles of the particle depolarization ratio at 532 nm and 710 nm are shown in (f) and (i), respectively.

areas describe the standard deviation of the mean profile. The individual mean values and standard deviations (vertical average) of the mean profiles are given in the respective plots. The standard deviation of the mean value of the mean profile (bold black lines) is smaller than (and not to be confused with) the mean value of the standard deviation of the mean profile (gray–shaded areas). The horizontal lines in the depolarization ratio plots denote the height range of averaging (0.5–1.4 and 1.5–5.0 km

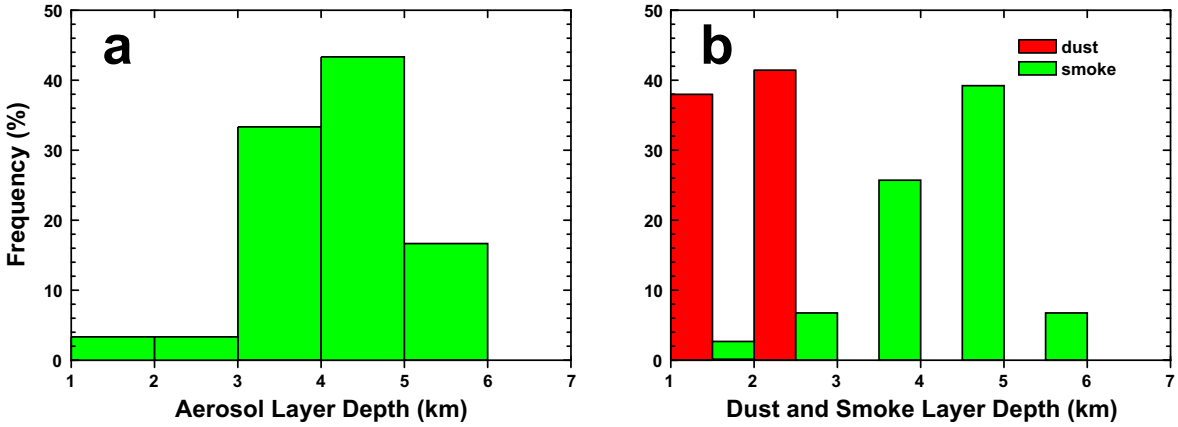

Figure 6.17: Frequency distributions of the depth of (a) the total aerosol layers and (b) the dust and smoke layers as inferred from measurements of the depolarization ratio for 60 individual measurements according to Figure 6.11.

asl). The mean profiles of the backscatter and extinction coefficients illustrate the wavelength dependence of these parameters within the smoke–dominated plume which was usually observed above 1.5 km height. A quantitative measure of the wavelength dependence is given by the respective Ångström exponents which all show mean values of about 0.7±0.4. These values are much larger than the values of 0.1–0.3 observed for pure mineral dust during SAMUM–1 (Figure 6.8j, k, and l). However, they are also lower than typical values for biomass–burning or forest–fire smoke which usually vary between 1.5 and 2.0 (see Section 4.1 or Balis et al. 2003, Campbell et al. 2003, Cattrall et al. 2005, Eck et al. 1999, Müller et al. 2005, Wandinger et al. 2002). The Ångström exponents derived from the column–integrated measurements of the Sun photometer on days during which the elevated dust/smoke layer was present varied between 0.4 and 0.8 (see Figure 6.11a). However, these values include the contribution of the mineral dust layer in the lowermost 1.5 km height.

Lidar–ratio profiles in the height region from 1.5–5.0 km asl showed no wavelength dependence with mean values of 67±14 sr at 355 and 532 nm. The particle depolarization ratios at 532 and 710 nm showed a slight spectral variation with values of 0.15±0.05 and 0.2±0.1, respectively. The latter finding might be due to the averaging process. Groß et al. (2011a) show that in cases when elevated dust/smoke layers were present the particle depolarization ratio within these layers showed values of 0.12–0.16 at 355, 532, and 710 nm. The same was found for the measurement case presented in Section 6.2.2. The linear particle depolarization ratios within the lowermost 1.4 km of the atmospheric column (Figure 6.16f and j) indicate the dominance of mineral dust near the surface. However, mean values of 0.23±0.09 at 532 nm and 0.3±0.1 at 710 nm for the 17 analyzed measurements are too low to represent pure dust conditions. As in the elevated layer, the low values are caused by averaging over the whole measurement period without emphasizing the absence of mineral dust during the last measurement days (see Figure 6.11).

Figure 6.17 gives an overview of the depth of the total (maritime, dust, and smoke)

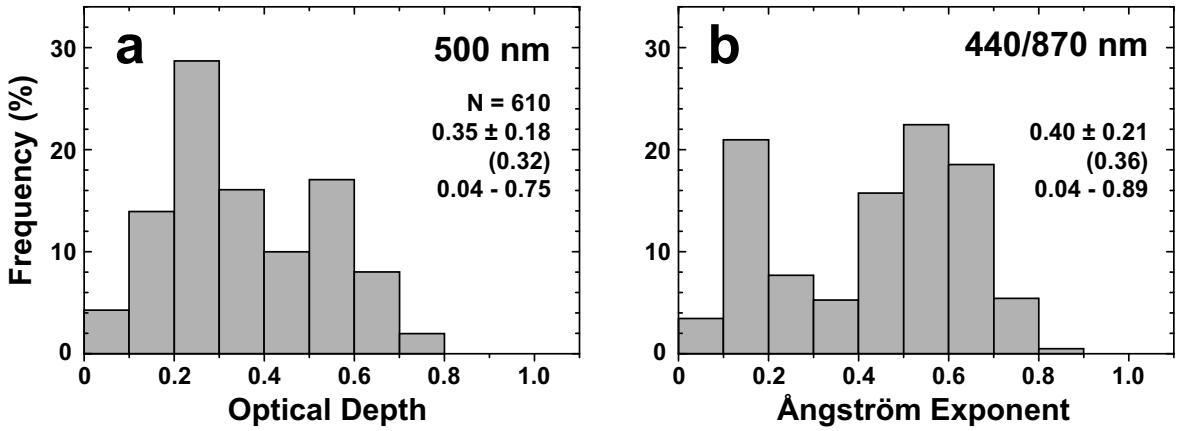

Figure 6.18: Frequency distributions of the 500–nm optical depth and 440/870–nm Ångström exponents measured with Sun photometer during SAMUM–2a. Numbers in the figure denote the mean value with standard deviation, the median, and the range of observed values.

aerosol layer and the individual depths of the dust and mixed dust/smoke layers observed over Praia during SAMUM–2a. As can also be seen in Figure 6.11, rather thin aerosol layers with depths of little larger than 1.0 km (during the period of pure dust around 29 January 2008) were observed as well as layers of up to 6.0 km height. In case of several kilometer deep aerosol layers, the lower part consisted of 1.0–2.0 km deep dust layers (red in Figure 6.17b) which were usually topped by 3.0–6.0 km deep mixed dust/smoke layers. As expected and previously observed, transport of pure mineral dust during winter is restricted to the lowermost 2.0 km of the atmosphere (see Section 2.3).

Figure 6.18 gives a summary of the Sun photometer observations during SAMUM–2a. A mean AOT of 0.35±0.18 was observed at 500 nm. The mean Ångström exponent of 0.40±0.21 can be considered as representative for winter conditions, because the frequency distribution of this parameter shows two distinct modes. The first maximum at 0.1–0.2 represents pure dust conditions (e.g., as on 29 January 2008) while the second maximum at 0.4–0.8 describes the presence of the pure dust layer and an elevated dust/smoke layer which was observed on most days of SAMUM–2a (see Figure 6.11 and Toledano et al. 2011). The latter values are smaller than the ones derived from the lidar measurements presented on Figure 6.16j, k, and l because they incorporate the contribution of the pure dust layer which decreases the total Ångström exponent.

Table 6.1 lists the measurement days of SAMUM–2a which were found suitable for aerosol–type separation and subsequent inversion of the retrieved optical data set for pure biomass–burning smoke (see Section 4.2). The table gives the time range of data analysis and the height range for which 3+2 smoke data sets could be obtained. However, not every inversion led to reasonable results even though the optical input data seemed adequate. For each day the range of results of the effective radius and the SSA as obtained from the inversion of input data sets for a number of 250–m height bins is given. The case study of 31 January 2009 is presented in Section 6.2.2 and

Table 6.1: SAMUM–2a measurements that were chosen for aerosol–type separation and subsequent inversion of the optical data set for biomass–burning smoke.

day of 2008	measurement time (UTC)	number of 250–m bins	height range (m)	range of r_{eff}	range of SSA
22 January	2020–2230	5	1620–2820	0.23–0.29	0.66–0.84
23 January	2040–2240	5	1020–2820	0.16–0.35	0.73–0.86
26 January	0130–0230	5	1620–2820	0.12–0.28	0.68–0.89
31 January	2132–2232	11	1620–4620	0.10–0.32	0.65–0.89
3 February	2038–2220	10	2220–4920	0.16–0.36	0.63–0.85
5 February	2038–2252	5	2820–4020	0.13–0.16	0.73–0.82
6 February	2010–2235	5	3120–4320	0.26–0.35	0.64–0.76

in Tesche et al. (2009a). Further cases of 22 January 2008 and 3 February 2008 are discussed in Tesche et al. (2011b).

Frequency distributions of lidar ratios and Ångström exponents for the measured total aerosol (upper panels) and the pure biomass–burning smoke (lower panels) are shown in Figure 6.19. The histograms contain the optical properties of the 46 height levels (see Table 6.1) which show reasonable input parameters and led to trustworthy inversion results. The mean values of the total lidar ratios and Ångström exponents for the seven days (upper panel) are in agreement with the mean values of SAMUM–2a presented in Figure 6.11. Compared to the values for the total aerosol, mean smoke lidar ratios as retrieved by aerosol–type separation are higher with values of 87±17 sr at 355 nm and 79±17 sr at 532 nm and also show a larger spread of values. From the aerosol–type separation the contribution of mineral dust to the optical properties measured in the elevated dust/smoke layer was estimated to vary between 40% and 60%. If this is considered and the dust lidar ratio of 55 sr at 355 and 532 nm as obtained during SAMUM–1 is assumed (see Section 6.1.4), the lidar ratio of the pure smoke aerosol can be expected to be in the range of 75–85 sr to result in values of 67 sr for the dust/smoke mixture. Previous studies estimated the smoke lidar ratio from long–term AERONET time series (60 sr at 550 nm, Cattrall et al. 2005), from elastic–backscatter lidar measurements during DABEX (70–130 sr at 532 nm, Pelon et al. 2008), and from micro–pulse lidar observations during SAFARI–2000 (50–90 sr at 523 nm, Campbell et al. 2003, McGill et al. 2003). These values were obtained with the help of radiative–transfer calculations or by adjustment of the smoke lidar ratio to retrieve extinction (backscatter × lidar ratio) profiles which were in agreement with optical depth measured with Sun photometer at the surface. In the CALIPSO data retrieval the lidar ratio of biomass–burning smoke is set to 70 sr at 532 nm (Omar et al. 2009). This value was retrieved from simulations with size distributions that are typically derived from the inversion of AERONET measurements of biomass–burning smoke. Direct measurements of pure biomass–burning or forest–fire smoke with Raman lidar are scarce and usually describe situations of long–range transport. Measurements during DABEX (Heese and Wiegner 2008) showed values around 75 sr at 355 nm. Other lidar measurements in Europe resulted in a wide range of values between 40 and 80 sr at 355 and 532 nm (Wandinger et al. 2002) or even found smoke lidar ratios which were restricted

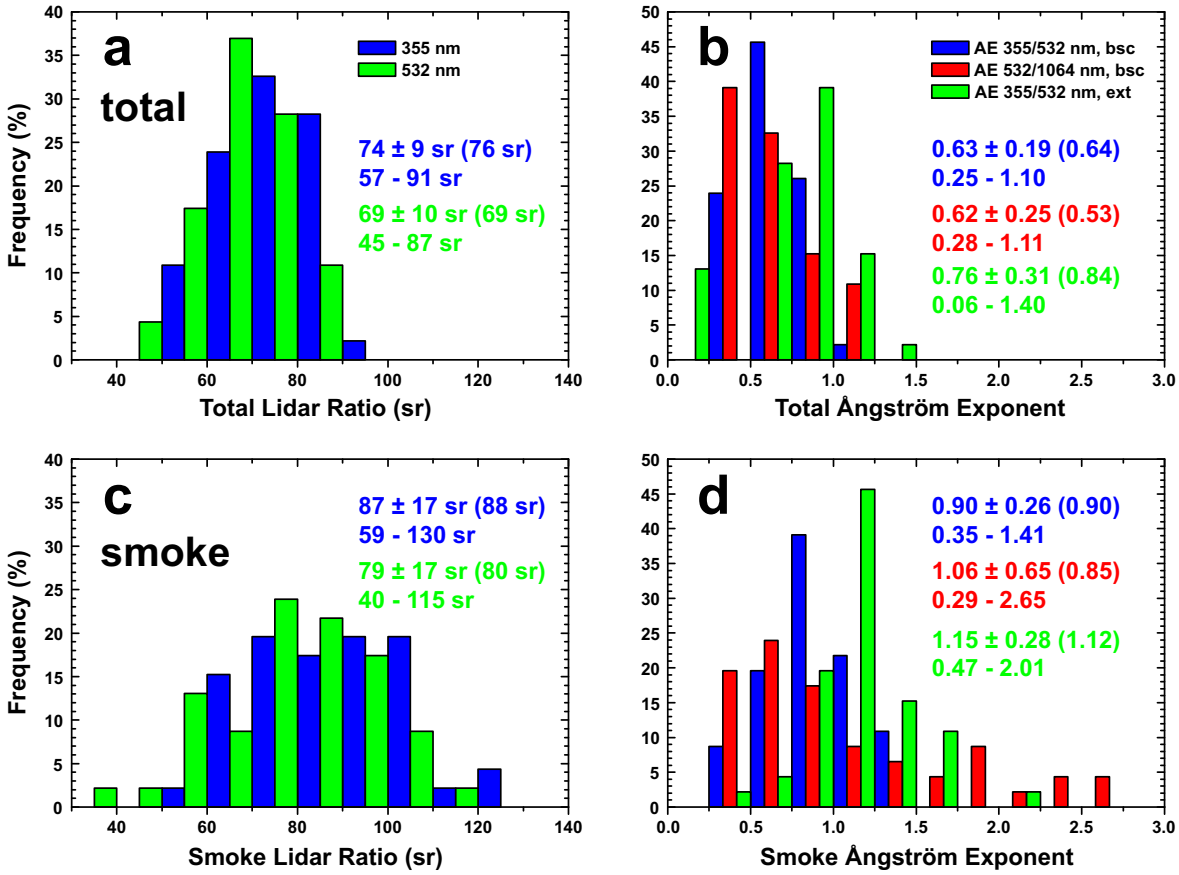

Figure 6.19: Frequency distributions of total (dust+smoke, upper panel) and pure smoke (lower panel) lidar ratios (left) and Ångström exponents (right) for the 46 inversion levels (see Table 6.1). Numbers in the plots indicate the mean value with standard deviation, the median, and the total range of the respective distribution.

to values below 60 sr (Balis et al. 2003, Müller et al. 2005, 2007). Elevated plumes of combustion smoke were observed with Raman lidar at the Maldives during INDOEX. Ansmann et al. (2000) and Franke et al. (2001, 2003) found 532–nm lidar ratios of 60–90 sr within air masses that crossed the central eastern parts of India before being advected to the measurements site. Biofuel combustion (mainly fuelwood) is dominant in this region.

Ångström exponents for pure smoke in Figure 6.19d are in the range of 0.90–1.15. This represents an increase of up to 50% with respect to the values for the dust/smoke mixture. The increase is in agreement with the fact that pure smoke particles are more light absorbing and smaller than mineral dust or a mixture of dust and smoke (Eck et al. 1999). The values also agree with observations during INDOEX that showed Ångström exponents of 0.8–1.4 within pollution plumes from northern India (Franke et al. 2003).

As explained in Section 4.3, the inversion of the optical data set results in the number size distribution and the complex refractive index of the investigated aerosol particle ensemble. These retrieved microphysical particle properties are used to calculate the

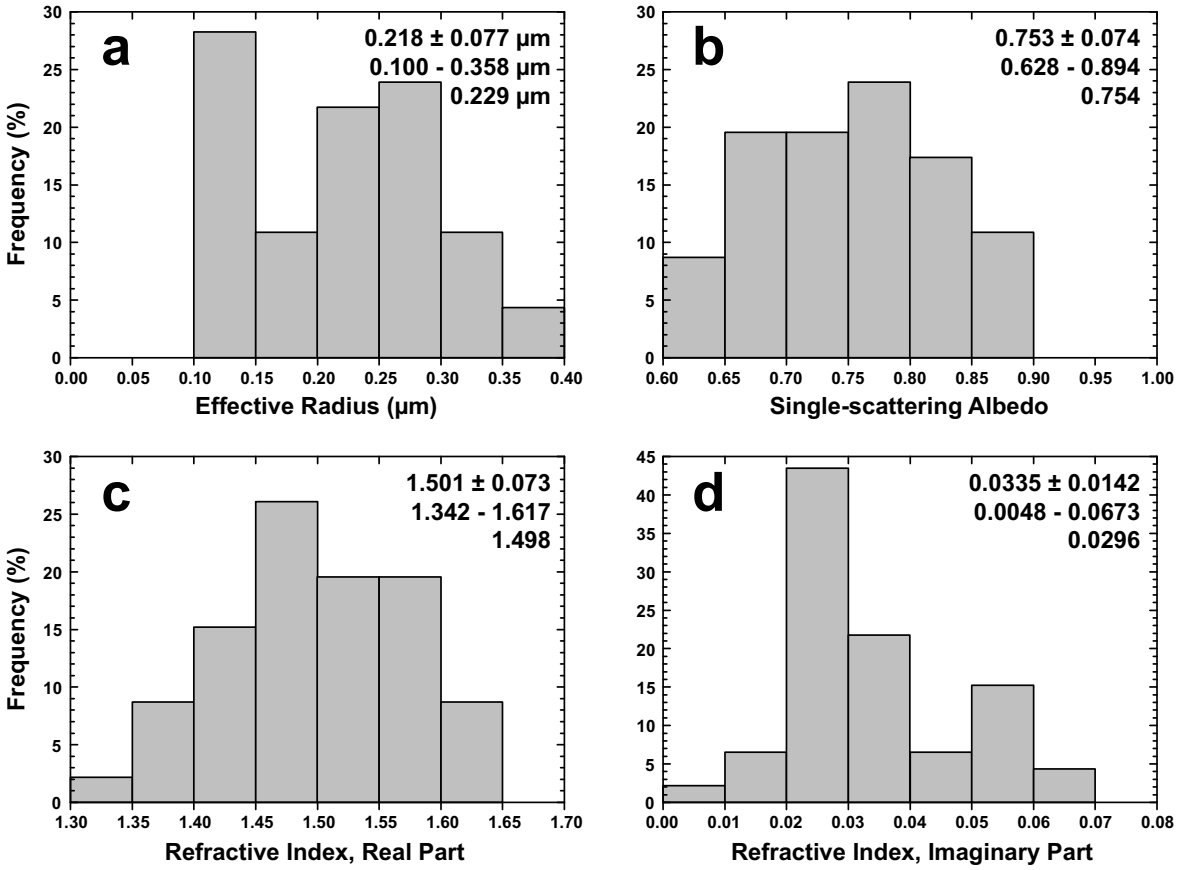

Figure 6.20: Frequency distributions of effective radius (a), single–scattering albedo at 532 nm (b), and real (c) and imaginary (d) part of the refractive index for pure biomass–burning smoke derived from inversion of individual measurements at 46 height levels (see Table 6.1). Numbers in the plots indicate the mean value with standard deviation, the total range of the respective distributions, and the median.

single–scattering albedo of the particles by means of Mie scattering theory. Figure 6.20 shows frequency distributions of the effective radius, the 532–nm single–scattering albedo, and the real and imaginary parts of the refractive index retrieved from the inversion of the 46 optical data sets (height levels, see Table 6.1). Effective radii between 0.10 and 0.36 μm with a mean value of 0.22±0.08 μm were obtained. This range of numbers is in agreement with inversion results of lidar observations of long–range transport of urban haze and biomass–burning aerosol during INDOEX (Ansmann et al. 2000, Müller et al. 2000, 2003), of layers of biomass–burning aerosol during LACE 98 (Wandinger et al. 2002), and of southeast Asian aerosol during PRIDE–PRD (Tesche et al. 2008). These investigations resulted in effective radii between 0.10 and 0.35 μm.

As shown in Figure 6.20b, the 532–nm SSA obtained for pure biomass–burning smoke was found to be 0.75±0.07 with values ranging from 0.63–0.89. Inversions of the lidar observations during INDOEX resulted in 532–nm SSA values between 0.75–0.90. The mean real and imaginary parts of the refractive index were found to be in the range of 1.55–1.68 and 0.02–0.07, respectively, for these cases (Ansmann et al. 2000, Müller et al.

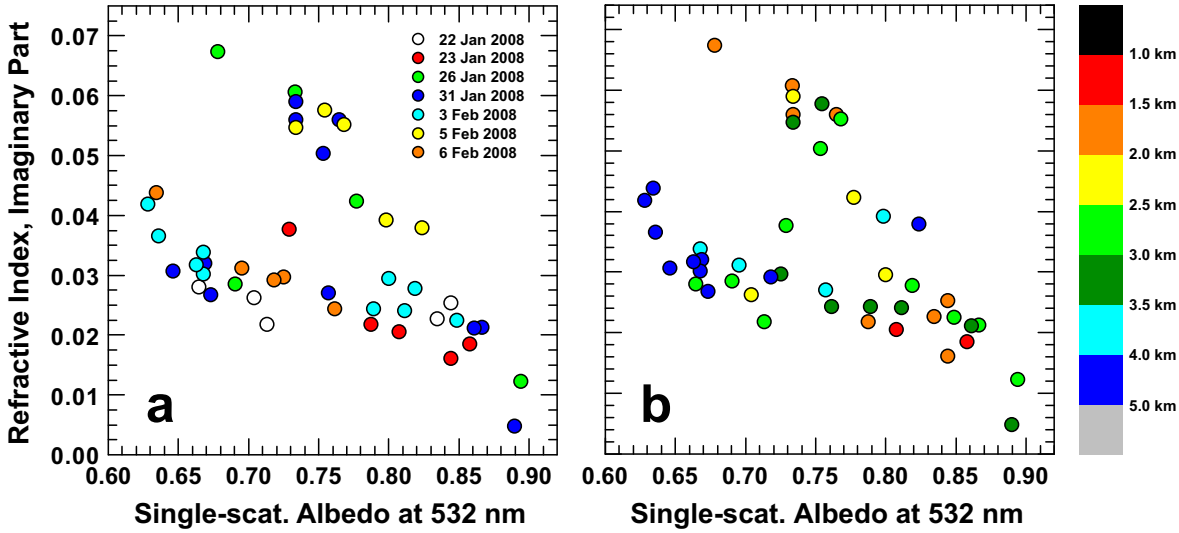

Figure 6.21: Correlation plot between the SSA and the imaginary part of the refractive index color coded according to (a) the measurement day (see Table 6.1) and (b) the height of the measured optical data. Numbers in the plots indicate mean, median, standard deviation, and total range of the respective distribution.

2003). During AMMA, Johnson et al. (2008a) found very low SSA of 0.81±0.05 for aged biomass–burning smoke. However, *in situ* measurements are likely to incorporate fine–mode dust (which would increase the SSA) while coarse–mode smoke particles (which would decrease the SSA) are cut off due to the sampling geometry. These effects could explain the lower SSA found with the lidar–based method for pure smoke aerosol during SAMUM–2a.

Eck et al. (2010) investigated the SSA as derived from Sun photometer observations for three sites in southern West Africa, India, and northeastern China which are regularly exposed to aerosol plumes of mixtures of fine and coarse particles (i.e., combustion and natural aerosol). For the site of Ilorin in Nigeria they found the column–integrated values of SSA to be lowest (with values around 0.8) in cases with a large fine–mode fraction, i.e., a large contribution of the fine mode to the measured total AOT. Biomass–burning aerosols are assumed to constitute the fine mode with radii below 0.6 μm. Toledano et al. (2011) performed a similar investigation based on the Sun photometer observations during SAMUM–2a. They found a decrease of the SSA with increasing fine–mode fraction. For the highest fine–mode fraction of 0.5–0.62 they found 532–nm SSAs below 0.85. However, these values contain the effect of the dust plume in the lowermost kilometer and the (up to 50%) dust mixed with smoke in the elevated layer.

Figure 6.21 shows the correlation of the retrieved values of the SSA and the imaginary part of the refractive index. The color coding refers to (a) the measurement day (see Table 6.1) and (b) the height interval of the respective input data set. The bimodal structure of the correlation can be designated to results of different days. On 22 January 2008, 23 January 2008, 3 February 2008, and 6 February 2008 a low slope (e.g., similar imaginary parts for different SSA) is observed while 26 January 2008

and 5 February 2008 show a high slope (e.g., an increase of the imaginary part with decreasing SSA). The results of 31 January 2008 show an indifferent behavior with values on both branches. Figure 6.21b shows that a stronger increase of the imaginary part with decreasing SSA is found in heights below 2.5 km. The blue dots indicate that generally the SSA seems to be smaller at larger heights.

A review of the intensive optical properties of biomass–burning aerosol as estimated from *in situ* measurements, forward calculations, and inversion studies is presented by Reid et al. (2005). This paper gives *"best estimates for median values of smoke optical properties, knowing full well that each fire has its own character and can deviate significantly from the mean."* The authors present literature values of the SSA (at wavelengths between 450 and 700 nm) in the range of 0.60–0.97 and 0.76–0.93 for fresh and aged smoke, respectively. The only laboratory study reviewed by Reid et al. (2005) is by Patterson and McMahon (1984) and Patterson et al. (1985) who report SSA at 550 nm of 0.74±0.06. These values are in the range of the presented inversion results. Finally, Reid et al. (2005) state that likely values of the single–scattering albedo at 550 nm are in the range of 0.82–0.92 with generally higher values for older smoke plumes. The SSA retrieved from the inversion of optical data for pure biomass–burning smoke vary between 0.63 and 0.89 with a mean value of 0.75±0.07 (see Figure 6.20a). These low values represent highly absorbing aerosols and are in the range of literature values presented by Reid et al. (2005) and references therein.

Reid et al. (2005) also point out that for the usual analysis of *in situ* measurements certain variables need to be varied in a *"reasonable way"* to achieve closure of the respective measurement. Mostly, the complex refractive index is the parameter of choice for this variation. After carefully analyzing the values used in the literature, Reid et al. (2005) state that by assuming an average size distribution for biomass–burning aerosol the complex index of refraction appears to be about 1.50±0.015i. Figures 6.20c and d show the mean value of the real part of the refractive index as retrieved from the inversion calculations to be 1.50±0.07. However, values as high as 1.62 were inferred as well. The retrieved values of the imaginary part of the refractive index show a bimodal distribution with an average of 0.034±0.014 which is larger than the value recommended by Reid et al. (2005). Most values are in the range of 0.02–0.04. This leads to a median value of 0.03 which is slightly smaller than the mean value. The range of values spreads between 0.005 and 0.067.

Heinold et al. (2011b) investigate the radiative feedback of Saharan dust and biomass–burning smoke for the time period of SAMUM–2a. They performed model runs with and without radiative feedback of the different aerosol layers. They find that the Hadley circulation is enhanced and smoke particles are transported more than 5° further north when the smoke radiative feedback is considered. This influence on the atmospheric dynamics is due to a change of the atmospheric heating rates by dust and smoke aerosols. For the simulations, Heinold et al. (2011b) use smoke SSA of 0.52 at 250–700 nm and 0.45 at 700–1530 nm. Such low values represent very fresh smoke from flaming combustion and are much lower than the findings of the inversion runs. Therefore, the authors state that in future model studies the more realistic SSA observed during SAMUM–2a

(e.g., the findings of the microphysical inversion) will need to be used in the model for a better characterization of the absorptive properties of the biomass–burning smoke.

Finally, the findings of the inversion calculations are compared with *in situ* observations performed in the framework of SAMUM–2a. Especially during local flights, similar aerosol conditions are observed by ground–based lidar and airborne *in situ* instruments. The comparison of these measurements comprise the essence of every closure study. Only if the optical properties derived from the *in situ* instruments are in agreement with the measured ones and (acceptable) closure is achieved, one can consider the radiative effects of the investigated aerosol as reproduced.

For three local flights in the vicinity of Cape Verde during SAMUM–2a on 25 January 2008, 4 February 2008, and 5 February 2008 Lieke et al. (2011) present height– and size–resolved observations of particle chemical properties. As can be seen in Figure 6 of Lieke et al. (2011), smoke–dominated layers can easily be identified by the large contribution of soot to the total mass of particles with aerodynamic diameters smaller than 0.5 μm. 80% to 95% of the particles with $d < 0.5\,\mu$m found at 2.0 and 3.3 km height on 25 January 2008, at 1.3 and 1.8 km height on 4 February 2008, and at 2.2 km height on 5 February 2008 were soot particles. No significant contribution of soot to the total aerosol mass for particles larger than a diameter of 0.5 μm was found for these layers. These observations confirm findings of this thesis: smoke occurs externally mixed with mineral dust in elevated layers and consists of rather small particles (larger particles are mineral dust). The same conclusion was drawn by Eck et al. (2010).

During SAMUM–2a spectrally resolved measurements of the SSA and the imaginary part of the refractive index were performed at ground level with a spectral optical absorption photometer (Müller et al. 2011). These observations were grouped to represent different aerosol conditions. Highest SSAs of 0.98–0.99 at 555 nm were measured during a period of pure maritime aerosol at Praia on 9–11 February 2008 (see Knippertz et al. 2011, Groß et al. 2011b). The SSA decreased to 0.92–0.95 during dust–dominated days and showed lowest values of 0.80–0.92 when, as the authors claim, smoke might have reached down to the surface between 6 and 9 February 2008. Downward mixing as described by Engelmann et al. (2011) may have caused the episodically occurring high smoke concentrations at ground level. The imaginary part of the refractive index was found to be 0.009 during this last period. Note that the *in situ* measurements of Müller et al. (2011) were performed 4 m above ground level. Even if smoke was mixed down to the surface, it might have occurred only in traces and mixed with dust or maritime aerosol. This fact might explain the lower values of the SSA and higher values of the imaginary part of the refractive index presented in Figure 6.20. From the inversion of the pure smoke data set a mean smoke SSA of 0.75 at 532 nm and a mean imaginary part of the refractive index of 0.034 were inferred. However, most of the retrieved values of the imaginary part of the refractive index were between 0.02 and 0.03.

Results of the single–particle analysis of size–resolved aerosol sampling are presented by Kandler et al. (2011). They mostly found real parts of the refractive index of 1.55–1.58 at 532 nm. Imaginary parts of particles with diameters smaller than 0.5 μm were found to be as high as 0.02 while they did not exceed values of 0.009 for larger particles.

Airborne *in situ* measurements of the particle size distribution during Falcon flights are presented by Petzold et al. (2011) and Weinzierl et al. (2011). For local flights on 22 and 23 January and 5 and 6 February 2008, the analysis of the measurements of the *in situ* instruments aboard the Falcon revealed SSA of 0.741–0.958 at 530 nm with a mean value of 0.812±0.048 (Andreas Veira, personal communication). The real part of the refractive index was found to be fixed at 1.561 while the imaginary part varied between 0.003 to 0.057 with a mean value of 0.033±0.012. Effective radii calculated from that part of the *in situ* size distributions which is assumed to be constituted by smoke particles were 0.47±0.21 μm on these days (Bernadett Weinzierl, personal communication). Note that no separation of the contributions of mineral dust and biomass–burning smoke to the total size distribution is possible for the *in situ* measurements. The general approach is to assume that mineral dust comprises the coarse mode of the size distribution while smoke particles constitute the smaller fine and accumulation modes. Even though small dust particles might be included in the retrieval of the complex refractive index and the SSA, the findings inferred from the *in situ* observations are in surprisingly good agreement with the inversion results (see Table 6.1). However, the latter show a much larger spread of the derived values. The larger smoke effective radius obtained from the *in situ* measurements is most probably caused by the influence of small mineral dust particles in the size range which is assumed to represent biomass–burning smoke. The artificially introduced cut in the size distribution (with smoke at smaller radii and dust at larger radii) does not consider the effect of small dust particles or large smoke particles in the respective opposite size ranges.

6.3 SAMUM–2b

From 24 May to 17 June 2008 additional lidar measurements with BERTHA were performed at Praia, Cape Verde (see Section 2.3). As during the previous SAMUM campaigns lidar measurements were accompanied by radiosonde ascends and Sun photometer observations (with the SP1A instrument only). These observations allowed for a comparison of winter and summer conditions at Cape Verde and of dust properties observed near the source regions during SAMUM–1 and in the beginning of long–range transport during SAMUM–2.

During the summer measurements the 532–nm rotational–Raman channels of BERTHA were operational and allowed for a retrieval of backscatter and extinction coefficients with the Raman method during daytime (see Section 5.4). Furthermore, the 532–nm volume depolarization ratio profile estimated from the measurements at 710 nm could be verified by comparing the corrected 532–nm backscatter profile to the results of the rotational–Raman channels (see Section 5.4.3.2). The PMT of the 1064–nm channel broke during the first days of the summer measurements and could only be replaced towards the end of the campaign. Thus this channel was operational only for few measurements which results in bad statistics of the 1064–nm backscatter coefficient and the 532/1064–nm backscatter–related Ångström exponent shown later in this section.

The arrival of the elevated dust layer in the night from 3–4 June 2008 as observed with BERTHA is presented as case study for the conditions during SAMUM–2b before general findings are discussed. Tesche et al. (2011a) present another SAMUM–2b case study of the evening measurement of 14 June 2008.

6.3.1 Overview

Before the case study is discussed a brief overview of the meteorological conditions during SAMUM–2b is provided. The advection of mineral dust to the measurement site at the Cape Verde islands during summer strongly depends on the occurrence of a local surface low over southern Mauritania which increases the pressure gradient between the African heat low and the Azores high. This frontier stretches over the tropical North Atlantic. Its location varies with the position of the Azores high. During the larger part of SAMUM–2b slow wind speed and low pressure gradients prevailed. Maritime aerosol was advected to the measurement site from northerly direction within the boundary layer. The main dust plume was located south of Cape Verde which led to comparably low dust optical depths at the measurement site. During the periods of high optical depth an undisturbed easterly flow with strong upper–level wind speeds transported mineral dust from the northern African source regions to the tropical north Atlantic. This configuration represents the classical air flow pattern for Saharan air plumes as described by Karyampudi et al. (1999).

Figure 6.22 gives an overview of the aerosol stratification observed during SAMUM–2b. Usually a 0.5–1.0 km deep maritime boundary layer (blue bars) topped by a 4–5 km

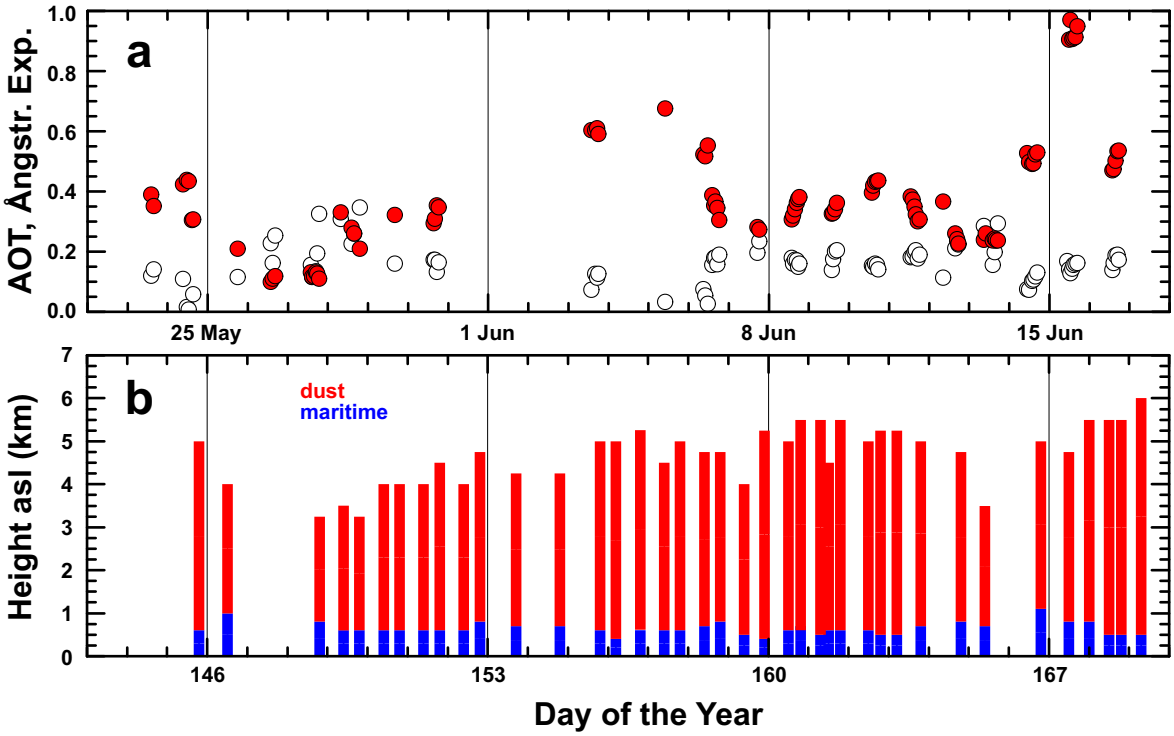

Figure 6.22: (a) SP1A Sun photometer observations (23 May–16 June 2008) of 532–nm AOT (red dots) and 532/1044–nm Ångström exponents (white dots). (b) Vertical extent of the aerosol layers as observed with lidar. Different aerosol types are inferred from BERTHA measurement of the linear volume depolarization ratio at 710 nm: maritime (blue, $\delta^{v} \approx 0$) and mineral dust (red, $\delta^{v} > 0.25$).

deep mineral dust layer (red bars) was observed. The time series of optical depth (532 nm, red dots) and Ångström exponents (532/1044 nm, white dots) obtained with the SP1A photometer corroborates the lidar findings from a column–integrated point of view. The low Ångström exponents of 0.1–0.3 represent large sea–salt particles and mineral dust. They further decreased during dust outbreak periods with optical depths larger than 0.5 on 29 May 2008, 4–6 June 2008, and 14–16 June 2008. The arrival of the elevated dust layer in the night from 3–4 June 2008 was observed with BERTHA and is presented as case study. Towards the end of the campaign the performance of BERTHA worsened due to problems with the laser.

6.3.2 Measurement Case: 3–4 June 2008

Figure 6.23 shows 10–day backward trajectories arriving at Praia at 0100 UTC on 4 June 2008. As in Figure 6.12, the trajectories are underlaid with a map of MODIS fire counts during the respective time period. Fire activity in southern West Africa ceases during summer because the ITCZ is located over the region (see Section 2.3). The areas of biomass–burning activity are located in central Africa and are separated from the dust source regions by the ITCZ. As a consequence of these changes, the

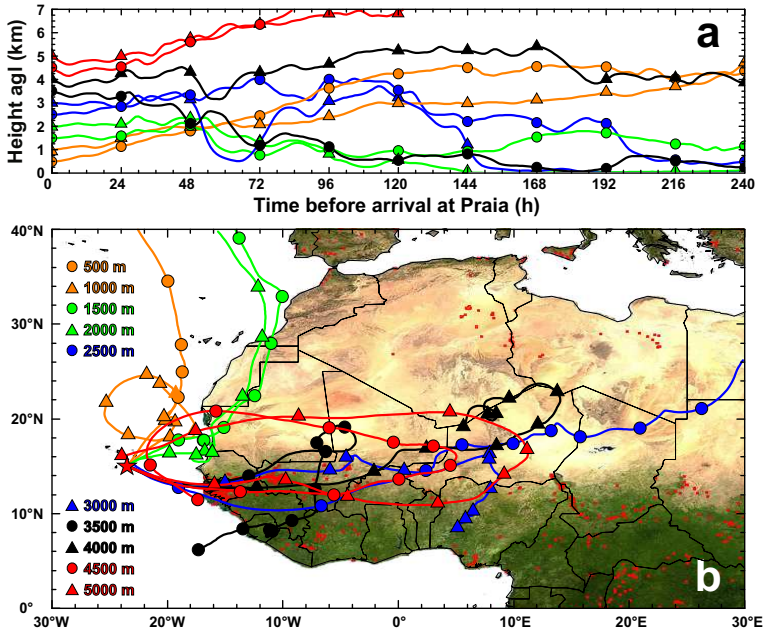

Figure 6.23: Ten–day HYSPLIT backward trajectories ending over Praia at 0100 UTC on 4 June 2008. The underlying MODIS fire map shows all locations of fires (red dots) detected within the 10–day period from 30 May to 8 June 2008.

trajectories in Figure 6.23 show a different behavior than the ones of the SAMUM–2a case in Figure 6.12.

The lowermost trajectory which arrives at 0.5 km height (orange circles) indicates that air was advected to Cape Verde straight from the North Atlantic. Air parcels arriving at 1.0 km height (orange triangles) also had no contact to continental Africa. Therefore, maritime aerosol dominated at these height levels. The air parcels arriving at 1.5 and 2.0 km height (green circles and triangles) spent several days at rather low levels over Western Sahara and Mauritania before being lifted to about 2.0 km height and being advected to Cape Verde within two days. Air parcels arriving between 2.5 and 4.0 km height (blue and black) crossed the source regions in Mauritania, Mali, Niger, and even Chad (2.5 km, blue circles). In the source regions (see Figure 2.1), these air parcels spent a considerable time in the lowermost kilometer of the atmosphere (and even closer to the surface) which suggests that they accumulated large amounts of mineral dust. The uppermost air parcels arriving at 4.5 and 5.0 km height (red circles and triangles) also lingered over typical source regions of mineral dust. However, they spent most of the time before the arrival at Cape Verde at altitudes that are rarely reached by dust particles. As shown in Figure 6.24 dust was observed at these height levels nevertheless the trajectories rather suggest clean conditions.

On 3–6 June 2008 dusty air was transported to Cape Verde with increased upper–level winds from easterly to southeasterly directions. At ground level slow northerly flow transported clean maritime aerosol to the measurement site. The observations of Sun photometer, lidar, and sounding in the night of 3–4 June 2008 are shown in Figure 6.24. Sun–photometer–derived 532–nm AOTs of 0.6 (green dots in a) are in good agreement

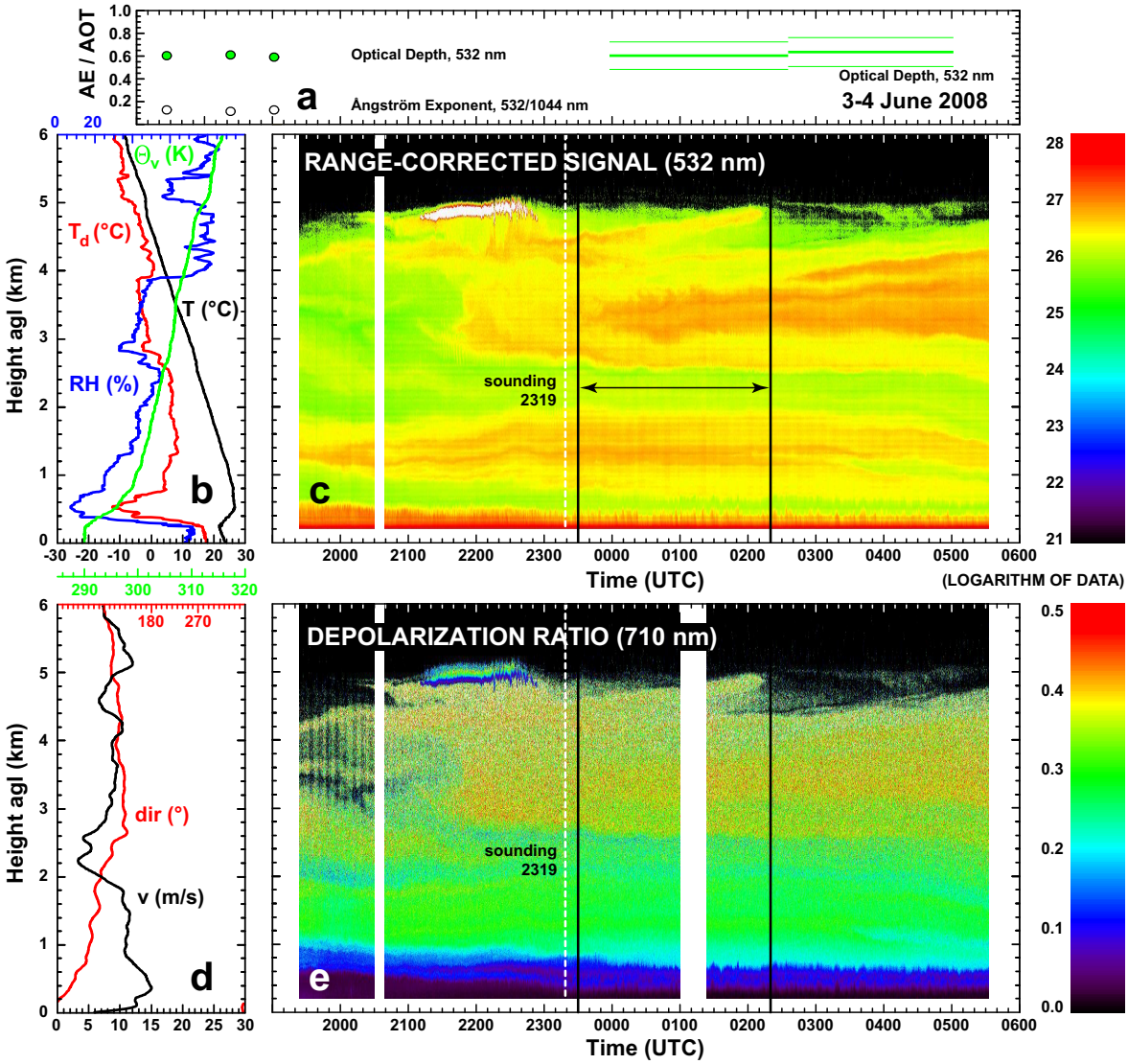

Figure 6.24: Same as Figure 6.3 but for the measurements at Cape Verde at 1924–0532 UTC on 3–4 June 2008. The meteorological profiles (b and d) originate from a sounding performed at 2319 UTC (dashed white line in c and e). The interval 2330–0220 UTC (between the black lines) was chosen for data analysis. 532–AOT (a) was observed with SP1A Sun photometer (green dots) and lidar (horizontal green lines) before and after sunset, respectively.

with the lidar observations of 0.60–0.63 during the night (green horizontal lines in a). The lidar–derived optical depth was obtained by integration of the 532–nm extinction coefficient in the height range from 1–5 km. An optical depth of 0.05 which is usually observed for purely maritime boundary layers (Kaufman et al. 2001) was added to represent the lowermost kilometer of the atmospheric column. The low Ångström exponents of 0.1 (white dots in a) clearly indicate the dominance of large mineral dust and sea–salt particles. The lidar measurement documents the descend of the top of the maritime boundary layer from 1.0 to 0.5 km height during the night. At 2.5–5.0 km on the other hand the arrival of a deep dust layer is visible in the time–height displays

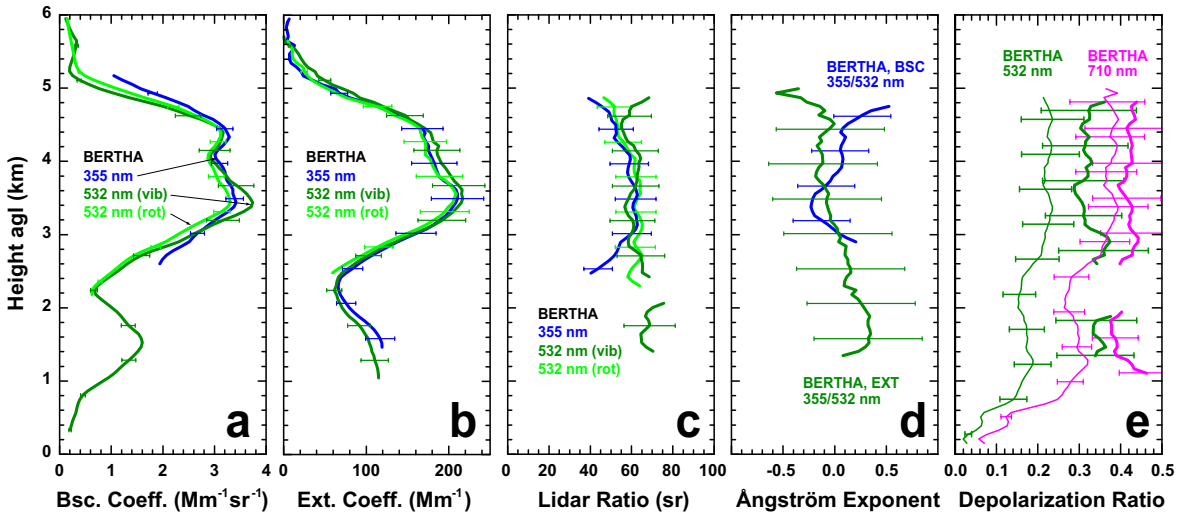

Figure 6.25: BERTHA nighttime measurement at 2330–0220 UTC on 3–4 June 2008. Backscatter (a), extinction (b), and lidar–ratio profiles (c) were measured at 355 nm (blue) and 532 nm (vibrational–Raman channel in dark green and rotational–Raman channel in light green). The 1064–nm elastic–backscatter channel was broken. Therefore, Ångström exponents (d) could only be derived for the short wavelengths pair 355/532 nm. Linear volume and particle depolarization ratios (e) are shown as thin and bold lines, respectively. Linear volume (thin) and particle (bold) depolarization ratios at 532 nm (dark green) are retrieved from measurements at 710 nm (magenta).

of the 532–nm range–corrected signal (c) and the 710–nm volume depolarization ratio (e) at around 2130 UTC. The stratification observed in the lidar measurement is also visible in the profiles of the 2319 UTC sounding (shown in b and d, white dashed line in c and e). The maritime boundary layer is characterized by wind that turns from north to east with height and shows velocities above 10 m/s. A temperature inversion and a strong decrease of relative humidity mark the top of this layer. The deep dust plume was divided by an inversion and a layer of rather slow winds (below 5 m/s). This step is also visible in the lidar plots. In the lower dust layer (1.0–2.0 km height) easterly winds with velocities above 10 m/s dominated, while slightly slower winds from east–southeasterly direction prevailed in the upper layer (2.5–5.0 km height). As found during other observations the top of the dust plume is marked by steps in the profiles of temperature and virtual potential temperature.

The lidar profiles of the analyzed time period 2330–0220 UTC (between the black lines in Figure 6.24c and e) are shown in Figure 6.25. All profiles are smoothed with a window length of 660 m, except for the depolarization–ratio profiles which are smoothed with 150 m window length. The backscatter profiles obtained with the rotational–Raman channels (light green) and the regular vibrational–Raman channel (dark green) are in good agreement. This finding corroborates that a reasonable 532–nm volume depolarization ratio profile (needed for the correction of polarization–dependent receiver transmission) was obtained from the measurements at 710 nm (see Section 5.4.3.2). Furthermore, the obtained 532–nm particle depolarization ratios (Figure 6.25e) of 0.29–0.35 are similar to the SAMUM–1 observations of 0.31±0.03 for pure dust (Freudenthaler et al.

2009). As observed within the dust layers investigated during SAMUM–2a, values of the particle depolarization ratio of 0.4 at 710 nm suggest this parameter to be wavelength–dependent for mineral dust. Even though a step is visible in the profile of the volume depolarization ratio and the corresponding time–height display in Figure 6.24e, the particle depolarization ratio profiles show rather constant values throughout the entire dust plume. Again, this emphasizes the necessity to strictly distinguish between volume and particle depolarization ratio. Within most of the literature the vague term depolarization ratio is used and in most cases just the volume depolarization ratio is presented.

The elevated pure dust layer that stretched from 3–5 km height agl shows wavelength–independent backscatter coefficient of $3\,\mathrm{Mm^{-1}sr^{-1}}$. The weaker, lower layer at 1–2 km height only shows values of $2\,\mathrm{Mm^{-1}sr^{-1}}$. 355–nm backscatter profiles were only trustworthy above 2.5 km height due to problems with the overlap of laser beam and RFOV. The extinction coefficients also show no wavelength dependence with maximum values of $200\,\mathrm{Mm^{-1}}$ in the upper layer. Consequently, Ångström exponents of backscatter and extinction vary around zero (in both layers). Lidar ratios of around 60 sr at 355 and 532 nm were found in the upper layer and also seem to be valid in the lower layer (dark green line in c). This is in fair agreement with SAMUM–1 observations of 55±5 sr (see Section 6.1.4 and Tesche et al. 2009a).

Overall, the observations of 3 June 2008 suggest that the optical properties of mineral dust are not altered during the first days of intercontinental transport. This conclusion is in agreement with CALIPSO observations (Liu et al. 2008a, b). However, the 532–nm lidar ratio of 55–60 sr retrieved from the ground–based measurements with BERTHA is considerably larger than the value of 40 sr that is assumed in the CALIPSO retrieval (Omar et al. 2009, 2010). An explanation of this discrepancy based on the SAMUM–2b measurements at Cape Verde and multiple–scattering calculations is given by Wandinger et al. (2010) and is discussed at the end of the following section.

6.3.3 General Findings and Discussion

Mean profiles of the SAMUM–2b measurements are presented in Figure 6.26. Due to the breakdown of the PMT of the 1064–nm channel, only few 1064–nm backscatter profiles could be obtained during the last days of the measurement campaign. Therefore, and due to the coexistence of a maritime boundary layer and an elevated dust layer, a 1064–nm dust lidar ratio could not be retrieved. The inhomogeneous conditions complicate the combination of column–integrated Sun photometer measurements with height–resolved lidar observations. The backscatter– and extinction–related Ångström exponents within the dust layers are in agreement with the observations in Morocco. The 532/1064–nm backscatter–related Ångström exponent was slightly larger than the one observed during SAMUM–1. However, this deviation is probably caused by the small number of measurements ($N = 5$) with the 1064–nm channel.

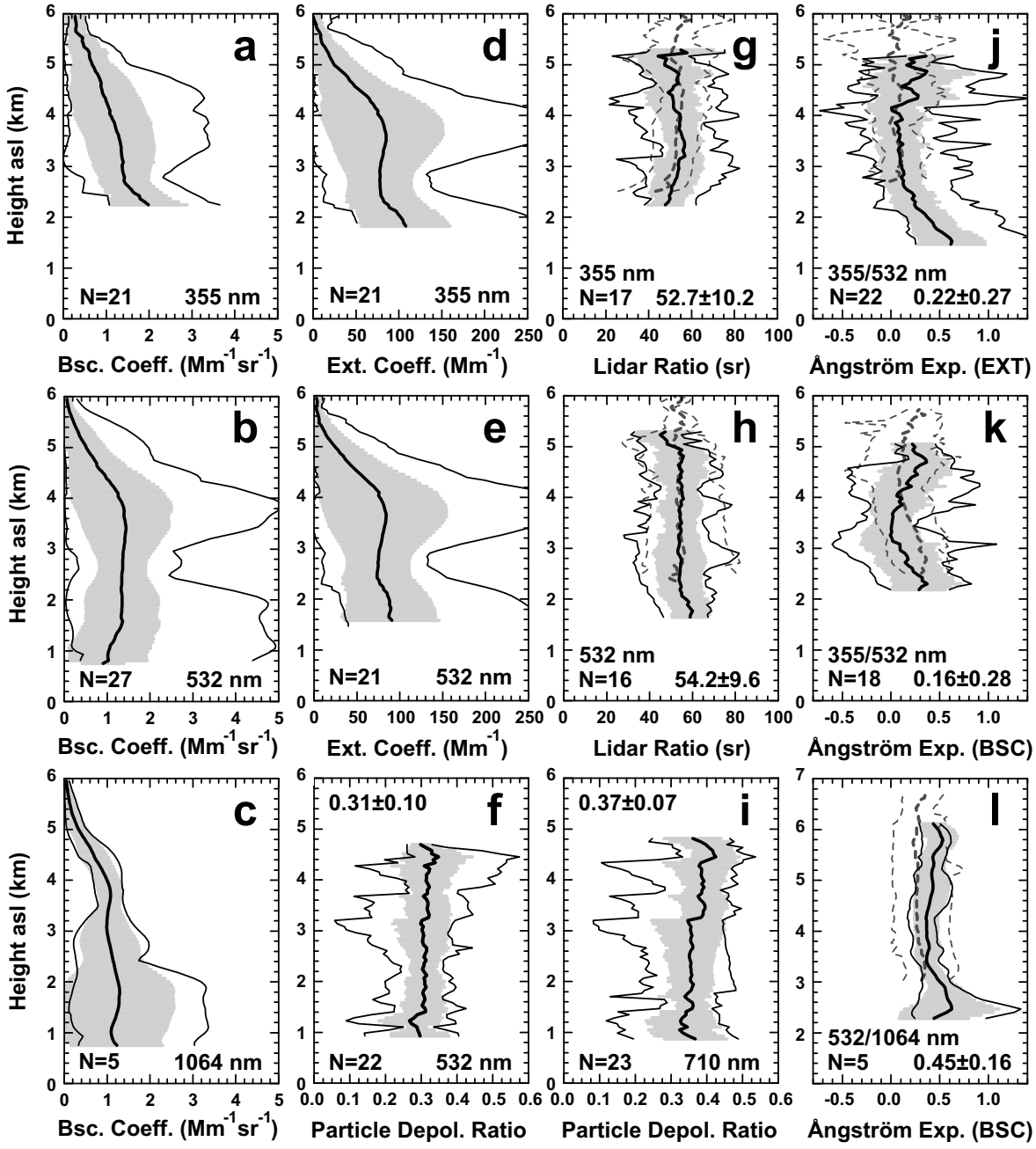

Figure 6.26: Same as Figure 6.16 but for SAMUM–2b. The dashed gray profiles in g, h, j, and k represent the findings of SAMUM–1 in Morocco (see Figure 6.8).

The mean lidar ratios of 53±10 sr and 54±10 sr at 355 and 532 nm, respectively, that were found in the dust layer from 1–6 km height asl are similar to the ones of SAMUM–1 (see Section 6.1.4 and Tesche et al. 2009a). For direct comparison, findings of SAMUM–1 are indicated as dashed gray lines in Figures 6.26g, h, j, k, and l (see Figure 6.8). The SAMUM–2b measurements corroborate the wavelength dependence of the particle depolarization ratio with values of 0.31±0.10 and 0.37±0.07 at 532 and 710 nm, respectively. 710–nm volume depolarization ratios were measured with much higher accuracy

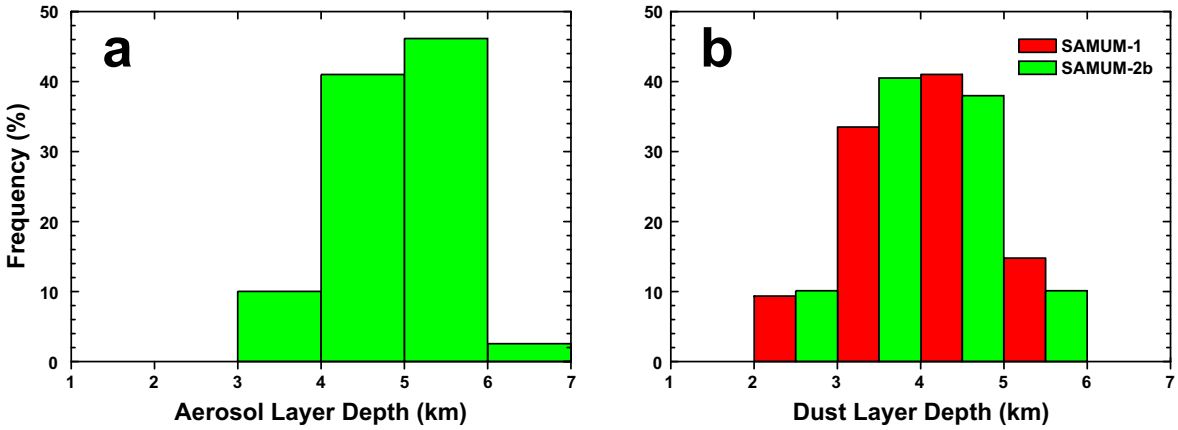

Figure 6.27: Frequency distributions of the depth of (a) the total aerosol layer and (b) the dust layer as extracted from observations of the depolarization ratio during 39 individual measurements according to Figure 6.22. The dust layer depth during SAMUM–2b at Cape Verde is compared to the findings during SAMUM–1 in Morocco.

compared to SAMUM–1 (see Section 5.4.2). They allowed for a calculation of particle depolarization ratios with sufficiently small error bars to draw this conclusion. Because the correction of the 532–nm elastic–backscatter channel with the extrapolated 532–nm volume depolarization ratio led to results that are in good agreement with the independently retrieved 532–nm rotational–Raman backscatter coefficients, it can be expected that the 532–nm volume depolarization ratio profiles and thus the obtained 532–nm particle depolarization ratios are reliable within their error bars of 12%–30% (increasing with height due to signal noise). Because the intensive parameters of SAMUM–1 and SAMUM–2b are in good agreement (see Figure 6.26) and the 710–nm depolarization ratios measured at Cape Verde are much more reliable compared to the ones measured in Morocco (Esselborn et al. 2009, Freudenthaler et al. 2009), the 710–nm particle depolarization ratio of 0.37 ± 0.07 can be expected to represent the conditions close to the dust source (i.e., during SAMUM–1) as well. This conclusion results in a spectrum of the dust depolarization ratio with values of 0.26±0.06, 0.31±0.03, 0.37±0.07, and 0.27±0.04 at 355, 532, 710, and 1064 nm, respectively (see Chapter 7).

Figure 6.27a gives an overview of the depth of the observed total aerosol layer (maritime aerosol and mineral dust) which varied between 3.0 and almost 7.0 km (see also Figure 6.22). As for the observation of the complex aerosol stratification during SAMUM–2a, the measurement of the depolarization ratio allowed for a discrimination between the maritime boundary layer and the elevated dust layer. In Figure 6.27b the depth of the pure dust layer observed during SAMUM–2b is compared to the findings of SAMUM–1 (see Figure 6.10c). The depth of the aerosol layer close to the source in Morocco and after thousands of kilometers of transport at Cape Verde are in surprisingly good agreement. As expected (Karyampudi et al. 1999), the dust layer looses contact to the ground when it is transported westwards from the African coast. However, the geometrical properties of the dust plume remain unaltered, i.e., the expected descent of the dust layer top does not seem to occur within the first thousands of kilometers of summertime transport. This is in agreement with the study of the height–resolved

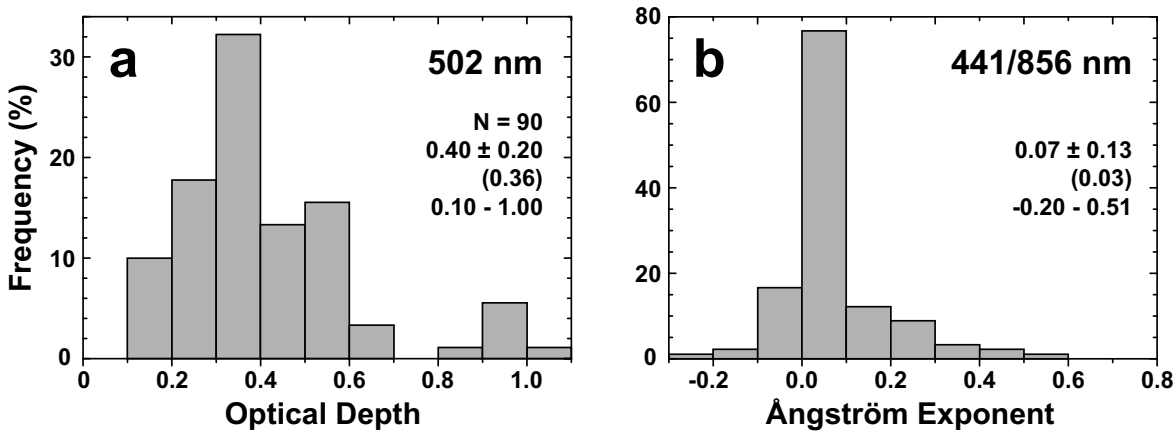

Figure 6.28: Frequency distributions of (a) the 502–nm optical depth and (b) 441/856–nm Ångström exponents measured with SP1A Sun photometer during SAMUM–2b. Numbers in the figure denote the mean value with standard deviation, the median, and the range of observed values.

global distribution of mineral dust from the first year of CALIPSO lidar measurements by Liu et al. (2008a). The study shows that even west of 30° W the dust layer top sometimes reaches up to 6 km height.

Figure 6.28 gives a summary of observations with the SP1A Sun photometer (1–h mean values) during SAMUM–2b. Even though the histograms of AOT during winter (500 nm, see Figure 6.18a) and summer look quite similar, the summertime mean AOT of 0.4 at 502 nm was slightly higher. The largest value of 1.0 at 502 nm was observed in the end of the campaign on 15 June 2008 (see Figure 6.22). The dominance of mineral dust during summer is also visible in the observation of the Ångström exponent. Over 70% of the observations showed Ångström exponents in the range of 0–0.1. The presence of layers of rather pure Saharan dust is also visible in the AERONET time series on Sal island which is obtained since April of 1993 and is often used in the literature as an example for dusty conditions (Holben et al. 2001, Sinyuk et al. 2003, Cattrall et al. 2005).

Just after the end of SAMUM–1 in summer of 2006 the space–borne CALIPSO lidar started its operation. This instrument measures elastically backscattered signals at 532 and 1064 nm and cross–polarized backscattered light at 532 nm (Winker et al. 2009, Omar et al. 2009, Liu et al. 2009, Young and Vaughan 2009). For the analysis of CALIPSO measurements, a lidar ratio needs to be assumed (see Section 3.3.1). For the retrieval algorithm, lidar ratios for different aerosol types were derived from AERONET observations (Omar et al. 2003, 2009). The value of the lidar ratio is selected according to the geographical location and the values of the color ratio[1] and of the volume depolarization ratio. Version 2 of the CALIPSO data retrieval applies dust lidar ratios of 40 and 30 sr at 532 and 1064 nm, respectively (Omar et al. 2003, 2009). The study by Liu et al. (2008b) presents CALIPSO lidar observations of long–range transport of Saharan dust from Africa to the United States of America in August 2006.

[1] the ratio of the attenuated backscatter coefficients at 532 and 1064 nm

By using the dust optical depth derived from MODIS as a constraint in the extinction retrieval Liu et al. (2008b) obtained column dust lidar ratios of 41±5 sr at 532 nm and 52–55±10 sr at 1064 nm. Omar et al. (2010) applied version 3 of the CALIPSO data retrieval (the lidar ratio at 1064 nm was raised to 55 sr) to measurements performed in the framework of NASA's contribution to AMMA (NAMMA). By including *in situ* measurements of microphysical particle properties performed aboard the NASA DC–8 aircraft, they also found dust lidar ratios of 40 sr at 532 nm. Due to the cutoff of the aerosol inlet, the particle size distributions obtained during NAMMA (the mean radius of the coarse mode of the size distribution used in Omar et al. (2010) is 1.696 μm) do not include the giant particles observed in Falcon *in situ* observations during SAMUM–1 (Weinzierl et al. 2009).

All in all, the observations of SAMUM–2b are in surprisingly good agreement with the observations of SAMUM–1 in Morocco. This consistence facilitates studies which combine microphysical dust properties measured aboard the Falcon research aircraft in Morocco with BERTHA observations at Cape Verde during summer to evaluate the dust data retrieval of the space–borne CALIPSO lidar. Lidar measurements during SAMUM–2 were synchronized with overpasses of the CALIPSO satellite at distances below 500 km from the measurement site. Wandinger et al. (2010) showed that the 532–nm dust lidar ratio of 40 sr assumed in the CALIPSO data retrieval results in backscatter coefficients that are in good agreement with BERTHA observations. CALIPSO–derived extinctions coefficients on the other hand were up to 40% smaller than the ones observed with BERTHA. The comparison of measurements of BERTHA and CALIPSO presented in Wandinger et al. (2010) includes multiple–scattering calculations based on real dust size distributions with effective radii between 3 and 6 μm as measured in pure Saharan dust layers during SAMUM–1 in Morocco (Weinzierl et al. 2009). The calculations showed that the space–borne lidar system is affected by considerable multiple–scattering effects. Consequently, this effect leads to an underestimation of dust extinction coefficients and dust AOT of 10%–40%. The lidar ratios for the CALIPSO retrieval are derived from an aerosol model which uses dust size distributions with a dust effective radius of 0.4 μm. These size distributions originate from AERONET inversions of Sun photometer measurements and do not incorporate the large particles that were found in the airborne *in situ* measurements during SAMUM–1. Large particles have a big effect on the investigated optical properties—even if they occur in low concentrations. The low 532–nm dust lidar ratio of 40 sr in the CALIPSO retrieval accounts for the effect of multiple–scattering (i.e., it represents an effective lidar ratio) and thus leads to backscatter profiles which are in very good agreement with ground–based measurements. To obtain reliable values of the extinction coefficient from these backscatter profiles, Wandinger et al. (2010) recommend the use of a second look–up table with a dust lidar ratio of 55 sr (as obtained from the measurements of SAMUM–1 and SAMUM–2b). Otherwise, a systematic underestimation of up to 40% will be introduced to the global data set of CALIPSO–derived dust AOTs. This quantity is commonly used in modeling studies for the investigation of the radiative effect and global distribution of mineral dust aerosol. In recent years such investigations entered the spotlight of the scientific community—also because CALIPSO observations enabled global, height–resolved dust studies for the first time. For users which only

consider the provided CALIPSO level 2 products in their global aerosol studies the multiple–scattering effect might introduce serious systematic errors.

The study of Wandinger et al. (2010) contains a second important message that might not be obvious immediately. The discrepancy between ground–based and space–borne extinction profiles can be explained with multiple–scattering calculations that apply mean effective radii from *in situ* measurements of the dust size distributions during SAMUM–1. This consensus can be considered as another closure of the measurements within the dust column closure experiment SAMUM–1. As a consequence, the accuracy of the *in situ* dust size distributions obtained during SAMUM–1 is confirmed.

7 SAMUMmary: Milestones and Outlook

This thesis presented the results of the observations with the multiwavelength polarization Raman lidar BERTHA during SAMUM–1 in Morocco and SAMUM–2 at Cape Verde. Calibration measurements and corrections that turned out to be necessary to assure a high quality of the data measured with BERTHA were discussed. This chapter summarizes the comprehensive milestones found from the SAMUM lidar measurements. As suggested by Sokolik et al. (2001), SAMUM was designed to consist of two stages: one experiment close to the source region of mineral dust in northern Africa and one experiment in the regime of long–range transport of Saharan dust to the Americas. The two SAMUM experiments provided excellent comparability of the observations because they were performed with identical equipment and personnel. The SAMUM–1 findings for pure mineral dust allowed for a sophisticated exploitation of the lidar data collected during SAMUM–2. This course of action corroborated the design of SAMUM as a two–step experiment. The SAMUM closure experiments can be considered a success for several reasons. The overall idea of conducting the measurements necessary to obtain an overdetermined data set for closure studies on mineral dust was satisfied. Perfect conditions to conduct the desired studies were met and none of the instruments suffered of critical malfunctions. In contrast to previous studies which mostly concentrated on *in situ* measurements, the strategy of SAMUM included comprehensive efforts for vertical profiling of the encountered aerosol layers. A unique data set of lidar observations was collected with four state–of–the–art systems. During all SAMUM campaigns, 472 h of lidar measurements with BERTHA were performed on 83 days. 189 h of measurements were analyzed within the framework of this thesis—calibration measurements not included. 148 h of measurements were found to be unsuitable for analysis. The rejection was mostly due to strong signal noise (usually during daytime measurements), low–level clouds (which cause strong signal attenuation), clouds and/or virgae above the aerosol layers (which inhibit the choice of an appropriate reference value), or missing calibration measurements. A total number of 147 radiosondes was launched in addition to and accompanying the measurements with BERTHA.

The mean values of the intensive parameters lidar ratio, Ångström exponent, and linear particle depolarization ratio (which are usually applied for aerosol characterization with lidar) found for the aerosol types observed during SAMUM are shown in Table 7.1. Values of the linear particle depolarization ratio during SAMUM–1 were taken from Freudenthaler et al. (2009). For SAMUM–2a, the optical properties of maritime aerosol

Table 7.1: Overview of the intensive lidar parameters observed during SAMUM. Values for SAMUM–1 were taken from Section 6.1.4 (lidar ratios and Ångström exponents) and Freudenthaler et al. (2009) (linear particle depolarization ratios). SAMUM–2 values were taken from Sections 6.2.3 and 6.3.3 except for the results for maritime aerosol and dust which were taken from Groß et al. (2011a). Depolarization parameters d are only given for the mean values of the linear particle depolarization ratio.

	SAMUM–1	**SAMUM–2a**				**SAMUM–2b**
	Morocco May/June 2006	Cape Verde January/February 2008				Cape Verde May/June 2008
	dust	maritime	dust+smoke	dust	smoke	dust
S_{355} (sr)	53 ± 7	17	67 ± 14	58	87 ± 17	53 ± 10
S_{532} (sr)	55 ± 7	18	67 ± 12	61	79 ± 17	54 ± 10
S_{1064} (sr)	55 ± 13	–	–	–	–	–
$\mathring{a}^{\alpha}_{355/532}$	0.06 ± 0.21	–	0.67 ± 0.38	–	1.15 ± 0.28	0.22 ± 0.27
$\mathring{a}^{\beta}_{355/532}$	0.19 ± 0.20	–	0.71 ± 0.28	–	0.90 ± 0.26	0.16 ± 0.45
$\mathring{a}^{\beta}_{532/1064}$	0.28 ± 0.16	–	0.67 ± 0.27	–	1.06 ± 0.65	0.45 ± 0.16
$\delta^{\mathrm{p}}_{355}$	0.26 ± 0.06	0.03	0.16 ± 0.04	0.25	–	–
$\delta^{\mathrm{p}}_{532}$	0.31 ± 0.03	0.03	0.16 ± 0.03	0.30	0.05 ± 0.02	0.31 ± 0.10
$\delta^{\mathrm{p}}_{710}$	0.28 ± 0.05[1]	–	0.18 ± 0.03	0.36	–	0.37 ± 0.07
d_{355}	0.413	0.058	0.276	0.400	–	–
d_{532}	0.473	0.058	0.276	0.462	0.095	0.473
d_{710}	0.438[1]	–	0.305	0.529	–	0.540

[1] the SAMUM–2b value of 0.37 ± 0.07 ($d = 0.54$) is assumed to be representative for SAMUM–1 (see text)

and mineral dust and the linear particle depolarization ratios at 355 and 532 nm were taken from Groß et al. (2011a). The remaining numbers were derived in the framework of this thesis. In addition to the lidar–specific parameters, the depolarization parameter is given (Gimmestad 2008).

Because of the location in the vicinity of the source regions of mineral dust, SAMUM–1 observations were considered to represent pure dust conditions. The analysis of the lidar measurements together with the meteorological profiles from radiosounding corroborated the assumption of a well–mixed dust layer. Identical results for the dust layers observed during SAMUM–1 were found with four different lidars. The lidar ratios, Ångström exponents, and linear particle depolarization ratios which are presented in the second column of Table 7.1 are considered to represent the properties of pure Saharan dust.

The dust lidar ratio was found to be wavelength–independent with values of about 55 sr at 355, 532, and 1064 nm. Similar values were found during dusty periods of SAMUM–2a (58 sr at 355 nm and 61 sr at 532 nm, Groß et al. 2011a) and during SAMUM–2b (53 sr at 355 nm and 54 sr at 532 nm, see Section 6.3.3). Estimates of the lidar ratio are needed as input parameter for the analysis of elastic–backscatter lidar observations of mineral dust according to Klett's method. The direct measurement under pure dust conditions gives a guideline for the interpretation of observations at remote loca-

tions. The large spread of dust lidar ratios of 40–70 sr found from lidar observations in southern and central Europe (Mattis et al. 2002, Balis et al. 2004, Mona et al. 2006, Papayannis et al. 2008) as well as in Korea and Japan (Sakai et al. 2002, Murayama et al. 2003, 2004, Noh et al. 2007) usually results in a discussion of the presented findings without knowledge of the typical value for pure mineral dust.

Another milestone of the SAMUM observations is the spectrally resolved, quantitative measurement of the linear particle depolarization ratio. Until SAMUM–1, depolarization profiling was mostly used to separate layers of spherical scatterers from those of non–spherical ones, i.e., it was used qualitatively to validate, whether observed clouds or virgae contain ice crystals or if mineral dust is detected during favorable meteorological conditions. The measurements in Morocco provided first insight into the wavelength–dependence of the dust depolarization ratio with values of 0.26±0.06 at 355 and 1064 nm, 0.31±0.03 at 532 nm, and 0.37±0.07 at 710 nm. Note that the findings of SAMUM–2b are expected to also be representative for the pure dust conditions encountered during SAMUM–1. This is because the improved calibration setup for the measurement of the linear volume depolarization ratio which was implemented after SAMUM–1 is assumed to result in more reliable results than the experimental approach of SAMUM–1. Recent laboratory studies found 532–nm particle depolarization ratios of Saharan and Asian dust to be in the range of 0.39±0.05 (Sakai et al. 2010).

Following the suggestion by Gimmestad (2008), the linear particle depolarization ratio is transformed to the depolarization parameter. For the mean dust depolarization ratios obtained from the SAMUM measurements, these values are 0.413 at 355 nm, 0.473 at 532 nm, 0.540 at 710 nm, and 0.425 at 1064 nm. Consequently, the scattering matrices for randomly oriented dust particles at the respective wavelengths can be calculated according to Equation (3.28). As an example, the scattering matrix at 532 nm is

$$\mathbf{F}(180^\circ, 532\,\mathrm{nm}) = \begin{bmatrix} 1 & 0 & 0 & 0 \\ 0 & 0.527 & 0 & 0 \\ 0 & 0 & -0.527 & 0 \\ 0 & 0 & 0 & -0.053 \end{bmatrix}.$$

The lidar ratio and linear particle depolarization ratio can only be measured with lidar, because other instruments are not able to perform measurements in the backward direction. As mentioned in Section 3.1, the scattering phase function at 180°—and thus the lidar ratio and the linear particle depolarization ratio—is very sensitive to the shape, size, and complex refractive index of the scattering particles. Therefore, the results of the spectrally–resolved SAMUM–1 observations of the dust lidar ratio and the dust depolarization ratio provide the unique opportunity to validate numerical models that were developed to simulate light scattering by large non–spherical particles. These models can only be considered reliable, if they succeed to reproduce the findings of laboratory or field measurements. To reproduce the observed optical and radiative properties of mineral dust constitutes the final step of the closure studies and—ultimately—confirms that the underlaying effects are properly understood. Promising results are obtained in the study by Gasteiger et al. (2011) who appled

ensembles of (realistically) irregularly shaped particles to reproduce the high dust depolarization ratios measured during SAMUM (see discussion in Section 6.1.4). For the SAMUM–1 measurement example of 19 May 2006, which is discussed in detail by Müller et al. (2010a, b) and Tesche et al. (2009a), they can reproduce the measured dust lidar ratios and dust depolarization ratios. Gasteiger et al. (2011) furthermore capture the increase of the linear particle depolarization ratio from 355 to 710 nm which was observed in dust periods during SAMUM–2a (Groß et al. 2011b). Even though Gasteiger et al. (2011) are able to reproduce observations of dusty cases during SAMUM–1 and SAMUM–2a, they highlight that mineralogical inhomogeneities are hard to capture. As a consequence, particle mixtures which reproduce the lidar measurements of one case remarkably well usually fail for the next measurement case.

The observations of SAMUM–2a showed complex aerosol conditions with a maritime boundary layer close to the surface, a Saharan dust layer in the lowermost 1–2 km, and an up to 5 km deep elevated layer which consisted of a mixture of biomass–burning smoke and mineral dust. Lidar ratios of 60–80 sr at 355 and 532 nm (with mean values of 67±14 sr, see fourth column in Table 7.1) observed in the latter layer were in the range of previous observations (Wandinger et al. 2002, Heese and Wiegner 2008). A method for a height–resolved separation of the contributions of different aerosol types to the backscatter and extinction coefficients based on measurements of the linear particle depolarization ratio was developed in the framework of this thesis and applied to the mixed dust/smoke layers observed during SAMUM–2a. The contribution of mineral dust to the elevated layer was found to vary from 40%–60%. Considering this dust fraction and the dust lidar ratio of 55 sr found during SAMUM–1, the observed (mixed) mean lidar ratio of 67 sr would be obtained, if lidar ratios of pure biomass–burning smoke were in the range of 75–85 sr. Such values are in agreement with observations during DABEX (Heese and Wiegner 2008) and other studies of African biomass–burning smoke that, in some cases, estimated even higher values of 90–130 sr (Campbell et al. 2003, Pelon et al. 2008) from elastic–backscatter lidar measurements.

The mean linear particle depolarization ratio for the the dust/smoke mixture observed in the elevated layers during SAMUM–2a was 0.16 at 355 and 532 nm, and 0.18 at 710 nm (see Table 7.1 and Groß et al. 2011b). The first value corresponds to a depolarization factor of 0.276. Thus the scattering matrix of randomly oriented particles of the dust/smoke mixture at 532 nm was found to be

$$\mathbf{F}(180^\circ, 532\,\mathrm{nm}) = \begin{bmatrix} 1 & 0 & 0 & 0 \\ 0 & 0.724 & 0 & 0 \\ 0 & 0 & -0.724 & 0 \\ 0 & 0 & 0 & -0.448 \end{bmatrix}.$$

The spectral information of multiwavelength lidar data can be used to derive microphysical particle properties by means of an inversion algorithm (see Section 4.3). Because this algorithm applies Mie scattering theory which cannot be used to describe the scattering properties of large non–spherical dust particles, an inversion of lidar data is only possible for the pure biomass–burning smoke data set derived from the aerosol–type separation. The spectral separation procedure led to smoke Ångström exponents that

were, on average, increased by about 50% with respect to the ones of the dust/smoke mixture. This is in agreement with the association that pure smoke particles are smaller than the particles in an almost even mixture of dust and smoke. The aerosol–type separation led to smoke lidar ratios of 87±17 sr at 355 nm and 79±17 sr at 532 nm. The values are increased with respect to the mixture because smaller smoke particles are also more absorbing than mineral dust particles. The analysis of the inversion calculations led to smoke effective radii of 0.22±0.08 μm. These values are similar to findings for elevated smoke layers observed during INDOEX (Franke et al. 2003, Müller et al. 2003). The SSA was low with an average value of 0.75±0.07 at 532 nm. Such low values denote highly absorbing particles. The *in situ* observations aboard the Falcon research aircraft (Weinzierl et al. 2011) during local flights on 22/23 January and 5/6 February 2008 at height levels that are assumed to be dominated by the presence of biomass–burning smoke led to effective radii of 0.47±0.21 μm. These values were calculated from the measured particle size distribution of the dust/smoke mixture. No physical separation of the different particle types was possible. Therefore, it was assumed that the smaller smoke particles constitute the smaller fine and accumulation modes while the larger dust particles were located in the coarse mode. The contribution of small dust particles to the lower size ranges might influence the larger effective radii (compared to the inversion results) found from the *in situ* measurements. The SSA at 530 nm was found to be 0.81±0.05 with individual values as low as 0.74. Considered that the influence of small dust particles (with SSA of 0.98) to these results might have been of the order of 15%, the SSA for pure biomass–burning smoke could have been as low as 0.70. This corroborates the very low values found from the inversion of the optical data of pure biomass–burning smoke.

During SAMUM–2b, pure dust layers up to 6 km height were observed above a 0.5–1.0 km deep maritime boundary layer. Improvements of the calibration setup of the 710–nm depolarization channels of the BERTHA receiver allowed for high–quality measurements of the linear volume depolarization ratio during SAMUM–2. A linear relationship between the linear volume depolarization ratios at 532 and 710 nm was retrieved from coincident measurements of MULIS and BERTHA during SAMUM–2a. The relation was applied to transform volume depolarization–ratio measurements at 710 nm to 532 nm. The resulting 532–nm dust depolarization ratios observed during SAMUM–2b showed no variation from the values observed during SAMUM–1 (see Table 7.1). However, the most important finding of SAMUM–2b is the wavelength–dependence of the linear particle depolarization ratio with values of 0.31±0.10 at 532 nm and 0.37±0.07 at 710 nm. As presented in Figures 6.26g, h, j, k, and l and Table 7.1 no differences of intensive parameters were found between the summer observations in Morocco and at Cape Verde. This agreement suggests that no significant changes in particle microphysics occur during the first days of transport. This conclusion corroborates airborne observations during SAMUM–1 that also showed a high number of surprisingly large particles during flights over the Atlantic ocean (Weinzierl et al. 2009). The frequency distributions of the depth of the dust layers of 3–5 km as observed during summer in Morocco and at Cape Verde (see Figure 6.27b) furthermore revealed that there is little difference between the geometric properties of the dust layer close to the source region and several thousand kilometers away to the west. The suggested effects like

the descent of the dust layer top (Karyampudi et al. 1999) or the settling of larger particles all seem to occur west of Cape Verde, further downstream of the transport to the Americas.

From the respective one–month observations during SAMUM–2 detailed information about the aerosol conditions in the outflow of the African continent during winter and summer was obtained. Note that SAMUM–2 was the first field experiment that covered both modes of transport (i.e., winter and summer) of African aerosols over the Atlantic ocean. Especially the extensive field measurements during winter provide missing experimental background to the scientific community. Previous studies only captured snapshots because they were limited to a rather short time period (Tanré et al. 2003, Haywood et al. 2008) or only considered passive satellite remote sensing without the possibility of vertical profiling (Kaufman et al. 2005). In a study based on space–borne CALIPSO lidar observations over the tropical Atlantic, Ben-Ami et al. (2009) could not properly identify the (top of the) smoke–dominated layers which were observed during SAMUM–2a. This deficit is due to the bad signal–to–noise ratio of the CALIPSO measurements in this aerosol layer.

Even though CALIPSO observations are a good tool for global height–resolved studies of dust aerosols, one has to keep in mind that they are not corrected for multiple–scattering. This effect can cause a significant underestimation of the particle optical depth and the related column lidar ratio (Young and Vaughan 2009) in any case of the presence of dust particles (Wandinger et al. 2010). The influence of multiple scattering on ground–based lidar observations of desert dust is negligible. Thus such instruments are good tools for the validation of the space–borne measurements. Lidar measurements during SAMUM–2 were synchronized with overpasses of the CALIPSO satellite and used for the validation of the products of the CALIPSO data retrieval. From these coincident measurements it was found that an underestimation of, on average, 30% is introduced to CALIPSO dust extinction coefficients due to multiple–scattering effects (Wandinger et al. 2010). Consequently, CALIPSO–derived dust AOT which is often used for modeling studies is systematically too low.

What are the future implications of the SAMUM experiment? First of all, the collected data need to be exploited exhaustively for various kinds of closure studies. This includes comparisons of active and passive remote sensing with *in situ* observations. An exemplary study is presented in Müller et al. (2010a, b) who try to explain weak points of the non–spherical particle model of the AERONET retrieval (Dubovik et al. 2006). The findings of SAMUM–1 should be considered as the benchmark for the test of improved non–spherical particle models. Gasteiger et al. (2011) show how the use of realistically shaped particles and particle mixtures improves the agreement between modeling and measurement. Plenty of work needs to be put into such models which are needed for the optical closure studies and the analysis of measurements with passive sensors.

There are further unresolved questions. Are the optical, microphysical, and chemical properties of Saharan dust obtained during SAMUM–1 also valid for Asian dust? After which time or range of intercontinental transport do these properties start to deviate

from the observations close to the source region? How does aging affect mineral dust particles? What is the amount of mineral dust transported around the globe? Where is it deposited and what are the consequences of this deposition?

To resolve these outstanding problems further observations in the design of SAMUM are necessary. Subsequent studies of Saharan dust might be in the form of ship–based observations along latitudinal transects between Africa and the Americas or as a column closure experiment in the Caribbean. For studies of Asian dust, the two–step SAMUM approach as suggested by Sokolik et al. (2001) needs to be repeated for measurement sites in central Asia and eastern China, Korea, or Japan during the Asian dust season between March and May.

To gain further insight in the microphysical properties of mineral dust particles and to validate non–spherical particle models, laboratory studies need to be conducted. Sakai et al. (2010) showed that the dust depolarization ratio can be retrieved from such experiments. The findings are in good agreement with SAMUM observations during pure dust conditions. Volten et al. (2001) report findings of the scattering matrices of mineral dust at 441.6 and 632.8 nm. Such information needs to be provided for a broader wavelength range to improve the understanding of the interaction of light with non–spherical dust particles and to test non–spherical particle models (Dubovik et al. 2006, Gasteiger et al. 2011).

Apart from the focus on mineral dust there is another point to be considered in future lidar studies. In recent years, 3+2 Raman lidars with the capabilities of BERTHA became available at several stations for long–term monitoring of atmospheric aerosol—especially in the framework of EARLINET. Such instruments can be used for comprehensive aerosol studies including height–resolved aerosol characterization and studies of long–range transport. These systems furthermore provide the possibility of subsequent inversion of the 3+2 data set of the measured optical properties. The inversion results give an estimate of the microphysical particle properties which are useful for a wider community. Several EARLINET stations (especially in the Mediterranean) are regularly affected by long–range transport of mineral dust layers. The presence of such dust events needs to be verified. The best tool for this is the measurement of the depolarization ratio—quantitatively instead of qualitatively (as is currently done with most systems). As shown by the application of the aerosol–type separation to complex mixtures of different kinds of aerosols (Groß et al. 2011b, Tesche et al. 2009a, 2011b), it is evident that only well–characterized $3\alpha+2\beta+1\delta$ polarization Raman lidars can provide the necessary information to adequately characterize such aerosol mixtures.

8 Appendix

8.1 Error Discussion

In this section the equations for the calculation of the errors of the quantities examined in this thesis are provided and discussed. If possible, error bars were derived analytically by applying Gaussian error propagation. The random error of a quantity F, which is assumed to be a function of $a, b, \ldots, x$, is derived by forming the respective partial derivations as

$$\frac{\Delta F(a,b,\ldots,x)}{F(a,b,\ldots,x)} = \frac{\sqrt{\left(\frac{\partial F(a,b,\ldots,x)}{\partial a}\Delta a\right)^2 + \left(\frac{\partial F(a,b,\ldots,x)}{\partial b}\Delta b\right)^2 + \cdots + \left(\frac{\partial F(a,b,\ldots,x)}{\partial x}\Delta x\right)^2}}{F(a,b,\ldots,x)}.$$

Some errors had to be estimated when Poisson statistics could not be applied, i.e., when analog signals were measured as voltage instead of number of single photons.

Systematic errors are caused by systematic effects that are unrelated to the state of the atmosphere, e.g., the correction of the overlap effect (see Section 5.4.3.1) and of signals compromised by polarization–dependent receiver transmission (see Section 5.4.3.2) as well as the transformation of the depolarization ratio measurement to another wavelength (see Section 5.4.3.3). Systematic errors can also be introduced because an instrument is handled differently by different operators. The latter effect stayed constant during SAMUM because the lidar systems were supervised by the same personnel. Furthermore, calibration measurements for the analysis of volume depolarization ratio profiles measured with BERTHA during SAMUM–2 were performed by one person only. Systematic errors can be accounted for, when their sources and effects are well understood. To correct the dust measurements for the effect of polarization dependent receiver transmission was a fundamental challenge of this work.

Note that all quantities discussed in this section are dependent on height and wavelength. For convenience the height–dependence is not explicitly stated in the following equations.

8.1.1 Backscatter Coefficients

Total Particle Backscatter Coefficient

The error of the particle backscatter coefficient obtained from elastic–backscatter and Raman signals is relatively small and mainly depends on signal noise and the uncertainty of the profiles of temperature and pressure used in the calculation. Especially in regions of large temperature gradients (inversion layers) errors can be introduced, if wrong profiles of meteorological parameters are used. This problem can be neglected, if the length of the vertical smoothing window is chosen appropriately large. The best way to avoid the introduction of errors from the temperature profile is to use current profiles of nearby soundings. Radiosondes were launched during each lidar measurement of SAMUM to obtain reliable profiles of temperature and pressure.

The error introduced by a wrong choice of the Ångström exponent $\mathring{a}$ is below 1% and thus negligible. For the analysis of dust–dominated days (SAMUM–1 and SAMUM–2b) $\mathring{a} = 0$ was used while $\mathring{a}$ was set to unity when signals from SAMUM–2a were analyzed.

Usually, the largest error of the particle backscatter coefficient derived with the Raman method is due to a wrong assumption of the reference value. Cirrus clouds in the measurements were used to validate the chosen reference values. Due to the large size of the ice crystals, the backscatter coefficient shows no wavelength dependence in cirrus clouds. Starting from a trustworthy analysis of the 1064–nm backscatter profile (which shows a negligible influence of Rayleigh scattering) reference values at the other measurement wavelengths were varied accordingly to obtain wavelength independent backscatter coefficients in a cirrus cloud.

The random errors of the particle backscatter coefficients calculated from nighttime measurements according to the Raman method (see Section 3.3.2) are estimated to be

$$\frac{\Delta\beta^{\mathrm{p}}_{355}}{\beta^{\mathrm{p}}_{355}} = \frac{\Delta\beta^{\mathrm{p}}_{1064}}{\beta^{\mathrm{p}}_{1064}} = 0.05$$

and

$$\frac{\Delta\beta^{\mathrm{p}}_{532}}{\beta^{\mathrm{p}}_{532}} = 0.10\,.$$

The error of the 532–nm backscatter coefficient is larger, because the correction of polarization–dependent receiver transmission of the 532–nm elastic–backscatter channel introduces additional errors. As mentioned in Section 5.4.3.2, the volume depolarization ratio δ^{v} and the transmission ratio D at the wavelength of the affected measurement channel need to be known for an appropriate correction. Because these two variables are also affected by individual errors, the total uncertainty of β^{p}_{532} is increased. The error of the volume depolarization ratio is discussed below. The transmission ratio obtained from calibration measurements at $\Theta_{\mathrm{z}} = 45°$ was used for the correction of atmospheric measurements with $\Theta_{\mathrm{z}} = 5°$ because these results showed the best agreement with the unaffected backscatter profiles obtained with MULIS and the rotational–Raman channels. The comparison with profiles derived from the measurements of MULIS and HSRL suggest that the error introduced by this correction is

below 5%. Thus the total error of the Raman backscatter coefficient at 532 nm increases to the aforementioned value of 0.10.

During daytime measurements, extinction profiles could only be obtained according to Klett's method (see Section 3.3.1). The uncertainty resulting from the assumption of the particle lidar ratio can be very high, especially if the detected signal is weak or if very inhomogeneous aerosol conditions are met (and the assumption of a constant lidar ratio is not fulfilled, Sasano et al. 1985). The use of a height–dependent lidar ratio does not necessarily reduce the uncertainty of the solution because its assumption requires *a priori* knowledge of the type of aerosol at different height levels. For validation of the daytime analysis, the height integral of the lidar–derived extinction coefficient (backscatter coefficient times input lidar ratio) is compared to AOTs measured with Sun photometer at the respective wavelength. In this approach large uncertainties can occur, if the overlap effect is not considered appropriately. In case of the homogeneous dust layers observed during SAMUM–1, the extinction coefficient in the overlap region was set to the first reliable value in the dust layer. In maritime environment like at Cape Verde, an optical depth of 0.05 at 500 nm is usually observed in the maritime boundary layer (Kaufman et al. 2001). This value was added to the AOT derived from the lidar measurements above the maritime boundary layer. However, the focus of this thesis is on nighttime measurements for which Raman signals allow for an independent retrieval of particle backscatter and extinction coefficients and thus the particle lidar ratio.

A detailed discussion of the factors contributing to the uncertainty of the backscatter coefficients obtained from elastic–backscatter and Raman signals can be found in Ansmann et al. (1992) and Ansmann and Müller (2005).

Dust Backscatter Coefficient

The dust backscatter coefficient at 532 nm was derived by using Equation (4.7). The error of β^{d}_{532} was calculated as

$$\frac{\Delta\beta^{\mathrm{d}}_{532}}{\beta^{\mathrm{d}}_{532}} = \frac{\sqrt{\left(\frac{\Delta\beta^{\mathrm{p}}_{532}}{\beta^{\mathrm{p}}_{532}}\right)^2 + \left(\frac{(1+\delta^{\mathrm{s}}_{532})\delta^{\mathrm{p}}_{532}}{(\delta^{\mathrm{p}}_{532}-\delta^{\mathrm{s}}_{532})(1+\delta^{\mathrm{p}}_{532})}\frac{\Delta\delta^{\mathrm{p}}_{532}}{\delta^{\mathrm{p}}_{532}}\right)^2 + }}{\left(\frac{(1+\delta^{\mathrm{s}}_{532})\delta^{\mathrm{d}}_{532}}{(\delta^{\mathrm{d}}_{532}-\delta^{\mathrm{s}}_{532})(1+\delta^{\mathrm{d}}_{532})}\frac{\Delta\delta^{\mathrm{d}}_{532}}{\delta^{\mathrm{d}}_{532}}\right)^2 + \left(\frac{(\delta^{\mathrm{p}}_{532}-\delta^{\mathrm{d}}_{532})\delta^{\mathrm{s}}_{532}}{(\delta^{\mathrm{d}}_{532}-\delta^{\mathrm{s}}_{532})(\delta^{\mathrm{p}}_{532}-\delta^{\mathrm{s}}_{532})}\frac{\Delta\delta^{\mathrm{s}}_{532}}{\delta^{\mathrm{s}}_{532}}\right)^2}}.$$

Linear volume and particle depolarization ratios were provided by MULIS. Their uncertainties together with the one of the linear dust depolarization ratio (from the SAMUM–1 measurements) were taken from Freudenthaler et al. (2009) as

$$\frac{\Delta\delta^{\mathrm{p}}_{532}}{\delta^{\mathrm{p}}_{532}} = \frac{\Delta\delta^{\mathrm{d}}_{532}}{\delta^{\mathrm{p}}_{532}} = 0.10\,.$$

Because the assumed value of the smoke depolarization ratio originated from the literature (with a variety of values that accumulate at about $\delta^{\mathrm{s}}_{532} = 0.05$) its uncertainty was investigated by means of a sensitivity study. The absolute values of the dust and

smoke depolarization ratios were varied by ±0.04 and ±0.03, respectively, to investigate the contribution of these two input parameters. Note that the variation of $\delta^{\mathrm{d}}_{532}$ was chosen to be larger than the errors reported by Freudenthaler et al. (2009). The variations showed that the results of the aerosol–type separation are more sensitive to errors of the dust depolarization ratio than to errors of the smoke depolarization ratio. The whole variety of possible results (except for the extreme combinations of $\Delta\delta^{\mathrm{d}}_{532} = -0.04$, $\Delta\delta^{\mathrm{s}}_{532} = -0.03$ and $\Delta\delta^{\mathrm{d}}_{532} = +0.04$, $\Delta\delta^{\mathrm{s}}_{532} = +0.03$) was covered, if a value of

$$\frac{\Delta\delta^{\mathrm{s}}_{532}}{\delta^{\mathrm{s}}_{532}} = 0.2$$

was used for the calculation of the error of the dust backscatter coefficient. This value is reasonable because it also covers most of the observations of fresh and aged smoke recorded in the literature (see Section 4.2). The profile of $\Delta\beta^{\mathrm{d}}_{532}$ showed higher values in mixed dust/smoke layers (ML) compared to pure dust or dust–dominated layers (DL). Average values of

$$\frac{\Delta\beta^{\mathrm{d}}_{532}}{\beta^{\mathrm{d}}_{532}} = 0.14 \text{ (DL) and } 0.20 \text{ (ML)}$$

were found for the SAMUM–2a data set. In cases with a distinct edge between the two layers, the strong gradient in the profile of the volume depolarization ratio causes an error peak in the transition zone between dust and mixed dust/smoke layers (Tesche et al. 2009b). The spike vanishes in cases of an even mixture of dust and smoke throughout the atmospheric column.

The dust backscatter coefficients at wavelengths different from 532 nm were calculated according to Equation (4.9). The backscatter–related Ångström exponents for mineral dust and their respective errors were taken from the SAMUM–1 data set (see Figure 6.8). Errors were calculated as

$$\frac{\Delta\beta^{\mathrm{d}}_{\lambda}}{\beta^{\mathrm{d}}_{\lambda}} = \sqrt{\left(\frac{\Delta\beta^{\mathrm{d}}_{532}}{\beta^{\mathrm{d}}_{532}}\right)^2 + \left(\mathring{a}_{355/532}\frac{\lambda}{532}\frac{\Delta\mathring{a}}{\mathring{a}}\right)^2}$$

with

$$\frac{\Delta\mathring{a}^{\beta,\mathrm{d}}_{355/532}}{\mathring{a}^{\beta,\mathrm{d}}_{355/532}} = 1.05$$

and

$$\frac{\Delta\mathring{a}^{\beta,\mathrm{d}}_{532/1064}}{\mathring{a}^{\beta,\mathrm{d}}_{532/1064}} = 0.57\,.$$

The analysis of the SAMUM–2a data resulted in mean errors of

$$\frac{\Delta\beta^{\mathrm{d}}_{355}}{\beta^{\mathrm{d}}_{355}} = 0.19 \text{ (DL) and } 0.24 \text{ (ML)}$$

and

$$\frac{\Delta\beta^{\mathrm{d}}_{1064}}{\beta^{\mathrm{d}}_{1064}} = 0.17 \text{ (DL) and } 0.22 \text{ (ML)}\,.$$

Smoke Backscatter Coefficient

The 532–nm smoke backscatter coefficient was calculated in the same manner as the one for mineral dust. Consequently, errors of β^{s}_{532} show the same dependencies and were calculated as

$$\frac{\Delta\beta^{\mathrm{s}}_{532}}{\beta^{\mathrm{s}}_{532}} = \frac{\sqrt{\left(\frac{\Delta\beta^{\mathrm{p}}_{532}}{\beta^{\mathrm{p}}_{532}}\right)^2 + \left(\frac{(1+\delta^{\mathrm{d}}_{532})\delta^{\mathrm{p}}_{532}}{(1+\delta^{\mathrm{p}}_{532})(\delta^{\mathrm{p}}_{532}-\delta^{\mathrm{d}}_{532})}\frac{\Delta\delta^{\mathrm{p}}_{532}}{\delta^{\mathrm{p}}_{532}}\right)^2 +}}{\left(\frac{(\delta^{\mathrm{d}}_{532}+1)\delta^{\mathrm{s}}_{532}}{(\delta^{\mathrm{s}}_{532}-\delta^{\mathrm{d}}_{532})(1+\delta^{\mathrm{s}}_{532})}\frac{\Delta\delta^{\mathrm{s}}_{532}}{\delta^{\mathrm{s}}_{532}}\right)^2 + \left(\frac{(\delta^{\mathrm{p}}-\delta^{\mathrm{s}})\delta^{\mathrm{d}}}{(\delta^{\mathrm{s}}-\delta^{\mathrm{d}})(\delta^{\mathrm{p}}-\delta^{\mathrm{d}})}\frac{\Delta\delta^{\mathrm{d}}}{\delta^{\mathrm{d}}}\right)^2}}.$$

The error of the smoke backscatter coefficient can only be obtained for mixed dust/smoke layers and is of the order of the error of the dust backscatter coefficient within pure dust layers with

$$\frac{\Delta\beta^{\mathrm{s}}_{532}}{\beta^{\mathrm{s}}_{532}} = 0.08\ldots0.14\,.$$

Smoke backscatter coefficients at the other wavelengths were calculated by subtracting dust backscatter from the total backscatter coefficients. Thus errors were calculated as

$$\frac{\Delta\beta^{\mathrm{s}}_{\lambda}}{\beta^{\mathrm{s}}_{\lambda}} = \sqrt{\left(\frac{\Delta\beta^{\mathrm{p}}_{\lambda}}{\beta^{\mathrm{p}}_{\lambda}}\right)^2 + \left(\frac{\Delta\beta^{\mathrm{d}}_{\lambda}}{\beta^{\mathrm{d}}_{\lambda}}\right)^2}$$

and showed mean values of

$$\frac{\Delta\beta^{\mathrm{s}}_{355}}{\beta^{\mathrm{s}}_{355}} = 0.20\ldots0.30$$

and

$$\frac{\Delta\beta^{\mathrm{s}}_{1064}}{\beta^{\mathrm{s}}_{1064}} = 0.18\ldots0.50$$

for the analyzed days of the SAMUM–2a data set.

8.1.2 Extinction Coefficients

Total Particle Extinction Coefficient

As in case of the particle backscatter coefficient large errors of the particle extinction coefficient of up to 10% can be introduced by strong gradients in the profiles of pressure and temperature. During SAMUM this uncertainty was weakened by using radiosonde ascends. The error introduced by a bad assumption of the Ångström exponent is 2%–4%. As in case of the backscatter coefficient the temporal variability of atmospheric aerosol conditions and the occurence of clouds in the measurement can introduce large errors of the extinction coefficient. Cloud screening and an appropriate choice of averaging time and vertical smoothing length reduces the noise of the Raman signals and thus also controls the error of the extinction coefficient.

According to Ansmann et al. (1992) total extinction coefficients calculated from Raman signals are assumed to have errors of

$$\frac{\Delta\alpha^{\mathrm{p}}_{355}}{\alpha^{\mathrm{p}}_{355}} = \frac{\Delta\alpha^{\mathrm{p}}_{532}}{\alpha^{\mathrm{p}}_{532}} = 0.15\,.$$

Dust Extinction Coefficient

Dust extinction coefficients were calculated from the derived dust backscatter coefficients and the dust lidar ratios from SAMUM–1. The errors were obtained as

$$\frac{\Delta\alpha^{\mathrm{d}}_{\lambda}}{\alpha^{\mathrm{d}}_{\lambda}} = \sqrt{\left(\frac{\Delta\beta^{\mathrm{d}}_{\lambda}}{\beta^{\mathrm{d}}_{\lambda}}\right)^2 + \left(\frac{\Delta S^{\mathrm{d}}_{\lambda}}{S^{\mathrm{d}}_{\lambda}}\right)^2}\,.$$

The SAMUM–1 dust lidar ratio was 55±5 sr at 355 and 532 nm. Thus the relative error is

$$\frac{\Delta S^{\mathrm{d}}_{355}}{S^{\mathrm{d}}_{355}} = \frac{\Delta S^{\mathrm{d}}_{532}}{S^{\mathrm{d}}_{532}} = 0.13\,.$$

Because backscatter coefficient, lidar ratio, and their respective errors contribute evenly to the error of the extinction coefficient, increased/decreased errors of $\alpha^{\mathrm{d}}_{\lambda}$ are due to deviations of the dust backscatter coefficient and its uncertainty while the absolute contribution of the dust lidar ratio and its error remain constant. As in the case of the dust backscatter coefficient, reliable measurements of the particle depolarization ratio as well as a trustworthy assumption of the dust depolarization ratio are the major factors that regulate the results of the dust extinction coefficient.

Smoke Extinction Coefficient

The error of the smoke extinction coefficient was calculated from the errors of total aerosol and dust extinction coefficients as

$$\frac{\Delta\alpha^{\mathrm{s}}_{\lambda}}{\alpha^{\mathrm{s}}_{\lambda}} = \sqrt{\left(\frac{\Delta\alpha^{\mathrm{p}}_{\lambda}}{\alpha^{\mathrm{p}}_{\lambda}}\right)^2 + \left(\frac{\Delta\alpha^{\mathrm{d}}_{\lambda}}{\alpha^{\mathrm{d}}_{\lambda}}\right)^2}\,.$$

While the total extinction coefficient is strongly dependent on the noise of the detected Raman signals (that can be decreased by choosing appropriate temporal and spatial smoothing windows) the error of the smoke extinction coefficient is modulated by the error of the dust backscatter coefficient. The analysis of the SAMUM–2a data set resulted in mean errors of

$$\frac{\Delta\alpha^{\mathrm{s}}_{355}}{\alpha^{\mathrm{s}}_{355}} = 0.20\ldots0.30$$

and

$$\frac{\Delta\alpha^{\mathrm{s}}_{532}}{\alpha^{\mathrm{s}}_{532}} = 0.15\ldots0.40$$

depending on the measured total backscatter and extinction coefficients. Errors of $\alpha^{\mathrm{s}}_{\lambda}$ generally decrease with increasing total backscatter and extinction coefficients.

8.1.3 Lidar Ratios

In case of a Raman lidar, which measures backscatter and extinction coefficients independent of each other, the lidar ratio can easily be calculated. The lidar ratio of pure dust is a statistical quantity derived from the average value and standard deviation of measurements of SAMUM–1 (see Figure 6.8). The random error of the lidar ratio was calculated as

$$\frac{\Delta S_\lambda}{S_\lambda} = \sqrt{\left(\frac{\Delta \alpha_\lambda}{\alpha_\lambda}\right)^2 + \left(\frac{\Delta \beta_\lambda}{\beta_\lambda}\right)^2}\,.$$

This approach resulted in values on the order of 15% at 355 nm and of 20% at 532 nm. The necessity to correct the 532–nm elastic–backscatter signal caused an increase in the uncertainty of the lidar ratio at this wavelength.

The aerosol–type separation of the SAMUM–2a dataset resulted in smoke lidar ratios with errors of

$$\frac{\Delta S^{\mathrm{s}}_{355}}{S^{\mathrm{s}}_{355}} = 0.30 \ldots 0.40$$

and

$$\frac{\Delta S^{\mathrm{s}}_{532}}{S^{\mathrm{s}}_{532}} = 0.25 \ldots 0.45\,.$$

8.1.4 Ångström Exponents

Ångström exponents can be calculated for all quantities that are measured at different wavelengths. Values calculated from extinction coefficients can be directly compared to optical–depth measurements from a nearby Sun photometer, if the observed aerosol layer can be assumed to be well–mixed from ground level to its top, i.e., as in case of SAMUM–1. Statistical results of dust Ångström exponents from SAMUM–1 measurements are assumed to be representative for pure dust. The error of the Ångström exponent was calculated as

$$\frac{\Delta \mathring{a}_{\lambda_1/\lambda_2}}{\mathring{a}_{\lambda_1/\lambda_2}} = \frac{1}{\ln X_{\lambda_1}/X_{\lambda_2}} \sqrt{\left(\frac{\Delta X_{\lambda_1}}{X_{\lambda_1}}\right)^2 + \left(\frac{\Delta X_{\lambda_2}}{X_{\lambda_2}}\right)^2}$$

with X being β, α, or S. Ångström exponents for pure biomass–burning smoke which were obtained by applying the aerosol–type separation method to the SAMUM–2a data set generally showed reliable values (around unity and larger, with an increase compared to values for data unscreened of the influence of mineral dust) but are afflicted with large errors of

$$\frac{\Delta \mathring{a}^{\beta,\mathrm{s}}_{355/532}}{\mathring{a}^{\beta,\mathrm{s}}_{355/532}} = 0.25 \ldots 0.80\,,$$

$$\frac{\Delta \mathring{a}^{\beta,\mathrm{s}}_{532/1064}}{\mathring{a}^{\beta,\mathrm{s}}_{532/1064}} = 0.40 \ldots 0.90\,,$$

and

$$\frac{\Delta\, \mathring{a}^{\alpha,\mathrm{s}}_{355/532}}{\mathring{a}^{\alpha,\mathrm{s}}_{355/532}} = 0.30 \ldots 1.00\,.$$

Note that errors of the Ångström exponent increase dramatically, if the uncertainty of the input parameters increases.

8.1.5 Volume Depolarization Ratios

The uncertainty of the analog signals of the depolarization channels 710p and 710s was estimated to describe the noise of the individual signals. In the same way, the error of the ratio of the two channels was estimated to account for the noise of this signal ratio. Saturation effects of the detector can produce oscillations at distances beyond the signal peak. In that case, weaker signals at greater distances are underestimated because the background value of the analog detection channel becomes negative. This effect causes systematic errors of the measured signals and thus of the calibration function which is needed for the calculation of the volume depolarization ratio. Ultimately, the effect results in systematically erroneous profiles of the volume depolarization ratio. To avoid oscillations of the background, the high voltage (analog detection) of the depolarization channels was adjusted to keep the maximum signals to an appropriate level. This approach was validated by test measurements with a pulse generator, which were performed after SAMUM–2. The calibration factor V^* for the determination of the volume depolarization ratio is dependent on height and only the use of the calibration function $V^*(z)$ instead of a constant factor led to a realistic decrease of the volume depolarization ratio at the top of the aerosol layer. Values of the depolarization ratio are more trustworthy in regions of strong return signals (in the near range or from mineral dust that produces strong signals in the perpendicular channel) than at the top of an aerosol layer. Because the random error increases with height due to the decrease of signal intensity.

Volume Depolarization Ratio at 710 nm

One of the crucial parameters for adequate measurements of the volume depolarization ratio is the cross–talk between parallel and perpendicular channel. Therefore, the position of the respective channels behind the PBS (transmission or reflection of a certain signal) is chosen in a way to minimize the contribution of the usually much stronger parallel signal to the measurement of the perpendicular channel. In the BERTHA receiver, co–polarized light is measured in the reflected branch (${}^{\parallel}R = 0.999$ and ${}^{\perp}R = 0.05$) of the PBS while cross–polarized light is measured in the transmitted branch (${}^{\perp}T = 0.95$ and ${}^{\parallel}T = 0.001$).

For the calculation of the error of the linear volume depolarization ratio at 710 nm as measured with BERTHA the original transmission and reflection of the parallel components of the backscattered light by the PBS were simplified to ${}^{\parallel}T = 0$ and ${}^{\parallel}R = 1$, i.e., the transmission of parallel polarized light into the perpendicular channel

was neglected. This can be achieved by placing a polarizer in front of the perpendicular channel to screen the transmitted fraction of parallel polarized light from the detected signal. As a consequence, Equation (3.21) simplifies to

$$\delta^{\mathrm{v}}_{710} \approx \frac{V^*\delta^*}{{}^{\perp}RV^*\delta^*G - {}^{\perp}T} = \tilde{\delta^{\mathrm{v}}}$$

and the error of $\delta^{\mathrm{v}}_{710}$ can be approximated as

$$\frac{\Delta\tilde{\delta^{\mathrm{v}}}}{\tilde{\delta^{\mathrm{v}}}} = \frac{2V^*\,{}^{\perp}R\delta^*G - {}^{\perp}T}{{}^{\perp}RV^*\delta^*G - {}^{\perp}T}\sqrt{\left(\frac{\Delta V^*}{V^*}\right)^2 + \left(\frac{\Delta\delta^*}{\delta^*}\right)^2 + \left(\frac{\Delta G}{G}\right)^2 + \frac{\left(\frac{-V^*\delta^*G\,{}^{\perp}R}{2V^*\,{}^{\perp}R\delta^*G - {}^{\perp}T}\frac{\Delta\,{}^{\perp}R}{{}^{\perp}R}\right)^2 + \left(\frac{{}^{\perp}T}{2V^*\,{}^{\perp}R\delta^*G - {}^{\perp}T}\frac{\Delta\,{}^{\perp}T}{{}^{\perp}T}\right)^2}{}}.$$

The errors of the calibration factor ΔV^* and of the ratio of perpendicular to parallel signal $\Delta\delta^*$ are discussed below. The value of the gain ratio of the depolarization channels was found to be $G = 0.726 \pm 0.04$ (see Table 5.1) with a generously estimated error that includes results of calibration measurements at all zenith angles of the scanner unit. Values of ${}^{\perp}R = 0.05 \pm 0.05$ and ${}^{\perp}T = 0.95 \pm 0.05$ for a common PBS were used for the calculation of the linear volume depolarization ratio and its uncertainty.

Calibration Factor

Profiles of the calibration factor $V^*_{\pm 22.5^\circ}$ were obtained from the analysis of calibration measurements with the HWP set to $\phi_1 = +22.5^\circ$ and $\phi_2 = -22.5^\circ$ (see Section 5.4.2). The signal ratios were merged to

$$V_{+22.5^\circ} = \frac{P^{\mathrm{R}}_{+22.5^\circ}}{P^{\mathrm{T}}_{+22.5^\circ}} \text{ and } V_{-22.5^\circ} = \frac{P^{\mathrm{R}}_{-22.5^\circ}}{P^{\mathrm{T}}_{+22.5^\circ}}$$

and the constant properties of the PBS were set to

$$Q = \frac{{}^{\parallel}T + {}^{\perp}T}{{}^{\parallel}R + {}^{\perp}R}$$

with the estimate of $\Delta Q = 0.05$. The error of the calibration factor was then calculated as

$$\frac{\Delta V^*_{\pm 22.5^\circ}}{V^*_{\pm 22.5^\circ}} = \frac{\sqrt{\left(\frac{\Delta D}{D}\right)^2 + \left(\frac{\Delta Q}{Q}\right)^2 + \left(\frac{(V_{+22.5^\circ}V_{-22.5^\circ})^2}{2}\frac{\Delta V_{+22.5^\circ}}{V_{+22.5^\circ}}\right)^2 + \left(\frac{(V_{+22.5^\circ}V_{-22.5^\circ})^2}{2}\frac{\Delta V_{-22.5^\circ}}{V_{-22.5^\circ}}\right)^2}}{}.$$

The random error of the individual ratios $\Delta V_{+22.5^\circ}$ and $\Delta V_{-22.5^\circ}$ of the depolarization channels 710p and 710s was estimated from the signal noise in a way that the error bars of a smoothed profile cover the majority of the points of the unsmoothed profile.

As mentioned earlier a bias can be introduced by overshoots when the detector is exposed to too strong signals. During the measurements the high voltage of the analog channels was adjusted in a way to assure moderate signals. After SAMUM–2, when BERTHA was back in Leipzig, measurements with a pulse generator were performed to investigate the reaction of the analog channels to very strong signals. Such a study, for which strong light pulses were lead through the lidar detector, simulates the effect of strong return signals from the planetary boundary layer. Too strong signals in the near range can cause a significant underestimation of signals in the far range and thus introduce a source for systematic error at larger heights. The test measurements revealed that the voltage adjustment of the measurements during SAMUM–2 ensures signal intensities that should not introduce large errors to the measured signals. The test measurements with maximum signals set to values as encountered during SAMUM–2 resulted in background–to–pulse maximum ratios of 1/10000 and 1/20000 for the parallel and perpendicular channel, respectively. These measurements also revealed that the contrast between signal maximum and background decreases quickly, if the signal maximum is too large.

Measured Signal Ratio

While V^* describes instrument properties that need to be considered for the calculation of the linear volume depolarization ratio, the atmospheric information is contained in the profile of δ^*_{710}. The latter was measured with the HWP set to its zero position ($\phi = 0°$) as $\delta^*_{710} = P^{\mathrm{s}}_{0°}/P^{\mathrm{p}}_{0°}$. The random error was calculated as

$$\frac{\Delta\delta^*}{\delta^*} = \sqrt{\left(\frac{\Delta P^{\mathrm{s}}_{0°}}{P^{\mathrm{s}}_{0°}}\right)^2 + \left(\frac{\Delta P^{\mathrm{p}}_{0°}}{P^{\mathrm{p}}_{0°}}\right)^2}\,.$$

The uncertainties of the measured profiles of $P^{\mathrm{p}}_{0°}$ and $P^{\mathrm{s}}_{0°}$ were estimated from the signal noise in the same way as the errors of the signal ratios needed for the calculation of the calibration factor. As in case of calibration measurements, strong signals can produce overshoots that introduce systematic errors to the retrieval. As during the calibration, maximum signals were kept to moderate values to minimize this effect.

In summary, the random error of the volume depolarization ratio at 710 nm varied between 10% in the near range (strong and smooth signals) and 15%–20% in the upper parts of the aerosol layers (low signal–to–noise ratio). The uncertainty is dominated by the errors of δ^*_{710} and $V^*_{\pm 22.5°}$ with contributions of up to 10 and 7 percentage points, respectively. The properties of the PBS account for a maximum error of 6 percentage points, if the probably excessive errors of 0.05 are applied in the error calculation. However, systematic errors can always be introduced, if strong signals are not weakened properly by adjusting the high voltage of the depolarization channels.

532–nm Volume Depolarization Ratio derived from measurements at 710 nm

The volume depolarization ratio at 710 nm was extrapolated to 532 nm by using the linear relation of Equation (5.21). The error of this method is composed of the error

in the retrieval of the volume depolarization ratio at 710 nm and the error of the extrapolation itself. Comparisons of profiles extrapolated to 532 nm and measured by MULIS at 532 nm generally showed a difference below 15%. Thus the error of the extrapolated volume depolarization ratio was calculated as

$$\Delta\delta^{\mathrm{v}}_{532} = \sqrt{(0.63983\,\Delta\delta^{\mathrm{v}}_{710})^2 + (0.15\,\delta^{\mathrm{v}}_{532})^2}\,.$$

Because a constant maximum offset between extrapolated and measured profiles was assumed, variations of the error of the extrapolated volume depolarization ratio are related to the uncertainty in the retrieval of the 710–nm volume depolarization ratio. The application of the depolarization extrapolation to the data collected during SAMUM–2 led to 532–nm volume depolarization ratio profiles with errors of 20%–30%. Due to the decrease of the signal–to–noise ratio with height, the uncertainty of the volume depolarization ratio increases with height.

8.1.6 Particle Depolarization Ratios

The calculation of the particle depolarization ratio according to Equation (3.23) requires knowledge of the profiles of the volume depolarization ratio δ^{v}, the molecular depolarization ratio δ^{m}, the molecular backscatter coefficient β^{m}, and the particle backscatter coefficient β^{p}. The random error of the linear particle depolarization ratio was calculated as

$$\begin{aligned}\Delta\delta^{\mathrm{p}} \;=\; & \sqrt{\left(\frac{\beta^{\mathrm{p}}(1+\delta^{\mathrm{m}})^2(\beta^{\mathrm{m}}+\beta^{\mathrm{p}})}{\left[\beta^{\mathrm{m}}(\delta^{\mathrm{m}}-\delta^{\mathrm{v}})+\beta^{\mathrm{p}}(1+\delta^{\mathrm{m}})\right]^2}\Delta\delta^{\mathrm{v}}\right)^2 + \\ & \left(\frac{\beta^{\mathrm{m}}\beta^{\mathrm{p}}(1+\delta^{\mathrm{v}})^2}{\left[\beta^{\mathrm{m}}(\delta^{\mathrm{m}}-\delta^{\mathrm{v}})+\beta^{\mathrm{p}}(1+\delta^{\mathrm{m}})\right]^2}\Delta\delta^{\mathrm{m}}\right)^2 + \\ & \left(\frac{\beta^{\mathrm{p}}(1+\delta^{\mathrm{m}})(\delta^{\mathrm{v}}-\delta^{\mathrm{m}})(1-\delta^{\mathrm{v}})}{\left[\beta^{\mathrm{m}}(\delta^{\mathrm{m}}-\delta^{\mathrm{v}})+\beta^{\mathrm{p}}(1+\delta^{\mathrm{m}})\right]^2}\Delta\beta^{\mathrm{m}}\right)^2 + \\ & \left(\frac{\beta^{\mathrm{m}}(1+\delta^{\mathrm{m}})(\delta^{\mathrm{m}}-\delta^{\mathrm{v}})(\delta^{\mathrm{v}}+1)}{\left[\beta^{\mathrm{m}}(\delta^{\mathrm{m}}-\delta^{\mathrm{v}})+\beta^{\mathrm{p}}(1+\delta^{\mathrm{m}})\right]^2}\Delta\beta^{\mathrm{p}}\right)^2}\,.\end{aligned}$$

The individual errors for the input parameters at the respective wavelengths were calculated as previously described.

The error of the particle depolarization ratio is dominated by the uncertainty of the volume depolarization ratio and the particle backscatter coefficient. It furthermore depends strongly on their absolute values in a way that particle depolarization ratios cannot be retrieved accurately in regions of weak aerosol backscatter signals. The molecular contribution to the calculation of the particle depolarization ratio is of minor importance at 532 nm and 710 nm. Even large deviations in the molecular backscatter coefficient and the molecular depolarization ratio of 50% cause negligible variations in the profile of the particle depolarization ratio. The analysis of the SAMUM data set resulted in errors of the particle depolarization ratio that were about 5 percentage points higher than that of the respective volume depolarization ratio profiles.

8.2 List of Abbreviations

Abbreviation	Description
a	analog
ACE–2	North Atlantic Regional Aerosol Characterization Experiment 2
AD–Net	Asian Dust Network
AERONET	Aerosol Robotic Network
agl	above ground level
AMMA	African Monsoon Multidisciplinary Analysis
AOT	aerosol optical thickness
asl	above sea level
BERTHA	Backscatter Extinction lidar–Ratio Temperature Humidity Apparatus
CALIPSO	Cloud–Aerosol Lidar and Infrared Pathfinder Satellite Observation
DABEX	Dust and Biomass–burning Experiment
DLR	Deutsches Zentrum für Luft– und Raumfahrt (German Aerospace Center)
DREAM	Dust Regional Atmospheric Model
EARLINET	European Aerosol Research Lidar Network
Giovanni	GES–DISC (Goddard Earth Sciences Data and Information Services Center) Interactive Online Visualization and Analysis Infrastructure
HSRL	high spectral resolution lidar
HWP	half–wave plate
HYSPLIT	hybrid single–particle Lagrangian integrated trajectories model
IfT	Leibniz–Institut für Troposphärenforschung (Leibniz Institute for Tropospheric Research)
INDOEX	Indian Ocean Experiment
IR	infrared
ITCZ	inter–tropical convergence zone
LACE 98	Lindenberg Aerosol Characterization Experiment 1998
LAGRANTO	Lagrangian analysis tool
lidar	light detection and ranging
LITE	Lidar–in–space Technology Experiment
LT	local time
MIM	Meteorological Institute of the Ludwig–Maximilians–Universität Munich
MISR	Multi–angle Imaging Spectroradiometer
MODIS	Moderate Resolution Imaging Spectroradiometer
MULIS	Multiwavelength Lidar System
NAMMA	NASA's contribution to AMMA
Nd:YAG	neodym–doted yttrium–aluminum–granat
PBS	polarizing beam splitter cube
pc	photon counting

PMT	photomultiplier tube
POLIS	Portable Lidar System
PRIDE	Puerto Rican Dust Experiment
PRIDE–PRD	Program of Regional Integrated Experiments on Air Quality over Pearl River Delta of China
radar	radio detection and ranging
RFOV	receiver field of view
SAL	Saharan air layer
SAMUM	Saharan Mineral Dust Experiment
SHADE	Saharan Dust Experiment
SPM	Sun photometer
SSA	single–scattering albedo
SSARA	Sun–Sky Automatic Radiometer
Ti:Sa	titanium–sapphire
UAE^2	United Arab Emirates Unified Aerosol Experiment
UTC	universal time coordinated
UV	ultraviolet

8.3 List of Symbols

Symbol	Description	Unit
$\parallel$	the co–polarized component of a quantity	
$\perp$	the cross–polarized component of a quantity	
R	the reflected component of a quantity	
T	the transmitted component of a quantity	
Greek Symbols		
$\alpha(\lambda, R)$	total extinction coefficient	m^{-1}
$\alpha^{\mathrm{d}}(\lambda, R)$	dust extinction coefficient	m^{-1}
$\alpha^{\mathrm{m}}(\lambda, R)$	molecular extinction coefficient	m^{-1}
$\alpha^{\mathrm{nd}}(\lambda, R)$	non–dust extinction coefficient	m^{-1}
$\alpha^{\mathrm{p}}(\lambda, R)$	particle extinction coefficient	m^{-1}
$\alpha^{\mathrm{s}}(\lambda, R)$	smoke extinction coefficient	m^{-1}
$\beta(\lambda, R)$	total backscatter coefficient	$\mathrm{m}^{-1}\mathrm{sr}^{-1}$
$\beta^{\mathrm{d}}(\lambda, R)$	dust backscatter coefficient	$\mathrm{m}^{-1}\mathrm{sr}^{-1}$
$\beta^{\mathrm{m}}(\lambda, R)$	molecular backscatter coefficient	$\mathrm{m}^{-1}\mathrm{sr}^{-1}$
$\beta^{\mathrm{nd}}(\lambda, R)$	non–dust backscatter coefficient	$\mathrm{m}^{-1}\mathrm{sr}^{-1}$
$\beta^{\mathrm{p}}(\lambda, R)$	particle backscatter coefficient	$\mathrm{m}^{-1}\mathrm{sr}^{-1}$
$\beta^{\mathrm{s}}(\lambda, R)$	smoke backscatter coefficient	$\mathrm{m}^{-1}\mathrm{sr}^{-1}$
γ	Lagrange multiplier	
$\Gamma(n)$	penalty term	
$\delta^{\mathrm{v}}(\lambda, R)$	linear volume depolarization ratio	
$\delta^{\mathrm{d}}(\lambda, R)$	linear dust depolarization ratio	
$\delta^{\mathrm{m}}(\lambda, R)$	linear molecular depolarization ratio	
$\delta^{\mathrm{nd}}(\lambda, R)$	linear non–dust depolarization ratio	
$\delta^{\mathrm{o}}(\lambda, R)$	linear maritime depolarization ratio	
$\delta^{\mathrm{p}}(\lambda, R)$	linear particle depolarization ratio	
$\delta^{\mathrm{s}}(\lambda, R)$	linear smoke depolarization ratio	
ϵ_p	sum of experimental and mathematical error	
$\boldsymbol{\epsilon}$	vector of ϵ_p	
$\epsilon_p^{\mathrm{exp}}$	experimental (measurement) error	
$\epsilon_p^{\mathrm{math}}$	mathematical residual error	
ζ	position of a sheet polarizer	$^\circ$
$\eta(\lambda)$	transmission	
Θ	scattering zenith angle	$^\circ$
Θ_{Z}	zenith view angle of a lidar system	$^\circ$
λ	wavelength	m
λ_0	laser wavelength	m
λ_{R}	wavelength of Raman–scattered light	m
ν	wave number	m^{-1}
ν_{in}	wave number of incident light	m^{-1}
ν_{out}	wave number of Raman–scattered light	m^{-1}

σ^{m}	scattering cross–section of molecules	m^2
τ_{p}	laser pulse length	s
Φ	scattering azimuth angle	$^\circ$
φ	angle between the planes of polarization of emitted and detected light	$^\circ$
ϕ	offset angle between zero positions of a half–wave plate and the parallel channel	$^\circ$

Latin Symbols

$\mathring{a}_{\lambda_1,\lambda_2}(R)$	Ångström exponent	
$\mathring{a}^{\alpha}_{\lambda_1,\lambda_2}(R)$	extinction–related Ångström exponent	
$\mathring{a}^{\alpha,\mathrm{d}}_{\lambda_1,\lambda_2}(R)$	extinction–related Ångström exponent of dust	
$\mathring{a}^{\alpha,\mathrm{nd}}_{\lambda_1,\lambda_2}(R)$	extinction–related Ångström exponent of non–dust	
$\mathring{a}^{\alpha,\mathrm{s}}_{\lambda_1,\lambda_2}(R)$	extinction–related Ångström exponent of smoke	
$\mathring{a}^{\beta}_{\lambda_1,\lambda_2}(R)$	backscatter–related Ångström exponent	
$\mathring{a}^{\beta,\mathrm{d}}_{\lambda_1,\lambda_2}(R)$	backscatter–related Ångström exponent of dust	
$\mathring{a}^{\beta,\mathrm{nd}}_{\lambda_1,\lambda_2}(R)$	backscatter–related Ångström exponent of non–dust	
$\mathring{a}^{\beta,\mathrm{s}}_{\lambda_1,\lambda_2}(R)$	backscatter–related Ångström exponent of smoke	
$\mathring{a}^{S}_{\lambda_1,\lambda_2}(R)$	lidar–ratio–related Ångström exponent	
a_1	element of $\boldsymbol{F}(180^\circ)$	
a_2	element of $\boldsymbol{F}(180^\circ)$	
A_{T}	area of the receiver telescope	m^2
$A_{p,j}(m)$	kernel matrix	
$\mathbf{A}$	weight matrix	
$B_j(r)$	triangular base functions	
c	speed of light	m/s
c_0	speed of light in vacuum $c_0 = 299792458\,\mathrm{m/s}$	m/s
d	depolarization factor	
E	energy	W
$\boldsymbol{E}$	electric field vector	
$\boldsymbol{F}(\Theta,\Phi)$	4×4 transformation matrix	
$F_{ij}(\Theta,\Phi)$	elements of $\boldsymbol{F}(\Theta)$	
g_p	optical input data β_λ and α_λ	
$\mathbf{g}$	vector of optical input data	
G	gain ratio of the depolarization channels	
h	Planck constant $h = 6.62606896 \times 10^{-34}\,\mathrm{m^2kg/s}$	$\mathrm{m^2kg/s}$
$\mathbf{H}$	smoothing matrix	
I	Stokes parameter of total intensity	
$K(D,\delta^{\mathrm{v}})$	correction term	
$K_p(r,m)$	kernel function	
m	complex refractive index	
n^{p}	particle number concentration	m^{-3}
n^{m}	molecular number concentration	m^{-3}
n_{R}	number concentration of inelastically scattering molecules	m^{-3}

$n(r)$	particle number size distribution	m^{-3}
$O(\lambda, R)$	overlap function	
$p(\Theta)$	scattering phase function	
$P_0(\lambda)$	emitted laser energy	W
$P(\lambda, R)$	lidar signal/detected energy	W
Q	Stokes parameter of intensity along the x and y axes	
$Q_p(r, m)$	dimensionless backscatter or extinction efficiency	
r	particle radius	m
r_{eff}	effective particle radius	m
$r_{\max}$	upper size range of inversion	m
$r_{\min}$	lower size range of inversion	m
R	range	m
R_0	reference height	m
${}^{\parallel}R$	reflectance of co–polarized light	
${}^{\perp}R$	reflectance of cross–polarized light	
$\boldsymbol{S}_0$	Stokes vector of incident light	
$\boldsymbol{S}$	Stokes vector of scattered light	
$S(\lambda, R)$	lidar ratio	sr
$S^{\mathrm{d}}(\lambda, R)$	dust lidar ratio	sr
$S^{\mathrm{m}}(\lambda, R)$	molecular lidar ratio	sr
$S^{\mathrm{nd}}(\lambda, R)$	non–dust lidar ratio	sr
$S^{\mathrm{p}}(\lambda, R)$	particle lidar ratio	sr
$S^{\mathrm{s}}(\lambda, R)$	smoke lidar ratio	sr
t	time	s
${}^{\parallel}T$	transmittance of co–polarized light	
${}^{\perp}T$	transmittance of cross–polarized light	
U	Stokes parameter of intensity along the $-45°/+45°$ axes	
V	Stokes parameter of right– and left–hand circular intensity	
V^{R}	amplification factor of reflected light	
V^{T}	amplification factor of transmitted light	
V^*	relative amplification factor	
w_j	weight factor	
$\mathbf{w}$	vector of weight factors	
x	Cartesian coordinate	
x	size parameter	
y	Cartesian coordinate	
z	Cartesian coordinate	

Bibliography

Ackermann, J., 1998: The extinction–to–backscatter ratio of tropospheric aerosol: A numerical study. *J. Atmos. Oceanic Technol.*, **15**, 1043–1050.

Althausen, D., D. Müller, A. Ansmann, U. Wandinger, H. Hube, E. Clauder, and S. Zörner, 2000: Scanning 6–wavelength 11–channel aerosol lidar. *J. Atmos. Oceanic Technol.*, **17**, 1469–1482.

Alvarez, R. J., L. M. Caldwell, V. H. Li, D. A. Krueger, and C.-Y. She, 1990: High–spectral–resolution lidar measurement of tropospheric backscatter ratio with barium atomic blocking filters. *J. Atmos. Ocean. Technol.*, **7**, 876–881.

Alvarez, J. M., M. A. Vaughan, C. A. Hostetler, W. H. Hunt, and D. M. Winker, 2006: Calibration technique for polarization–sensitive lidars. *J. Atmos. Oceanic Technol.*, **23**, 683–699.

Amiridis, V., D. S. Balis, S. Kazadzis, E. Giannakaki, A. Papayannis, and C. Zerefos, 2005: Four–year aerosol observations with a Raman lidar at Thessaloniki, Greece, in the framework of the European Aerosol Research Lidar Network (EARLINET). *J. Geophys. Res.*, **110**, 10.1029/2005JD006190.

Ångström, A., 1964: The parameters of atmospheric turbidity. *Tellus*, **16**, 10.1111/j.2153-3490.1964.tb00144.x.

Ansmann, A., M. Riebesell, U. Wandinger, C. Weitkamp, E. Voss, W. Lahmann, and W. Michaelis, 1992: Combined Raman elastic–backscatter LIDAR for vertical profiling of moisture, aerosol extinction, backscatter, and LIDAR ratio. *Appl. Phys.*, **55**, 10.1007/BF00348608.

Ansmann, A., U. Wandinger, M. Riebesell, C. Weitkamp, and W. Michaelis, 1992: Independent measurement of extinction and backscatter profiles in cirrus clouds by using a combined Raman elastic–backscatter lidar. *Appl. Opt.*, **31**, 10.1364/AO.31.007113.

Ansmann, A., D. Althausen, U. Wandinger, K. Franke, D. Müller, F. Wagner, and J. Heintzenberg, 2000: Vertical profiling of the Indian aerosol plume with six–wavelength lidar during INDOEX: A first case study. *Geophys. Res. Lett.*, **27**, 10.1029/1999GL010902.

Ansmann, A., U. Wandinger, A. Wiedensohler, and U. Leiterer, 2002a: Lindenberg Aerosol Characterization Experiment 1998 (LACE 98): Overview. *J. Geophys. Res.*, **107**, 10.1029/2000JD000233.

Ansmann, A., F. Wagner, D. Müller, D. Althausen, A. Herber, and coauthors, 2002b: European pollution outbreaks during ACE 2: optical particle properties inferred from multiwavelength lidar and star–Sun photometry. *J. Geophys. Res.*, **107**, 10.1029/2001JD001109.

Ansmann, A., J. Bösenberg, A. Chaikovsky, A. Comerón, S. Eckhardt, R. Eixmann, V. Freudenthaler, P. Ginoux, L. Komguem, H. Linné, and coauthors, 2003: Long–range transport of Saharan dust to northern Europe: The 11–16 October 2001 outbreak observed with EARLINET. *J. Geophys. Res.*, **108**, 10.1029/2003JD003757.

Ansmann, A. and D. Müller, 2005: *Lidar and Atmospheric Aerosol Particles*, in: LIDAR: Range–Resolved Optical Remote Sensing of the Atmosphere, ed. by C. Weitkamp, Springer. 105–142.

Ansmann, A., M. Tesche, D. Althausen, D. Müller, V. Freudenthaler, B. Heese, M. Wiegner, G. Pisani, P.Knippertz, and O. Dubovik, 2008: Ice formation in Saharan dust over northern Africa observed during SAMUM. *J. Geophys. Res.*, **113**, 10.1029/2007JD008785.

Ansmann, A., M. Tesche, P. Knippertz, E. Bierwirth, D. Althausen, D. Müller, and O. Schulz, 2009a: Vertical profiling of convective dust plumes in southern Morocco during SAMUM. *Tellus*, **61B**, 10.1111/j.1600-0889.2008.00384.x.

Ansmann, A., M. Tesche, P. and Seifert, D. Althausen, R. Engelmann, J. Fruntke, U. Wandinger, I. Mattis, and D. Müller, 2009b: Evolution of the ice phase in tropical altocumulus: SAMUM lidar observations over Cape Verde. *J. Geophys. Res*, **114**, 10.1029/2008JD011659.

Ansmann, A., H. Baars, M. Tesche, D. Müller, D. Althausen, R. Engelmann, T. Pauliquevis, and P. Artaxo, 2009c: Dust and smoke transport from Africa to South America: Lidar profiling over Cape Verde and the Amazon rainforest. *Geophys. Res. Lett.*, **36**, 10.1029/2009GL037923.

Ansmann, A., A. Petzold, K. Kandler, I. Tegen, M. Wendisch, D. Müller, B. Weinzierl, T. Müller, and J. Heintzenberg, 2011: Saharan Mineral Dust Experiments SAMUM–1 and SAMUM–2: What have we learned? *Tellus*, **63B**, submitted.

Arshinov, Y., S. Bobrovnikov, I. Serikov, A. Ansmann, U. Wandinger, D. Althausen, I. Mattis, and D. Müller, 2005: Daytime operation of a pure rotational Raman lidar by use of a Fabry–Perot interferometer. *Appl. Opt.*, **44**, 10.1364/AO.44.003593.

Balis, D. S., V. Amiridis, C. Zerefos, E. Gerasopoulos, M. Andreae, P. Zanis, A. Kazantzidis, S. Kazadzis, and A. Papayannis, 2003: Raman lidar and sunphotometric measurements of aerosol optical properties over Thessaloniki, Greece, during a biomass burning episode. *Atmos. Environ.*, **37**, 10.1016/S1352-2310(03)00581-8.

Balis, D. S., V. Amiridis, S. Nickovic, A. Papayannis, and C. Zerefos, 2004: Optical properties of Saharan dust layers as detected by a Raman lidar at Thessaloniki, Greece. *Geophys. Res. Lett.*, **31**, 10.1029/2004GL019881.

Barbosa, P., D. Stroppiana, J.-M. Grégoire, and J. C. Pereira, 1999: An assessment of vegetation fire in Africa (1981–1991): Burned areas, burned biomass, and atmospheric emissions. *Global Biogeochem. Cycles*, **108**, 10.1029/1999GB900042.

Behrendt, A., 2005: *Temperature Measurements with Lidar*, in: LIDAR: Range–Resolved Optical Remote Sensing of the Atmosphere, ed. by C. Weitkamp, Springer. 273–306.

Ben-Ami, Y., I. Koren, and O. Altaratz, 2009: Patterns of North African dust transport over the Atlantic: winter vs. summer, based on CALIPSO first year data. *Atmos. Chem. Phys.*, **9**, 10.5194/acp-9-7867-2009.

Ben-Ami, Y., I. Koren, Y. Rudich, P. Artaxo, S. T. Martin, and M. O. Andreae, 2010: Transport of North African dust from the Bodélé depression to the Amazon Basin: A case study. *Atmos. Chem. Phys.*, **10**, 10.5194/acp-10-7533-2010.

Berthier, S., P. Chazette, P. Couvert, J. Pelon, F. Dulac, F. Thieuleux, C. Moulin, and T. Pain, 2006: Desert dust aerosol columnar properties over ocean and continental Africa from Lidar In–space Technology Experiment (LITE) and Meteosat synergy. *J. Geophys. Res.*, **111**, 10.1029/2005JD006999.

Bierwirth, E., M. Wendisch, A. Ehrlich, B. Heese, M. Tesche, D. Althausen, A. Schladitz, T. Müller, S. Otto, T. Trautmann, T. Dinter, W. von Hoyningen-Huene, and R. Kahn, 2009: Spectral surface albedo over Morocco and its impact on the radiative forcing of Saharan dust. *Tellus*, **61B**, 10.1111/j.1600-0889.2008.00395.x.

Bohren, C. F. and D. R. Huffman, 1983: *Absorption and Scattering of Light by Small Particles*. John Wiley, New York, 544 pp.

Bösenberg, J., A. Ansmann, J. M. Baldasano, D. Balis, C. Böckmann, B. Calpini, A. Cheikovsky, P. Flamant, and coauthors, 2001: EARLINET: A European Aerosol Research Lidar Network. *Laser Remote Sensing of the Atmosphere. Selected papers of the 20th International Laser Radar Conference*, 155–158.

Bucholtz, A., 1995: Rayleigh–scattering calculations for the terrestrial atmosphere. *Appl. Opt.*, **34**, 10.1364/AO.34.002765.

Cairo, F., G. D. Donfrancesco, A. Adriani, L. Pulvirenti, and F. Fierli, 1999: Comparison of various linear depolarization parameters measured by lidar. *Appl. Opt.*, **38**, 10.1364/AO.38.004425.

Campbell, J. R., E. J. Welton, J. D. Spinhirne, Q. Ji, S.-C. Tsay, S. J. Piketh, M. Barenburg, and B. N. Holben, 2003: Micropulse lidar observations of tropospheric aerosols over northeastern South Africa during the ARREX and SAFARI 2000 dry season experiments. *J. Geophys. Res.*, **108**, 10.1029/2002JD002563.

Cattrall, C., J. Reagan, K. Thome, and O. Dubovik, 2005: Variability of aerosol and spectral lidar and backscatter and extinction ratios of key aerosol types derived from selected Aerosol Robotic Network locations. *J. Geophys. Res.*, **110**, 10.1029/2004JD005124.

Chen, W.-N., S.-Y. Chang, C. C.-K. Chou, Y.-W. Chen, and J.-P. Chen, 2007a: Study of relationship between water–soluble Ca^2+ and lidar depolarization ratio for spring aerosol in the boundary layer. *Atmos. Environ.*, **41**, 10.1016/j.atmosenv.2006.10.012.

Chen, W.-N., F.-J. Tsai, C. C.-K. Chou, S.-Y. Chang, Y.-W. Chen, and J.-P. Chen, 2007b: Optical properties of Asian dust in the free atmosphere measured by Raman lidar at Taipei, Taiwan. *Atmos. Environ.*, **41**, 10.1016/j.atmosenv.2007.06.001.

Chiapello, I., G. Bergametti, L. Gomes, B. Chatenet, F. Dulac, J. Pimenta, and E. S. Suares, 1995: An additional low layer transport of Sahelian and Saharan dust over the North–Eastern Tropical Atlantic. *Geophys. Res. Lett.*, **22**, 10.1029/95GL03313.

Chiapello, I., G. Bergametti, B. Chatenet, P. Bousquet, F. Dulac, and E. Soares, 1997: Origins of African dust transported over the northeastern tropical Atlantic. *J. Geophys. Res.*, **102**, 10.1029/97JD00259.

Chiapello, I., C. Moulin, and J. M. Prospero, 2005: Understanding the long–term variability of African dust transport across the Atlantic as recorded in both Barbados surface concentrations and large–scale Total Ozone Mapping Spectrometer (TOMS) optical thickness. *J. Geophys. Res.*, **110**, 10.1029/2004JD005132.

Cooke, W., B. Koffi, and J.-M. Grégoire, 1996: Seasonality of vegetation fires in Africa from remote sensing data and application to a global chemistry model. *J. Geophys. Res.*, **101**, 10.1029/96JD01835.

DeTomasi, F., A. Blanco, and M. R. Perrone, 2003: Raman lidar monitoring of extinction and backscattering of African dust layers and dust characterization. *Appl. Opt.*, **42**, 10.1364/AO.42.001699.

Dinter, T., W. von Hoyningen-Huene, J. P. Burrows, A. Kokhanovsky, E. Bierwirth, M. Wendisch, D. Müller, R. Kahn, and M. Diouri, 2009: Retrieval of aerosol optical thickness for desert conditions using MERIS observations during the SAMUM campaign. *Tellus*, **61B**, 10.1111/j.1600-0889.2008.00391.x.

Draxler, R. R. and G. D. Rolph, 2003: HYSPLIT (Hybrid Single–Particle Lagrangian Integrated Trajectory). Model access via NOAA ARL READY Website: http://www.arl.noaa.gov/ready/hysplit4.html.

Dubovik, O., A. Sinyuk, T. Lapyonok, B. N. Holben, M. Mishchenko, P. Yang, T. F. Eck, H. Volten, and coauthors, 2006: Application of spheroid models to account for aerosol particle nonsphericity in remote sensing of desert dust. *J. Geophys. Res.*, **111**, 10.1029/2005JD006619.

Duce, R. A., C. K. Unni, B. J. Ray, J. M. Prospero, and J. T. Merrill, 1980: Long–range atmospheric transport of soil dust from Asia to the tropical North Pacific: temporal variability. *Science*, **209**, science.209.4464.1522.

Eck, T. F., B. N. Holben, J. S. Reid, O. Dubovik, A. Smirnov, N. T. O'Neill, I. Slutsker, and S. Kinne, 1999: Wavelength dependence of the optical depth of biomass burning, urban, and desert dust aerosols. *J. Geophys. Res.*, **104**, 10.1029/1999JD900923.

Eck, T. F., B. N. Holben, A. Sinyuk, R. T. Pinker, P. Goloub, H. Chen, B. Chatenet, Z. Li, and coauthors, 2010: Climatological aspects of the optical properties of fine/coarse mode aerosol mixtures. *J. Geophys. Res.*, **115**, 10.1029/2010JD014002.

Eloranta, E. E., 2005: *High Spectral Resolution Lidar*, in: LIDAR: Range–Resolved Optical Remote Sensing of the Atmosphere, ed. by C. Weitkamp, Springer. 143–163.

Engelstaedter, S., I. Tegen, and R. Washington, 2006: North African dust emissions and transport. *Earth–Science Reviews*, **79**, 10.1016/j.earscirev.2006.06.004.

Engelstaedter, S. and R. Washington, 2007: Atmospheric controls on the annual cycle of North African dust. *J. Geophys. Res.*, **112**, 10.1029/2006JD007195.

Engelmann, R., A. Ansmann, M. Tesche, P. Seifert, D. Althausen, J. Fruntke, U. Wandiger, I. Mattis, and D. Müller, 2011: Doppler lidar observations of horizontal and vertical wind fields in aerosol layers over Cape Verde during SAMUM–2. *Tellus*, **63B**, submitted.

Esselborn, M., M. Wirth, A. Fix, M. Tesche, and G. Ehret, 2008: Airborne high spectral resolution lidar for measuring aerosol extinction and backscatter coefficients. *Appl. Opt.*, **47**, 10.1364/AO.47.000346.

Esselborn, M., M. Wirth, A. Fix, B. Weinzierl, K. Rasp, M. Tesche, and A. Petzold, 2009: Spatial distribution and optical properties of Saharan dust observed by airborne high spectral resolution lidar during SAMUM 2006. *Tellus*, **61B**, 10.1111/j.1600-0889.2008.00394.x.

Evan, A. T., J. Dunion, J. A. Foley, A. K. Heidinger, and C. S. Velden, 2006: New evidence for a relationship between Atlantic tropical cyclone activity and African dust outbreaks. *Geophys. Res. Lett.*, **33**, 10.1029/2006GL026408.

Evan, A. T. and S. Mukhopadhyay, 2010: African dust over the northern tropical Atlantic: 1955–2008. *J. Appl. Meteor. Climatol.*, **49**, 10.1175/2010JAMC2485.1.

Fernald, F. G., 1984: Analysis of atmospheric lidar observations: some comments. *Appl. Opt.*, **23**, 10.1364/AO.23.000652.

Fiebig, M., A. Petzold, U. Wandinger, M. Wendisch, C. Kiemle, A. Stifter, M. Ebert, T. Rother, and U. Leiterer, 2002: Optical closure for an aerosol column: Method, accuracy, and inferable properties applied to a biomass–burning aerosol and its radiative forcing. *J. Geophys. Res.*, **107**, 10.1029/2000JD000192.

Flynn, C. J., A. Mendoza, Y. Zheng, and S. Mathur, 2007: Novel polarization–sensitive micropulse lidar measurement technique. *Opt. Express*, **15**, 10.1364/OE.15.002785.

Franke, K., A. Ansmann, D. Müller, and D. Althausen, 2001: One–year observations of particle lidar ratio over the tropical Indian Ocean with Raman lidar. *Geophys. Res. Lett.*, **28**, 10.1029/2001GL013671.

Franke, K., A. Ansmann, D. Müller, D. Althausen, C. Venkataraman, M. S. Reddy, F. Wagner, and R. Scheele, 2003: Optical properties of the Indo–Asian haze layer over the tropical Indian Ocean. *J. Geophys. Res.*, **108**, 10.1029/2002JD002473.

Freudenthaler, V., M. Esselborn, M. Wiegner, B. Heese, M. Tesche, A. Ansmann, D. Müller, D. Althausen, M. Wirth, A. Fix, G. Ehret, P. Knippertz, C. Toledano, J. Gasteiner, M. Garhammer, and M. Seefeldner, 2009: Depolarization–ratio profiling at several wavelengths in pure Saharan dust during SAMUM 2006. *Tellus*, **61B**, 10.1111/j.1600-0889.2008.00396.x.

Garrison, V. H., E. A. Shinn, W. T. Foreman, D. W. Griffin, C. W. Holmes, C. A. Kellogg, M. S. Majewski, L. L. Richardson, K. B. Ritchie, and G. W. Smith, 2003: African and Asian dust: from desert soils to coral reefs. *BioScience*, **53**, 469–480.

Gasteiger, J., M. Wiegner, C. Toledano, S. Groß, V. Freudenthaler, M. Tesche, and K. Kandler, 2011: Modelling of scattering properties of non–spherical particles. *Tellus*, **63B**, submitted.

Gimmestad, G. G., 2008: Reexamination of depolarization in lidar measurements. *Appl. Opt.*, **47**, 10.1364/AO.47.003795.

Ginoux, P., J. M. Prospero, O. Torres, and M. Chin, 2004: Long–term simulation of global dust distribution with the GOCART model: Correlation with North Atlantic Oscillation. *Environmental Modelling & Software*, **19**, 10.1016/S1364-8152(03)00114-2.

Goudie, A. S. and N. J. Middleton, 2001: Saharan dust storms: Nature and consequences. *Earth–Science Reviews*, **56**, 10.1016/S0012-8252(01)00067-8.

Grein, M., 2006: *Charakterisierung und Erweiterung der Empfängeroptik des IfT–Ramanlidars MARTHA für kombinierte Aerosol- und Wolkenmessungen*. Diploma Thesis (in German), University of Leipzig.
URL `http://lidar.tropos.de/en/publikation/publist_dd.html`

Groß, S., M. Tesche, V. Freudenthaler, C. Toledano, M. Wiegner, A. Ansmann, D. Althausen, and M. Seefeldner, 2011a: Characterization of Saharan dust, marine aerosols and a mixture of biomass burning aerosols and dust by means of multiwavelength depolarization and Raman measurements during SAMUM–2. *Tellus*, **63B**, submitted.

Groß, S., V. Freudenthaler, M. Wiegner, A. Greiß, M. Tesche, J. Gasteiger, A. Schladitz, and C. Toledano, 2011b: Characterization of the planetary boundary layer during SAMUM–2 by means of lidar measurements. *Tellus*, **63B**, accepted.

Hair, J. W., L. M. Caldwell, D. A. Krueger, and C.-Y. She, 2001: High–spectral–resolution lidar with iodine–vapor filters: Measurement of atmospheric–state and aerosol profiles. *Appl. Opt.*, **40**, 10.1364/AO.40.005280.

Haustein, K., C. Pérez, J. M. Baldasano, D. Müller, M. Tesche, A. Schladitz, V. Freudenthaler, B. Heese, M. Esselborn, B. Weinzierl, K. Kandler, and W. von

Hoyningen-Huene, 2009: Regional dust model performance during SAMUM 2006. *Geophys. Res. Lett.*, **36**, 10.1029/2008GL036463.

Haywood, J. M., J. Pelon, P. Formenti, N. Bharmal, M. Brooks, G. Capes, P. Chazette, C. Chou, S. Christopher, H. Coe, and coauthors, 2008: Overview of the Dust and Biomass–burning Experiment and African Monsoon Multidisciplinary Analysis Special Observing Period–0. *J. Geophys. Res.*, **113**, 10.1029/2008JD010077.

Heese, B., V. Freudenthaler, M. Seefeldner, and M. Wiegner, 2002: POLIS: A new POrtable LIdar System for ground–based and airborne measurements of aerosols and clouds. In: *Lidar Remote Sensing in Atmospheric and Earth Sciences*, L. R. Bissonnette, G. Roy, and G. Vallee, Eds., 71–74.

Heese, B. and M. Wiegner, 2008: Vertical aerosol profiles from Raman polarization lidar observations during the dry season AMMA field campaign. *J. Geophys. Res.*, **113**, 10.1029/2007JD009487.

Heese, B., D. Althausen, T. Dinter, M. Esselborn, T. Müller, M. Tesche, and M. Wiegner, 2009: Vertically resolved dust optical properties during SAMUM: Tinfou compared to Ouarzazate. *Tellus*, **61B**, 10.1111/j.1600-0889.2008.00404.x.

Heinold, B., I. Tegen, M. Esselborn, K. Kandler, P. Knippertz, D. Müller, A. Schladitz, M. Tesche, B. Weinzierl, and coauthors, 2009: Regional Saharan dust modelling during the SAMUM 2006 campaign. *Tellus*, **61B**, 10.1111/j.1600-0889.2008.00387.x.

Heinold, B., I. Tegen, M. Esselborn, K. Kandler, P. Knippertz, D. Müller, A. Schladitz, M. Tesche, B. Weinzierl, and coauthors, 2011a: Regional modelling of Saharan dust and land fire smoke: Model description and validation. *Tellus*, **63B**, submitted.

Heinold, B., I. Tegen, S. Bauer, and M. Wendisch, 2011b: Regional modelling of radiative effects and feedbacks of Saharan dust and biomass burning aerosol. *Tellus*, **63B**, submitted.

Heintzenberg, J., 2009: The SAMUM–1 experiment over southern Morocco: Overview and introduction. *Tellus*, **61B**, 10.1111/j.1600-0889.2008.00403.x.

Hinkley, E. D., Ed., 1976: *Laser monitoring of the atmosphere*. Springer, 396 pages.

Holben, B. N., T. F. Eck, I. Slutsker, D. Tanré, J. P. Buis, A. Setzer, E. Vermote, J. A. Reagan, Y. J. Kaufman, T. Nakajima, F. Lavenu, I. Jankowiak, and A. Smirnov, 1998: AERONET—A federated instrument network and data archive for aerosol characterization. *Remote Sens. Environm.*, **66**, 10.1016/S0034-4257(98)00031-5.

Holben, B. N., D. Tanré, A. Smirnov, T. F. Eck, I. Slutsker, N. Abuhassan, W. W. Newcomb, J. S. Schafer, B. Chatenet, and coauthors, 2001: An emerging ground–based aerosol climatology: Aerosol optical depth from AERONET. *J. Geophys. Res.*, **106**, 10.1029/2001JD900014.

Huang, J., C. Zhang, and J. M. Prospero, 2010: African dust outbreaks: A satellite perspective of temporal and spatial variability over the tropical Atlantic Ocean. *J. Geophys. Res.*, **115**, 10.1029/2009JD012516.

Huneeus, N. and O. Boucher, 2007: One–dimensional variational retrieval of aerosol extinction coefficient from synthetic LIDAR and radiometric measurements. *J. Geophys. Res.*, **112**, 10.1029/2006JD007625.

Husar, R. B., D. M. Tratt, B. A. Schichtel, S. R. Falke, F. Li, D. Jaffe, S. Gassó, T. Gill, N. S. Laulainen, F. Lu, and coauthors, 2001: Asian dust events of April 1998. *J. Geophys. Res.*, **106**, 10.1029/2000JD900788.

Johnson, B. T., S. R. Osborne, J. M. Haywood, and M. A. J. Harrison, 2008a: Aircraft measurements of biomass burning aerosol over West Africa during DABEX. *J. Geophys. Res.*, **113**, 10.1029/2007JD009451.

Johnson, B. T., B. Heese, S. A. McFarlane, P. Chazette, A. Jones, and N. Bellouin, 2008b: Vertical distribution and radiative effects of mineral dust and biomass burning aerosol over West Africa during DABEX. *J. Geophys. Res.*, **113**, 10.1029/2008JD009848.

Kaaden, N., A. Massling, A. Schladitz, T. Müller, K. Kandler, L. Schütz, B. Weinzierl, A. Petzold, M. Tesche, and coauthors, 2009: State of mixing, shape factor, number size distribution, and hygroscopic growth of the Saharan anthropogenic and mineral dust aerosol at Tinfou, Morocco. *Tellus*, **61B**, 10.1111/j.1600-0889.2008.00388.x.

Kahn, R., A. Petzold, M. Wendisch, E. Bierwirth, T. Dinter, M. Esselborn, M. Fiebig, B. Heese, P. Knippertz, and coauthors, 2009: Desert dust aerosol air mass mapping in the western Sahara, using particle properties derived from space–based multi–angle imaging. *Tellus*, **61B**, 10.1111/j.1600-0889.2008.00398.x.

Kalashnikova, O. V., R. Kahn, I. N. Sokolik, and W.-H. Li, 2005: Ability of multiangle remote sensing observations to identify and distinguish mineral dust types: Optical models and retrievals of optically thick plumes. *J. Geophys. Res.*, **110**, 10.1029/2004JD004550.

Kalu, A. E., 1979: The African dust plume: Its characteristics and propagation across West Africa in winter. *SCOPE*, **14**, 95–118.

Kandler, K., L. Schütz, C. Deutscher, M. Ebert, H. Hofmann, S. Jäckel, R. Jaenicke, P. Knippertz, K. Lieke, and coauthors, 2009: Size distribution, mass concentration, chemical and mineralogical composition, and derived optical parameters of the boundary layer aerosol at Tinfou, Morocco, during SAMUM 2006. *Tellus*, **61B**, 10.1111/j.1600-0889.2008.00385.x.

Kandler, K., K. Lieke, N. Benker, M. Küpper, C. Emmel, D. Müller-Ebert, M. Ebert, A. Schladitz, L. Schütz, and S. Weinbruch, 2011: Ground–based off–line aerosol measurements at Praia, Cape Verde, during the Saharan Mineral Dust Experiment

campaign, Part 2: Electron–microscopical individual particle analysis. *Tellus*, **63B**, submitted.

Karyampudi, V. M., S. P. Palm, J. A. Reagen, H. Fang, W. B. Grant, R. M. Hoff, C. Moulin, H. F. Pierce, O. Torres, E. V. Browell, and S. H. Melfi, 1999: Validation of the Saharan dust plume conceptual model using lidar. *Bull. Am. Meteorol. Soc.*, **80**, 1045–1075.

Kaufman, Y. J., A. Smirnov, B. N. Holben, and O. Dubovik, 2001: Baseline maritime aerosol: Methodology to derive the optical thickness and scattering properties. *Geophys. Res. Lett.*, **28**, 10.1029/2001GL013312.

Kaufman, Y. J., D. Tanré, J.-F. Léon, and J. Pelon, 2003: Retrievals of profiles of fine and coarse aerosols using lidar and radiometric space measurements. *IEEE Trans. Geosci. Remote Sens.*, **41**, 10.1109/TGRS.2003.814138.

Kaufman, Y. J., I. Koren, L. A. Remer, D. Tanré, P. Ginoux, and S. Fan, 2005: Dust transport and deposition observed from the Terra–Moderate Resolution Imaging Spectroradiometer (MODIS) spacecraft over the Atlantic Ocean. *J. Geophys. Res.*, **110**, 10.1029/2003JD004436.

Klett, J. D., 1981: Stable analytical inversion solution for processing lidar returns. *Appl. Opt.*, **20**, 10.1364/AO.20.000211.

Klett, J. D., 1985: Lidar inversion with variable backscatter/extinction ratios. *Appl. Opt.*, **24**, 10.1364/AO.24.001638.

Knippertz, P. and A. H. Fink, 2006: Synoptic and dynamic aspects of an extreme springtime Saharan dust outbreak. *Quart. J. Roy. Meteorol. Soc.*, **132**, 10.1256/qj.05.109.

Knippertz, P., C. Deutscher, K. Kandler, T. Müller, O. Schulz, and L. Schütz, 2007: Dust mobilization due to density currents in the Atlas region: Observations from the SAMUM 2006 field campaign. *J. Geophys. Res.*, **112**, 10.1029/2007JD008774.

Knippertz, P., 2008: Dust mobilization in the West African heat trough—the role of the diurnal cycle and of extratropical synoptic disturbances. *Meteorol. Zeitschr.*, **17**, 553–563.

Knippertz, P., A. Ansmann, D. Althausen, D. Müller, M. Tesche, E. Bierwirth, T. Dinter, T. Müller, W. von Hoyningen-Huene, and coauthors, 2009: Dust mobilization and transport in the northern Sahara during SAMUM 2006—A meteorological overview. *Tellus*, **61B**, 10.1111/j.1600-0889.2008.00380.x.

Knippertz, P., M. Tesche, B. Heinold, K. Kandler, and C. Toledano, 2011: Dust mobilization and transport from West Africa to Cape Verde—A meteorological overview of SAMUM–2. *Tellus*, **63B**, accepted.

Kolgotin, A. and D. Müller, 2008: Theory of inversion with two–dimensional regularization: profiles of microphysical particle properties derived from multiwavelength lidar measurements. *Appl. Opt.*, **47**, 10.1364/AO.47.004472.

Kovalev, V. A., 2004: *Elastic Lidar: Theory, Practice, and Analysis Methods*. John Wiley & Sons, 615 pages.

Lieke, K., K. Kandler, C. Emmel, A. Petzold, B. Weinzierl, D. Scheuvens, M. Ebert, S. Weinbruch, and L. Schütz, 2011: Particle chemical properties in the vertical column based on aircraft observations in the vicinity of Cape Verde. *Tellus*, **63B**, submitted.

Liu, D., Z. Wang, Z. Liu, D. Winker, and C. Trepte, 2008a: A height resolved global view of dust aerosols from the first year CALIPSO lidar measurements. *J. Geophys. Res.*, **113**, 10.1029/2007JD009776.

Liu, M., D. L. Westphal, S. Wang, A. Shimizu, N. Sugimoto, J. Zhou, and Y. Chen, 2003: A high–resolution numerical study of the Asian dust storms of April 2001. *J. Geophys. Res.*, **108**, 10.1029/2002JD003178.

Liu, Z., I. Matsui, and N. Sugimoto, 1999: High–spectral–resolution lidar using an iodine absorption filter for atmospheric measurements. *Opt. Eng.*, **38**, 10.1117/1.602218.

Liu, Z., N. Sugimoto, and T. Murayama, 2002: Extinction–to–backscatter ratio of Asian dust observed with high–spectral–resolution lidar and Raman lidar. *Appl. Opt.*, **41**, 10.1364/AO.41.002760.

Liu, Z., A. Omar, M. Vaughan, J. Hair, C. Kittaka, Y. Hu, K. Powell, C. Trepte, D. Winker, and coauthors, 2008b: CALIPSO lidar observations of the optical properties of Saharan dust: A case study of long–range transport. *J. Geophys. Res.*, **113**, 10.1029/2007JD008878.

Liu, Z., M. Vaughan, D. Winker, C. Kittaka, B. Getzewich, R. Kuehn, A. Omar, K. Powell, C. Trepte, and C. Hostetler, 2009: The CALIPSO lidar cloud and aerosol discrimination: Version 2 algorithm and initial assessment of performance. *J. Atmos. Oceanic Technol.*, **26**, 10.1175/2009JTECHA1229.1.

Léon, J.-F., D. Tanré, J. Pelon, Y. J. Kaufman, J. M. Haywood, and B. Chatenet, 2003: Profiling of a Saharan dust outbreak based on a synergy between active and passive remote sensing. *J. Geophys. Res.*, **108**, 10.1029/2002JD002774.

Mahowald, N. M., C. Luo, J. del Corral, and C. S. Zender, 2003: Interannual variability in atmospheric mineral aerosols from a 22–year model simulation and observational data. *J. Geophys. Res.*, **108**, 10.1029/2002JD002821.

Mattis, I., A. Ansmann, D. Müller, U. Wandinger, and D. Althausen, 2002: Dual–wavelength Raman lidar observations of the extinction–to–backscatter ratio of Saharan dust. *Geophys. Res. Lett.*, **29**, 10.1029/2002GL014721.

Mattis, I., M. Tesche, M. Grein, V. Freudenthaler, and D. Müller, 2009: Systematic error of lidar profiles caused by a polarization–dependent receiver transmission: quantification and error correction scheme. *Appl. Opt.*, **48**, 10.1364/AO.48.002742.

McGill, M. J., D. L. Hlavka, W. D. Hart, E. J. Welton, and J. R. Campbell, 2003: Airborne lidar measurements of aerosol optical properties during SAFARI–2000. *J. Geophys. Res.*, **108**, 10.1029/2002JD002370.

Measures, R. M., 1984: *Laser Remote Sensing: Fundamentals and Applications*. John Wiley & Sons, 524 pages.

Mie, G., 1908: Beiträge zur Optik trüber Medien, speziell kolloidaler Metallösungen. *Annalen der Physik*, **25**, 377–447.

Mishchenko, M. I., L. D. Travis, R. A. Kahn, and R. A. West, 1997: Modeling phase functions for dustlike tropospheric aerosols using a shape mixture of randomly oriented polydisperse spheroids. *J. Geophys. Res.*, **102**, 10.1029/96JD02110.

Mona, L., A. Amodeo, M. Pandolfi, and G. Pappalardo, 2006: Saharan dust intrusions in the Mediterranean area: Three years of Raman lidar measurements. *J. Geophys. Res.*, **111**, 10.1029/2005JD006569.

Müller, D., U. Wandinger, and A. Ansmann, 1999a: Microphysical particle parameters from extinction and backscatter lidar data by inversion with regularization: Theory. *Appl. Opt.*, **38**, 10.1364/AO.38.002346.

Müller, D., U. Wandinger, and A. Ansmann, 1999b: Microphysical particle parameters from extinction and backscatter lidar data by inversion with regularization: Simulation. *Appl. Opt.*, **38**, 10.1364/AO.38.002358.

Müller, D., F. Wagner, U. Wandinger, A. Ansmann, M. Wendisch, D. Althausen, and W. von Hoyningen-Huene, 2000: Microphysical particle parameters from extinction and backscatter lidar data by inversion with regularization: Experiment. *Appl. Opt.*, **39**, 10.1364/AO.39.001879.

Müller, D., U. Wandinger, D. Althausen, and M. Fiebig, 2001: Comprehensive particle characterization from three–wavelength Raman–lidar observations: Case study. *Appl. Opt.*, **40**, 10.1364/AO.40.004863.

Müller, D., I. Mattis, U. Wandinger, A. Ansmann, D. Althausen, O. Dubovik, S. Eckhardt, and A. Stohl, 2003: Saharan dust over a central European EARLINET–AERONET site: Combined observations with Raman lidar and Sun photometer. *J. Geophys. Res.*, **108**, 10.1029/2002JD002918.

Müller, D., I. Mattis, U. Wandinger, A. Ansmann, D. Althausen, and A. Stohl, 2005: Raman lidar observations of aged Siberian and Canadian forest fire smoke in the free troposphere over Germany in 2003: Microphysical particle characterization. *J. Geophys. Res.*, **110**, 10.1029/2004JD005756.

Müller, D., A. Ansmann, I. Mattis, M. Tesche, U. Wandinger, D. Althausen, and G. Pisani, 2007: Aerosol–type–dependent lidar ratio observed with Raman lidar. *J. Geophys. Res.*, **112**, 10.1029/2006JD008292.

Müller, D., B. Heinold, M. Tesche, I. Tegen, D. Althausen, L. Alados-Arboledas, V. Amiridis, A. Amodeo, A. Ansmann, and coauthors, 2009: EARLINET observations of the 14–22–May long–range dust transport event during SAMUM 2006: validation of results from dust transport modeling. *Tellus*, **61B**, 10.1111/j.1600-0889.2008.00400.x.

Müller, D., B. Weinzierl, A. Petzold, K. Kandler, A. Ansmann, T. Müller, M. Tesche, V. Freudenthaler, M. Esselborn, B. Heese, D. Althausen, A. Schladitz, S. Otto, and P. Knippertz, 2010a: Mineral dust observed with AERONET Sun photometer, Raman lidar, and in situ instruments during SAMUM 2006: Shape–independent particle properties. *J. Geophys. Res.*, **115**, 10.1029/2009JD012520.

Müller, D., A. Ansmann, V. Freudenthaler, K. Kandler, C. Toledano, A. Hiebsch, J. Gasteiger, M. Esselborn, M. Tesche, B. Heese, D. Althausen, B. Weinzierl, A. Petzold, and W. von Hoyningen-Huene, 2010b: Mineral dust observed with AERONET Sun photometer, Raman lidar, and in situ instruments during SAMUM 2006: Shape–dependent particle properties. *J. Geophys. Res.*, **115**, 10.1029/2009JD012523.

Müller, T., A. Schladitz, A. Massling, N. Kaaden, K. Kandler, and A. Wiedensohler, 2009: Spectral absorption coefficients and imaginary parts of refractive indices of Saharan dust during SAMUM–1. *Tellus*, **61B**, 10.1111/j.1600-0889.2008.00399.x.

Müller, T., A. Schladitz, and A. Wiedensohler, 2011: Spectral particle absorption coefficients, single scattering albedos, and imaginary parts of refractive indices at Cape Verde Island during SAMUM–2. *Tellus*, **63B**, submitted.

Murayama, T., H. Okamoto, N. Kaneyasu, H. Kamataki, and K. Miura, 1999: Application of lidar depolarization measurement in the atmospheric boundary layer: Effects of dust and sea–salt particles. *J. Geophys. Res.*, **104**, 10.1029/1999JD900503.

Murayama, T., N. Sugimoto, I. Uno, K. Kinoshita, K. Aoki, N. Hagiwara, Z. Liu, I. Matsui, T. Sakai, and coauthors, 2001: Ground–based network observation of Asian dust events of April 1998 in east Asia. *J. Geophys. Res.*, **106**, 10.1029/2000JD900554.

Murayama, T., S. J. Masonis, J. Redemann, T. L. Anderson, B. Schmid, J. M. Livingston, P. B. Russell, B. Huebert, S. G. Howell, and coauthors, 2003: An intercomparison of lidar–derived aerosol optical properties with airborne measurements near Tokyo during ACE–Asia. *J. Geophys. Res.*, **108**, 10.1029/2002JD003259.

Murayama, T., D. Müller, K. Wada, A. Shimizu, M. Sekiguchi, and T. Tsukamoto, 2004: Characterization of Asian dust and Siberian smoke with multi–wavelength Raman lidar over Tokyo, Japan, in spring 2003. *Geophys. Res. Lett.*, **31**, 10.1029/2004GL021105.

Myhre, G., A. Grini, J. M. Haywood, F. Stordal, B. Chatenet, D. Tanré, J. K. Sundet, and I. S. A. Isaksen, 2003: Modeling the radiative impact of mineral dust during the Saharan Dust Experiment (SHADE) campaign. *J. Geophys. Res.*, **108**, 10.1029/2002JD00256.

Myhre, G., C. R. Hoyle, T. F. Berglen, B. T. Johnson, and J. M. Haywood, 2008: Modeling of the solar radiative impact of biomass burning aerosols during the Dust and Biomass–burning Experiment (DABEX). *J. Geophys. Res.*, **113**, 10.1029/2008JD009857.

Nickovic, S., A. Papadopoulos, O. Kakaliagou, and G. Kallos, 2001: Model for prediction of desert dust cycle in the atmosphere. *J. Geophys. Res.*, **106**, 10.1029/2000JD900794.

Nishizawa, T., H. Okamoto, N. Sugimoto, I. Matsui, A. Shimizu, and K. Aoki, 2007: An algorithm that retrieves aerosol properties from dual–wavelength polarized lidar measurements. *J. Geophys. Res.*, **112**, 10.1029/2006JD007435.

Noh, Y. M., Y. J. Kim, B. C. Choi, and T. Murayama, 2007: Aerosol lidar ratio characteristics measured by a multi–wavelength Raman lidar system at Anmyeon Island, Korea. *Atmos. Res.*, **86**, 10.1016/j.atmosres.2007.03.006.

Nousiainen, T., K. Muinonen, and P. Räisänen, 2003: Scattering of light by large Saharan dust particles in a modified ray optics approximation. *J. Geophys. Res.*, **108**, 10.1029/2001JD001277.

Nousiainen, T., 2009: Optical modeling of mineral dust particles: A review. *Journal of Quantitative Spectroscopy and Radiative Transfer*, **110**, 10.1016/j.jqsrt.2009.03.002.

Omar, A. H., D. M. Winker, J.-G. Won, M. A. Vaughan, C. A. Hostetler, and J. A. Reagan, 2003: Selection algorithm for the CALIPSO lidar aerosol extinction–to–backscatter ratio. *IEEE Geoscience and Remote Sensing Symposium 2003: Proceedings*, **3**, 1526–1530.

Omar, A. H., D. M. Winker, C. Kittaka, M. A. Vaughan, Z. Liu, Y. Hu, C. R. Trepte, R. R. Rogers, R. A. Ferrare, and coauthors, 2009: The CALIPSO automated aerosol classification and lidar ratio selection algorithm. *J. Atmos. Oceanic Technol.*, **26**, 10.1175/2009JTECHA1231.1.

Omar, A. H., Z. Liu, M. Vaughan, K. Thornhill, C. Kittaka, S. Ismail, Y. Hu, G. Chen, K. Powell, D. Winker, C. Trepte, E. Winstead, and B. Anderson, 2010: Extinction–to–backscatter ratios of Saharan dust layers derived from in–situ measurements and CALIPSO overflights during NAMMA. *J. Geophys. Res.*, **115**, 10.1029/2010JD014223.

Otto, S., E. Bierwirth, B. Weinzierl, K. Kandler, M. Esselborn, M. Tesche, M. Wendisch, and T. Trautmann, 2009: Radiative effects of a Saharan dust plume observed during SAMUM assuming non–spherical dust particles. *Tellus*, **61B**, 10.1111/j.1600-0889.2008.00381.x.

Papayannis, A., V. Amiridis, L. Mona, G. Tsaknakis, D. Balis, J. Bösenberg, A. Chaikovski, F. DeTomasi, I. Grigorov, I. Mattis, and coauthors, 2008: Systematic lidar observations of Saharan dust over Europe in the frame of EARLINET (2000–2002). *J. Geophys. Res.*, **113**, 10.1029/2007JD009028.

Parrington, J., W. H. Zoller, and N. K. Aras, 1983: Asian Dust: Seasonal transport to the Hawaiian Islands. *Science 8*, **220**, science.220.4593.195.

Patterson, E. M. and C. K. McMahon, 1984: Absorption characteristics of forest fire particulate matter. *Atmos. Environ.*, **18**, 10.1016/0004-6981(84)90027-1.

Patterson, E. M., C. K. McMahon, and D. E. Ward, 1985: Absorption properties and graphitic carbon emission factors of forest fire smoke. *Geophys. Res. Lett.*, **13**, 10.1029/GL013i002p00129.

Pelon, J., M. Mallet, A. Mariscal, P. Goloub, D. Tanré, D. Bou Karam, C. Flamant, J. Haywood, B. Pospichal, and S. Victori, 2008: Microlidar observations of biomass burning aerosol over Djougou (Benin) during African Monsoon Multidisciplinary Analysis Special Observation Period 0: Dust and Biomass–Burning Experiment. *J. Geophys. Res.*, **113**, 10.1029/2008JD009976.

Pérez, C., S. Nickovic, J. M. Baldasano, M. Sicard, F. Rocadenbosch, and V. E. Cachorro, 2006a: A long Saharan dust event over the western Mediterranean: Lidar, Sun photometer observations, and regional dust modeling. *J. Geophys. Res.*, **111**, 10.1029/2005JD006579.

Pérez, C., S. Nickovic, G. Pejanovic, and J. M. Baldasano, 2006b: Interactive dust–radiation modeling: A step to improve weather forecasts. *J. Geophys. Res.*, **111**, 10.1029/2005JD006717.

Petzold, A., K. Rasp, B. Weinzierl, M. Esselborn, T. Hamburger, A. Dörnbrack, K. Kandler, L. Schütz, P. Knippertz, M. Fiebig, and A. Virkkula, 2009: Saharan dust absorption and refractive index from aircraft–based observations during SAMUM 2006. *Tellus*, **61B**, 10.1111/j.1600-0889.2008.00383.x.

Petzold, A., A. Veira, S. Mund, C. Kiemle, M. Esselborn, and B. Weinzierl, 2011: Modification of dust properties after mixing with anthropogenic pollution. *Tellus*, **63B**, submitted.

Piironen, P. and E. W. Eloranta, 1994: Demonstration of a high–spectral–resolution lidar based on an iodine absorption filter. *Opt. Lett.*, **19**, 10.1364/OL.19.000234.

Platt, C. M. R., 1978: Lidar backscatter from horizontal ice crystal plates. *J. Appl. Meteor.*, **17**, 482–488.

Platt, C. M. R., N. L. Abshire, and G. T. McNice, 1978: Some microphysical properties of an ice cloud from lidar observation of horizontally oriented crystals. *J. Appl. Meteor.*, **17**, 1220–1224.

Prospero, J. M. and T. N. Carlson, 1972: Vertical and areal distribution of Saharan dust over the western equatorial North Atlantic Ocean. *J. Geophys. Res.*, **77**, 5255–5265.

Prospero, J. M. and T. N. Carlson, 1980: Saharan air outbreaks over the tropical North Atlantic. *Pure and Appl. Geophys.*, **119**, 677–691.

Prospero, J. M., P. Ginoux, O. Torres, S. E. Nicholson, and T. E. Gill, 2002: Environmental characterization of global sources of atmospheric soil dust identified with the nimbus 7 Total Ozone Mapping Spectrometer (TOMS) absorbing aerosol product. *Rev. Geophys.*, **40**, 10.1029/2000RG000095.

Reichardt, J., R. Baumgart, and T. J. McGee, 2003: Three–signal method for accurate measurements of depolarization ratio with lidar. *Appl. Opt.*, **42**, 10.1364/AO.42.004909.

Reid, J. S., J. E. Kinney, D. L. Westphal, B. N. Holben, E. J. Welton, S.-C. Tsay, D. P. Eleuterio, J. R. Campbell, and coauthors, 2003: Analysis of measurements of Saharan dust by airborne and ground–based remote sensing methods during the Puerto Rico Dust Experiment (PRIDE). *J. Geophys. Res.*, **108**, 10.1029/2002JD002493.

Reid, J. S., T. F. Eck, S. A. Christopher, R. Koppmann, O. Dubovik, D. P. Eleuterio, B. N. Holben, E. A. Reid, and J. Zhang, 2005: A review of biomass burning emissions part III: intensive optical properties of biomass burning particles. *Atmos. Chem. Phys.*, **5**, 10.5194/acp-5-827-2005.

Reid, J. S., S. J. Piketh, A. L. Walker, R. P. Burger, K. E. Ross, D. L. Westphal, R. T. Bruintjes, B. N. Holben, C. Hsu, and coauthors, 2008: An overview of UAE^2 flight operations: Observations of summertime atmospheric thermodynamic and aerosol profiles of the southern Arabian Gulf. *J. Geophys. Res.*, **113**, 10.1029/2007JD009435.

Russell, P. B. and J. Heintzenberg, 2000: An overview of the ACE–2 clear sky column closure experiment (CLEARCOLUMN). *Tellus*, **52B**, 10.1034/j.1600-0889.2000.00013.x.

Sakai, T., T. Shibata, Y. Iwasaka, T. Nagai, M. Nakazato, T. Matsumura, A. Ichiki, Y.-S. Kim, K. Tamura, D. Troshkin, and S. Hamdi, 2002: Case study of Raman lidar measurements of Asian dust events in 2000 and 2001 at Nagoya and Tsukuba, Japan. *Atmos. Environ.*, **36**, 10.1016/S1352-2310(02)00664-7.

Sakai, T., T. Nagai, Y. Zaizen, and Y. Mano, 2010: Backscattering linear depolarization ratio measurements of mineral, sea–salt, and ammonium sulfate particles simulated in a laboratory chamber. *Appl. Opt.*, **49**, 10.1364/AO.49.004441.

Sasano, Y., E. V. Browell, and S. Ismail, 1985: Error caused by using a constant extinction/backscattering ratio in the lidar solution. *Appl. Opt.*, **24**, 10.1364/AO.24.003929.

Sassen, K., 1974: Depolarization of laser light backscattered by artificial clouds. *J. Appl. Meteor.*, **13**, 923–933.

Sassen, K., 1991: The polarization lidar technique for cloud research: A review and current assessment. *Bull. Amer. Meteor. Soc.*, **72**, 1848–1866.

Sassen, K., 2005: *Polarization in Lidar*, in: LIDAR: Range–Resolved Optical Remote Sensing of the Atmosphere, ed. by C. Weitkamp, Springer. 19–42.

Schepanski, K., I. Tegen, B. Laurent, B. Heinold, and A. Macke, 2007: A new Saharan dust source activation frequency map derived from MSG–SEVIRI IR–channels. *Geophys. Res. Lett.*, **34**, 10.1029/2007GL030168.

Schepanski, K., I. Tegen, and A. Macke, 2009: Saharan dust transport and deposition towards the tropical northern Atlantic. *Atmos. Chem. Phys.*, **9**, 10.5194/acp-9-1173-2009.

Schladitz, A., T. Müller, A. Massling, N. Kaaden, K. Kandler, M. Ebert, S. Weinbruch, C. Deutscher, and A. Wiedensohler, 2009: In situ measurements of optical properties at Tinfou (Morocco) during the Saharan Mineral Dust Experiment SAMUM 2006. *Tellus*, **61B**, 10.1111/j.1600-0889.2008.00397.x.

Schotland, R. M., K. Sassen, and R. Stone, 1971: Observations by lidar of linear depolarization ratios for hydrometeors. *J. Appl. Meteor*, **10**, 1011–1017.

Shimizu, H., S. A. Lee, and C. Y. She, 1983: High spectral resolution lidar system with atomic blocking filters for measuring atmospheric parameters. *Appl. Opt.*, **22**, 10.1364/AO.22.001373.

Shimizu, A., N. Sugimoto, I. Matsui, K. Arao, I. Uno, T. Muramaya, N. Kagawa, K. Aoki, A. Uchiyama, and A. Yamazaki, 2004: Continuous observations of Asian dust and other aerosols by polarization lidars in China and Japan during ACE–Asia. *J. Geophys. Res.*, **109**, 10.1029/2002JD003253.

Shipley, S. T., D. H. Tracy, E. W. Eloranta, J. T. Trauger, J. T. Sroga, F. L. Roesler, and J. A. Weinman, 1983: High spectral resolution lidar to measure optical scattering properties of atmospheric aerosols. 1: Theory and instrumentation. *Appl. Opt.*, **22**, 10.1364/AO.22.003716.

Sinyuk, A., O. Torres, and O. Dubovik, 2003: Combined use of satellite and surface observations to infer the imaginary part of refractive index of Saharan dust. *Geophys. Res. Lett.*, **30**, 10.1029/2002GL016189.

Slingo, A., T. P. Ackerman, R. P. Allan, E. I. Kassianov, S. A. McFarlane, G. J. Robinson, J. C. Barnard, M. A. Miller, J. E. Harries, J. E. Russell, and S. Dewitte, 2006: Observations of the impact of a major Saharan dust storm on the atmospheric radiation balance. *Geophys. Res. Lett.*, **33**, 10.1029/2006GL027869.

Sokolik, I. N., D. M. Winker, G. Bergametti, D. A. Gillette, G. Carmichael, Y. J. Kaufman, L. Gomes, L. Schütz, and J. E. Penner, 2001: Introduction to special section: Outstanding problems in quantifying the radiative impacts of mineral dust. *J. Geophys. Res.*, **106**, 10.1029/2000JD900498.

Su, J., M. P. McCormick, Z. Liu, K. H. Leavor, R. B. Lee III, J. Lewis, and M. T. Hill, 2010: Obtaining ground–based lidar geometrical form factor using coincident spaceborne lidar measurements. *Appl. Opt.*, 10.1364/AO.49.000108.

Sugimoto, N., I. Uno, M. Nishikawa, A. Shimizu, I. Matsui, X. Dong, Y. Chen, and H. Quan, 2003: Record heavy Asian dust in Beijing in 2002: Observations and model analysis of recent events. *Geophys. Res. Lett.*, **30**, 10.1029/2002GL016349.

Sugimoto, N. and C. H. Lee, 2006: Characteristics of dust aerosols inferred from lidar depolarization measurements at two wavelengths. *Appl. Opt.*, **45**, 10.1364/AO.45.007468.

Sun, D., K. M. Lau, and M. Kafatos, 2008: Contrasting the 2007 and 2005 hurricane seasons: Evidence of possible impacts of Saharan dry air and dust on tropical cyclone activity in the Atlantic basin. *Geophys. Res. Lett.*, **35**, 10.1029/2008GL034529.

Tanré, D., J. Haywood, J. Pelon, J. F. Léon, B. Chatenet, P. Formenti, P. Francis, P. Goloub, E. J. Highwood, and G. Myhre, 2003: Measurement and modeling of the Saharan dust radiative impact: Overview of the Saharan Dust Experiment (SHADE). *J. Geophys. Res.*, **108**, 10.1029/2002JD003273.

Tesche, M., A. Ansmann, D. Müller, D. Althausen, R. Engelmann, M. Hu, and Y. Zhang, 2007: Particle backscatter, extinction, and lidar ratio profiling with Raman lidar in South and North China. *Appl. Opt.*, **46**, 10.1364/AO.46.006302.

Tesche, M., D. Müller, A. Ansmann, M. Hu, and Y. Zhang, 2008: Retrieval of microphysical properties of aerosol particles from one–wavelength Raman lidar and multiwavelength Sun photometer observations. *Atmos. Envir.*, **42**, 10.1016/j.atmosenv.2008.02.014.

Tesche, M., A. Ansmann, D. Müller, D. Althausen, I. Mattis, B. Heese, V. Freudenthaler, M. Wiegner, M. Esselborn, G. Pisani, and P. Knippertz, 2009a: Vertical profiling of Saharan dust with Raman lidars and airborne HSRL in southern Morocco during SAMUM. *Tellus*, **61B**, 10.1111/j.1600-0889.2008.00390.x.

Tesche, M., A. Ansmann, D. Müller, D. Althausen, R. Engelmann, V. Freudenthaler, and S. Groß, 2009b: Vertically resolved separation of dust and smoke over Cape Verde by using multiwavelength Raman and polarization lidars during Saharan Mineral Dust Experiment 2008. *J. Geophys. Res.*, **114**, 10.1029/2009JD011862.

Tesche, M., A. Ansmann, D. Müller, D. Althausen, S. Groß, V. Freudenthaler, and M. Esselborn, 2011a: Profiling of Saharan dust and biomass–burning smoke with multiwavelength polarization Raman lidar at Cape Verde. *Tellus*, **63B**, accepted.

Tesche, M., A. Ansmann, D. Müller, A. Althausen, I. Mattis, V. Freudenthaler, S. Groß, B. Weinzierl, and A. Petzold, 2011b: Microphysical properties of biomass–burning smoke over Cape Verde as inferred from multiwavelength polarization Raman lidar measurements. *Tellus*, **63B**, accepted.

Toledano, C., M. Wiegner, M. Garhammer, M. Seefeldner, J. Gasteiger, D. Müller, and P. Koepke, 2009: Spectral aerosol optical depth characterization of desert dust during SAMUM 2006. *Tellus*, **61B**, 10.1111/j.1600-0889.2008.00382.x.

Toledano, C., M. Wiegner, S. Groß, V. Freudenthaler, J. Gasteiger, D. Müller, T. Müller, A. Schladitz, B. Torres, and N. O'Neill, 2011: Sun photometer observations during SAMUM 2008: Retrieval of spectral particle optical depth, Ångström exponents, and microphysical properties. *Tellus*, **63B**, submitted.

Uematsu, M., R. A. Duce, J. M. Prospero, L. Chen, J. T. Merrill, and R. L. McDonald, 1983: Transport of mineral aerosol from Asia over the North Pacific Ocean. *J. Geophys. Res.*, **88**, 5343–5352.

Uno, I., K. Yumimoto, A. Shimizu, Y. Hara, N. Sugimoto, Z. Wang, Z. Liu, and D. M. Winker, 2008: 3D structure of Asian dust transport revealed by CALIPSO lidar and a 4DVAR dust model. *Geophys. Res. Lett.*, **35**, 10.1029/2007GL032329.

van de Hulst, H. C., 1957: *Light Scattering by Small Particles*. Dover Publications, 470 pages.

VanCuren, R. and T. Cahill, 2002: Asian aerosols in North America: Frequency and concentration of fine dust. *J. Geophys. Res.*, **107**, 10.1029/2002JD002204.

Veselovskii, I., A. Kolgotin, V. Griaznov, D. Müller, U. Wandinger, and D. N. Whiteman, 2002: Inversion with regularization for the retrieval of tropospheric aerosol parameters from multiwavelength Raman lidar sounding. *Appl. Opt.*, **41**, 10.1364/AO.41.003685.

Volten, H., O. Muñoz, E. Rol, J. de Haan, W. Vassen, J. Hovenier, K. Muinonen, and T. Nousiainen, 2001: Scattering matrices of mineral aerosol particles at 441.6 nm and 632.8 nm. *J. Geophys. Res.*, **106**, 10.1029/2001JD900068.

Wandinger, U., D. Müller, C. Böckmann, D. Althausen, V. Matthias, J. Bösenberg, V. Weiß, M. Fiebig, M. Wendisch, A. Stohl, and A. Ansmann, 2002: Optical and microphysical characterization of biomass–burning and industrial pollution aerosols from multiwavelength lidar and aircraft measurements. *J. Geophys. Res.*, **107**, 10.1029/2000JD000202.

Wandinger, U. and A. Ansmann, 2002: Experimental determination of the lidar overlap profile with Raman lidar. *Appl. Opt.*, **41**, 10.1364/AO.41.000511.

Wandinger, U., 2005a: *Introduction to Lidar*, in: LIDAR: Range–Resolved Optical Remote Sensing of the Atmosphere, ed. by C. Weitkamp, Springer. 1–18.

Wandinger, U., 2005b: *Raman Lidar*, in: LIDAR: Range–Resolved Optical Remote Sensing of the Atmosphere, ed. by C. Weitkamp, Springer. 241–271.

Wandinger, U., M. Tesche, P. Seifert, A. Ansmann, D. Müller, and D. Althausen, 2010: Size matters: Influence of multiple scattering on CALIPSO light–extinction profiling in desert dust. *Geophys. Res. Lett.*, **37**, 10.1029/2010GL042527.

Washington, R. and M. C. Todd, 2005: Synoptic and dynamic aspects of an extreme springtime Saharan dust outbreak. *Geophys. Res. Lett.*, **32**, 10.1029/2005GL023597.

Weinzierl, B., A. Petzold, M. Esselborn, M. Wirth, K. Rasp, K. Kandler, L. Schütz, P. Koepke, and M. Fiebig, 2009: Airborne measurements of dust layer properties, particle size distribution and mixing state of Saharan dust during SAMUM 2006. *Tellus*, **61B**, 10.1111/j.1600-0889.2008.00392.x.

Weinzierl, B., A. Petzold, M. Esselborn, M. Wirth, and K. Rasp, 2011: Airborne observations of dust and smoke layers based on Falcon in situ and HSR lidar observations. *Tellus*, **63B**, submitted.

Weitkamp, C., Ed., 2005: *LIDAR: Range–resolved optical remote sensing of the atmosphere*. Springer, 460 pages.

Wernli, H. and H. C. Davies, 1997: A Lagrangian–based analysis of extratropical cyclones, I: the method and some applications. *Quart. J. Roy. Meteorol. Soc.*, **123**, 10.1002/qj.49712353811.

Westbrook, C. D., A. J. Illingworth, E. J. O'Connor, and R. J. Hogan, 2010: Doppler lidar measurements of oriented planar ice crystals falling from supercooled and glaciated layer clouds. *Q. J. R. Meteorol. Soc.*, **136**, 10.1002/qj.528.

Wiegner, M., H. Quenzel, D. Rabus, W. Volker, P. Volger, J. Ackermann, C. Kahler, F. Fergg, and G. Wildgruber, 1995: Mobile three–wavelength backscatter lidar of the Meteorological Institute of the University of Munich. *Proc. SPIE*, **2505**, 10.1117/12.219632.

Wiegner, M., J. Gasteiger, K. Kandler, B. Weinzierl, K. Rasp, M. Esselborn, V. Freudenthaler, B. Heese, C. Toledano, M. Tesche, and D. Althausen, 2009: Numerical simulations of optical properties of Saharan dust aerosols with emphasis on linear depolarization ratio. *Tellus*, **61B**, 10.1111/j.1600-0889.2008.00381.x.

Winker, D. M., M. A. Vaughan, A. Omar, Y. Hu, K. A. Powell, Z. Liu, W. H. Hunt, and S. A. Young, 2009: Overview of the CALIPSO mission and CALIOP data processing algorithms. *J. Atmos. Oceanic Technol.*, **26**, 10.1175/2009JTECHA1281.1.

Wu, L., 2007: Impact of Saharan air layer on hurricane peak intensity. *Geophys. Res. Lett.*, **34**, 10.1029/2007GL029564.

Young, S. A. and M. A. Vaughan, 2009: The retrieval of profiles of particulate extinction from Cloud–Aerosol Lidar Infrared Pathfinder Satellite Observations (CALIPSO) data: Algorithm description. *J. Atmos. Oceanic Technol.*, **26**, 10.1175/2008JTECHA1221.1.

Acknowledgment

I would like to thank all the people that enabled and supported this work.

First of all I thank Prof. Dr. Jost Heintzenberg and Prof. Dr. Lucas Alados Arboledas for reviewing the thesis.

I want to express my gratitude to Albert Ansmann who taught me how to handle aerosol lidar data. His supervision of this work kept me from loosing track and his curiosity for new results has been a great motivation.

I like to thank Detlef Müller for introducing me to the world of the microphysical inversion of lidar data and for the confidence he has in my findings. Sometimes it's really hard to trust any of the reasonable results.

I specially like to thank Ulla Wandinger for her patience and accuracy in proofreading this thesis. Her corrections certainly increased the quality of the text. A blank page has always been a triumph.

To participate in all the field campaigns during the last years was plenty of fun. For this I want to thank the people who usually have to take BERTHA out and are a guarantee for smooth and successful field measurements. In particular I want to thank Helgard Hube who always makes sure that we have all the things we are looking for—in the field and at home. It really is hard work to collect useful lidar data and special thanks go to Dietrich Althausen who always kept BERTHA running and taught me how to operate this monster. He patiently answered all questions about the system and was of great help for all the calibration measurements.

I am grateful to Ina Mattis, Ronny Engelmann, and Patric Seifert for providing me with *ILDA* and *lidar_eval_gui* and for the help I got when I encountered problems with their software or demanded new features.

Also, I would like to thank the entire lidar group of IfT for the pleasant and creative environment in which work doesn't really feel like work. Generally, I want to say thanks for the great atmosphere at this institute—during work as well as during badminton or basketball matches.

The SAMUM experiments were very successful, most of all because of the excellent cooperation between all the participants. I specially like to thank Volker Freudenthaler and Silke Groß of Munich University who taught me a lot about depolarization measurements and how things can't be done. I also like to thank Michael Esselborn and Bernadett Weinzierl of DLR for the fruitful cooperation. Our constant sharing of

results enabled an incredibly comprehensive analysis of the SAMUM measurements.

Last but not least I want to thank my family who understood my shortage of time during the last years and always supported my plans. Regretfully, I discover that most of them did not live to see me succeed. At last, I like to express my special gratitude to my beloved Peggy even though she has been quite annoying with her constant complaint that it's time to finish this thesis. Here you go!